Dynamics of outflows driven by winds from supermassive black holes

Lewis Green
B.Sc. (Hons.) Keele

Doctor of Philosophy

Department of Physics, Keele University

December 2019

Abstract

Feedback is a key element of galaxy evolution, and the accretion of gas onto a central supermassive black hole (SMBH) is an important source of feedback. Modelling the energy released as an optically thick wind (with speed v_w) allows observable relationships between galactic properties to be derived. Models of wind feedback predict that the momentum-flux of an outflow at large scales will exceed that of the wind source. This so-called momentum-boosting of large-scale outflows and the presence of small-scale winds have both been observed in many local active galaxies. This thesis analyses the dynamical properties of wind-driven shells in order to investigate momentum-boosting in active galaxies and the observed correlation between SMBH mass ($M_{\rm BH}$) and stellar velocity dispersion (σ).

The effects of ambient gas pressure on wind-driven shells are analysed and it is shown that shells can be become confined by this pressure. The inclusion of ambient pressure is also shown to formally alter previously derived $M_{\rm BH} - \sigma$ relations. For energy-driven shells at large scales it is found that there is an upper limit to momentum-boosting for a given $M_{\rm BH} v_w$ combination, and that maximum possible boosting occurs for a fixed ratio of wind and shell kinetic energies. It is demonstrated that observed large-scale outflows have momentum-boosts which are consistent with maximal boosting, and therefore such a scenario may be commonplace for large-scale outflows. By considering maximally boosted shells an $M_{\rm BH} - \sigma$ relation is derived which allows for the interpretation of the scatter in the $M_{\rm BH} - \sigma$ data as a distribution in momentum-boosts.

These conclusions and the dynamics of shells are further examined for the case of a growing SMBH and therefore a non-steady wind. It is shown that infalling shells are capable of resuming outward motion due to the ever-growing wind force, and that conditions required for shells to be driven to large radii are not significantly different from the steady wind case. The conclusions regarding maximal momentum-boosting for steady winds are demonstrated to still be valid for non-steady winds.

Acknowledgements

My sincere thanks go to Dean McLaughlin for all of his supervision, assistance and support as I undertook this research. You gave me the first chance to study physics many years ago, and I truly appreciate all of your help.

I give thanks to Keele University for being my home for so long, and to all of the institutions which provide research funding here.

To Rachel who means the world to me, you make my life better with every passing day, and I don't know where I'd be without you. My thanks go out to my family whose support and kindness have always been essential to me.

And to Harvey, you will never be forgotten.

Lewis Green
Keele Astrophysics Group
October 2018

Contents

List of Figures

List of Tables

1 Introduction

For nearly a century galaxies have been studied as fundamental structures within the universe, yet their formation remains an open problem in modern astrophysics. As we now know it is dark matter haloes which are the fundamental units of cosmic structure. These haloes form out of density perturbations in the early universe, and grow hierarchically through the gradual addition of further dark matter to strongly bound cores (e.g., the review of Frenk & White 2012). It is within these haloes where baryonic matter condenses to form stars. The subsequent evolution of the galaxy depends on the hydrodynamical evolution of the constituent gaseous medium, and the effects produced during the formation of stars and supermassive black holes (SMBHs).

Stars, gas, and dark matter are the quintessential constituents of galaxies, but there is mounting observational evidence to suggest that central SMBHs are also present within all large galaxies (see Kormendy & Ho 2013 for a review). This has led to the discovery that the mass of the SMBH ($M_{\rm BH}$) correlates with global properties of its host galaxy. The most prominent of these correlations with the SMBH mass are with bulge luminosity; $L_{\rm bulge}$ and bulge mass; $M_{\rm bulge}$ (Magorrian et al. 1998), and stellar velocity dispersion; σ (Ferrarese & Merritt 2000; Gebhardt et al. 2000). These correlations may be the result of primary correlations between the SMBH mass and properties of the dark matter halo (Ferrarese 2002; Volonteri, Natarajan & Gültekin 2011; Larkin & McLaughlin 2016). The sphere of influence of an SMBH is far too small to permit any current causal connection between the black hole gravity and these global galactic properties. Therefore, these phenomenological correlations are thought to be indicative of coevolution between the SMBH and the galaxy (Kormendy & Richstone 1995). Such coevolution may be through a process within the gaseous protogalaxy which causes the growth of the SMBH to affect the structure of its host, which in turn leads to the cessation of further black hole growth. Such a process is an example of *feedback* (Silk & Rees 1998; Haehnelt, Natarajan & Rees 1998).

SMBHs have masses in the range: $M_{\rm BH} \sim 10^6 - 10^9 M_\odot$, and have grown primarily

through the accretion of gas. The total energy released in growing an SMBH exceeds the typical binding energy of large galaxies, and therefore the formation of the SMBH has the capability to significantly affect its host (Silk & Rees 1998; King & Pounds 2015). A possible consequence of SMBH growth is that the accretion occurs at a rate high enough to drive an optically thick wind into the gaseous protogalaxy (Fabian 1999; King & Pounds 2003). This wind can sweep up ambient gas into an outflow consisting of shocked wind and gas, and if strong enough it has the ability to clear the galaxy of ambient gas and halt further accretion onto the SMBH. The result of this process would be a dormant central SMBH with a mass related to the depth of the galaxy's potential well, and therefore correlating with present day stellar properties (King 2003; Murray, Quataert & Thompson 2005).

The dynamics of a wind-driven outflow can be broadly separated into two limiting regimes based on whether the shocked wind is efficiently cooled (momentum-driving) or not (energy-driving). Outflows are expected to begin momentum-driven, but will ultimately transition to the energy-driven regime (Faucher-Giguère & Quataert 2012). Simple analytical models of protogalactic outflows driven by winds within both regimes have predicted SMBH masses required for the outflow to reach large radii which are consistent with the observed $M_{\rm BH}-\sigma$ correlation (King 2005; McQuillin & McLaughlin 2013; Zubovas & Nayakshin 2014). Further studies have been able to relate this SMBH mass to properties of dark matter haloes (McQuillin & McLaughlin 2012), and consequently show how the $M_{\rm BH}-\sigma$ correlation relates to the redshift evolution of galaxies (Larkin & McLaughlin 2016). Numerical simulations of wind-driven outflows have reinforced these results, and have shown that they are also applicable to local active galaxies. Active galaxies and low redshift quasars host observable outflows, and such simulations are capable of analysing the anisotropy of outflows and assessing which driving regime is dominant (Costa, Sijacki & Haehnelt 2014; Zubovas & Nayakshin 2014; Hartwig, Volonteri & Dashyan 2018).

A key insight is that the outflows observed in active galaxies are analogous to the outflows which have occurred in protogalaxies at high redshift. These gas outflows have been observed over a wide range of scales within active galaxies. At small

(10−100pc) galactic scales observations from *Chandra*, *XMM-Newton* and *Suzaku* of X-ray absorption are consistent with fast $v_w \sim 0.01 - 0.1c$ winds with mass loss rates typically $\dot{M}_w \sim M_\odot$ yr^{-1} (e.g. Sako et al. 2001; Pounds et al. 2003b; Tombesi et al. 2010; Gofford et al. 2013). These winds can have momentum-fluxes of similar order to the central source, $\dot{M}_w v_w \approx L_{\rm AGN}/c$. At larger (1−10kpc) galactic scales observations of molecular (CO and OH) absorption are consistent with outflows travelling at more moderate speeds ($v_{\rm out} \sim 100 - 1000$ km s^{-1}), but with large mass outflow rates $\dot{M}_{\rm out} \sim 100 - 1000 M_\odot$ yr^{-1} (e.g. Sturm et al. 2011; Cicone et al. 2014). The momentum-fluxes of these large-scale outflows are found to be boosted to many times that of the source. For a limited number of galaxies the presence of small scale winds and large scale outflows have been observed within the same system (Tombesi et al. 2015; Feruglio et al. 2015), and it is these objects which are the most promising for testing the dynamical predictions of the wind feedback model at these limiting galactic scales.

In order to remain analytically tractable most of the analytical models of wind-driven outflows have retained a number of simplifying assumptions which are restrictive. One such assumption is that the ram pressure of the ambient medium can be neglected. Although it is included in some calculations (Faucher-Giguère & Quataert 2012) its effects have yet to be examined in their own right. A further assumption commonly found is that the SMBH mass is constant. This is in contradiction to the core assumption that the SMBH is growing via the accretion of matter, and there are few analytical studies which have treated this issue in isolation (see Gilli et al. 2017). This thesis attempts to address these issues; by first investigating the dynamical effects of ambient gas pressure, and then by extending the results at large scales to obtain a clear observational context in terms of momentum-boosting, and ultimately going on to introduce the temporal aspects of SMBH growth.

1.1 Galaxies

1.1.1 Galaxy Morphologies

Galaxies were first recognised by the appearance of their stellar content (Hubble 1926), and can be broadly grouped into four types: *ellipticals, lenticulars, spirals* and *irregulars*. This led to the development of the Hubble-Sandage classification scheme (Hubble 1936; Sandage 1961) which is represented concisely as the Hubble 'Tuning fork' shown in Figure 1.1. Originally thought of as an evolutionary path the *Hubble sequence* shown in Figure 1.1 led to the convention that elliptical galaxies are referred to as *early-type* galaxies, and spiral galaxies are referred to as *late-type*.

Elliptical galaxies are ellipsoidal (or spheroidal) in appearance. They are denoted EN, with $N \equiv 10 \times (1 - b/a)$, where $0 < N < 7$, and with a and b the apparent major and minor axes of the ellipsoid respectively. Hence an E0 galaxy appears circular, whereas an E7 ($b/a = 0.3$) galaxy appears as a highly elongated ellipse. Extremely flattened elliptical galaxies with axis ratios $b/a < 0.3$ have not been observed.

Ellipticals can be subdivided further on whether they appear 'boxy' or 'disky' (see Figure 1.1), with very disky ellipticals being similar in appearence to *lenticular* galaxies. Lenticular galaxies consist of a central condensation of stars, called *the bulge* (which itself structurally resembles an elliptical galaxy), and *the envelope*, a flatter, less concentrated region of stars beyond the bulge. Lenticular galaxies can be subclassified based on whether or not the galaxy displays a bar-like structure of stars across the galactic centre. They are denoted $S0_m$ (or $SB0_m$ if a bar is present), where m denotes the presence of absorbing dust around the bulge, and ranges between 1 (no absorbing dust) to 3 (high level of absorbing dust). Lenticular galaxies can be viewed as an intermediate morphological type between elliptical and spiral galaxies.

Most spiral galaxies have a spheroidal bulge situated in a disk which hosts spiral concentrations of stars. These are called the *spiral arms* of the galaxy. Spiral galaxys are subdivided based on whether they contain a bar, and are denoted Sa, Sb or Sc (equivalently SBa, SBb, and SBc for barred spirals). Sa galaxies have luminous bulges,

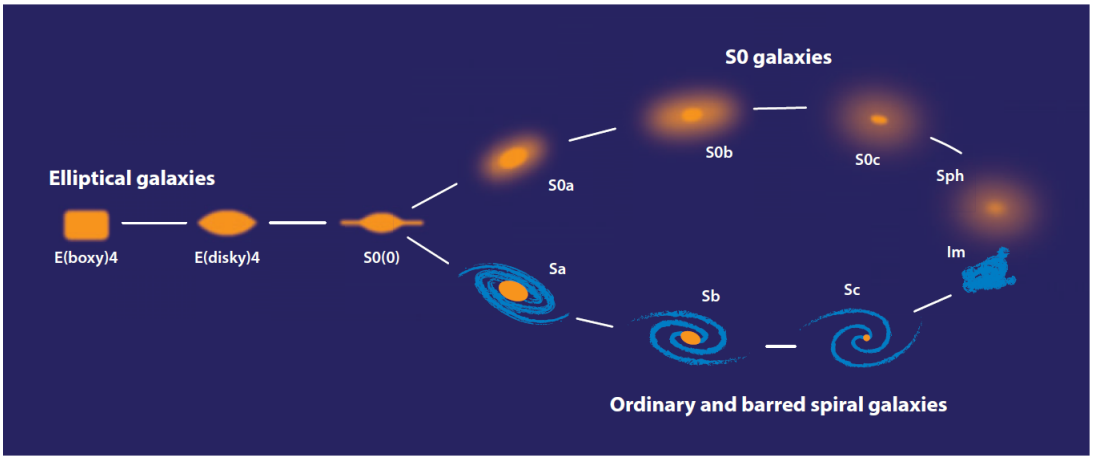

Figure 1.1: The Hubble sequence showing the range of galaxy morphologies. On the left are the elliptical galaxies which are subdivided into boxy (E(boxy)n) and disky (E(disky)n) types (shown here with $n = 4$). The ellipticals are connected to the lenticular (top) and spiral galaxy (bottom) branches through the S0 lenticulars. The lenticular branch shows the three different types (left-to-right: S0a,S0b,S0c) of lenticulars based on their (decreasing) bulge-to-total light ratios. The spiral branch shows the three different types (left-to-right: Sa,Sb,Sc) of spirals based on the (decreasing) prominance of the bulge and the (increasing) diffuseness of the spiral arms. The two branches connect through the dwarf-spheroidals and irregular Im galaxies. (See Kormendy & Bender 2012 for discussion and original image.)

and possess tightly wound spiral arms. These three properties become progressively reduced in Sb, Sc and Sd spirals, such that the bulge is progressively less luminous (ultimately vanishing in an Sd spiral), and the spiral arms are progressively less defined. The same subdivision can be extended to lenticular galaxies by considering their bulge-to-disk ratio. Bulge dominated lenticulars can therefore be denoted S0a, with S0b and S0c having progressively smaller bulge-to-disk ratios.

Any galaxies that cannot be readily placed within the Hubble Sequence are referred to as *irregular galaxies*. These galaxies display asymmetry and lack a clearly defined nucleus. They are broadly grouped into two categories. Irr I galaxies are defined as those which show some structure, and are labeled Sm if spiral structure is present, or labelled Im if not. Irr I galaxies could be considered as an extension of

the spiral branch (see Figure 1.1). Irr II galaxies however have little structure, and therefore cannot be classified within the Hubble sequence.

Ellipticals, spirals, and irregulars have a further subtype: the *dwarf galaxy*. Dwarf galaxies are the smaller counterparts of these galaxy types, and are denoted with a lower case d, such as dE for a dwarf-elliptical galaxy. Dwarf elliptical galaxies typically have masses of $10^7 - 10^9 M_\odot$, and luminosities between $10^5 - 10^7 L_\odot$. This is the lower end of the observed range of masses $10^5 - 10^{12} M_\odot$ and luminosities $10^5 - 10^{12} L_\odot$ of ellipticals. Dwarf spheroidal galaxies are another distinct dwarf galaxy type, with luminosities even lower than those of dwarf ellipticals. Dwarf ellipticals are very common whereas dwarf-spirals are very rare. Locally, dwarf galaxies are the most common galaxy type, but due to their low luminosities they become difficult to detect at greater distances.

The Hubble-Sandage scheme is one of many such visual classification schemes (see Binney & Merrifield 1998 for an overview), which are very useful in describing the broader structural features which are helpful in understanding the evolution and internal dynamics of galaxies. However, when faced with large sample sizes of galaxies, alternative and more detailed approaches are used which utilise parameters that can be derived from galaxy light distributions via computational analysis. The surface brightness distributions of galaxies can be fitted by surface brightness functions $I(R)$ of *projected distance* R from the galaxy's centre which vary based on the morphological type of the galaxy. For elliptical galaxies and the bulges of spiral and S0 type galaxies the $R^{1/4}$ law (de Vaucouleurs 1948) can be used:

$$I(R) = I_e 10^{-3.33\left[(R/R_e)^{1/4}-1\right]}, \tag{1.1}$$

where R_e is the *effective* (or *half-light*) *radius*, defined as the projected radius within which half the total luminosity is emitted, and I_e is the intensity at the half-light radius.

Dwarf ellipticals and the disks of spiral galaxies are better fitted by an exponential function:

$$I(R) = I_0 \exp\left(-R/h\right), \tag{1.2}$$

with I_0 the central surface brightness, and h the disk scale length. Both the de Vaucouleurs law and exponential function can be encompassed within a generalised form

which was introduced by Sérsic (Sérsic 1968):

$$I(R) = I_e 10^{-b_n\left[(R/R_e)^{1/n}-1\right]}\,, \tag{1.3}$$

where the constant b_n is defined such that half the total luminosity is within $R < R_e$. The parameter n is known as the Sérsic index, and if $n = 4$ then the $R^{1/4}$ law is recovered whereas if $n = 1$ then the resulting light distribution is exponential in form. The Sérsic index has been shown to correlate with elliptical galaxy and bulge luminosities (Graham 2001; Graham & Guzmán 2003).

1.1.2 Galaxy Masses

The masses of spiral galaxies can be estimated as a function of the circular speeds V_c of the rotating stars and gas in the disk by assuming a spherically symmetric mass distribution, and equating the centripetal acceleration to the gravitational acceleration. This leads to the equation:

$$M_{\rm sp}(r) = \frac{V_c^2 r}{G}\,. \tag{1.4}$$

When reaching large radii the mass of a spiral galaxy should converge and equation (1.4) predicts that the rotation velocities fall off as $r^{-1/2}$ (i.e. are Keplerian). However, observations of spirals have shown that the rotation velocities tend to a constant at large radii beyond the luminous regions (Rubin & Ford 1970; Ostriker, Peebles & Yahil 1974, see also Figure 1.2) which by equation (1.4) implies the presence of dark matter with a roughly linear dependence on r at large galactic radii.

The masses of galaxy bulges or elliptical galaxies can be determined from their stellar dynamics. In galaxies the stars compose a gravitationally bound system which is assumed to be in dynamical equilibrium. This assumption is justified as long as the crossing time of the galaxy is much less than the age of the galaxy: $t_{\rm cr} = R/\langle v\rangle \ll t_{\rm age}$, where R is the galaxy radius and $\langle v\rangle$ is the average speed of a star. If this is the case then the system in equilibrium satisfies the *virial theorem* (see Binney & Tremaine 2008 for its derivation):

$$2K + W = 0\,, \tag{1.5}$$

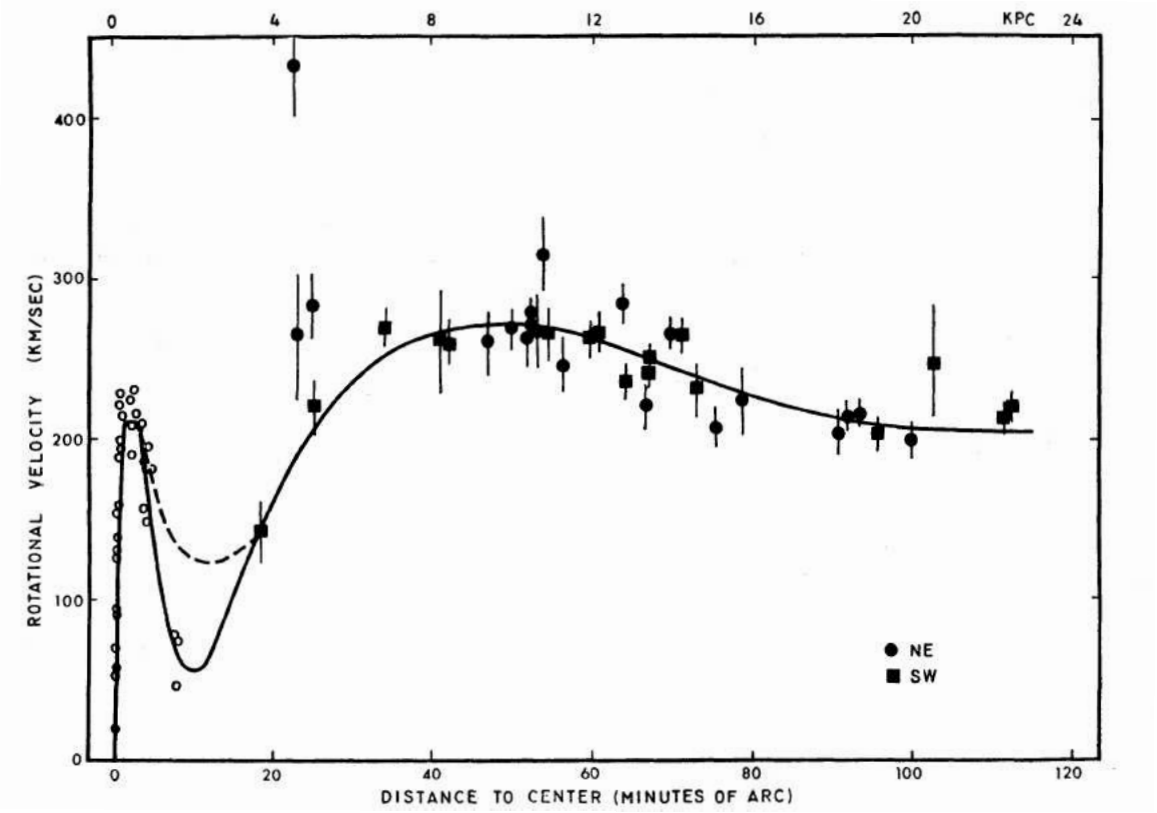

Figure 1.2: Rotation velocities in the spiral galaxy M31 plotted against distance to the galaxy centre. The solid curve is the adopted rotation curve, and the dashed curve is a second rotation curve which requires the density to always be positive. (Reproduced from Rubin & Ford 1970)

where $K = M\left\langle v^2\right\rangle/2$ is the global kinetic energy of the stellar system with total mass M, and W is the gravitational potential energy. If the velocity dispersion is assumed to be isotropic then the line-of-sight velocity dispersion is related to the mean square speed by: $\left\langle v^2\right\rangle = 3\sigma^2_{l.o.s}$. Equation (1.5) leads to: $2K = 3M\sigma^2_{\rm l.o.s} = -W$, and the *gravitational radius* can be introduced as a useful scale:

$$r_g \equiv \frac{GM}{3\sigma^2_{\rm l.o.s}} \simeq 3.6\ {\rm kpc}\left(\frac{M}{10^{11}M_\odot}\right)\left(\frac{200\ {\rm km\ s^{-1}}}{\sigma_{\rm l.o.s}}\right)^2. \tag{1.6}$$

Assuming a power law density distribution $\rho \propto r^{p-3}$ for a galaxy, with $p > 0$, and assuming also that the mass converges within the radius R means that the mass of a

galaxy can be expressed as:

$$M(R) = \int_0^R 4\pi r^2 \rho(r)\, dr = \frac{4\pi \rho_{\rm gr} r_g^3}{p} \left(\frac{R}{r_g}\right)^p , \tag{1.7}$$

where $\rho_{\rm gr}$ is the density at r_g. Using equation (1.5) allows the mass of the system to be expressed as:

$$M(R) = \frac{3(2p-1)}{p} \frac{R\sigma^2_{\rm l.o.s}}{G} . \tag{1.8}$$

For a system with constant density ($p = 3$) the multiplicative factor is $3(2p-1)/p = 5$, and for a system with linear mass growth ($p = 1$) the factor is $3(2p-1)/p = 3$. Equation (1.8) is a useful estimate for the mass of a bulge or elliptical galaxy, but it is valid only for globally defined values of M and σ.

By observing the motions of globular clusters surrounding elliptical galaxies it has been shown that the velocity dispersion remains approximately constant outside of the galaxy (Côté et al. 2003). This would indicate the presence of unobservable dark mass, or *dark matter* (Zwicky 1933) surrounding the galaxy in a *halo* with a linear dependence on r. A simple model of dark matter which replicates the $M(r) \propto r$ behaviour is the singular isothermal sphere (SIS). The SIS has a centrally singular density profile:

$$\rho(r) = \frac{\sigma^2}{2\pi G r^2} , \tag{1.9}$$

which is obtained by considering an isothermal self-gravitating sphere of gas with temperature:

$$T = \frac{m\sigma^2}{k_B} , \tag{1.10}$$

where k_B is the Boltzmann constant, and m is the mass of an individual particle. Equation (1.10) shows that the velocity dispersion is constant at all radii within the SIS. The mass profile of the SIS is:

$$M(r) = \int_0^r 4\pi u^2 \rho(u)\, du = \frac{2\sigma^2 r}{G} . \tag{1.11}$$

This replicates the linear r dependence of dark matter at large radii in ellipticals, and the combined dark matter and stellar mass at large radii in spirals. Despite its singular

nature and infinite mass the SIS halo model is still routinely used as a zeroth-order model for treating dark matter haloes. More effective models of dark matter haloes have been found from numerical simulations of dark matter within a cosmological context, and this subject is treated in more detail in Section 1.2.

1.1.3 Galaxy Colours

Through the analysis of large sample sizes obtained from the *SDSS* and *2dF* galaxy surveys it was found that galaxies can be broadly separated into *red* and *blue sequences* (see Figure 1.3). Red galaxies were found mainly to be high-mass early-type galaxies with little to no star formation, and are often dubbed 'old, red and dead' galaxies. Blue galaxies were found mainly to be late-type galaxies undergoing star formation.

Early-type galaxies lose their gas reservoir rapidly over time scales less than 250 Myr, and move quickly through the green valley (from blue to red). Late-type galaxies lose their gas reservoir over longer time scales of around 1 Gyr, and therefore move more slowly through the green valley (Schawinksi et al. 2014). This leads to the question of what was responsible for rapidly clearing gas and consequently shutting off the star formation in early-type galaxies at higher redshift. A first step towards understanding how this may have occurred can be gained by looking at a further galaxy type: active galaxies.

1.1.4 Active Galaxies

Active galaxies are those which possess very luminous *active galactic nuclei* (AGN) relative to their total luminosity. AGN were discovered as extragalactic quasi-stellar radio sources (Schmidt 1963) and consequently dubbed *quasars*. Quasars can be millions of times more radio luminous than our own Galaxy, but strong radio emission is not a necessary feature of most quasars (Sandage 1965). The luminosities of quasars can be $10^1 - 10^5$ more luminous than the Milky Way, which has a luminosity of $L_{\rm MW} \sim 10^{10} L_{\odot}$. Most of the radiation emitted from AGN is non-thermal, and therefore from a non-

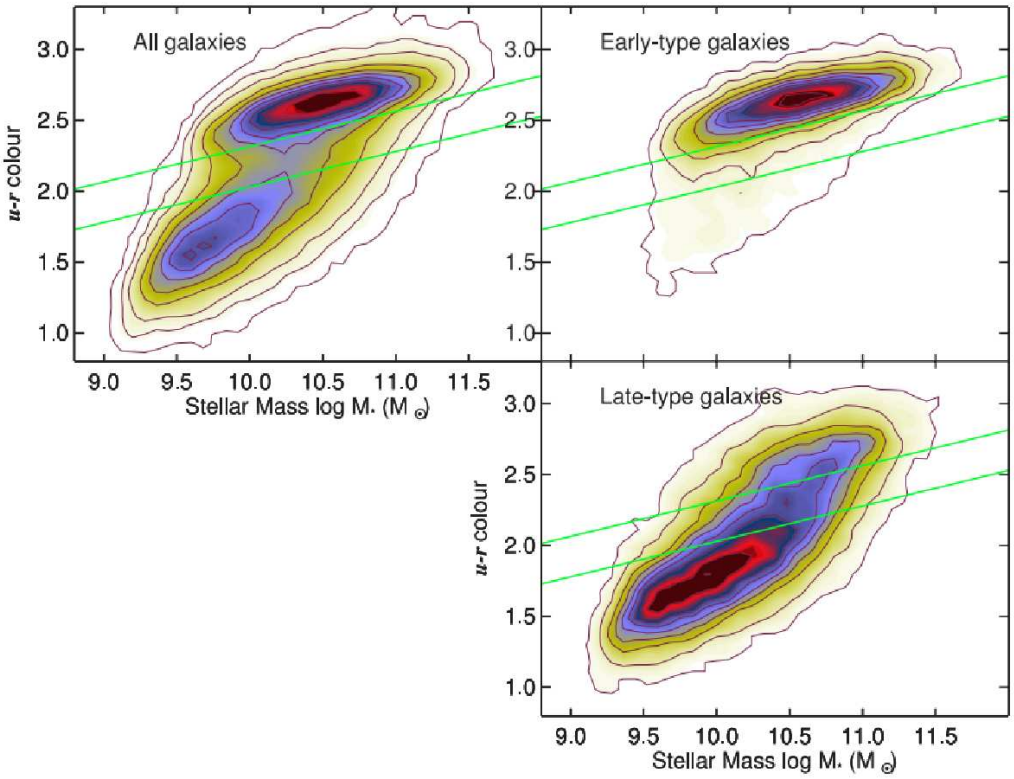

Figure 1.3: Galaxy colour as a function of stellar mass. Galaxy morphologies were determined using Galaxy Zoo visual classifications (Lintott et al. 2008). The left panel shows all galaxies, the top-right shows early-type galaxies, and the bottom-right shows late-type galaxies. This figure shows that most early-type galaxies occupy the red-sequence. Late-type galaxies peak in the blue-sequence but also reach into the red-sequence. The green lines indicate the 'green valley' which is a transitional phase for both early- and late-type galaxies. (Reproduced from Schawinksi et al. 2014)

stellar source. Normal elliptical galaxies which are collections of stars can be treated as black bodies, and therefore their spectra occupy a small range in wavelengths with weaker radiation at shorter wavelengths (relative to the optical band). AGN however have broad spectra which occupy a wide range of wavelengths, and feature strong emission lines relative to normal galaxies as shown in Figure 1.4. The emission from AGN can be highly variable with luminosities changing on timescales which can be as short as days.

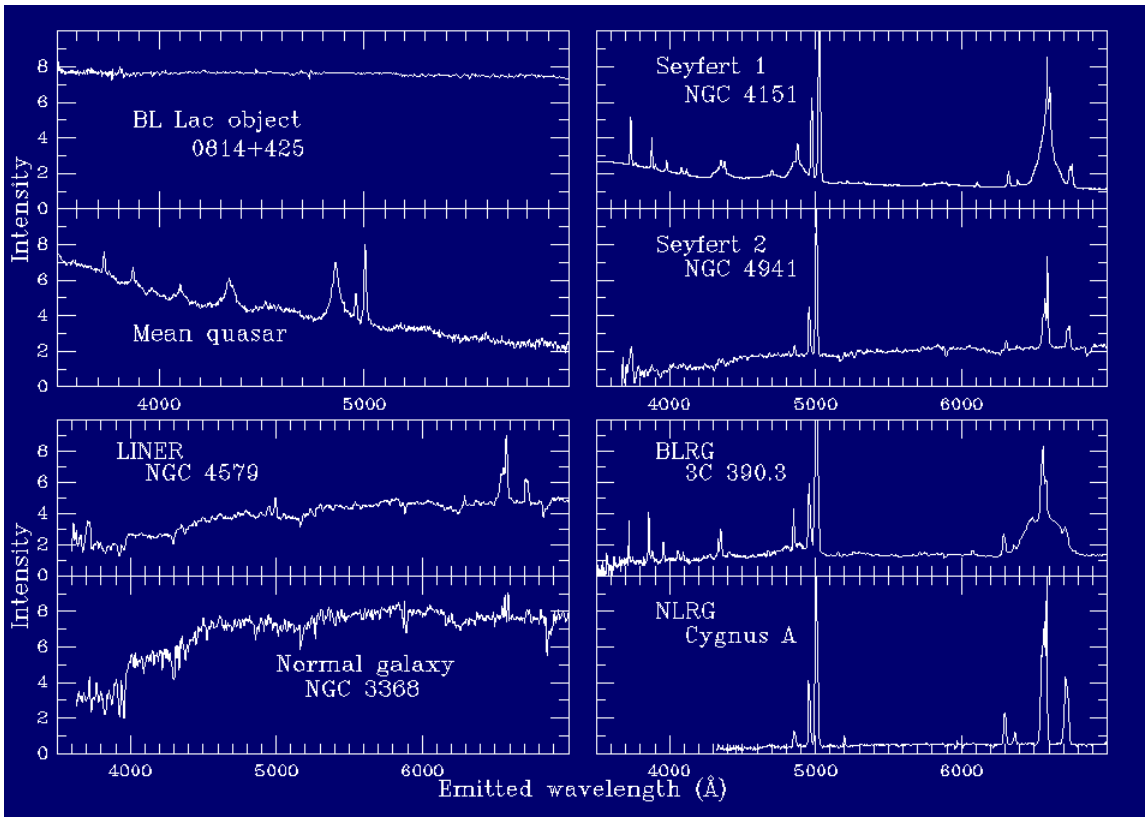

Figure 1.4: Comparison of AGN spectra. Each panel shows intensity against wavelength. The top-left panel shows the spectrum for the BL Lac object 0814+425 (upper) and a composite spectrum of multiple quasars (lower). The bottom-left panel shows the spectra for the LINER in NGC 4579 (upper) and the normal spiral galaxy NGC 3368 (lower). The top-right panel shows the spectra for the Seyfert I galaxy NGC 4151 (upper) and the Seyfert II galaxy NGC 4951 (lower). The bottom-right panel shows the spectra of broad-line radio galaxy (BLRG) 3C 390.3 (upper) and narrow-line radio galaxy (NLRG) Cygnus A (lower). (Reproduced from https://pages.astronomy.ua.edu/keel/agn)

A class of radio-loud AGN which exhibit rapid variability are *blazars* (or BL Lac objects) which have spectra devoid of any emission lines typically seen in quasars. A class of radio-quiet AGN which are analogous to low-luminosity ($0.1 - 10 L_{\rm MW}$) quasars are Seyfert galaxies which display narrow emission lines consistent with gas velocities

of $500 - 1000$ km s^{-1}. Seyfert galaxies can be divided into two classes: Seyfert Is which display broad-line emission (in addition to narrow-line emission) indicating gas velocities of $1000 - 5000$ km s^{-1}; and Seyfert IIs which display only narrow-line emission. These were unified (Antonucci 1993; Miller 1994) under the scheme illustrated in Figure 1.5 in which Seyfert II galaxies differ only from Seyfert Is simply by their orientation. In Seyfert IIs the broad emission-line region (BLR) is obscured by a dusty torus. There are also radio-loud galaxies which (like Seyfert galaxies) exhibit narrow- and broad-line emission, and their spectra are shown in Figure 1.4. A further type of AGN are low-ionisation nuclear emission-line regions (LINERs) which are less luminous than other AGN, but are very common amongst local galaxies. The high luminosities of AGN, their compact form, variability, and the observed broad-band spectra indicate that the source of their energy is compact and non-stellar in nature. These features of AGN suggest that the required source of high energy is a central accreting supermassive black hole (SMBH) (Salpeter 1964; Lynden-Bell 1969; Rees 1977). The radiation from AGN is emitted by particles as they accelerate during their infall onto the SMBH via a succession of quasi-circular orbits. For a particle with rest mass m_0 and angular momentum per unit mass l close to a Schwarzschild black hole the following radial equation of motion applies (see Krolik 1999):

$$\frac{1}{c^2}\left(\frac{dr}{ds}\right)^2 = \left(\frac{E_\infty}{m_0 c^2}\right)^2 - \left(1 - \frac{2GM_{\rm BH}}{rc^2}\right)\left(1 + \frac{l^2}{c^2 r^2}\right) , \tag{1.12}$$

where s is the proper time, and E_∞ is the particle's energy at infinity. Equation (1.12) can be analysed as if it were a classical equation of motion by relating E_∞ to a pseudo-energy of the particle by $E_* = (E_\infty/m_0c^2)^2/2$, and the effective potential can be written:

$$V_{\rm eff}(r) = \frac{1}{2}\left(1 - \frac{2GM_{\rm BH}}{rc^2}\right)\left(1 + \frac{l^2}{c^2 r^2}\right) . \tag{1.13}$$

The effective potential has extrema when:

$$r_m = \frac{l^2}{2GM_{\rm BH}}\left[1 \pm \sqrt{1 - 12(GM_{\rm BH}/lc)^2}\right] , \tag{1.14}$$

only if $l \geq \sqrt{12}GM_{\rm BH}/c$. The smallest stable orbit occurs at $r_{\rm min} = 6GM_{\rm BH}/c^2$, i.e.

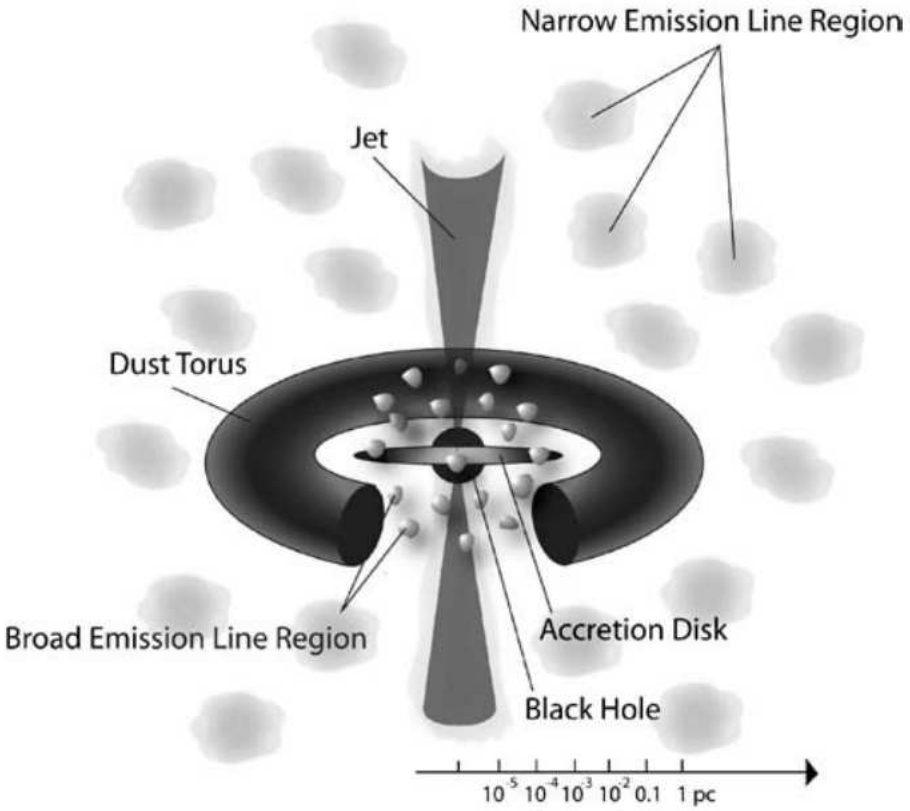

Figure 1.5: AGN unification scheme. The central SMBH is surrounded by a gaseous accretion disk which is approximately 0.001pc across. At a distance of around 0.1pc are the fast moving gas clouds in the BLR which produce the broad emission-lines observed in some AGN spectra. Optically thick cold gas surrounds the BLR in the form of a torus which is $\sim$ 10pc across, and which obscures the BLR in Seyfert II galaxies. At a distance of approximately 100pc small slow moving low density gas clouds are located. The jets inject energy into this region which is emitted by the clouds and is observed as narrow emission-lines in AGN spectra. (Reproduced from Ferrarese & Ford 2005)

three times the Schwarzschild radius:

$$r_S \equiv \frac{2GM_{\rm BH}}{c^2}\,. \tag{1.15}$$

The maximum efficiency of energy conversion (denoted η) for gas falling into a Schwarzschild black hole is found from the binding energy E_b of a particle at the radius of smallest stable orbit. The binding energy can be found by subtracting the energy of

the particle at infinity from the rest mass of the particle; first by finding the pseudo-energy of the particle $E_*(r_{\min}) = V_{\text{eff}}(r_{\min}) = 4/9$, and then by finding the energy at infinity $E_\infty = \sqrt{2E_*(r_{\min})}m_0c^2 = (\sqrt{8}/3)m_0c^2$ and subtracting it from the rest mass energy to give $E_b = (1 - \sqrt{8}/3)m_0c^2 \simeq 0.057m_0c^2$. Therefore the accretion efficiency for a Schwarzschild black hole is approximately $\eta \equiv E_b/m_0c^2 \simeq 0.06$. For a rotating (Kerr) black hole, the angular momentum of the black hole leads to a smallest stable orbit for the infalling particle to be much smaller, and consequently the binding energy of the particle to be much larger. This means that the accretion efficiency could be as high as $\eta = 0.42$ for a rotating black hole.

For hydrogen gas falling toward the black hole at a distance far enough away that Newtonian physics applies ($r \gg r_S$) the outwards force on the infalling particles due to radiation emitted with luminosity L is:

$$F_{\text{rad}} = \frac{\sigma_T}{4\pi r^2}\frac{L}{c}\,, \tag{1.16}$$

where σ_T is the Thomson cross section. The force due to radiation depends on distance in the same way as that from gravitation due to the black hole:

$$F_{\text{grav}} = -\frac{GM_{\text{BH}}m_p}{r^2}\,, \tag{1.17}$$

where m_p is the proton mass. Balancing these two forces: $F_{\text{rad}} + F_{\text{grav}} = 0$ leads to a critical luminosity called the Eddington luminosity:

$$L_{\text{Edd}} = \frac{4\pi GM_{\text{BH}}m_pc}{\sigma_T} \simeq 1.3 \times 10^{38}\left(\frac{M_{\text{BH}}}{M_\odot}\right)\ \text{erg s}^{-1}\,, \tag{1.18}$$

where m_p is the proton mass, and $\sigma_T/m_p \equiv \kappa \simeq 0.04\ \text{m}^2\ \text{kg}^{-1}$ is the Thomson scattering opacity.

If an accreting black hole produces radiation with luminosity L_{Edd} then it is said to be accreting at the Eddington rate $\dot{M}_{\text{Edd}} \equiv L_{\text{Edd}}/\eta c^2$. Considering a black hole which accretes with efficiency η at a constant fraction q of the Eddington rate shows that such a black hole grows exponentially:

$$\frac{dM_{\text{BH}}}{dt} = \frac{q}{\eta}\dot{M}_{\text{Edd}} = \frac{q}{\eta}\frac{4\pi GM_{\text{BH}}}{\kappa c} \implies M_{\text{BH}}(t) = M_0\exp\left[\frac{4\pi qGt}{\eta\kappa c}\right]\,. \tag{1.19}$$

The Salpeter (or e-folding) time is therefore (Salpeter 1964):

$$t_S = \frac{M_{\rm BH}(t)}{\dot{M}_{\rm BH}(t)} = \frac{\eta\kappa c}{4\pi q G} \simeq (4.5\times10^7)\left(\frac{\eta}{0.1}\right)\left(\frac{1}{q}\right)\ {\rm yr}\,. \tag{1.20}$$

An estimate of typical SMBH masses can be obtained by considering the luminosity function of quasars (Soltan 1982). Since the luminosity function of quasars varies with redshift (see Figure 1.6) any expression for the number density of quasars with luminosity L would also be a function of redshift: $n(L,z)\,dL$. Therefore the density of mass accreted by these black holes would be the product of the number of quasars with luminosity L (divided by ηc^2) and integrated over cosmic time. The density can also be expressed in terms of the number of quasars N in redshift interval dz with flux densities S in the interval dS:

$$\begin{aligned}\rho_{\rm BH} &= \frac{1}{\eta c^2}\int\int Ln(L,z)\,dL\,dt \\ &= \frac{4\pi}{\eta c^3}\int\int (1+z)S\,N(S,z)\,dS\,dz\,.\end{aligned} \tag{1.21}$$

Considering that the peak in quasar activity is $z\sim2$ (see Figure 1.6) we can assume $1+z\sim3$, and $\int SN(S)dS$ can be found from the counts of radio quiet quasars. A corrective factor of $F_{\rm bol}/10F_B$ can be applied which accounts for the conversion of B-band luminosities to bolometric luminosities (Krolik 1999). Then comparing with the density of galaxies with luminosities close to the characteristic luminosity of field galaxies: $L_* = 2\times10^6(H/0.75)^3$ G pc^{-3} gives the mean BH mass per galaxy to be:

$$\langle M_{\rm BH}\rangle = 1.6\times10^7\left(\frac{F_{\rm bol}}{10F_B}\right)\left(\frac{\langle1+z\rangle}{3}\right)\left(\frac{H}{0.75}\right)^{-1}\left(\frac{\eta}{0.1}\right)^{-1}\,. \tag{1.22}$$

This means that at the centre of every large galaxy should reside a 'dead quasar' in the form of an SMBH with a mass of order: $M_{\rm BH}\approx10^7M_\odot$.

There is mounting observational evidence to support this result (Kormendy & Ho 2013). The measured SMBH masses (see Section 1.3) are also found to correlate with global properties of their host galaxies such as bulge mass and velocity dispersion (see Section 1.4). Since these galactic properties are outside the direct gravitational influence of the SMBH it is likely that the SMBH and the galaxy interacted via a process

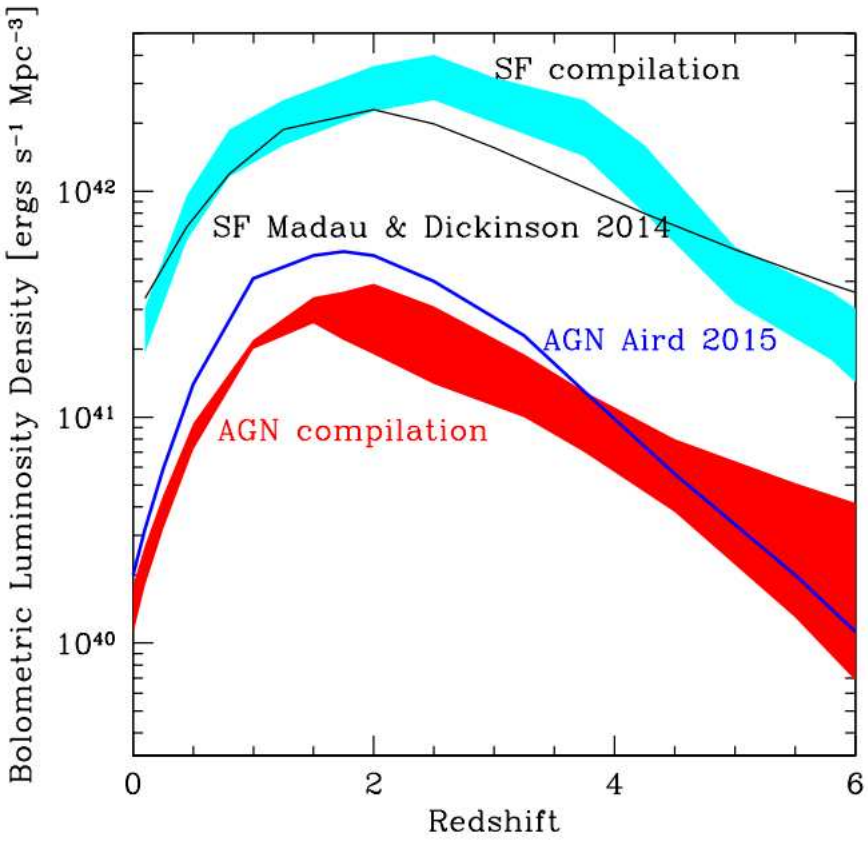

Figure 1.6: Evolution of AGN bolometric luminosity density as a function of redshift. The red band is computed from a compilation of X-ray luminosity functions integrated in the range $\log L_X = 42-45$ (see Fiore et al. 2017 for details). The solid blue line is the bolometric AGN luminosity density from Aird et al. (2015). The cyan band shows the UV luminosity density (reflecting star formation) averaged from Santini et al. (2009), Gruppioni et al. (2015), Bouwens et al. (2011) and Bouwens et al. (2015), and the black line is the same from the review by Madau & Dickinson (2014). (Reproduced from Fiore et al. 2017)

at higher redshift. This interaction is likely to have occurred during the accretion phase of the SMBH.

If the large masses of these central SMBHs were the result of gas accretion within protogalaxies then they must have released a large amount of radiative energy back into the gas feeding the black hole. The energy released in forming a $10^7 M_\odot$ black

hole is:

$$E_{\rm acc} = \eta M_{\rm BH} c^2 \sim 2 \times 10^{60} \left(\frac{M_{\rm BH}}{10^7 M_\odot} \right) \ {\rm erg}\,. \tag{1.23}$$

This is larger than the binding energy of a host bulge of mass $10^{11} M_\odot$ (as shown in the review by King & Pounds 2015):

$$E_{\rm bulge} \sim M_{\rm bulge} \sigma^2 \sim 8 \times 10^{58} \left(\frac{\sigma}{200 \ {\rm km \ s^{-1}}} \right)^2 \ {\rm erg}\,. \tag{1.24}$$

This means that these now dormant SMBHs can significantly affect their host galaxy during their growth. The energy released during accretion may be able to couple with the ambient gas in the protogalaxy either through an optically thick wind (King & Pounds 2003) or by radiation pressure on dust (Fabian 1999). If this occurs then the surrounding gas could be driven away from the SMBH, and in doing so halt further accretion onto the SMBH. The clearing of gas from the galaxy and termination of accretion resulting from the growth of an SMBH is an example of a feedback process. Such a feedback process could explain the rapid clearing of gas in early-type galaxies which result in them becoming 'red and dead', and how SMBH masses come to correlate with the global properties of their host galaxy.

In order to understand the feedback process in detail it is required that properties of dark matter haloes are introduced properly, and this is carried out in Section 1.2. This is then followed by an overview of SMBHs, and how they correlate with galactic properties in Sections 1.3 and 1.4, respectively. In Section 1.5 some of the physical processes responsible for feedback and the observational evidence in support of these processes are explained. This chapter concludes with an outline of the thesis in Section 1.6.

1.2 Dark Matter Haloes

1.2.1 ΛCDM Cosmology

Nonbaryonic dark matter is the dominant form of matter in the universe accounting for approximately 85% of all matter (Planck collaboration 2016). A small fraction of baryonic matter is dark, i.e. non-luminous matter such as SMBHs and planets. The favoured cosmological model of dark matter is *cold dark matter* (CDM) (Blumenthal et al. 1984) which requires the velocities of dark matter particles to be cold in the early universe in order to account for the small scale clumping required to explain the observed galactic scale fluctuations. CDM favours the hierarchical merging of smaller dark matter structures formed from matter density perturbations which are upscaled from cosmic inflation to form larger haloes as opposed to the fragmentation of bigger structures (see review by Frenk & White 2012).

1.2.2 Halo Density Profiles

N-body simulations of structure formation in ΛCDM cosmologies lead to the use of double power law profiles for the dark matter density in haloes. The $(\alpha', \beta', \gamma')$ profile of dark matter haloes utilises a 'universal' double power law density function of the form (An & Zhao 2013):

$$\rho_{\rm DM}(r/r_{\rm sc}) = \rho_{\rm sc} 2^{(\beta'-\gamma')/\alpha'} \left(\frac{r}{r_{\rm sc}}\right)^{-\gamma'} [1 + (r/r_{\rm sc})^{\alpha\,\prime}]^{(\gamma'-\beta')/\alpha'} \ . \tag{1.25}$$

Five parameters define these profiles: $\rho_{\rm sc}$ is the density at the scale radius $r_{\rm sc}$. The scale radius marks the region of transition from the $-\gamma'$ inner logarithmic slope to the $-\beta'$ outer logarithmic slope, and α' dictates the degree of this transition (Merritt et al. 2006). For realistic dark matter haloes the parameter γ' is typically ~ 1, i.e. shallower than the singular isothermal sphere at small radii (see equation 1.9). At large radii the parameter β' is typically $\sim 3-4$, and therefore steeper than the singular isothermal sphere (Dehnen & McLaughlin 2005). This means that the circular speed curves of

these non-isothermal haloes:

$$V_c^2(r) = \frac{GM_{\rm DM}(r)}{r}\,, \tag{1.26}$$

will have a well defined peak at a radius denoted $r_{\rm pk}$.

The so-called Hernquist profile (Hernquist 1990; Dubinski & Carlberg 1991) has the parameter values: $(\alpha', \beta', \gamma') = (1, 4, 1)$. This profile has a projection very close to the $R^{1/4}$ law, but unlike the Sérsic profile it has an analytical mass distribution (see Table 1.1). The mass profile $M(r)$ of the Hernquist halo scales like r^2 at small radii and converges at large radii. Two other profiles that are included in equation (1.25) are the Moore profile (Moore et al. 1998; Moore et al. 1999) which has: $(\alpha', \beta', \gamma') = (1, 3, 1.5)$, and the NFW profile (Navarro, Frenk & White 1996, 1997) which has: $(\alpha', \beta', \gamma') = (1, 3, 1)$. The NFW profile also scales like $M(r) \propto r^2$ at small radii, but instead of converging at large radii it diverges logarithmically instead.

Despite the empirical justification for the profile given by equation (1.25), there is no theoretical motivation for this form. An alternative is to begin with the simpler empirical fact, and perhaps more fundamental aspect that simulated haloes satisfy a $\rho - \sigma$ relation of the form (Taylor & Navarro 2001; Hansen 2004):

$$\frac{\rho(r)}{\sigma_r^{\epsilon'}} \propto r^{-\xi}\,, \tag{1.27}$$

where σ_r is the radial component of velocity dispersion, $\xi \sim 1 - 2$, and $\epsilon' \simeq 3$. This equation can then be used as a constraint when deriving the halo density profile from the spherical Jeans equation:

$$\frac{d}{dr}\rho\sigma_r^2 + \frac{2B(r)}{r}\rho\sigma_r^2 = -\rho(r)\frac{GM(r)}{r^2}\,, \tag{1.28}$$

which for $B = 0$ is effectively the equation of hydrostatic support. Departure from this equation is quanitified by the parameter $B(r) = 1 - (\sigma_\theta^2 + \sigma_\phi^2)/2\sigma_r^2$ which characterises the anisotropy (with $B \sim 0$ implying isotropy). The Jeans equation can then be solved leading to a family of solutions (Dehnen & McLaughlin 2005). In the isotropic case, the following Dehnen-McLaughlin profile can be obtained:

$$\rho(r) = \frac{5}{9}\frac{M_{\rm tot}}{\pi r_{\rm sc}^3}\frac{(r/r_{\rm sc})^{-7/9}}{\left[1 + (r/r_{\rm sc})^{4/9}\right]^6}\,. \tag{1.29}$$

In terms of the parameters in equation (1.25) this profile has $(\alpha', \beta', \gamma') = (\frac{4}{9}, \frac{31}{9}, \frac{7}{9})$, and as with the other profiles it has a well defined peak in $V_c(r)$.

Further haloes of interest are the Burkert profile which is suitable for the mass profiles of dwarf galaxies (Burkert 1995), and the Einasto profile which applies a Sérsic-type fitting function (equation 1.3) for the three-dimensional mass density profile (Einasto 1965). Each of these profiles is detailed in Table 1.1. They perform comparatively well with one another in describing dark matter haloes (for an overview see Merritt et al. 2006). A comparison of the density, mass and circular speed curves of the SIS halo (equation 1.9) with the non-isothermal haloes from Table 1.1 are shown in Figure 1.7. This figure shows that for all of the listed non-isothermal haloes the density profiles are shallower than isothermal at small radii and steeper than isothermal at large radii, and that all haloes possess a well defined peak in their circular speed curves at $r_{\rm pk}$.

1.2.3 Protogalactic Gas

Dark matter haloes accrete baryonic matter within their deep potential wells leading to the formation of stars. This *cosmological infall* of gas is expected to occur supersonically, which causes shocks to form and the infalling gas to become thermalised (Rees & Ostriker 1977). If the heated gas cools then it will lose pressure support and fall to the centre. This will increase the density and lead to star formation in the halo core. Estimates of cooling rates indicate that massive dark matter haloes should have 'overcooled'. This would lead to the formation of more massive galaxies than any seen today (White & Rees 1978; White & Frenk 1991; Benson et al. 2003). A solution to this overcooling problem is a feedback process which is capable of limiting cooling by energy injection back into the gas. Such a process may arise from supernovae during star formation as the gas condenses, or from radiative accretion onto a central black hole (see Sections 1.1.4 and 1.5). The energy from supernovae is insufficient to heat the entire halo, and therefore energy input from AGN is favoured (see review by Benson 2010). This energy is likely to be in the form of an outflow due to super-Eddington ac-

cretion (King 2009). Much like how AGN feedback is invoked to explain how early-type galaxies become 'red and dead' the overcooling problem is another aspect of galaxy formation where the presence of a centrally accreting SMBH is warranted. The question of how these black holes form, and how they are detected is treated in the following section.

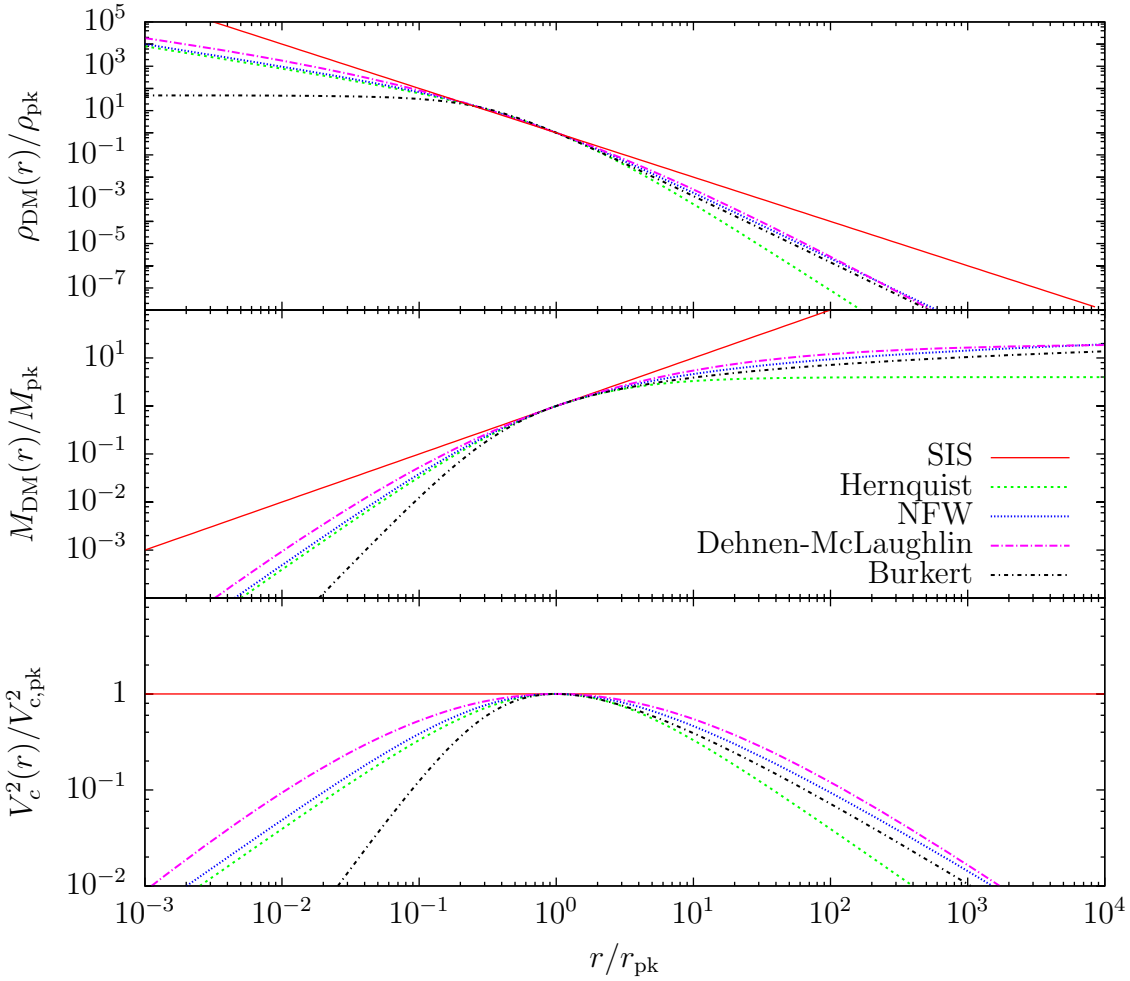

Figure 1.7: Density, mass, and circular speed curves for the SIS, Hernquist, NFW, Dehnen-McLaughlin, Burkert, and Moore dark matter haloes plotted against halo radius. The halo radii are normalised to $r_{\rm pk}$: $x \equiv r/r_{\rm pk}$. *Top:* Density distributions normalised to the density at $x = 1$. *Middle:* Mass distributions normalised to halo mass at $x = 1$. *Bottom:* Circular speed profiles normalised to the circular speed at $x = 1$.

	$\rho_{\rm DM}(x)$	$M_{\rm DM}(x)$	$V_c(x)$
SIS	$\dfrac{\sigma^2}{2\pi G x^2}$	$\dfrac{2\sigma^2 x}{G}$	$2\sigma^2$
Hernquist	$\dfrac{8\rho_{\rm pk}}{x}\,(1+x)^{-3}$	$4M_{\rm pk}x^2\,(1+x)^{-2}$	$\dfrac{4GM_{\rm pk}}{r_{\rm pk}}x\,(1+x)^{-2}$
NFW	$\dfrac{4\rho_{-2}}{\mathcal{R}x}\,(1+\mathcal{R}x)^{-2}$	$M_{\rm pk}\dfrac{\ln(1+\mathcal{R}x)-\mathcal{R}x/\,(1+\mathcal{R}x)}{\ln(1+\mathcal{R})-\mathcal{R}/(1+\mathcal{R})}$	$\dfrac{GM_{\rm pk}}{r_{\rm pk}}\dfrac{\ln(1+\mathcal{R}x)-\mathcal{R}x/\,(1+\mathcal{R}x)}{x\,[\ln(1+\mathcal{R})-\mathcal{R}/(1+\mathcal{R})]}$
Dehnen-McLaughlin	$\dfrac{2^6\rho_0\left[(11/9)^{9/4}x\right]^{-7/9}}{\left\{1+\left[(11/9)^{9/4}x\right]^{4/9}\right\}^6}$	$M_{\rm pk}\left(\dfrac{20}{11}\right)^5\left(\dfrac{(11/9)x^{4/9}}{1+(11/9)x^{4/9}}\right)^5$	$\dfrac{GM_{\rm pk}}{r_{\rm pk}}\left(\dfrac{1}{x}\right)\left(\dfrac{20}{11}\right)^5\left(\dfrac{(11/9)x^{4/9}}{1+(11/9)x^{4/9}}\right)^5$
Burkert	$\dfrac{4\rho_0}{(1+\mathcal{R}x)(1+\mathcal{R}^2x^2)}$	$M_{\rm pk}\dfrac{\ln\left[(1+\mathcal{R}x)\sqrt{1+\mathcal{R}^2x^2}\right]-\tan^{-1}(\mathcal{R}x)}{\ln\left[(1+\mathcal{R})\sqrt{1+\mathcal{R}^2}\right]-\tan^{-1}(\mathcal{R})}$	$\dfrac{GM_{\rm pk}}{r_{\rm pk}}\dfrac{\ln\left[(1+\mathcal{R}x)\sqrt{1+\mathcal{R}^2x^2}\right]-\tan^{-1}(\mathcal{R}x)}{x\{\ln\left[(1+\mathcal{R})\sqrt{1+\mathcal{R}^2}\right]-\tan^{-1}(\mathcal{R})\}}$
Moore	$\dfrac{2^{3/2}\rho_0}{(\mathcal{R}x)^{3/2}(1+\mathcal{R}x)^{3/2}}$	$M_{\rm pk}\dfrac{\sinh^{-1}\left(\sqrt{\mathcal{R}x}\right)-\sqrt{\mathcal{R}x/(1+\mathcal{R}x)}}{\sinh^{-1}\left(\sqrt{\mathcal{R}}\right)-\sqrt{\mathcal{R}/(1+\mathcal{R})}}$	$\dfrac{GM_{\rm pk}}{r_{\rm pk}}\dfrac{\sinh^{-1}\left(\sqrt{\mathcal{R}x}\right)-\sqrt{\mathcal{R}x/(1+\mathcal{R}x)}}{x\left[\sinh^{-1}\left(\sqrt{\mathcal{R}}\right)-\sqrt{\mathcal{R}/(1+\mathcal{R})}\right]}$

Table 1.1: Dark matter profile density, mass, and circular speed functions. For the non-isothermal haloes $x \equiv r/r_{\rm pk}$. The constant for the NFW halo is: $\mathcal{R} = r_{\rm pk}/r_{-2} \simeq 2.163$, whereas for the Burkert halo: $\mathcal{R} = r_{\rm pk}/r_0 \simeq 3.245$, and Moore halo: $\mathcal{R} = r_{\rm pk}/r_0 \simeq 1.055$.

1.3 Supermassive Black Holes

1.3.1 Growth from Seed Black Holes

As discussed in Section 1.1.4, SMBHs with masses $\sim 10^7 M_\odot$ reside in the centres of most galaxies (Ferrarese & Ford 2005; Kormendy & Ho 2013), but how they formed remains an unsolved and complex problem in astrophysics. Growth of these SMBHs by accretion is responsible for powering quasars observed at redshifts as high as $z > 6$ (Barth et al. 2003) which indicates the presence of SMBHs when the universe was less than 1 Gyr old. Before SMBHs can grow by accretion of gas there must be a *seed black hole* to begin with. There are many possible explanations for how these seeds may have formed (Rees 1978), but three popular explanations are (see Volonteri 2010 for a review): direct gas collapse (Haehnelt & Rees 1993), stellar mergers in high redshift galaxy clusters (Devecchi & Volonteri 2009), and Population III remnants (Madau & Rees 2001). Direct collapse of halo gas toward the centre of a protogalaxy can produce and subsequently feed a seed black hole with its mass in the range $10^4 - 10^5 M_\odot$. Stellar mergers of compact nuclear star clusters during the first episodes of star formation could lead to the formation of seed stars with masses: $10^2 - 10^4 M_\odot$ on timescales as short as 3 Myr (Volonteri 2010). Population III stars are the earliest stars to form in the universe, and their remnants could form black hole seeds with masses in the range $10^2 - 10^3 M_\odot$.

The development from a seed black hole into an SMBH occurs through the accretion of protogalactic gas. This process can be broadly separated into two modes: a *quasar mode* during which the black hole rapidly accretes at or near to the Eddington rate (equation 1.19), and a radio mode during which the black hole accretes at a lower rate which produces weak optical but strong radio emission (see Harrison 2014 for a review). Most of the SMBH growth occurs during the quasar phase when large amounts of gas are driven into the black hole through galaxy mergers. This gas forms a luminous accretion disk around the black hole, and the radiation released is responsible for the feedback process in which winds from the accretion disk couple with the ambient

gas and limit further accretion (see Section 1.5). During the radio mode energy is also injected into the surrounding gas in the form of highly collimated jets. Both of these modes can be observed in the AGN of local active galaxies, which can be treated as the low redshift analogues of the formative processes which occurred at high redshift in protogalaxies.

1.3.2 Reverberation Mapping

If the AGN within active galaxies are the result of a centrally accreting SMBH, then the mass of the SMBH can be determined from properties of the AGN spectrum. As discussed in Section 1.1.4, the unification scheme for AGN (Antonucci 1993; Urry & Padovani 1995) has the central SMBH and accretion disk obscured by a thick molecular torus. Within this torus is the *broad emission line region* (BLR) shown in Figure 1.5. The BLR is comprised of small dense clouds of gas which are ionised by the radiation from the central SMBH, and can be observed in the form of broad emission lines. These emission lines vary in response to changes in the continuum radiation, and show a delayed response which indicates the size of the BLR to be 10 to 100 times larger than the accretion disk which is about $\sim 1000 r_S$. Determining the size of the BLR $R_{\rm BLR}$ in this manner and using the virial theorem (Section 1.1.2) the mass of the SMBH can be found from:

$$M_{\rm BH} = \frac{F R_{\rm BLR} \sigma^2}{G}\,, \tag{1.30}$$

where σ is the velocity dispersion inferred from the emission line width, and F is a factor of order unity which takes into account the geometry of the BLR. This is the process of reverberation mapping (Blandford & McKee 1982; Netzer & Peterson 1997 - see Peterson & Bentz 2006 for a review) and has led to the determination of many SMBH masses (Kaspi et al. 2000; Grier et al. 2012).

1.3.3 Stellar Dynamical Methods for SMBH Detection

Reverberation mapping only works in the detection of accreting SMBHs, and therefore another method must be used for finding the now quiescent SMBHs present in the centres of normal galaxies (see Section 1.1.4).

The inner parsecs of the Milky Way host a dense nuclear star cluster (Becklin & Neugebauer 1968), hot gaseous clouds of ionised hydrogen, and a clumpy torus of cool molecular gas. At the centre is the compact and optically dark radio source Sgr A* (Balick & Brown 1974) which is currently the best evidence for the existence of an SMBH. By monitoring the Keplerian stellar orbits (of innermost arcsecond 'S-stars') around this object it has been determined that this is an SMBH of mass: $M_{\rm BH} \simeq 4.4 \times 10^6 M_\odot$ (Gillessen et al. 2009, see Genzel, Eisenhauer & Gillessen 2010 for a review).

For more distant systems stars can be used as dynamical tracers around the SMBH as long as they lie within its sphere of influence:

$$r_{\rm inf} = \frac{GM_{\rm BH}}{\sigma^2}\,. \tag{1.31}$$

If the galaxy is treated as a collisionless stellar system with a distribution function $f(\mathbf{x}, \mathbf{v}, t)$ which describes the density of stars in the phase space $(\mathbf{x}, \mathbf{v})$, then the number of stars within the element of volume $d\mathbf{x}d\mathbf{v}$ is given by $f(\mathbf{x}, \mathbf{v}, t)d\mathbf{x}d\mathbf{v}$. The stars passing through this phase space volume are governed by the continuity equation:

$$\frac{\partial f}{\partial t} + \mathbf{v}\cdot\nabla f - \nabla\Phi\cdot\frac{\partial f}{\partial \mathbf{v}} = 0\,, \tag{1.32}$$

where Φ is the total gravitational potential. Equation (1.32) is the collisionless Boltzmann equation, and it states that the phase space density is conserved along all paths.

Assuming a spherical potential the Jeans equation (1.28) can be obtained by taking the first moment of equation (1.32) (Merritt 2013), which can then be used to obtain an expression for the mass of the SMBH and stars:

$$M(r) = M_{\rm BH} + M_*(r) = \frac{r\sigma_r^2}{G}\left[-\frac{d\ln\rho(r)}{d\ln r} - \frac{d\ln\sigma_r^2(r)}{d\ln r} - 2B(r)\right]\,. \tag{1.33}$$

The first SMBH mass measurement using equation (1.33) assumed isotropy ($B = 0$, Sargent et al. 1978).

Relaxing the assumption of isotropy increases the complexity of SMBH mass measurements (see Ferrarese & Ford 2005 for a review). Developments in dealing with anisotropic systems (Schwarzschild 1979, 1993) have led to the construction of SMBH detection codes (Dressler & Richstone 1988; Kormendy & Richstone 1992). SMBH masses measured using these codes (Gebhardt et al. 2000, 2003) have been shown to agree with results from reverberation mapping, and with those from gas dynamical methods.

1.3.4 Gas Dynamical Methods for SMBH Detection

Most spiral galaxies and the majority of ellipticals show optical nebular line emission from ionised gas at their centres. Measuring the velocity V_c of particles in the (assumed circular) disk of ionised gas allows the interior mass to be measured directly from the rotational velocity of the gas (Harms et al. 1994; Ferrarese, Ford & Jaffe 1996):

$$V_c^2(r) = \frac{G(M_* + M_{\rm DM} + M_{\rm BH})}{r}\,. \tag{1.34}$$

The mass of the central SMBH is one of the free parameters which is obtained from a best fit to the data of the galaxy. The other parameters relate to the disk. They include the disk stellar mass to light ratio which is required to obtain its stellar mass density, the disk's systemic velocity, and its angle of inclination (Ferrarese & Ford 2005).

Gas dynamical mass measurements are technically simpler than stellar dynamical measurements. They lack the complexity associated with anisotropic stellar motions as the motion of the gas is simply characterised by one velocity $V_c(r)$ at every radius. However, there are a number of requirements which must be met in order for this model to work. The gas must orbit the galaxy's centre in the form of a regular symmetric disk, and should be free from perturbations due to turbulence (Barth et al. 2016), radiation pressure, or magnetic fields. Very few galaxies satisfy these criteria, and

therefore despite its simplicity the approach is less successful than stellar dynamical modelling.

Gas dynamical measurements have provided measurements for large samples of central SMBHs (Sarzi et al. 2002; Beifiori et al. 2009; Davis et al. 2013, 2017, 2018; Onishi et al. 2015; Barth et al. 2016; Smith et al. 2019). In turn these samples serve as constraints on the observed correlations between the SMBH and global properties of the galaxy (Kormendy & Ho 2013; Beifiori et al. 2012) which will be discussed in the following section.

1.4 Phenomenological Correlations

1.4.1 Galaxy Correlations

As outlined in Section 1.1.4, SMBHs in the centres of galaxies are expected to be ubiquitous, and this argument is supported by observations made using the techniques described in Section 1.3. As discussed in both of these sections, if an SMBH has grown via the accretion of gas in a highly active quasar phase then the energy released may have influenced global properties of the galaxy. This is supported by observed correlations between the SMBH mass and global stellar properties such as velocity dispersion and bulge mass. Before discussing these correlations it is important to outline how the stellar properties of the galaxy relate with one another. These correlations have a rich history and have many equivalent formulations.

An empirical relation between the luminosity of elliptical galaxies and their stellar velocity dispersion was provided by Faber & Jackson (1976). They found that the (B-band) luminosity measured inside the effective radius R_e correlates with the central velocity dispersion of the galaxy. The *Faber-Jackson relation* takes the following form:

$$L_{\rm gal} \propto \sigma^{a'} \tag{1.35}$$

where $a' \simeq 4$. This proportionality (with $a' = 4$) can be obtained from equation (1.8) using the virial theorem and by assuming a constant mass-luminosity ratio M/L and

a constant surface brightness $\propto L/R^2$.

An analogous relation for spiral galaxies was obtained by Tully & Fisher (1977). They obtained the rotation velocities $V_{\rm rot}$ of several spiral galaxies from Doppler broadened 21cm emission lines of neutral hydrogen. They found that the rotation velocities correlated with the intrinsic luminosity of the galaxies, but the slope is dependent on the passband. The *Tully-Fisher relation* has the following form:

$$L_{\rm gal,B} \propto V_{\rm rot}^{2.5}\,, \tag{1.36}$$

in the B blue waveband, and

$$L_{\rm gal,H} \propto V_{\rm rot}^{4}\,, \tag{1.37}$$

in the H infrared waveband (Aaronson & Mould 1983).

The Faber-Jackson relation is a projection of the *Fundamental Plane* for elliptical galaxies. The Fundamental Plane is a set of correlations which defines a plane in the space of effective radius R_e, velocity dispersion σ, and average effective surface brightness $\langle I\rangle_e \propto L/R_e$:

$$\log(R_e) = A'\log(\sigma) + B'\log(\langle I\rangle_e) + C' \tag{1.38}$$

with $A' \simeq 1.5$, $B' \simeq -0.8$ and $C' \simeq 0.15$ (see D'Onofrio et al. 2006 for a review).

1.4.2 SMBH Mass Correlations with the Host Spheroid

The earliest observed $M_{\rm BH}$ correlation was that between the SMBH mass and the (visual band) luminosity of the host bulge or elliptical galaxy (Dressler 1989; Kormendy & McClure 1993; Kormendy & Richstone 1995). This has been subsequently observed in larger samples (Marconi & Hunt 2003; Ferrarese & Ford 2005; Gültekin et al. 2009; McConnell & Ma 2013) using K-band (near infrared) luminosities to minimise the effects of internal absorption (extinction) and young (bright blue) stars. The relation can be expressed in the form (Kormendy & Ho 2013):

$$\frac{M_{\rm BH}}{10^9 M_\odot} = (0.544^{+0.067}_{-0.059}) \left(\frac{L_{\rm K,bulge}}{10^{11} L_{K_\odot}}\right)^{1.22\pm0.08}\,. \tag{1.39}$$

This relation is shown alongside the data from Kormendy & Ho (2013) in Figure 1.8. Kormendy & Richstone (1995) highlighted that this correlation is indicative of coevolution between the SMBH and the host bulge because the total bulge luminosity is outside of the direct influence of the SMBH.

The next natural step is to relate this to the stellar bulge mass $M_{\rm bulge}$ either through the virial theorem (Marconi & Hunt 2003) using equation (1.8), or through dynamical modelling to obtain a mass-to-light ratio (Magorrian et al. 1998; Häring & Rix 2004). Using the latter method the following correlation can be obtained (Kormendy & Ho 2013):

$$\frac{M_{\rm BH}}{10^9 M_\odot} = (0.49^{+0.06}_{-0.05}) \left(\frac{M_{\rm bulge}}{10^{11} M_\odot} \right)^{1.17 \pm 0.08} . \tag{1.40}$$

By considering the galaxy luminosity correlations in Section 1.4.1, the $M_{\rm BH} - L$ relation leads to the consideration of a possible correlation of SMBH mass with stellar velocity dispersion within the bulge. The $M_{\rm BH} - \sigma$ relation (Ferrarese & Merritt 2000; Gebhardt et al. 2000) is (Kormendy & Ho 2013):

$$\frac{M_{\rm BH}}{10^9 M_\odot} = (0.310^{+0.037}_{-0.033}) \left(\frac{\sigma}{200 \text{ km s}^{-1}} \right)^{4.38 \pm 0.29} . \tag{1.41}$$

This relation is shown alongside the data of Kormendy & Ho (2013) in Figure 1.8. The velocity dispersion is the line of sight velocity dispersion which is typically averaged within the effective radius $R_{\rm eff}$. Effective radii can be of the order $1 - 10$ kpc for large galaxies (Binney & Tremaine 2008). The effective radius is therefore much larger than the gravitational influence radius $r_{\rm inf}$ (see equation 1.31) of an SMBH with mass given by equation (1.41), and therefore far beyond the reach of the SMBH's direct gravitational influence. This again is an indication that the SMBH and its host spheroid are likely to have coevolved via a mutual process.

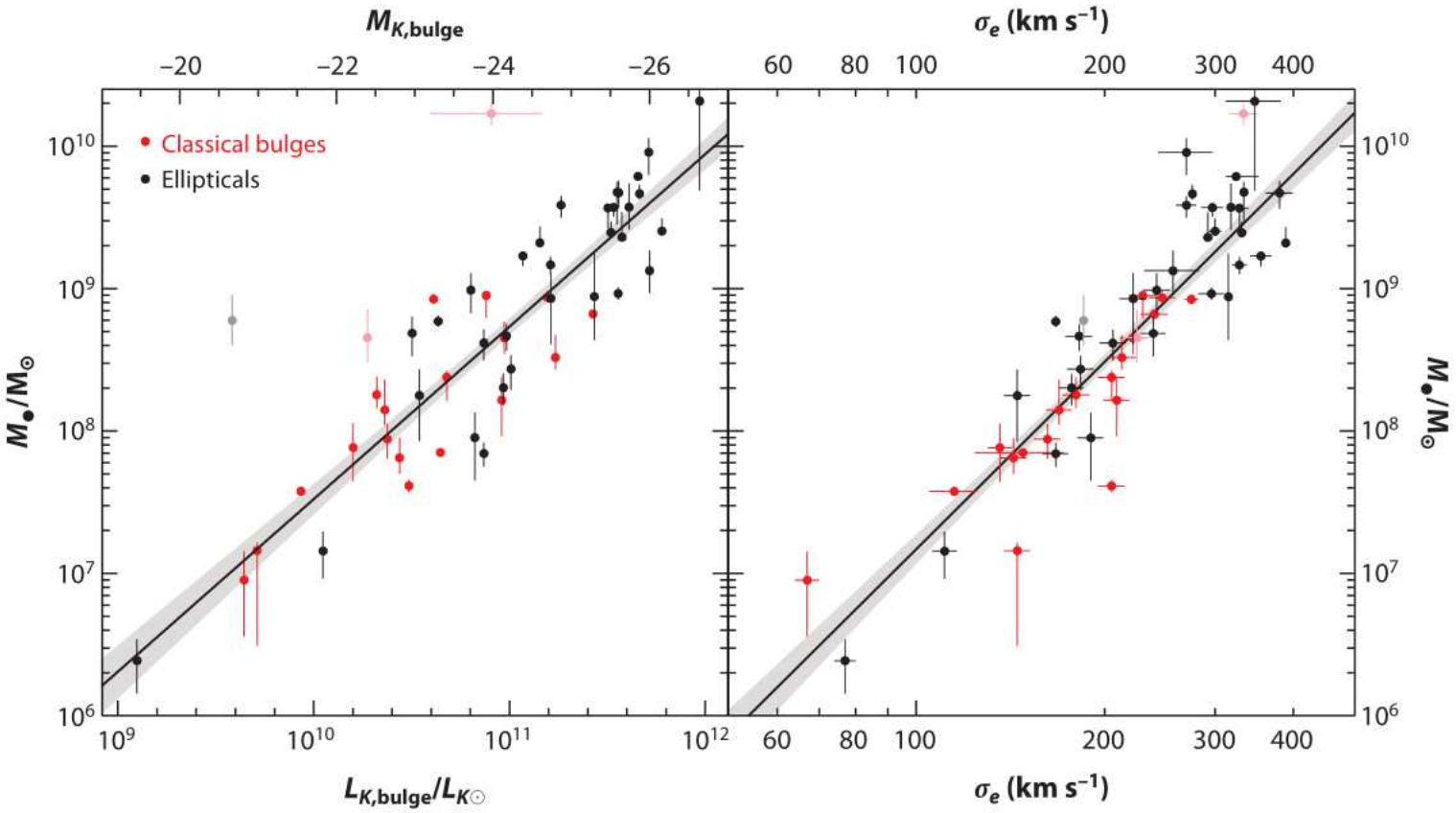

Figure 1.8: $M_{\rm BH} - L_K$ and $M_{\rm BH} - \sigma$ relations (reproduced from Kormendy & Ho 2013).

1.4.3 SMBH Mass Correlations with the Dark Matter Halo

Velocity dispersions are measured within the effective radii of galaxy bulges. Large scale circular velocities can be measured at radii an order of magnitude beyond this at radii where the gravity of the dark matter halo becomes dominant. In spiral galaxies the disk circular velocity can be measured directly from HI observations at large radii where the rotation velocity curve flattens. In elliptical galaxies the circular velocity can be obtained from the dynamical modelling of stellar motions (Gerhard et al. 2001). Measurements of circular velocity can be compared with bulge stellar velocity dispersion to obtain a $V_c - \sigma$ relation (Ferrarese 2002):

$$\log V_c = (0.84 \pm 0.09) \log \sigma + (0.55 \pm 0.19)\,. \tag{1.42}$$

The strength of the $V_c - \sigma$ correlation was found to be lowered when using larger sample sizes (Ho 2007), however this sample included nearly bulge-less galaxies where σ could only be measured at small scales from the central cluster. These galaxies increased the scatter in the $V_c - \sigma$ correlation. The $V_c - \sigma$ relation can be combined with the $M_{\rm BH} - \sigma$ relation (Ferrarese & Merritt 2000) to give a relation between $M_{\rm BH}$ and V_c (Volonteri, Natarajan & Gültekin 2011),:

$$\left(\frac{M_{\rm BH}}{10^8 M_\odot}\right) \simeq (0.25 \pm 0.07) \left(\frac{V_c}{200 \text{ km s}^{-1}}\right)^{4.22 \pm 0.93}\,, \tag{1.43}$$

(see also Baes et al. 2003). This relation may be as strong as the $M_{\rm BH} - \sigma$ relation (Volonteri, Natarajan & Gültekin 2011), yet there are objections as to how any properties of the dark matter halo could directly correlate with the SMBH mass (Kormendy & Bender 2011).

If the correlations were set by a gas clearing feedback event during an active quasar phase (see Section 1.1.4) then the resultant SMBH mass will be set by the gravitational potential of the gaseous protogalaxy. This potential is dominated by the gravitational potential of the dark matter, and can therefore lead to a correlation between $M_{\rm BH}$ and the maximum circular speed of the halo $V_{\rm c,pk}$ (McQuillin & McLaughlin 2012). How correlations at $z = 0$ may have arisen between $M_{\rm BH}$ and σ can then be

understood by determining the relationship between σ and $V_{\rm c,pk}$ at $z = 0$. Then by accounting for the redshift evolution of $V_{\rm c,pk}(z)$ the $M_{\rm BH}$ set at higher redshift can be related to the current stellar σ. The resultant $M_{\rm BH} - \sigma$ correlation is non-linear in log-log space (Larkin & McLaughlin 2016).

Throughout the preceding sections the requirement for negative feedback within protogalaxies has been indicated. This feedback occurs during an active growth phase of SMBHs which is expected (through theory and observation) to be present in all large galaxies (see Sections 1.1.4 and 1.3). The radiation released by an accreting SMBH (observed in quasars and local AGN) is likely to have a significant effect upon its host galaxy. This may explain the rapid depletion of gas and suppression of star formation in early-type galaxies (see Section 1.1.3), and prevent the overcooling of dark matter haloes (see Section 1.2). It may also explain how the central SMBH masses came to correlate with global stellar properties and even dark matter properties of their host galaxies (current section). The details of how this feeback occurs, and the observational support for such a process are discussed in the following section.

1.5 Feedback

1.5.1 SMBH Winds

This section outlines the key analytical and observational results relating to wind-driven outflows from an accreting SMBH. Much of the theory regarding the dynamics and structure of these outflows was developed in the context of stellar wind-blown bubbles. The theory of wind-blown bubbles will be covered in detail in Chapter 2.

As mentioned in Sections 1.1.4 and 1.3.1, the feedback produced when SMBHs grow through the rapid accretion of gas during a highly active quasar phase can significantly affect the host galaxy. If this energy can couple with the ambient gas in the galaxy in the form of an outflow, then it may clear the gas and halt further accretion onto the SMBH. A feedback process in which an outflow sweeps a galaxy clear of gas

in this manner would also lead to the cessation of star formation (Di Matteo, Springel & Hernquist 2005; Springel, Di Matteo & Hernquist 2005; Bower et al. 2006; Croton et al. 2006; Hopkins et al. 2008), and could account for how early-type galaxies deplete their gas reservoirs and inhibit star formation as outlined in Section 1.1.3. Another possible outcome of this feedback would be an SMBH mass which correlates with global properties of the galaxy such as those outlined in Section 1.4.

A mechanism by which the accretion energy couples with the ambient gas is through a mechanical wind of accretion disk material. King & Pounds (2003) developed the case of a super-Eddington accreting SMBH which produces a Compton-thick wind with constant speed v_w and a momentum-flux approximately equal to $L_{\rm Edd}/c$. They begin with the wind density:

$$\rho_w = \frac{\dot{M}_w}{4\pi v_w r^2}\,, \tag{1.44}$$

and consider the electron scattering optical depth τ which depends on this density and is integrated from infinity down to a radius R:

$$\tau = \int_R^\infty \kappa\rho_w\, dr = \frac{\kappa\dot{M}_w}{4\pi v_w R}\,, \tag{1.45}$$

where $\kappa = \sigma_T/m_p$ is the opacity. Defining the photospheric radius as the radius where $\tau = 1$ (single scattering), and requiring this to be close to the escape radius the following relationship is obtained:

$$\dot{M}_w v_w = \tau\frac{L_{\rm Edd}}{c}\,. \tag{1.46}$$

Therefore the energy flux of the wind is:

$$\dot{E}_w = \frac{1}{2}\dot{M}_w v_w^2 = \tau\frac{L_{\rm Edd} v_w}{2c}\,, \tag{1.47}$$

and the wind density can be expressed as:

$$\rho_w = \tau\frac{L_{\rm Edd}}{4\pi v_w^2 r^2 c}\,. \tag{1.48}$$

Observations of AGN do indicate the presence of small scale $r \sim 10 - 100 r_S$ winds. X-ray spectra from AGN show the absorption from ionised gas, or a 'warm absorber' (Halpern 1984; Reynolds & Fabian 1995; Sako et al. 2001). The warm

absorber corresponds to the motion of ions moving with velocities $v_w \sim 1000$ km s^{-1}. Higher-velocity winds have been detected in UV observations of broad absorption-line (BAL) quasars (Weymann et al. 1991; Ganguly et al. 2007), and in blueshifted X-ray absorption lines in quasar spectra which show highly ionised and fast $v_w \approx 0.1 - 0.25c$ winds (Chartas et al. 2002; Pounds et al. 2003b; Pounds et al. 2003a; Reeves, O'Brien & Ward 2003; Reeves et al. 2009). Further studies using XMM-Newton and Suzaku data found many more AGN winds with outflow velocities in the range $v_w \sim 0.03 - 0.3c$ (Cappi et al. 2006; Tombesi et al. 2010; Gofford et al. 2013) along with high mass outflow rates and energy fluxes. Particularly high mass outflow rates of $\dot{M}_w \sim 2M_\odot$ yr^{-1}, and energy rates $\dot{E}_w \sim 4.5 \times 10^{44}$ erg s^{-1} have been observed in the Seyfert Galaxy PG1211+143 (Pounds & Reeves 2007, 2009).

Winds with such high speeds are capable of sweeping the ambient gas into a shell and driving it with velocity v away from the SMBH. Such a fast moving shell at radius r would be bounded by two shock fronts (see chapter 2): one which travels forward into the ambient medium and one which travels back into the wind. Between the wind shock at $r_{\rm sw}$ and the shell of swept up gas is a region of shocked wind, and it is possible for the expansion of this region as the wind inputs energy to drive the shell outwards. Whether or not the pressure of the shocked wind region drives the shell is determined by whether it is efficiently cooled (with timescale $t_{\rm cool}$). This defines two limiting regimes: the *energy-driven* regime for which none of the thermal energy of the shell is radiated away ($t_{\rm cool} \gg r/v$), and the *momentum-driven* regime for which all of the thermal energy of the shocked wind is radiated away before the wind can replenish it ($t_{\rm cool} \ll r_{\rm sw}/v_w$). In the energy-driven regime the pressure of the expanding shocked wind region drives the shell, while in the momentum-driven regime this pressure is lost and it is the momentum transferred directly by the wind which drives the shell. For a more detailed discussion of these regimes see Sections 2.2.2 and 2.2.3.

For a momentum-driven shell from a wind with momentum-flux $\dot{M}_w v_w = \tau L_{\rm Edd}/c$ propagating within an SIS dark matter halo with gas tracing the dark matter directly, the shell will achieve a terminal velocity at large radii. The following SMBH mass must

be exceeded to have a positive coasting velocity at large radii (King 2003, 2005):

$$M_\sigma \equiv \frac{f_0 \kappa \sigma^4}{\tau \pi G^2} \simeq 4.56 \times 10^8 M_\odot \frac{1}{\tau} \left(\frac{f_0}{0.2} \right) \left(\frac{\sigma}{200 \text{ km s}^{-1}} \right)^4 , \tag{1.49}$$

(see also Fabian 1999; Murray, Quataert & Thompson 2005), with f_0 the gas to dark matter ratio. McQuillin & McLaughlin (2012) showed that exceeding M_σ is a necessary but not sufficient condition for the shell to reach large radii. They found that the shell also requires an initial momentum:

$$\frac{M_{\rm sh} v}{2 f_0 M_\sigma \sigma_0} > \sqrt{\frac{M_{\rm BH}}{2(M_{\rm BH} - M_\sigma)}} . \tag{1.50}$$

The dependence of a momentum-driven shell's velocity field on initial momentum in an SIS halo is shown in Figure 1.9 (with each curve corresponding to a different value of initial momentum) for three values of $M_{\rm BH} = 0.3 M_\sigma, 1.01 M_\sigma, 3 M_\sigma$. This figure shows that for $M_{\rm BH} > M_\sigma$ there are 'launch solutions' where (previously stalled) shells can resume outward motion from non-zero radii. It also shows that $M_{\rm BH} = 3 M_\sigma$ results in a momentum-driven shell with large radius terminal velocity $v_\infty = 2\sigma$: the escape velocity for a truncated isothermal sphere. Since momentum-driven shells in an SIS acquire a constant coasting speed at large radii the 'critical mass' M_σ can then be defined simply as the SMBH mass which allows a shell to reach large radii (i.e. positive coasting velocity). In the case of momentum-driven shells launched from constant mass SMBHs, this is equivalent to the SMBH mass which leads to shells that never stall. If changes are introduced such as including ambient pressure or a growing SMBH then these two masses may no longer be equivalent. This is because in these circumstances a shell may stall, and after a period of infall resume outward motion and reach large radii. SMBH masses just in excess of M_σ lead to shells with very small coasting velocities. Therefore a solution of interest will always be $v_\infty = 2\sigma$ where the shell achieves an appreciable velocity equal to the escape velocity for a truncated SIS.

An energy-driven shell sweeping up gas in an SIS halo will also achieve a constant terminal velocity. By equating this velocity to the escape velocity of a truncated SIS it can be shown that the product of SMBH mass and wind speed is required to be greater

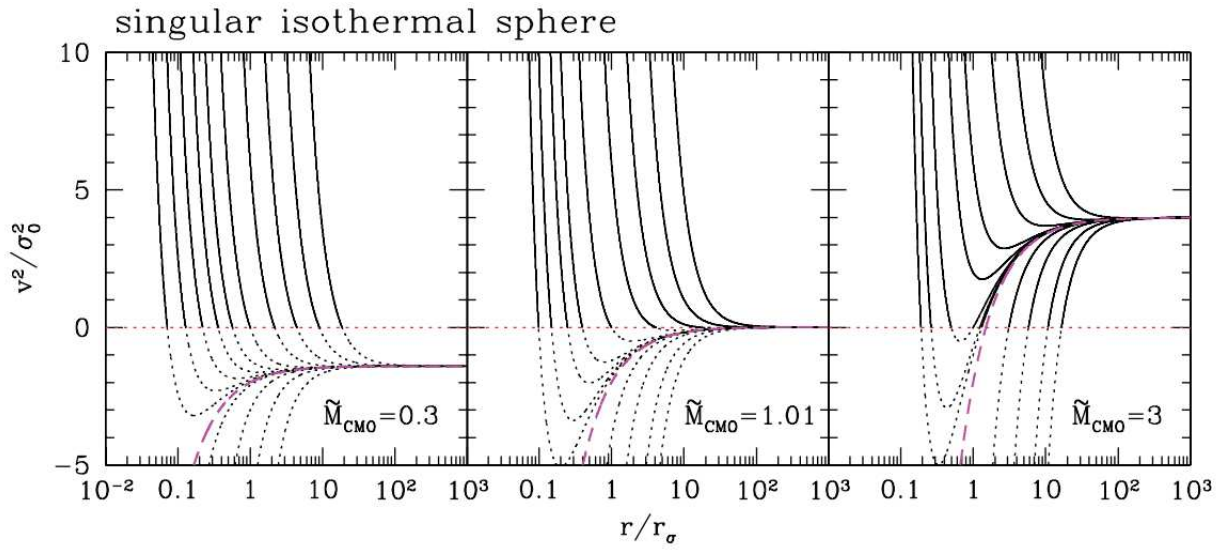

Figure 1.9: Velocity fields of momentum-driven shells in an SIS halo from McQuillin & McLaughlin (2012). Shown in the left panel are shells which are launched from a central massive object (SMBH or nuclear star cluster) with mass below the critical mass $\widetilde{M}_{\rm CMO} \equiv M_{\rm CMO}/M_\sigma < 1$, and therefore these shells go on to stall at finite radii. The middle panel shows the case where shells are just able to reach large radii. The right panel shows a range of shell solutions which can escape, and launch solutions which start from the $v^2 = 0$ line.

than (McQuillin & McLaughlin 2013):

$$M_{\rm BH} v_w \geq \frac{1}{\tau}\frac{4(4\gamma-3)}{(\gamma-1)}\frac{\kappa f_0}{\pi G^2}\sigma^5 \simeq \left(6.68\times10^6\right) M_\odot c \frac{1}{\tau}\left(\frac{f_0}{0.2}\right)\left(\frac{\sigma}{200\ {\rm km\ s^{-1}}}\right)^5 . \quad (1.51)$$

Equations (1.49) and (1.51) exhibit similar scalings to the $M_{\rm BH}-\sigma$ correlation which has $M_{\rm BH} \propto \sigma^{4-5}$ (see Section 1.4). Equation (1.49) has no additional parameter, but equation (1.51) includes the wind velocity. McQuillin & McLaughlin (2013) use equation (1.51) to interpret the scatter in the $M_{\rm BH}-\sigma$ data as a distribution in wind speeds, and they infer a median wind speed of $v_w = 0.035c$ from the data. When compared with actual wind speed distributions obtained from X-ray observations of local active galaxies (Tombesi et al. 2011; Gofford et al. 2013) (with median $v_w/c = 0.1, 0.056$ respectively) the inferred distribution of McQuillin & McLaughlin (2013) compares well. Equations (1.49) and (1.51) (with $v_w = 0.035c$) are shown in Figure 1.10 plotted

alongside the data of Gültekin et al. (2009) and McConnell & Ma (2013).

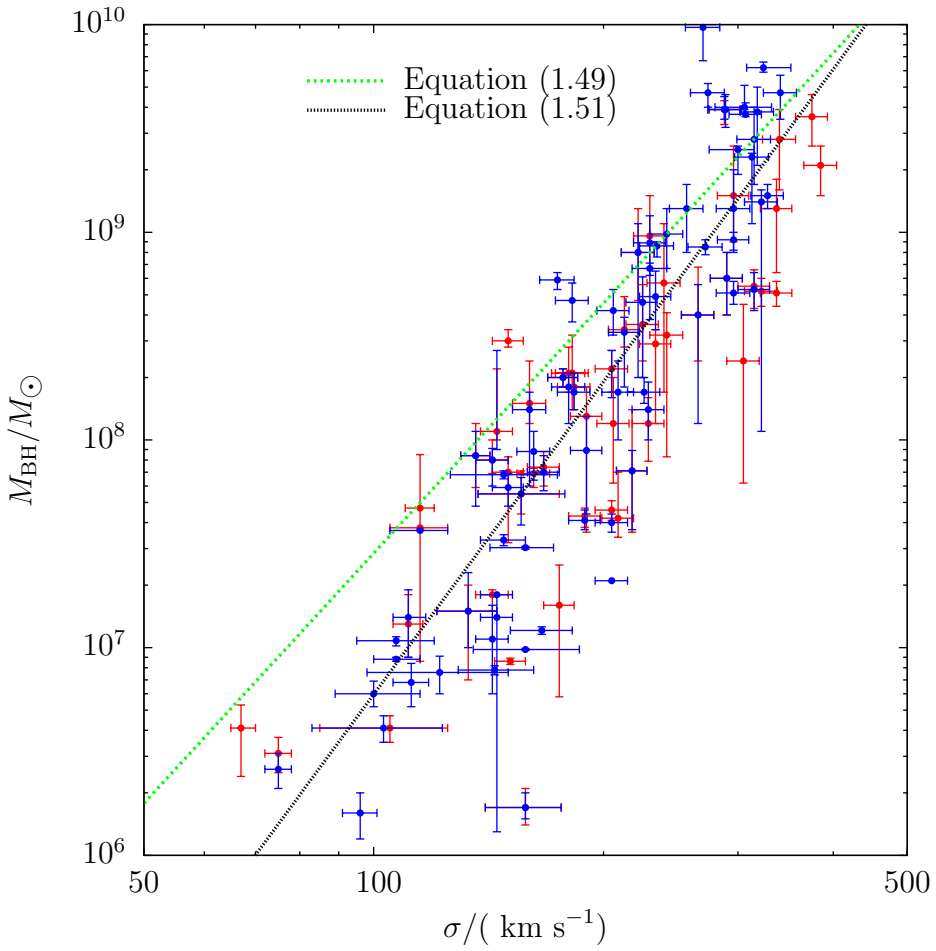

Figure 1.10: The derived $M_{\rm BH} - \sigma$ relations plotted alongside the data of Gültekin et al. (2009) and McConnell & Ma (2013).

Both of equations (1.49) and (1.51) for momentum- and energy-driven shells were obtained assuming an SIS halo. An improvement to equation (1.49) can be made by analysing a momentum-driven shell propagating into a non-isothermal halo. A critical SMBH mass is sought which leads to shells that never stall. By looking at the velocity fields (Figure 1.11), it can be seen that all solutions have a minimum in dv^2/dr before

accelerating at large radii. The critical case can be defined as the one where the velocity at this minimum is exactly zero for a shell launched with zero initial momentum. Then it can be shown that a momentum-driven shell with inital momentum greater than or equal to zero never stalls in a non-isothermal halo if its mass is greater than (McQuillin & McLaughlin 2012):

$$M_{\rm BH} \geq \frac{f_0 \kappa}{\pi G^2} \frac{V_{\rm c,pk}^4}{4} \simeq 1.14 \times 10^8 M_\odot \left(\frac{f_0}{0.2}\right) \left(\frac{V_{\rm c,pk}}{200 \text{ km s}^{-1}}\right)^4 , \tag{1.52}$$

where $V_{\rm c,pk}$ is the peak value of the halo's circular speed (see Section 1.2.2). This establishes a theoretical connection between the SMBH mass and dark matter halo. The redshift evolution of quasars can be taken into account by relating the circular speed at the time of gas blowout $V_{\rm c,pk}(z)$ in equation (1.52) with the $z = 0$ stellar velocity dispersion $\sigma_{\rm ap}(R_e)$ (measured within an aperture equal to the stellar effective radius) which leads to a non-linear $M_{\rm BH} - \sigma_{\rm ap}(R_e)$ correlation in log-log space (Larkin & McLaughlin 2016).

The dominant process responsible for cooling the shocked wind region is inverse Compton scattering (King 2003, 2005). By analysing cooling times for inverse Compton scattering (McQuillin & McLaughlin 2013; Faucher-Giguère & Quataert 2012), and from simulations of outflows (Costa, Sijacki & Haehnelt 2014) it has been shown that wind-driven outflows spend most of their time in the energy-driven regime. This may lead to the conclusion that equation (1.51) is preferable to equation (1.49). However, the correlation between $M_{\rm BH}$ and σ is likely to be established early-on in the momentum-driven regime, since in order to reach large enough radii that cooling becomes inefficient and the shell can transition to the energy-driven regime the central SMBH mass must exceed M_σ.

Smoothed particle hydrodynamics simulations of galaxies support the establishment of the $M_{\rm BH}$ correlations via the momentum deposition of a wind into the ambient gas (Debuhr, Quataert & Ma 2011). They also confirm the likelihood of high mass outflow rates at larger galactic radii which is consistent with energy-driven shells clearing gas and suppressing star formation (Debuhr, Quataert & Ma 2012; Costa, Sijacki & Haehnelt 2014). The gas blowout from feedback is a possible explanation for the

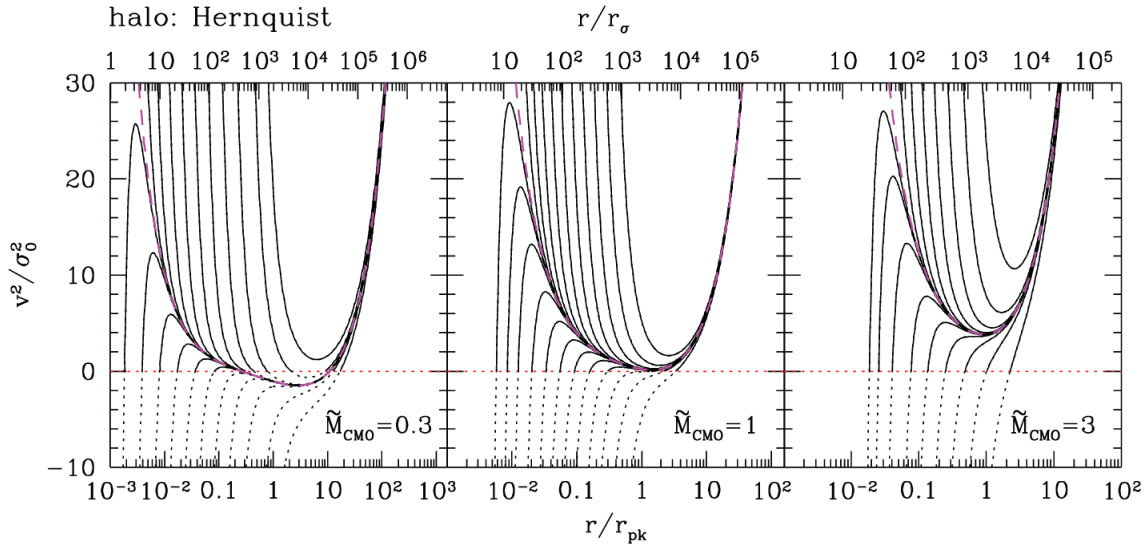

Figure 1.11: Velocity fields of momentum-driven shells in a Hernquist halo from McQuillin & McLaughlin (2012). This figure shows in order for shells with zero initial momentum (magenta curve) to reach large radii without stalling it is required that the mass of the central massive object (SMBH or nuclear star cluster) exceed the mass given by equation (1.52).

clearing of gas and cessation of star formation in early-type galaxies. It is also possible for gas outflows to cause 'positive feedback' by actually triggering star formation (Zubovas et al. 2013). This could be achieved either by forming stars within the shell which go on to enrich the intracluster medium (Ishibashi & Fabian 2012; Ishibashi, Fabian & Canning 2013), or even instead from radio mode feedback where the jets from a modestly accreting central SMBH induce star formation (Gaibler et al. 2012).

Many of the results using analytical approaches to model protogalactic outflows (obtaining equations 1.49−1.52 for example) have been obtained assuming a constant SMBH mass. This assumption conflicts with the fact that the SMBH is likely to be accreting mass at a substantial rate (as outlined in Sections 1.1.4 and 1.3.1). While some analytical work has been carried out on outflows from growing SMBHs (Gilli et al. 2017), a time dependent treatment which includes growing SMBHs, and which actually tracks shell infall dynamics following a stall and any subsequent potential re-expansion

has yet to be carried out. A natural extension of this time-dependent investigation is to incorporate cooling processes, which will allow for a full treatment of the outflow's evolution throughout its lifetime rather than simply assuming either momentum- or energy-driven. This will enable the conditions which specify the transition through dynamical regimes to be stated in terms of global parameters such as the rate of energy injection by the wind, or the dark matter halo mass.

1.5.2 Large Scale Outflows

In addition to the small scale winds observed from X-ray data, large $\sim$ kpc galactic scale outflows can be observed within quasars and local ultra luminous infrared galaxies (ULIRGs) in various forms of emission from the outflowing gas. These include emission from ionized gas (Greene, Zakamska & Smith 2012; Harrison et al. 2012), neutral atomic gas (Veilleux, Cecil & Bland-Hawthorn 2005; Rupke & Veilleux 2011), and molecular gas in CO millimetre (Feruglio et al. 2010; Cicone et al. 2012, 2014; Feruglio et al. 2017) and in OH (Sturm et al. 2011; Maiolino et al. 2012; González-Alfonso et al. 2014, 2017. Large scale outflows have much lower velocities than the small scale winds, often in the range $\sim 100 - 1000$km s^{-1}, but they typically have higher mass outflow rates of $10 - 1000 M_{\odot}$ yr^{-1}. These rates are often higher than the rates of star formation, and therefore the large scale outflows are the likely candidates for sweeping the galaxy clear of gas. Observations of large scale outflows have shown that their momentum-fluxes can be boosted relative to the source which have: $\dot{M}v/L_{\rm AGN}/c \gg 1$. These *momentum boosts* can be modest, such as $2 - 10 L_{\rm AGN}/c$ (Feruglio et al. 2017; Rupke, Gültekin & Veilleux 2017), or significantly larger with $\dot{M}v/L_{\rm AGN}/c \gg 10$ (Fiore et al. 2017; Rupke, Gültekin & Veilleux 2017).

This momentum boosting is inconsistent with momentum-driven shells, for which the momentum-flux can never exceed $\dot{M}_w v_w$. Instead it can only occur for energy-driven shells where the thermal energy transferred to the outflow by the wind is conserved, and therefore the pressure of hot shocked wind region can lead to momentum-fluxes far in excess of $\dot{M}_w v_w$. Zubovas & King (2012) obtained the terminal velocity for an

energy-driven shell propagating in an SIS halo in the limit that the wind is strong, where $M_{\rm BH}v_w \gg M_\sigma\sigma$, which leads to fast ($v \gg \sigma$) outflows, and found that the momentum boost on the shell is:

$$\frac{\dot{M}_{\rm sh}v}{\dot{M}_w v_w} \simeq \frac{v_w}{v}\,. \tag{1.53}$$

This expression for the momentum boost only applies for constant mass SMBHs launching fast ($v \gg \sigma$) shells within isothermal dark matter haloes (Zubovas & King 2012; Faucher-Giguère & Quataert 2012). Studies have also shown that the momentum boost has an upper limit which occurs as a result of the outflow having to do work against gravity (Richings & Faucher-Giguère 2018). It has also been demonstrated that momentum boosting can occur under certain circumstances in outflows driven by radiation pressure on dust (Ishibashi, Fabian & Maiolino 2018). It is important to note that not all large-scale outflows have momentum-boosts, and therefore may be consistent with momentum-driving (González-Alfonso et al. 2017).

For some systems both the small scale wind and resultant large scale molecular outflow have been observed (Tombesi et al. 2015, 2017; Feruglio et al. 2015). These systems provide a way of testing expressions such as equation (1.53) for the momentum-boost of the outflow. Figure 1.12 from Tombesi et al. (2015) shows equation (1.53) against observed values of $\dot{M}v$ for a number of systems, and indeed the relationship predicts a value of $v_w \sim 0.2c$ based on $\dot{M}v$ of the large scale outflow which agrees with their observed value for v_w. Broadly this comparison shows that the large scale momentum-fluxes are consistent with shells launched by winds with speeds in the range $v_w = 0.1 - 0.4c$.

According to equation (1.53) the level of momentum boosting is dependent on the small scale wind velocity close to the SMBH. Therefore this feature of outflows is very useful in connecting small and large scale outflows within a observational context. While some attempts have been made to compare simple analytical results with observational data (Feruglio et al. 2015; Tombesi et al. 2015), a detailed analytical treatment of momentum boosts within non-isothermal (or even isothermal) haloes has yet to be carried out. Another commonly overlooked aspect of these outflows is the dynami-

cal effect of the ambient gas ram pressure which is usually assumed to be negligible, but is included in more complete analytical treatments of wind-driven outflows within non-isothermal haloes (Faucher-Giguère & Quataert 2012; Gilli et al. 2017; Richings & Faucher-Giguère 2018).

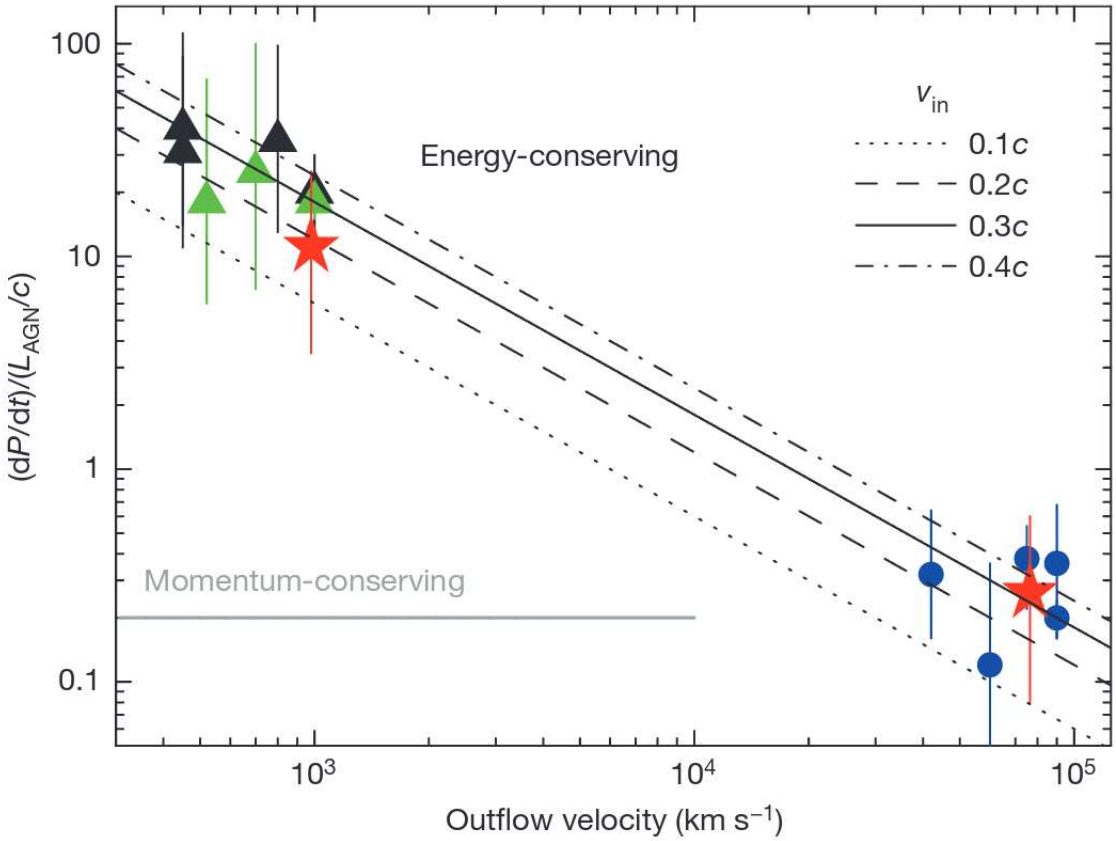

Figure 1.12: Momentum-fluxes of small and large scale outflows vs. outflow velocity. Reproduced from Tombesi et al. (2015). This plot has the momentum-flux of the outflow normalised to that of the wind plotted against the outflow velocity. The red stars correspond to the measured momentum-fluxes for F1111+3257, the green triangles are OH observations of ULIRGs, the black triangles are CO observations of ULIRGS, and the blue dots are small scale X-ray observations.

1.6 Outline of the Thesis

In Chapter 2 the aspects of wind-driven bubbles in the absence of gravity will be outlined. The intention is to familiarise the reader with the core theory utilised in the subsequent chapters, and to provide solutions which can be compared to results from later chapters which will include gravity. This chapter follows on from the work of Koo & McKee (1992) which generalised previous work on wind bubbles to cover power-law mass injection rates and power-law gas density profiles. I generalise this work further by introducing a power-law cooling function, and examine how variation in cooling rates impact the bubble dynamics.

Chapter 3 contains the treatment of shells launched by steady winds: i.e. those with $M_{\rm BH} = \text{const}$. The intention of this chapter is to lay the groundwork before introducing a time-dependent $M_{\rm BH}(t)$. This is achieved by developing previous work on steady winds through the inclusion of ambient pressure on the shell, and by examining both momentum- and energy-driven shells within isothermal and non-isothermal dark matter haloes. The emphasis of this chapter will be on how the shells propagate *in time* as well as their spatial behaviour, and this will require the infall dynamics of shells to be accounted for. Particular focus will be maintained on the momentum-boosts of shells in order to connect any conclusions to observations of active galaxies. This work will culminate in the analysis of how relationships obtained from these shells between the SMBH and global outflow and galactic properties can be applied to the $M_{\rm BH} - \sigma$ correlation described in Section 1.4, and observations of momentum-boosted outflows in active galaxies.

Chapter 4 follows on from Chapter 3 and shows the treatment of shells launched by non-steady winds: i.e. those with a growing $M_{\rm BH}(t)$. It will carry this out by introducing a form for the SMBH mass which allows the constant mass case and exponential mass case (see equation 1.19) to be recovered. Broadly, the aim of this chapter is to analyse the differences that emerge in shell dynamics from introducing a non-steady wind, and the results are to be compared directly back to Chapter 3. An estimate is sought for the critical SMBH mass which is required in order to have shells that can

reach large radii without stalling, and this is to be compared with any critical masses obtained in Chapter 3. The conclusions drawn relating to outflow or galactic properties from analysing shells driven by steady winds in Chapter 3 are to be reassessed in this chapter to see if they still apply for non-steady winds.

Chapter 5 discusses the results and conclusions from the previous chapters and provides possible directions for future work.

2 Dynamics of Wind-Driven Bubbles

In order to begin the discussion of wind driven outflows from supermassive black holes which were outlined in section 1.5, this chapter will review the theory and literature of wind-blown bubbles which result from a point source of mass injection inside of an ambient gas distribution. These bubbles exist as a shell-like structure bounded by two strong shocks. One of these strong shocks propagates back into the wind, and the other out into the ambient medium. The motion of this shock structure defines the motion of the bubble as a whole. This chapter will begin by explaining the development of these shocks, and how the gas properties within them are expected to vary.

This chapter will then provide an overview of how these bubbles evolve throughout their lifetimes, and extend the theory to include variable cooling rates. Much of this theory was developed within the context of stellar wind bubbles which were often considered in the absence of gravity (Avedisova 1972; Steigman, Strittmatter & Williams 1975; Castor, McCray & Weaver 1975; Weaver et al. 1977; Ostriker & McKee 1988; Koo & McKee 1992b; Koo & McKee 1992a). These analyses showed that the dynamics of the bubble can be broadly separated into two regimes: momentum-driven or energy-driven. As introduced in Section 1.5, which of these two regimes applies is determined by the efficiency of cooling in the shocked wind, and therefore the possible mechanisms for cooling are reviewed within this section. The original work in this chapter is the extension of the work by Koo & McKee (1992a) to include a general power-law form for the cooling function, and this enables the evolution of bubbles to be re-evaluated for different forms of cooling.

Much of the work on stellar wind bubbles was carried out assuming that inward gravitational forces could be neglected. In order to fully account for the dynamics of wind driven bubbles from SMBHs the effects of gravity must be included. This chapter will conclude with an overview of attempts thus far to properly account for gravity acting on such bubbles, and set up the equations of motion of SMBH wind driven bubbles under gravity which will be analysed throughout this thesis.

2.1 Bubble Formation and Structure

2.1.1 Shock Structure

The following analysis concerns an ideal gas consisting of particles with mass m in a distribution with density ρ_g, temperature T, pressure P_g, and ratio of specific heats $C_P/C_V = \gamma$. Any perturbations within the gas will propagate as waves with adiabatic sound speed c_s given by:

$$c_s = \sqrt{\frac{\gamma P_g}{\rho_g}} = \sqrt{\frac{\gamma k_B T}{m}}\,. \tag{2.1}$$

A point source within the gas distribution can be introduced which injects mass in the form of an isotropic steady wind with speed v_w and density $\rho_w(t)$. This leads to the creation of a spherical boundary (with radius r_c) between the wind and the ambient gas called a *contact discontinuity* through which the gas properties describing the wind and the ambient medium are expected to change rapidly. If the wind speed is supersonic $v_w > c_s$, then the wind acts as a piston driving into and sweeping up the ambient gas. This causes the density profile of the ambient gas close to the contact discontinuity to become much steeper than the undisturbed ambient gas (see Frank, King & Raine 2002 for details). This steepening of the density profile leads to the formation of a shockwave which has a thickness of the order of the mean free path λ_d for the gas particles (see Figure 2.1).

This results in the creation of a shell-like region of shocked ambient gas between the contact discontinuity and the *forward shock* (with radius r_s) which drives into the undisturbed ambient gas. This region is often what is meant when referring to *the shell*. As the shell gains mass its inertia increases, and from momentum conservation its velocity will drop below v_w. This leads to a second shock front dubbed the *reverse (or, wind) shock* (with radius $r_{\rm sw}$). This creates another shell-like region (consisting of shocked wind - see Figure 2.2) which is bounded by the contact discontinuity and the wind shock driving back into the freely flowing wind (Koo & McKee 1992b). The region of shocked ambient medium will be referred to as 'the shell', while the term

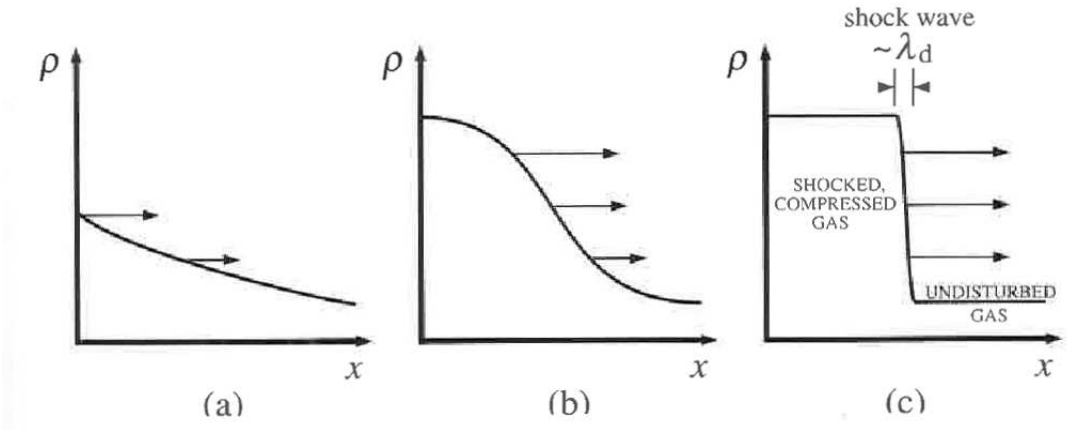

Figure 2.1: The development of a shock in a constant density medium. The plots show gas density against position in the gas. From left to right shows the motion of a region of gas which increases in density as it sweeps up more gas which is distributed uniformly. The result is a region of high density shocked gas bounded by a shock of thickness $\sim \lambda_d$ which moves into the ambient gas (reproduced from Frank, King & Raine 2002).

'wind bubble' is used to describe the entire structure which also includes the shocked wind.

2.1.2 Jump Conditions

Across the shocks the gas density, velocity, and pressure change from their pre-shock values ρ_1, v_1, P_1 (such as in the undisturbed ambient gas or freely flowing wind) to the post-shock values ρ_2, v_2, P_2 (such as in the shocked ambient gas or shocked wind regions) all defined in the frame of reference where the shock is at rest. For a one-dimensional steady flow these changes are given by the Rankine-Hugoniot jump conditions. These conditions are obtained from mass, momentum, and energy conservation across the

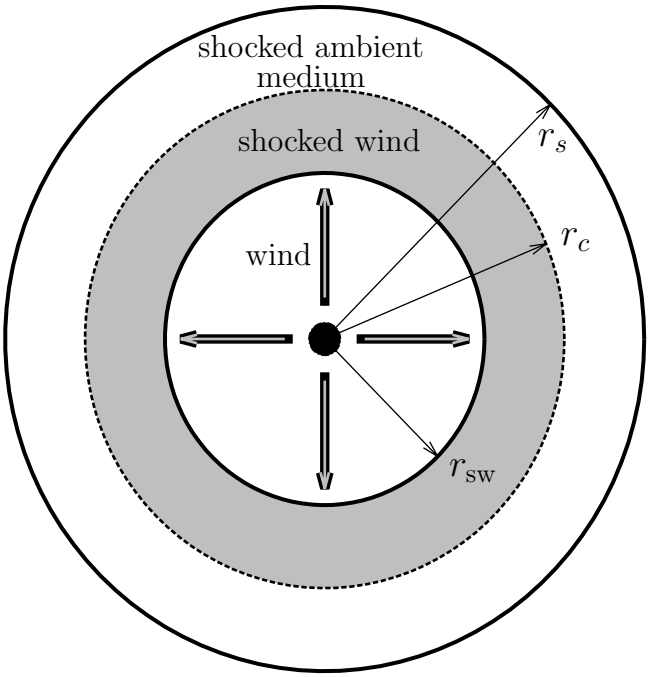

Figure 2.2: The structure of a wind bubble. In the centre is the point source from which the wind emanates. The wind and the ambient gas distribution are separated by the contact discontinuity at r_c which is shown as the dotted line. Either side of the contact discontinuity are the shocked wind region (shown in grey) which is separated from the freely flowing wind by a strong shock at $r_{\rm sw}$, and the shocked ambient medium which is separated from the undisturbed ambient medium by a strong shock at r_s. Both strong shocks are depicted as solid black lines.

shocks (see Choudhuri 1998):

$$\begin{aligned} \frac{\rho_2}{\rho_1} = \frac{v_1}{v_2} &= \frac{(\gamma+1)\mathscr{M}^2}{2+(\gamma-1)\mathscr{M}^2} \\ &\rightarrow \frac{\gamma+1}{\gamma-1} \qquad (\mathscr{M} \gg 1)\,, \end{aligned} \tag{2.2}$$

and the pressure:

$$\frac{P_2}{P_1} = \frac{2\gamma\mathscr{M}^2-(\gamma-1)}{\gamma+1}\,, \tag{2.3}$$

where $\mathscr{M} = v_1/c_{s,1} = v_1/\sqrt{\gamma P_1/\rho_1}$ is the *Mach number* of the pre-shock medium. The pre-shock pressure can be written in terms of the Mach number: $P_1 = \rho_1 v_1^2/\gamma\mathscr{M}^2$. Equation (2.3) can then be rewritten as:

$$P_2 = \frac{2v_1^2\rho_1}{(\gamma+1)} - \frac{\gamma-1}{\gamma+1}\frac{v_1^2}{\mathscr{M}^2}\frac{\rho_1}{\gamma}\,. \tag{2.4}$$

In the so-called *strong shock limit* of $\mathscr{M} \gg 1$ equation (2.4) gives:

$$P_2 \to \frac{2v_1^2\rho_1}{(\gamma+1)} \qquad (\mathscr{M} \gg 1)\,. \tag{2.5}$$

2.2 Evolution of the Bubble Structure

This section now considers a spherically symmetric gas distribution which scales as a power law in radius. The gas is centred on a point mass producing a wind which drives an outflow, and it has the following density profile:

$$\rho_g(r) = \rho_s\left(\frac{r}{r_0}\right)^{p-3}\,, \tag{2.6}$$

where p is the scaling of the total gas mass with radius $M_g(r) \propto r^p$, r_0 is a characteristic radius, and ρ_s is the density at that radius. If the gas were distributed in the form of a singular isothermal sphere (SIS) (see Section 1.1.2) then $p = 1$. It is useful to define a mean density inside the radius r:

$$\bar{\rho}_g(<r) = \frac{M_g(r)}{\frac{4}{3}\pi r^3} = \frac{3}{p}\rho_g(r)\,. \tag{2.7}$$

Consider a mechanical wind from the point source injecting mass as a function of time:

$$\dot{M}_w(t) = \frac{M_{w,s}}{t_s}\left(\frac{t}{t_s}\right)^{\alpha}\,, \tag{2.8}$$

where α is the mass rate parameter, t_s is the scale time, and $M_{w,s}$ is defined as $\dot{M}_w(t_s)t_s$. Physically this mass may be a wind of stellar material, or a wind of accretion disk material from an accreting SMBH (see Section 1.5). The parameter value $\alpha = -1$

corresponds to a blast wave, and the value $\alpha = 0$ corresponds to a constant injection rate, whereas the values $\alpha = 1$ and $\alpha = 2$ correspond to an SMBH with constant and linear growth rates respectively (since $\dot{M}_w v_w \propto M_{\rm BH}$). The total mass injected by the wind at time t is therefore:

$$M_w(t) = \frac{M_{w,s}}{\alpha + 1} \left(\frac{t}{t_s} \right)^{\alpha+1} . \tag{2.9}$$

2.2.1 Free Expansion

At early times the wind mass exceeds the mass of swept up ambient medium, i.e. $M_w(t) \gg M_g(r_s) \approx M_g(r_c)$. During this time the shell is infinitesimally thin ($r_s \approx r_c$) as the ram pressure of the wind compresses the region of shocked ambient medium. At early times the wind can therefore be approximated as freely expanding. However, it is expected at later times and larger radii that the mass of swept up ambient medium will eventually exceed the mass of the wind: $M_w(t) \ll M_g(r_s)$.

It is useful to define a fiducial radius r_f and time:

$$t_f \equiv \frac{r_f}{v_w} , \tag{2.10}$$

at which the average wind density is equal to the mean gas density inside r_f. The density of the wind at r_f is given by mass conservation to be $\rho_w(r_f) = \dot{M}_w(t_f)/4\pi r_f^2 v_w$. Following Koo & McKee (1992a) and using $M_w(t_f)/t_f$ for the mass rate at t_f:

$$\rho_w(r_f) = \frac{M_w(t_f)}{4\pi r_f^2 v_w t_f} \equiv \frac{3\rho_s}{p} \left(\frac{r_f}{r_0} \right)^{p-3} = \bar{\rho}_g(r_f) . \tag{2.11}$$

This leads to:

$$r_f = \left[\frac{p M_{w,s}}{12\pi(\alpha+1)(\rho_s / r_0^{p-3})(v_w t_s)^{\alpha+1}} \right]^{1/(p-1-\alpha)} . \tag{2.12}$$

Then for times $t \ll t_f$ the wind can be treated as freely expanding, but for times $t \gg t_f$ the dynamics of the bubble are determined by the mass of swept up gas. The pre-shock ($r \lesssim r_{\rm sw}$) density of the wind depends on the crossing time of the wind: $t_{\rm cr} = r_{\rm sw}/v_w$,

and it can be written in terms of the fiducial quantities:

$$\begin{aligned}\rho_w(t - t_{\rm cr}, r_{\rm sw}) &= \frac{M_{w,s}}{4\pi r_{\rm sw}^2 v_w t_s^{\alpha+1}} \left(t - \frac{r_{\rm sw}}{v_w}\right)^{\alpha} \\ &= (\alpha+1)\bar{\rho}_g(r_f) \left(\frac{r_{\rm sw}}{r_f}\right)^{-2} \left(\frac{t}{t_f} - \frac{r_{\rm sw}}{r_f}\right)^{\alpha} .\end{aligned} \tag{2.13}$$

2.2.2 Radiative (Momentum-Driven) Bubble

As introduced in Section 1.5 if the cooling time of the shocked wind region $t_{\rm cool}$ is much less than the time taken for the wind to input more energy $t_{\rm cr} = r_{\rm sw}/v_w$ then the shell is driven directly by the momentum of the wind (McKee & Hollenbach 1987). This cooling requires that the wind shock is radiative and the region of shocked wind exists as a thin shell. If the forward shock is also radiative then the region of shocked ambient medium also occupies a thin region. In this case the shell is approximated as thin: $r_{\rm sw} \approx r_c \approx r_s$ (see Figure 2.3). If the forward shock is not radiative then any results obtained assuming a thin shell are no longer exact, but remain a good approximation (Koo & McKee 1992a). As long as the wind shock is radiative ($t_{\rm cool} \ll t_{\rm cr}$) the shell is expected to be momentum-driven.

The mass of the momentum-driven shell at time t consists of the mass of shocked wind injected up to the time $t - r/v_w$ combined with the mass of swept-up ambient medium. The momentum of the shell with radius $r = r_c \sim r_{\rm sw} \sim r_s$ and speed v is equal to the momentum of the wind $M_w v_w$ by momentum conservation:

$$\left[M_w\left(t - r/v_w\right) + \frac{4\pi\rho_s r_0^3}{p}\left(\frac{r}{r_0}\right)^p\right] v = M_w\left(t - r/v_w\right) v_w\,. \tag{2.14}$$

Equation (2.14) can be put in terms of the fiducial quantities (using equations 2.9 and 2.11):

$$\left(\frac{t}{t_f} - \frac{r}{r_f}\right)^{\alpha+1} = \left[\left(\frac{t}{t_f} - \frac{r}{r_f}\right)^{\alpha+1} + \frac{1}{3}\left(\frac{r}{r_f}\right)^p\right]\frac{v}{v_w}\,, \tag{2.15}$$

which can be solved to give:

$$\frac{t}{t_f} = \frac{r}{r_f} + \left[\frac{\alpha+2}{3(p+1)}\right]^{1/(\alpha+2)} \left(\frac{r}{r_f}\right)^{(p+1)/(\alpha+2)}\,, \tag{2.16}$$

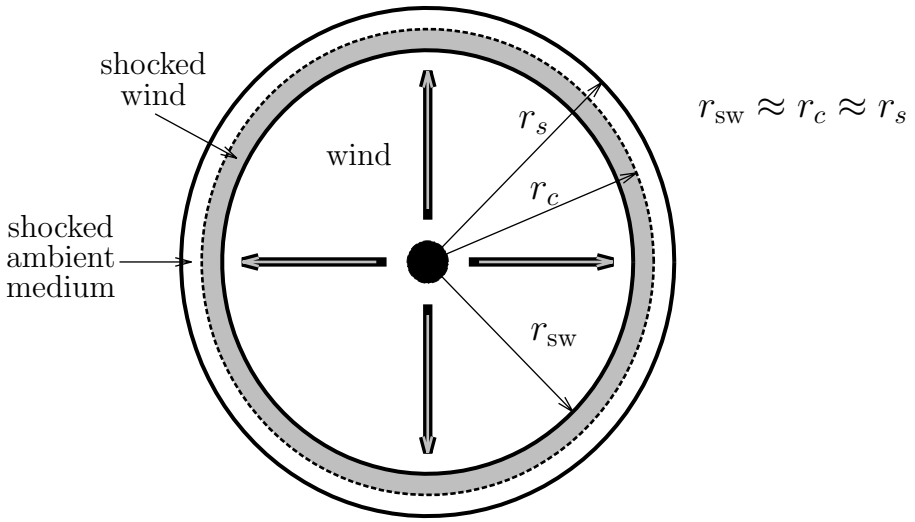

Figure 2.3: The structure of a radiative bubble with the thin shell approximation. The shocked wind region between $r_{\rm sw}$ and r_c (shown in grey) is cooled and confined to a thin shell in the radiative bubble. Under the thin shell approximation the region of shocked ambient medium between r_c and r_s is also assumed to be cooled.

which has the limiting behaviour:

$$r = v_w t \qquad (t \ll t_f)\,, \tag{2.17}$$

$$r = \left[\frac{\alpha+2}{3(p+1)}\right]^{1/(p+1)} \left(\frac{t}{t_f}\right)^{(\alpha+2)/(p+1)} r_f \qquad (t \gg t_f)\,. \tag{2.18}$$

Differentiating equation (2.16) with respect to time gives:

$$\frac{v_w}{v} - 1 = \frac{v_{\rm sw,w}}{v} = \frac{1}{3}\left[\frac{3(p+1)}{\alpha+2}\right]^{(\alpha+1)/(\alpha+2)} \left(\frac{r}{r_f}\right)^{(p-\alpha-1)/(\alpha+1)} , \qquad (2.19)$$

where $v_{\rm sw,w}$ is the (negative of the) velocity of the wind shock relative to the wind, and therefore $v_w = v_{\rm sw,w} + v$. This leads to the ratios:

$$\frac{v}{v_w} = \frac{1}{1 + v_{\rm sw,w}/v} , \qquad \frac{v_{\rm sw,w}}{v_w} = \frac{v_{\rm sw,w}/v}{1 + v_{\rm sw,w}/v} . \qquad (2.20)$$

Differentiating equation (2.16) with respect to time again shows shells with $\alpha + 1 < p$ are decelerating, $\alpha + 1 = p$ have constant velocity, and $\alpha + 1 > p$ are accelerating. The accelerating momentum-driven shells will be subject to the Rayleigh-Taylor instability (Koo & McKee 1992a).

The equations obtained in this section for the motion of momentum-driven shells can be used to analyse cooling times and understand the timescales over which the bubble remains radiative.

2.2.3 Adiabatic (Energy-Driven) Bubble

If the wind shock is not radiative then the shocked wind retains its thermal energy and the shell of shocked ambient medium is referred to as energy-driven. This means that the dynamics of the shell are determined primarily by the pressure of the hot shocked wind region (see Figure 2.4) which fills most of the bubble's volume (Avedisova 1972; Castor, McCray & Weaver 1975; Weaver et al. 1977). Without additional mass injection bubbles that transition to the energy-driven regime at $t > t_f$ will remain so for all time (Koo & McKee 1992a).

The internal energy of the shocked wind with pressure P and volume V is given by: $U = PV/(\gamma - 1)$. This is equal to the energy input by the wind minus losses from doing PdV work. The equation for energy conservation in the shocked wind is therefore:

$$\frac{d}{dt}\left[\frac{4}{3}\pi(r_c^3 - r_{sw}^3)\frac{P}{\gamma - 1}\right] = \frac{1}{2}\dot{M}_w v_w^2 - 4\pi(r_c^2 v_c - r_{\rm sw}^2 v_{\rm sw})P . \qquad (2.21)$$

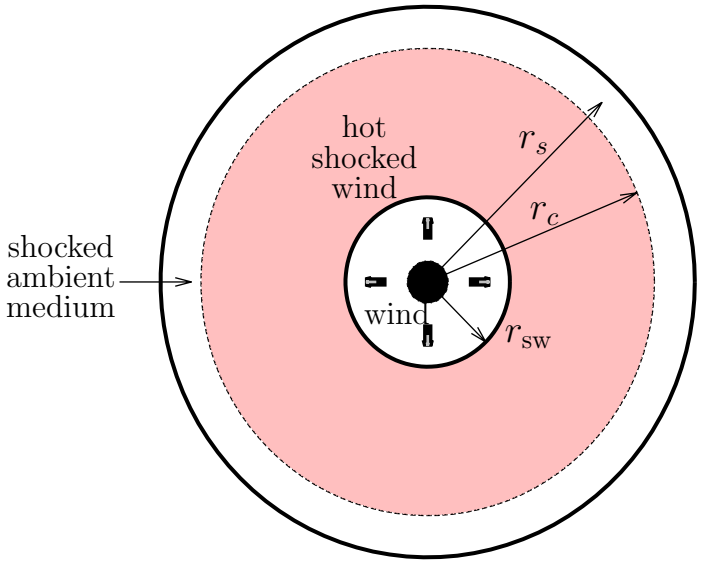

Figure 2.4: The structure of an energy-driven bubble. The shocked wind region shown in pink between $r_{\rm sw}$ and r_c is hot and occupies most of the region interior to r_c. The thermal expansion of this region drives the shell of shocked ambient medium located between r_c and r_s.

By assuming that most of the bubble is occupied by the hot shocked wind (i.e. $r_c \gg r_{\rm sw}$) equation (2.21) has the solution:

$$\frac{r_s}{r_f} = \frac{t_f^{(\alpha+3)/(p+2)}}{r_f} \left[\frac{3(\gamma-1)}{2(3\gamma-2)} \left(\frac{p+2}{\alpha+3} \right)^3 \frac{r_0^{p-3}}{4\pi\rho_s} \frac{M_{\rm w,s}}{t_s^{\alpha+1}} \right]^{1/(p+2)} \left(\frac{t}{t_f} \right)^{(\alpha+3)/(p+2)} . \qquad (2.22)$$

Equation (2.22) gives the radius of the shell of shocked ambient medium which is driven by the expansion of the hot shocked wind region.

2.2.4 Cooling Timescales

In this section previous work by Koo & McKee (1992a) is developed by introducing a general power-law cooling function, and the cooling times of the shocked wind and the shocked ambient medium are rederived. A characteristic cooling time is also introduced which will serve as a simple cooling timescale to be compared with the actual shocked wind and ambient medium cooling times. This section will conclude with an overview of the physical cooling processes and how they can be related to the power-law cooling function.

The cooling function $\Lambda(T)$ represents the energy emitted by a gas normalised to the number density of particles, and is a function of electron temperature T. A cooling function which is a power law in temperature will be adopted:

$$\Lambda(T) = \Lambda_s \left(\frac{T}{T_s}\right)^{\beta} , \tag{2.23}$$

where Λ_s is the value at the scale temperature T_s, and β is the cooling function parameter.

Cooling functions can be expressed in terms of a cooling time $t_{\rm cool} = E/\dot{E}$ with $\Lambda(T) = \dot{E}/n'$, and the thermal energy per particle is $E = x_t k_B T$:

$$t_{\rm cool} = \frac{x_t k_B T_s}{n' \Lambda_s} \left(\frac{T}{T_s}\right)^{1-\beta} , \tag{2.24}$$

where x_t is the number of particles per hydrogen nucleus, and n' is the number density of hydrogen.

Using the ideal gas law, and equations (2.2) and (2.4) in the strong shock limit leads to the cooling time:

$$t_{\rm cool} = \frac{\mathcal{C} v_1^{2-2\beta}}{\rho_1} , \tag{2.25}$$

where ρ_1 is pre-shock density, v_1 the pre-shock gas velocity, and $\mathcal{C}$ is defined to be:

$$\mathcal{C} = \left[\frac{2^{1-\beta}(\gamma-1)^{2-\beta}\mu_H^{2-\beta}}{(\gamma+1)^{3-2\beta} x_t^{-\beta} k_B^{-\beta}}\right] \frac{T_s^{\beta}}{\Lambda_s}, \tag{2.26}$$

where μ_H is the mean mass per hydrogen nucleus. It can be seen that $\beta = 1$ leads to a cooling time which is independent of the pre-shock gas velocity v_1.

Using equation (2.13) with (2.25) gives the cooling time of the shocked wind to be:

$$t_{\rm cool,sw} = \frac{\mathcal{C} v_{\rm sw}^{2-2\beta}}{\rho_w} = \frac{t_1}{\alpha+1}\left(\frac{v_{\rm sw}}{v_w}\right)^{2-2\beta}\left(\frac{r_{\rm sw}}{r_f}\right)^{2}\left(\frac{t}{t_f}-\frac{r_{\rm sw}}{r_f}\right)^{-\alpha}, \tag{2.27}$$

and the cooling time of the shocked ambient medium can be found by using equation (2.6):

$$t_{\rm cool,sa} = \frac{\mathcal{C} v_s^{2-2\beta}}{\rho_g(r_s)} = \frac{3t_1}{p}\left(\frac{v_s}{v_w}\right)^{2-2\beta}\left(\frac{r_s}{r_f}\right)^{3-p}, \tag{2.28}$$

where t_1 is the characteristic cooling time:

$$t_1 = \frac{\mathcal{C} v_w^{2-2\beta}}{\bar{\rho}_g(r_f)}\,. \tag{2.29}$$

The characteristic cooling time given by equation (2.29) is to be compared with the cooling times given by equations (2.27) and (2.28). If t_1 serves as an upper limit to $t_{\rm cool,sw}$ and $t_{\rm cool,sa}$ at a specific radius and for a particular range of parameters (α, p, β) then it may be used in place of these times when analysing bubble evolution.

Before analysing the cooling times given by equations (2.27)−(2.29) the cooling function should be physically motivated. In general the cooling function should represent all the possible cooling and heating rates of a gas, i.e. from collisional line radiation, continuum emission, recombination processes, photoionisation, collisional ionisation, and Compton cooling or heating (Sutherland & Dopita 1993). The cooling function also depends on the metallicity Z (the fraction of mass not in the form of H or He) of the gas:

$$\Lambda(T,Z) = \Lambda_{\rm lines} + \Lambda_{\rm cont} \pm \Lambda_{\rm rec} - \Lambda_{\rm photo} + \Lambda_{\rm coll} \pm \Lambda_{\rm Compton}\,. \tag{2.30}$$

Which of these processes is dominant depends on the temperature range. For example, in the temperature range 10^4 K $< T < 10^{7.5}$ K metal line cooling is expected to be dominant, and the cooling function takes the functional form (Draine 2011; Richings & Faucher-Giguère 2018):

$$\Lambda_{\rm line}(T) = \begin{cases} 5.0\times10^{-22}\left(\frac{T}{10^5\ {\rm K}}\right)^{2}\left(\frac{Z}{Z_\odot}\right) n_e n_H \text{ erg cm}^{-3}\text{ s}^{-1} & 10^4 < T \leq 10^5 \text{ K} \\ 5.0\times10^{-22}\left(\frac{T}{10^5\ {\rm K}}\right)^{-0.7}\left(\frac{Z}{Z_\odot}\right) n_e n_H \text{ erg cm}^{-3}\text{ s}^{-1} & 10^5 < T \leq 10^{7.5} \text{ K}\,. \end{cases} \tag{2.31}$$

At higher temperatures ($T > 10^7$ K) continuum (free-free, or Bremsstrahlung) cooling is dominant with the function:

$$\Lambda_{\rm ff} = 1.426 \times 10^{-27} T^{1/2} n_e n_H \times [g(1,T) + 0.4g(2,T)] \text{ erg cm}^{-3} \text{ s}^{-1} \quad (T > 10^{7.5} \text{ K}), \tag{2.32}$$

where g is defined by (Richings & Faucher-Giguère 2018):

$$g(Z_i, T) = \begin{cases} 0.79464 + 0.1243 \log_{10}(T/Z_i^2) & (T/Z_i^2) < 3.2 \times 10^5 \text{ K} \\ 2.13164 - 0.1240 \log_{10}(T/Z_i^2) & (T/Z_i^2) \geq 3.2 \times 10^5 \text{ K}, \end{cases} \tag{2.33}$$

where Z_i is the ion charge of species i.

Compton cooling occurs when low-energy photons scatter off high-energy electrons (i.e. inverse Compton scattering). At gas temperatures above 10^7 K Compton cooling is expected to be dominant. The cooling function for Compton cooling from a quasar radiation field with luminosity $L = \eta c^2 M_{\rm BH}$ can be approximated by (Sazonov et al. 2005):

$$\Lambda_{\rm Compton}(T) = 4.1 \times 10^{-35} (1.9 \times 10^7 - T) \frac{L}{r^2} \text{ erg cm}^{-3} \text{ s}^{-1}. \tag{2.34}$$

Costa, Sijacki & Haehnelt (2014) obtain a cooling time from this function, and also highlight that at higher temperatures $T \gtrsim 10^9$ K the inverse Compton cooling rate scales as $\propto T^2$.

The physically interesting values for β are therefore $-1 < \beta \leq -1/2$ for metal-line cooling, $\beta = 0$ for a constant cooling rate, $\beta = 1/2$ for free-free cooling, and $1 < \beta \leq 2$ for Compton cooling.

2.2.5 Cooling Times for a Momentum-Driven Bubble

Equations (2.27) and (2.28) are the general cooling times for the shocked wind and shocked ambient medium which have been extended to include general power law cooling. This section will analyse these cooling times for variation in the cooling parameter β. Equation (2.27) can be examined in the case that the bubble is momentum-driven

by using equations (2.19), (2.20) and (2.16), which leads to the following expression:

$$t_{\rm cool,sw} = \frac{t_1}{\alpha+1}\left(\frac{1}{3}\right)^{2-2\beta}\left[\frac{3(1-p)}{\alpha+2}\right]^{(\alpha+2)(2-2\beta)}\left(\frac{r_{\rm sw}}{r_f}\right)^{[(2-\alpha)(1+p)-2\beta(p-\alpha-1)]/(\alpha+2)}. \tag{2.35}$$

Consistency requires $t_{\rm cool,sw}/t \ll 1$, and therefore the bubble is momentum-driven (rather than energy-driven) for $t \ll t_f$ only if:

$$\begin{aligned} \beta &< 1 + \frac{1-p\alpha/2}{p-\alpha-1} \qquad p > (\alpha+1) \\ \beta &> 1 + \frac{1-p\alpha/2}{p-\alpha-1} \qquad p < (\alpha+1)\,, \end{aligned} \tag{2.36}$$

where $p > \alpha+1$ corresponds to decelerating bubbles, and $p < \alpha+1$ corresponds to accelerating bubbles. The condition given by equation (2.36) is shown as a contour plot in Figure 2.5, and tabulated for a range of α and p values in Table 2.1. Figure 2.5 and Table 2.1 show that higher values of p and α which produce decelerating momentum-driven bubbles are more restrictive on the cooling function parameter β, such as requiring it to be negative when $\alpha \sim 1.5$ and $p \sim 3$. Or, to put it another way, energy driven bubbles will occur in the free expansion stage if the level of cooling is low (smaller β), and the rate of energy injection is high (high α), along with lower small scale density (high p).

2.2.6 Critical Wind Velocity

The characteristic cooling time can be compared with the cooling time of the shocked ambient medium at $r_s = r_f$:

$$\frac{t_{\rm cool,sa}(r_f)}{t_1} = \frac{3}{p}\left(\frac{3\mathcal{A}^{(\alpha+1)/(\alpha+2)}+1}{3\mathcal{A}^{(\alpha+1)/(\alpha+2)}}\right)^{2\beta-2}, \tag{2.37}$$

where

$$\mathcal{A} = \left[\frac{\alpha+2}{3(1+p)}\right], \tag{2.38}$$

and similarly for the cooling time of the shocked wind, leading to the ratio:

$$\frac{t_{\rm cool,sw}(r_f)}{t_1} = (\alpha+1)^{-1}\left(3\mathcal{A}^{(\alpha+1)/(\alpha+2)}+1\right)^{2\beta-2}\mathcal{A}^{\alpha/(\alpha+2)}. \tag{2.39}$$

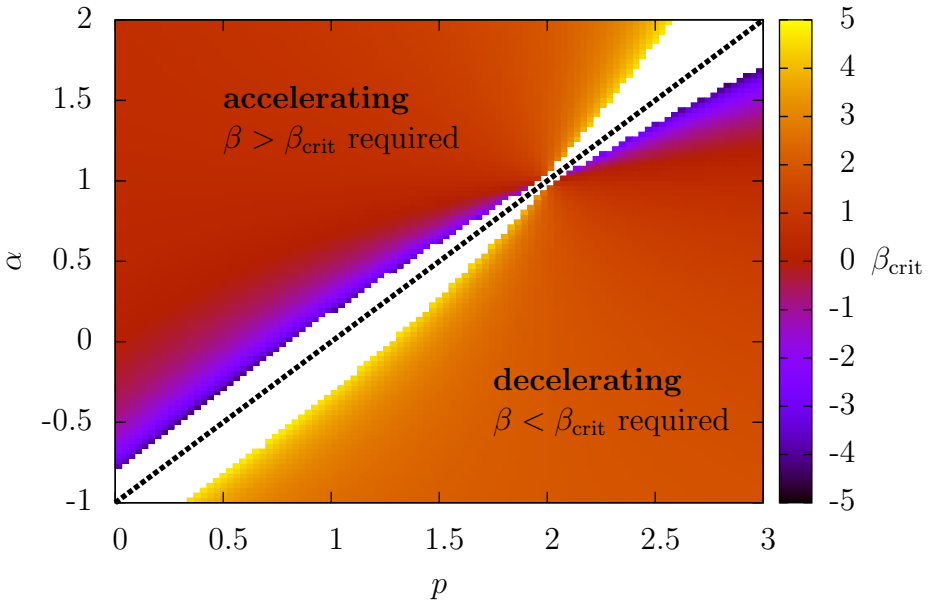

Figure 2.5: Contour plot of the cooling parameter β below which a momentum-driven bubble occurs at early times ($t \ll t_f$), as a function of gas density parameter p and wind growth parameter α. $\beta_{\rm crit}$ is given by equation (2.36).

The ratio of equation (2.39) with (2.37) gives:

$$\frac{t_{\rm cool,sw}}{t_{\rm cool,sa}} = \frac{p}{3(\alpha+1)} \left(3\mathcal{A}^{(\alpha+1)/(\alpha+2)}\right)^{2\beta-2} \mathcal{A}^{-\alpha/(\alpha+2)} \,. \tag{2.40}$$

Calculating these ratios shows for $\beta < 1$, over the range of α and p values considered in Table 2.1, that clearly:

$$t_{\rm cool,sw}(r_f) \ll t_1 \tag{2.41}$$

for all but a narrow range of α and p (Figure 2.6). For most combinations of α and p, typically:

$$t_{\rm cool,sw}(r_f) < t_{\rm cool,sa}(r_f) \lesssim t_1 \,. \tag{2.42}$$

which is highlighted in Figures 2.7 and 2.8.

		α						
		-1.0	-0.50	0.0	0.50	1.0	1.5	2.0
	0	$\pm\infty$	> -1.0	> 0	> 0.33	> 0.50	> 0.66	> 0.66
	0.5	< 3.5	$\pm\infty$	> -1.0	> 0.13	> 0.50	> 0.69	> 0.80
	1.0	< 2.5	< 3.5	$\pm\infty$	> -0.50	> 0.50	> 0.83	> 1.0
p	1.5	< 2.2	< 2.4	< 3.0	$\pm\infty$	> 0.50	> 1.1	> 1.3
	2.0	< 2.0	< 2.0	< 2.0	< 2.0	$\pm\infty$	> 2.0	> 2.0
	2.5	< 1.9	< 1.8	< 1.7	< 1.4	< 0.5	$\pm\infty$	> 4.0
	3.0	< 1.8	< 1.7	< 1.5	< 1.2	< 0.50	< -1.5	$\pm\infty$

Table 2.1: Cooling parameter β values for which a momentum-driven bubble occurs at early times as given by equation (2.36). Values for accelerating (rather than decelerating) bubbles are highlighted in grey.

Figure 2.6 shows that the cooling time of the shocked wind at the fiducial radius relative to t_1 is mainly dependent on variation in α, i.e. changing the rate at which energy is transferred to the bubble has a more significant effect on the cooling time of the shocked wind, than changing the density distribution of the ambient medium. Figure 2.7 for the cooling time of the shocked ambient medium at t_f relative to t_1 shows the inverse, that the density distribution of the ambient medium, rather than the rate of energy injection by the wind, is more important in determining the level of cooling. It can be seen from these figures that by increasing the level of cooling by increasing β, the ratio of $t_{\rm cool,sw}$ or $t_{\rm cool,sa}$ with t_1 simply increases. When the ratio of the two cooling times $t_{\rm cool,sw}(r_f)$ and $t_{\rm cool,sa}(r_f)$ are taken as in Figure 2.8, it can be seen that variations in both α and p affect the ratio similarly, and that the cooling times are more similar for a higher rate of cooling (higher β).

A useful distinction can be made between wind speeds for which the characteristic cooling time t_1 is much less than the fiducial time t_f, and wind speeds for which they

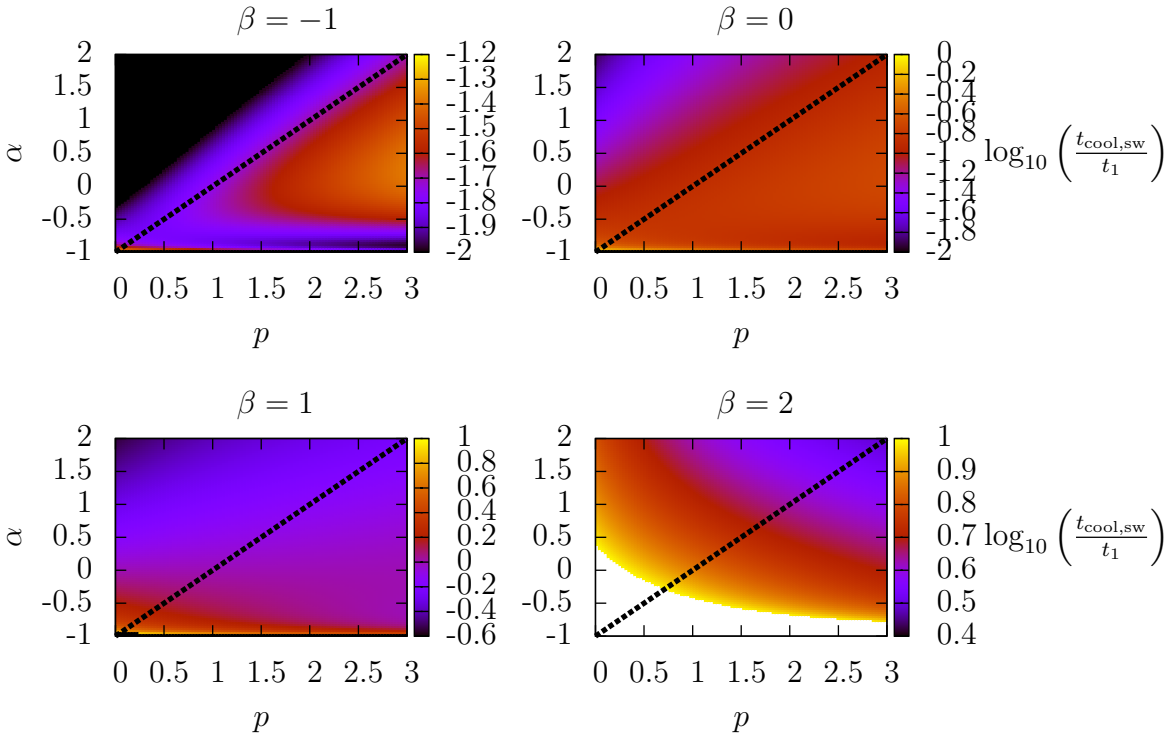

Figure 2.6: Contour plot of the ratio of the shocked wind cooling time at the fiducial radius $t_{\rm cool,sw}(r_f)$ with the characteristic cooling time t_1, as a function of gas density parameter p and wind growth parameter α.

are not. Therefore if $t_1 \ll t_f$ then both of the shock cooling times $t_{\rm cool,sw}(r_f)$ and $t_{\rm cool,sa}(r_f)$ are also likely to be much less than t_f if $\beta < 1$. This will lead to two distinct sequences, one where the bubbles leave the free-expansion stage in the momentum-driven regime $t_1 \ll t_f$, and one where the bubbles leave the free expansion stage in the energy-driven regime $t_1 \gg t_f$.

The critical wind velocity is defined as the wind velocity which leads to $t_1 = t_f$:

$$v_{\rm crit} = \left\{ \left(\frac{\dot{M}_{w,s}}{4\pi t_s^{\alpha+1}(\alpha+1)} \right)^{p-2} \left(\frac{3\rho_s}{p r_0^{p-3}} \right) \right\}^{1/[3p-(5-p)(\alpha+1)+2\beta(1-p+\alpha)]} , \qquad (2.43)$$

hence if $v_w < v_{\rm crit}$ these *slow winds* will leave the free expansion stage ($t > t_f$) as momentum-driven bubbles, whereas if $v_w > v_{\rm crit}$ then these *fast winds* will leave the

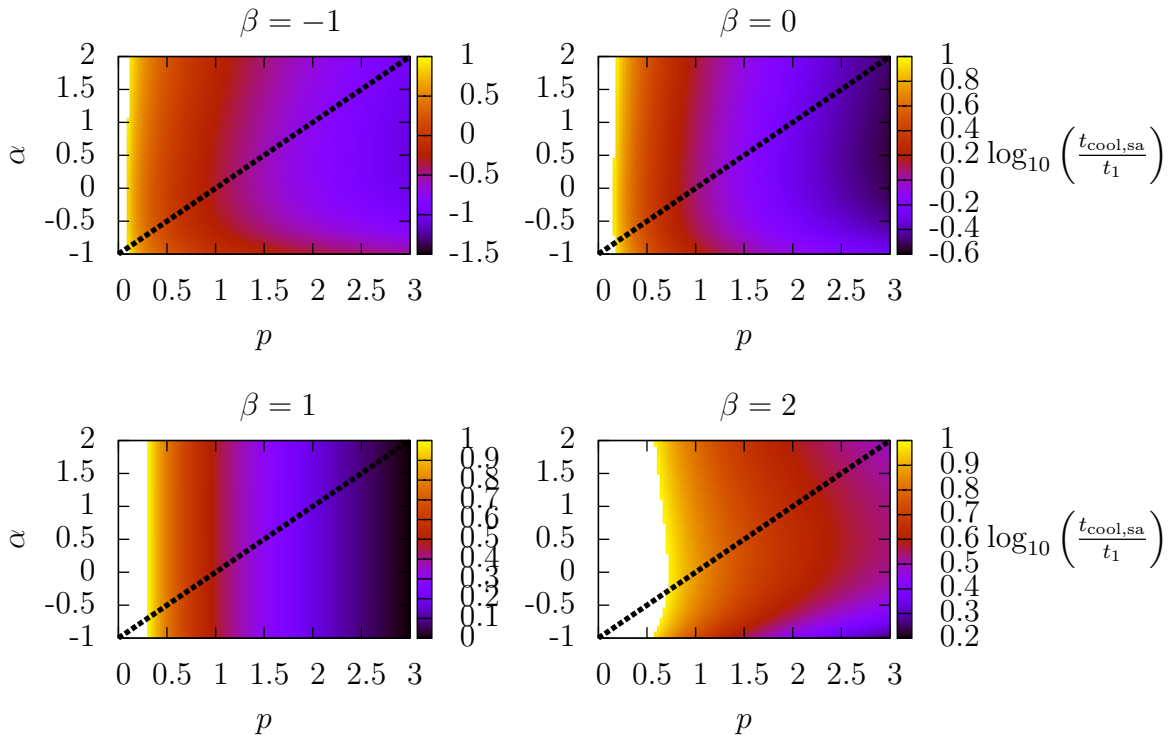

Figure 2.7: Contour plot of the ratio of the shocked ambient medium cooling time at the fiducial radius $t_{\rm cool,sa}(r_f)$ with the characteristic cooling time t_1, as a function of gas density parameter p and wind growth parameter α.

free expansion stage as energy driven bubbles. Slow winds will therefore follow a *radiative sequence*, and fast winds will follow an *adiabatic sequence* at times $t \gg t_f$. The characteristic cooling time can be expressed in terms of $v_{\rm crit}$:

$$\frac{t_1}{t_f} = \left(\frac{v_w}{v_{\rm crit}}\right)^{5-2\beta-(4-q\alpha-q)/(p-\alpha-1)} \tag{2.44}$$

There is a range of p therefore, for which these definitions are reversed, with slow winds following adiabatic sequences, and fast winds following radiative sequences. This happens if:

$$p < p_{\rm crit} = \frac{-9-5\alpha+2\beta+2\beta\alpha}{-6-\alpha+2\beta}\,. \tag{2.45}$$

This critical value is shown in Figure 2.9 for a range of cooling parameter β. The

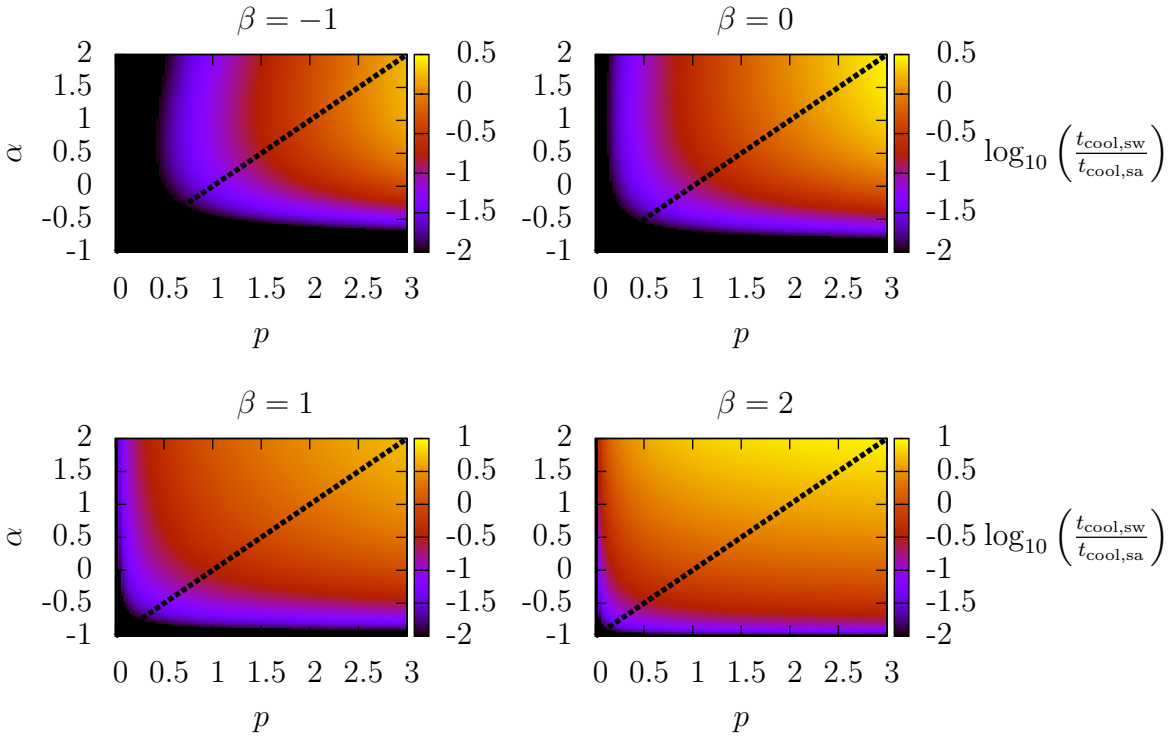

Figure 2.8: Contour plot of the ratio of the shocked wind cooling time at the fiducial radius $t_{\rm cool,sw}(r_f)$ with the shocked ambient medium cooling time at the fiducial radius $t_{\rm cool,sa}(r_f)$, as a function of gas density parameter p and wind growth parameter α.

regions shown in red correspond to combinations of p and α which result in the inverse behavior for slow and fast winds. For example, in the case of a fast wind where: $v_w \gg v_{\rm crit}$, if α is such that $p > p_{\rm crit}$, i.e. the combination of α and p is within the white region, then the bubble is energy-driven, due to $t_1 \gg t_f$. In contrast, if α and p are within the red region (of lower p values) then the bubble is momentum-driven.

2.2.7 Radiative Sequence

In order for this sequence to occur after the free expansion stage, it is required that the wind is slow: $v_w \ll v_{\rm crit}$, and $p > p_{\rm crit}$ (or contrastingly fast: $v_w \gg v_{\rm crit}$, but with:

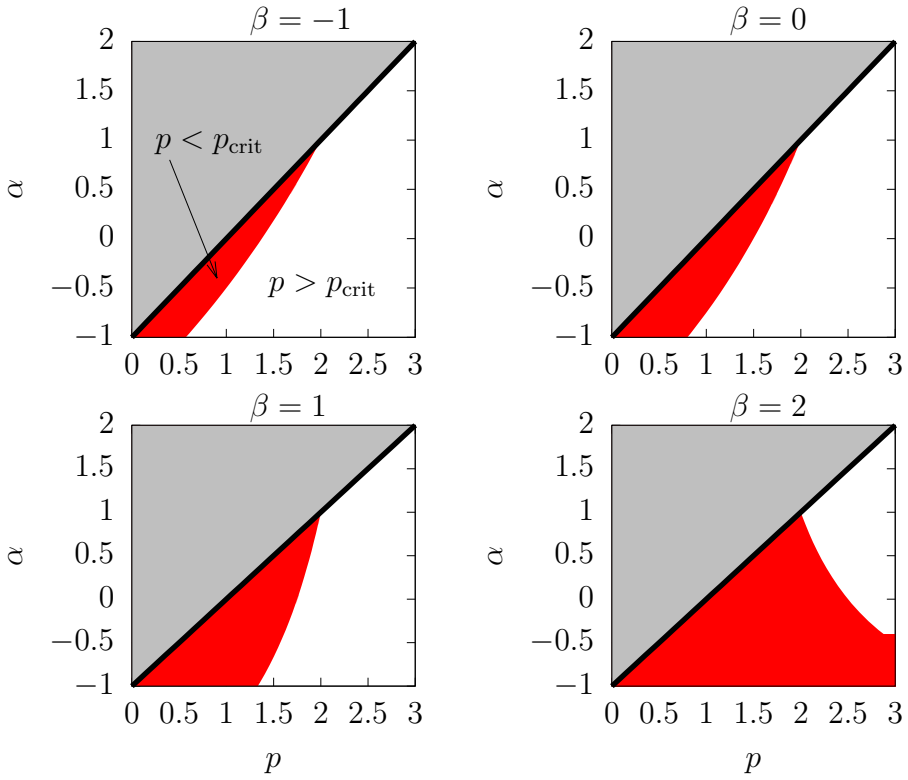

Figure 2.9: The critical density parameter resulting in the reversal of slow and fast winds. The plots for $\beta = -1$ and $\beta = 0$ are comparable to the plotted parameters of Koo & McKee (1992a) who assumed $\beta = -1/2$. This figure shows that for higher rates of cooling the reversal of slow and fast winds is more likely. Within this parameter space (red region) slow winds produce energy-driven shells rather than momentum-driven, and fast winds produce momentum-driven shells rather than energy-driven.

$p < p_{\rm crit}$). Whether the momentum-driven bubble becomes energy-driven depends on three time scales, the crossing time of the wind: $t_{\rm cr} = r_{\rm sw}/v_w$, the cooling time of the wind: $t_{\rm cool,sw}$, and the age of the bubble: t. As long as cooling time of the shocked wind is much less than the crossing time: $t_{\rm cool,sw} \ll t_{\rm cr}$, then the bubble remains momentum-driven. Beyond this the bubble can transition to a bubble which is partially radiative (a *PRB*); this occurs during the time $t_{\rm cr} \ll t_{\rm cool,sw} \ll t$. The transition to an energy-driven bubble occurs when $t_{\rm cool,sw} \gg t$. At any of these three stages the pressure of the ambient medium can potentially confine the bubble, leading

to either a pressure confined momentum-driven bubble, pressure confined PRB, or pressure confined energy-driven bubble.

The transition from the momentum-driven bubble to a PRB occurs for $t > t_r$, where t_r is given by $t_{\rm cool,sw} = t_{\rm cr}$. Setting these times equal to each other gives:

$$\frac{r}{v_w} = \frac{t_1}{\alpha+1}\left(\frac{v_{\rm sw}}{v_w}\right)^{2-2\beta}\left(\frac{r_{\rm sw}}{r_f}\right)^2\left(\frac{t_r}{t_f}-\frac{r}{r_f}\right)^{-\alpha}. \tag{2.46}$$

Using equation (2.16) with $t \gg t_f$, and the fact that $v_{\rm sw} \sim v_w$, gives the transition time to a partially radiative bubble:

$$\frac{t_r}{t_f} = \left[\frac{\alpha+2}{3(1+p)}\left(\frac{(\alpha+1)t_f}{t_1}\right)^{1+p}\right]^{1/[2-p\alpha]}. \tag{2.47}$$

Since $t_r \gg t_f$ (and $t_f \gg t_1$ in the typical radiative sequence) we require $2 - p\alpha > 0$, which restricts $\alpha < 2/p$. If this condition is met, and $t > t_r$ with $t \gg t_f$, the PRB occurs. During this stage the volume occupied by the hot portion of the shocked wind is much larger than that of the unshocked wind: $r_s^3 \gg r_{\rm sw}^3$, this arises since $t_{\rm cool,sw} \gg t_{\rm cr}$. However, most of the shocked wind mass is still cooled, and confined to a thin region close to r_c (see Figure 2.10).

The density of the hot shocked wind is approximately constant: $\rho_{\rm sw} = (\gamma_{\rm sw}+1)\rho_w/(\gamma_{\rm sw}-1)$, and the mass of the hot shocked wind can be approximated by:

$$M_{\rm sw}(t) \approx \int_{t-t_{\rm cool,sw}}^{t} \dot{M}_w(t)\,dt \tag{2.48}$$

which by mass conservation $4\pi r^3\rho_{\rm sw}/3 \sim M_{\rm sw}(t)$ gives:

$$\left(\frac{r_s}{r_f}\right)^3\left(\frac{r_{\rm sw}}{r_f}\right)^{-4} \approx \frac{3(\gamma_{\rm sw}-1)t_1}{(\alpha+1)(\gamma_{\rm sw}+1)t_f}\left(\frac{t}{t_f}\right)^{\alpha}. \tag{2.49}$$

Expressions for r_s and $r_{\rm sw}$ can be found by solving equation (2.49) (see Koo & McKee 1992a), which leads to the following proportionalities:

$$r_s \propto t^{(\alpha+4)/(2p+1)} \tag{2.50}$$

and

$$r_{\rm sw} \propto t^{[6+(p+2)\alpha]/[2(2p+1)]} \tag{2.51}$$

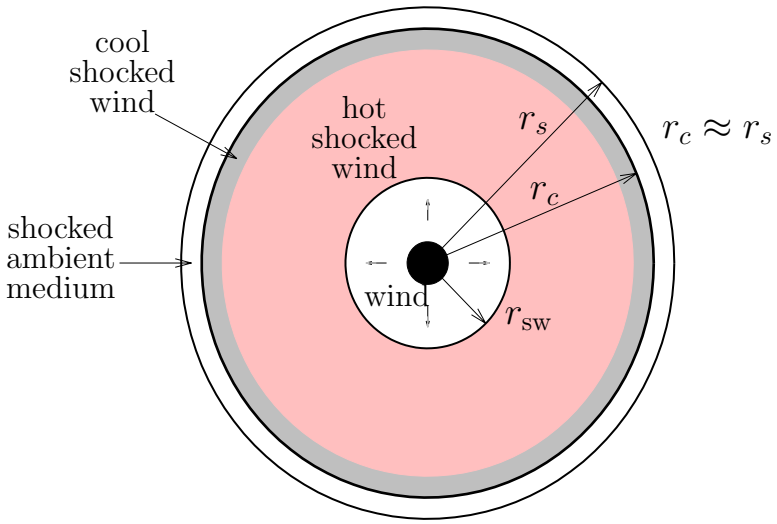

Figure 2.10: The structure of a partially radiative bubble (PRB). Much like the energy-driven bubble most of the PRB is occupied by hot shocked wind (shown in pink). However, unlike the energy-driven bubble the PRB has a region of cool shocked wind (shown in grey) close to the contact discontinuity.

which is to be compared with the radius of the momentum-driven bubble:

$$r \propto t^{(\alpha+2)/(q+1)} \,. \tag{2.52}$$

This shows that the wind shock will be at a smaller radius for a PRB than for a momentum-driven bubble, c.f. Figures 2.10 and 2.3. The ratio of r_s with $r_{\rm sw}$ increases in time, as expected for a PRB, which has an expanding hot shocked wind region.

Whether a PRB transitions to an energy-driven bubble can be determined by comparing the cooling time of the shocked wind $t_{\rm cool,sw}$ with the age of the bubble t:

$$\frac{t_{\rm cool,sw}}{t} \propto t^{(5-2p+\alpha-p\alpha)/(2p+1)} \tag{2.53}$$

which shows that if $\alpha+1 < (4-p)/(p-1)$, then the cooling time becomes larger than the age and the bubble becomes energy-driven. This transition time is $t_{\rm en}$, which for the ratio of ram pressures $f_P \equiv \rho_w v_w^2/\rho_g(r)v^2$ is:

$$t_{\rm en} = t_f \left\{ \left[\frac{3(\alpha+1)}{p f_P} \left(\frac{2q+1}{\alpha+4} \right)^2 \right]^{-3} \left[\frac{3(\gamma_{\rm sw}-1)}{(\gamma_{\rm sw}+1)} \right]^{p-1} \left(\frac{(\alpha+1)t_f}{t_1} \right)^{p+2} \right\}^{1/[4-p-(p-1)(\alpha+1)]}, \tag{2.54}$$

and the motion of the bubble is as described in Section 2.2.3.

For any of the three stages in the radiative sequence pressure confinement can occur. This happens when the ram pressure of the shell $\rho_g(r_s)v_s^2$ is equal to the ambient pressure $P_g(r_s)$. When this occurs the motion of the shell is subsonic, and there is no longer a forward shock.

In summary, during the radiative sequence a momentum-driven bubble transitions to a PRB at time t_r, which itself will eventually transition to an energy-driven bubble at time $t_{\rm en}$. At any of these stages it is possible for the bubble to become confined by the ambient pressure. If there is additional mass injected into the hot wind of an energy-driven bubble, such as via the evaporation of molecular clouds entrained in the outflow, then it is possible for the bubble to transition again to a momentum-driven or partially-radiative stage.

2.2.8 Adiabatic Sequence

In order for this sequence to occur after the free expansion stage, it is required that the wind is fast: $v_w \gg v_{\rm crit}$, and $p > p_{\rm crit}$ (or inversely, slow: $v_w \ll v_{\rm crit}$, but with $p < p_{\rm crit}$). Only one timescale is important in this sequence, which is the time $t_{\rm out}$ when the forward shock becomes radiative.

These bubbles leave the free expansion stage in the energy-driven regime and are described by the solutions in Section 2.2.3. They begin with a non-radiative forward shock, which will go on to become radiative. The ratio of the cooling time of the shocked ambient medium to the age of the bubble has the following proportionality:

$$\frac{t_{\rm cool,sa}}{t} \propto \frac{r_s^{3-p} v_s^3}{t} \propto t^{[10+(6-p)\alpha-7p]/(p+2)} \tag{2.55}$$

which for $p < p_{\rm crit}$ decreases with time and the ambient shock becomes radiative. This causes the shell of shocked ambient medium to collapse to a thin region at the time $t_{\rm out}$ which is found by setting $t_{\rm cool,sa} = t$:

$$\frac{t_{\rm out}}{t_f} = \left[(2\pi\xi')^{(6-p)/(p+2)} \frac{3}{q} \left(\frac{\alpha+3}{p+2} \right)^3 \right]^{(p+2)/[-10+2p-(6-p)\alpha]} \left(\frac{v_w}{v_{\rm crit}} \right)^{(p+2)/(p-\alpha-1)} , \tag{2.56}$$

where ξ' is a constant of order unity.

Energy-driven bubbles with or without radiative forward shocks can become pressure confined. Whether this occurs is determined by the comparison of the ram pressure of the shell $\rho_g(r_s) v_s^2$ with the ambient pressure $P_g(r_s)$. When the ambient pressure exceeds the ram pressure of the shell, the bubbles will become pressure confined.

2.3 Black Hole Winds and Gravity

For the momentum-driven bubble, gravitational forces due to the source point mass $M_{\rm BH}(t)$ and the surrounding dark matter halo with a radial mass distribution $M_{\rm DM}(r)$ can be introduced by including an extra term in equation (2.14):

$$\begin{aligned} \left[M_w \left(t - \frac{r}{v_w} \right) + \frac{4\pi\rho_s}{p} \left(\frac{r}{r_0} \right)^p \right] v = M_w \left(t - \frac{r}{v_w} \right) v_w \\ - \int_0^t \frac{G}{r^2} \left[M_w \left(t - \frac{r}{v_w} \right) + \frac{4\pi\rho_s}{p} \left(\frac{r}{r_0} \right)^p \right] \left[M_{\rm BH}(t) + M_{\rm DM}(r) \right] \, dt \, . \end{aligned} \tag{2.57}$$

Taking the time derivative of this equation and considering a more general radial gas distribution $M_g(r)$, and including the resistive pressure of the ambient medium gives

a general equation of motion for the momentum driven shell:

$$\frac{d}{dt}\left\{\left[M_w\left(t-\frac{r}{v_w}\right)+M_g(r)\right]v\right\}=\tau\frac{L_{\rm Edd}}{c}\left(t-\frac{r}{v_w}\right)-4\pi r^2P_g(r) \\ -\frac{G}{r^2}\left[M_w\left(t-\frac{r}{v_w}\right)+M_g(r)\right]\left[M_{\rm BH}(t)+M_{\rm DM}(r)\right], \tag{2.58}$$

where equation (1.46) has been used for the SMBH wind source. Many simplified cases of equation (2.58) have been solved and analysed. Most commonly, it is assumed that the bubble has left the free expansion stage: $M_w(t) \ll M_g(r)$, and therefore that the crossing time of the wind is negligible compared to the age of the bubble: $t \gg r/v_w$. These assumptions result in the following equation of motion:

$$\frac{d}{dt}\left[M_g(r)v\right]=\tau\frac{L_{\rm Edd}}{c}(t)-4\pi r^2P_g(r)-\frac{M_g(r)G}{r^2}\left[M_{\rm BH}(t)+M_{\rm DM}(r)\right]. \tag{2.59}$$

It is commonly assumed that $M_g(r) = f_0 M_{\rm DM}(r)$, i.e. that the gas traces the dark matter directly. In this case, and assuming that $P_g(r) = 0$, $M_{\rm BH}$ is constant, and that the dark matter distribution is an SIS (see equation 1.11) leads to the critical SMBH mass (see equation 1.49):

$$M_{\rm BH}=\frac{f_0\sigma^4}{\tau\pi G^2\kappa}, \tag{2.60}$$

which results in a positive terminal coasting velocity for the momentum driven shell (King 2003, 2005).

A critical mass which results in the escape of the shell has also been obtained for the case that the dark matter halo is non-isothermal (McQuillin & McLaughlin 2012):

$$M_{\rm BH}=\frac{f_0\kappa}{\pi G^2}\frac{V_{\rm c,pk}^4}{4}, \tag{2.61}$$

where $V_{\rm c,pk}$ is the peak of the halo's circular speed curve (see Section 1.2).

For an energy-driven bubble, equation (2.21) for energy conservation in the hot shocked wind can be extended to account for the work done against the gravity of the point source $M_{\rm BH}$ and the dark matter halo $M_{\rm DM}(r)$:

$$\frac{d}{dt}\left[\frac{4}{3}\pi(r_c^3-r_{sw}^3)\frac{P}{\gamma-1}\right]=\frac{L_{\rm Edd}(t)v_w}{2c}-4\pi(r_c^2v_c-r_{\rm sw}^2v_{\rm sw})P \\ -\frac{GM_g(r)v_c}{r_c^2}\left[M_{\rm BH}(t)+M_{\rm DM}(r)\right]-n\Lambda(T), \tag{2.62}$$

where the cooling function $\Lambda(T)$ is present for a PRB, but absent for an energy driven bubble. Rather than obtaining a power-law solution as in Section 2.2.3, a solution to the equation of motion for the shell is sought:

$$\frac{d}{dt}\left[M_g(r)v\right] = 4\pi r^2\left[P - P_g(r)\right] - \frac{GM_g(r)}{r^2}\left[M_{\rm BH}(t) + M_{\rm DM}(r)\right] , \tag{2.63}$$

where P satisfies equation (2.62), and $r = r_c \sim r_s$ is assumed.

Typically for the case of an energy-driven shell it is assumed that $r_{\rm sw} \ll r_c \sim r_s = r$, leading to:

$$\begin{aligned}\frac{d}{dt}\left[\frac{4}{3}\pi r^3\frac{P}{\gamma-1}\right] = \frac{L_{\rm Edd}(t)v_w}{2c} - 4\pi r^2 vP \\ - \frac{GM_g(r)v}{r^2}\left[M_{\rm BH}(t) + M_{\rm DM}(r)\right] .\end{aligned} \tag{2.64}$$

Equation (2.64) has been treated for the case of constant $M_{\rm BH}(t)$ and $P_g = 0$ within an SIS dark matter halo. Requiring that the terminal coasting speed v_∞ of the shell is equal to the escape speed of a truncated SIS, a critical mass - wind speed combination has been found (McQuillin & McLaughlin 2012):

$$M_{\rm BH}v_w = \frac{1}{\tau}\frac{4(4\gamma-3)}{(\gamma-1)}\frac{\kappa f_0}{\pi G^2}\sigma_0^5 . \tag{2.65}$$

Furthermore, it has been found that at large radii, the shell is expected to have a *momentum boost* (Zubovas & King 2012):

$$\frac{\dot{M}_{\rm sh}v_\infty}{L_{\rm Edd}/c} = \sqrt{\frac{\eta(\gamma+1)}{4\dot{m}}\frac{f_0}{f_c}\frac{v_\infty c}{\sigma_0^2}} \sim 20q^{1/6}\left(\frac{\sigma}{200\ {\rm km\ s^{-1}}}\right)^{-2/3} , \tag{2.66}$$

where $\dot{m} \equiv \dot{M}_w/\dot{M}_{\rm Edd}$, q is the fraction of Eddington luminosity introduced in Section 1.1.4, and f_c is the ratio of gas to all matter (i.e. accounting for star formation).

Since an analytical approach to solving equation (2.59), or equation (2.63) coupled with equation (2.64), by incorporating a time dependent black hole mass and ambient pressure has yet to be carried out, this goal will be the focus of the following two chapters in this thesis. In Chapter 3 equation (2.59) is analysed for the simplistic case that $M_{\rm BH}$ (and therefore $L_{\rm Edd}/c$) is constant. Similarly, equation (2.64) with

(2.63) is analysed under the same assumption, with tracking of shell infall behaviour also included. The main purpose of Chapter 3 is to demonstrate how the solutions to these simplified equations can be applied and understood within an observational context, and therefore to also frame the results from the subsequent chapters within this context.

In Chapter 4, for the first time the effects of a growing black hole with different growth profiles is investigated analytically. Therefore equations (2.59) and (2.64) with (2.63) are examined in their entirety.

3 Aspects of Steady Winds

As discussed in Section 1.5 observations of outflows within active galaxies have shown that their momentum-fluxes $\dot{M}v$ can vary greatly in relation to the radiative momentum-flux of the AGN: $L_{\rm AGN}/c$. If $L_{\rm AGN} \sim L_{\rm Edd}$ then the outflow can be understood as being driven by an optically thick wind from an accreting SMBH with momentum-flux $\dot{M}_w v_w \sim L_{\rm Edd}/c \sim L_{\rm AGN}/c$ (King & Pounds 2003). Support for the existence of such winds has been obtained from observations of active galaxies where outflow momentum-fluxes are typically measured to be of the order $L_{\rm AGN}/c$ at small galactic scales (Pounds & Reeves 2007, 2009; Tombesi et al. 2010; Gofford et al. 2013).

At large galactic scales the momentum-flux can vary over a significant range relative to the source: $\dot{M}_{\rm out} v_{\rm out} \sim (0.1 - 100) L_{\rm AGN}/c$ (Feruglio et al. 2017; Fiore et al. 2017; Rupke, Gültekin & Veilleux 2017), but typically these large-scale outflows will have momentum-fluxes which are boosted relative to $L_{\rm AGN}/c$. For momentum-fluxes which are less than or equal to $\dot{M}_w v_w$ the outflow could be modelled as being either momentum-driven or energy-driven (see Chapter 2). However, if the momentum-flux is boosted then it can only correspond to the energy-driven regime. By considering that the primary source of cooling for outflows from AGN is inverse Compton scattering (Ciotti & Ostriker 1997; King 2003), then it is more likely that the outflow will be energy-driven at large scales (Faucher-Giguère & Quataert 2012; McQuillin & McLaughlin 2013).

The dynamics of these outflows can be modelled as shells of swept-up gas blown by steady (constant force) winds travelling into ambient gas distributions. By utilising such models within the context of high-redshift protogalaxies which are treated as having a dark matter distribution in the form of a singular isothermal sphere (SIS), and by requiring that the shell be able to reach large radii the observed correlation between the SMBH mass and velocity dispersion (see Section 1.4) can be derived. This was carried out for a momentum-driven shell where it was found that the necessary

SMBH mass to reach large radii was (King 2005):

$$M_\sigma = \frac{f_0 \kappa \sigma_0^4}{\tau \pi G^2} \simeq 4.56 \times 10^8 M_\odot \frac{1}{\tau} \left(\frac{\sigma_0}{200 \text{km s}^{-1}} \right)^4 \left(\frac{f_0}{0.2} \right) . \tag{3.1}$$

Another relation was also obtained by using an energy-driven shell and requiring that the large radius coasting speed v_∞ of the shell was equal to the escape velocity of a truncated SIS (McQuillin & McLaughlin 2013). Unlike the momentum-driven case the derived necessary SMBH mass in the energy-driven case contains the wind speed as a free parameter:

$$M_{\rm BH} v_w \geq \frac{1}{\tau} \frac{4(4\gamma - 3)}{(\gamma - 1)} \frac{\kappa f_0}{\pi G^2} \sigma^5 \simeq 2.00 \times 10^{15} M_\odot \frac{1}{\tau} \left(\frac{f_0}{0.2} \right) \left(\frac{\sigma}{200 \text{ km s}^{-1}} \right)^5 . \tag{3.2}$$

This relationship was used to interpret the scatter in the $M_{\rm BH} - \sigma$ data as variations in the wind speeds of protogalaxies when they were cleared of gas (McQuillin & McLaughlin 2012). They found that the wind speed from fitting equation (3.2) to the $M_{\rm BH} - \sigma$ data compares very well with the median wind speeds from samples of local active galaxies.

These results can be improved by modelling the protogalaxy as a more realistic non-isothermal dark matter halo (see Section 1.2). A dark matter halo with a density profile which is shallower than an SIS at small radii but steeper at large radii has a well defined peak in its circular speed curve. By requiring that a momentum-driven shell can reach large radii in a non-isothermal dark matter halo without stalling it was shown that the sufficient SMBH mass is (McQuillin & McLaughlin 2012):

$$M_{\rm BH} \geq \frac{f_0 \kappa}{\tau \pi G^2} \frac{V_{\rm c,pk}^4}{4} \simeq 1.14 \times 10^8 M_\odot \frac{1}{\tau} \left(\frac{V_{\rm c,pk}}{4} \right)^4 \left(\frac{f_0}{0.2} \right) \tag{3.3}$$

This theoretical relation is very similar to the observational correlation between the SMBH mass and the large scale circular speed $V_{\rm c,a}$ (observationally determined from large scale gas velocities) in galaxies where the dark matter dominates (Volonteri, Natarajan & Gültekin 2011). By defining a characteristic velocity dispersion such that $\sigma_0 = \sqrt{2} V_{\rm c,pk}$ this becomes equation (3.1) and it can be related to the $M_{\rm BH} - \sigma$ data.

In addition to modelling outflows in gaseous protogalaxies these wind-driven shells can be used to model outflows in local active galaxies. The large-scale coasting velocity v_∞ for an energy-driven shell in an SIS halo has been used in the limit that the wind is very strong ($v_w \gg \sigma_0$) to obtain an expression for the large-scale momentum-boost of an energy-driven shell (Zubovas & King 2012):

$$\frac{\dot{M}_{\rm sh} v_\infty}{\dot{M}_w v_w} = \sqrt{\frac{\dot{M}_{\rm sh}}{\dot{M}_w}} \sim \frac{v_w}{v_\infty} \tag{3.4}$$

where the quantity $\sqrt{\dot{M}_{\rm sh}/\dot{M}_w}$ is referred to as the mass-loading factor, which is part of the overall 'boost factor' for the outflow. This relation has been used to compare with observational results from active galaxies with v_w/v_∞ corresponding to the 'boost factor' of the outflow for energy-driven shells (Tombesi et al. 2015; Feruglio et al. 2015). The issues with this relation are that it was obtained in the limit that the winds are fast ($v_w \gg \sigma_0$) and that typically $M_{\rm BH} \sim M_\sigma$ and $v_w \sim 0.1c$.

Within this chapter the dynamics of both momentum- and energy-driven wind-blown shells are studied with the inclusion of ambient pressure, with a methodology which is similar to the approaches previously used by McQuillin & McLaughlin (2012, 2013) in order to investigate the dynamics of shells. The aims of this chapter are: (1) to fully explore the dynamics of wind blown shells subject to ambient pressure within isothermal and non-isothermal galaxies with particular emphasis on their momentum-fluxes, (2) to demonstrate the approaches used to obtain SMBH masses for comparison with the $M_{\rm BH} - \sigma$ data and determine if this can be extended to include momentum-boosting, (3) to utilise a time-dependent approach in order to lay the groundwork for introducing a time-dependent SMBH mass in Chapter 4.

In Section 3.1 the equations of motion for momentum- and energy-driven shells are introduced, as are the methods which will be utilised for solving them. In Section 3.2 momentum-driven shells in isothermal and non-isothermal haloes are analysed with ambient pressure included and a new type of solution is found which corresponds to a pressure confined shell. This section concludes with an analysis of the momentum-fluxes $\dot{p}_{\rm sh}$ of momentum-driven shells and it is verified that they are approximated well

by the observable $\dot{M}_{\rm sh}v$ over the typical observational ranges for large-scale molecular outflows. Section 3.3 covers the dynamics of energy-driven shells with ambient pressure included, and confined shells are also found to occur in the energy-driven regime when ambient pressure is accounted for. This chapter concludes with a study of momentum-fluxes of energy-driven shells. By analysing the momentum-fluxes of shells at large radii in an SIS it is found that maximum momentum boosting always occurs at a specific speed $v_{\rm p,max}$. Requiring maximum boosting sets the wind energy and kinetic energy to have a specific ratio which is independent of changes to the constant inward forces in the SIS halo (such as ambient pressure). Changes to the gravitational force affect the specific value of $v_{\rm p,max}$, but not the ratio of kinetic and wind energy. This ratio is the boost-factor for the outflow, and it is shown for a small sample of outflows in active galaxies that they have velocities which are broadly distributed about the peak of maximum boosting. By requiring that shells have maximum momentum boosting at large radii in an SIS halo leads to the SMBH mass:

$$M_{\rm BH} = \frac{f_0 \kappa \sigma_0^4}{2\pi\tau G^2} \left[\frac{4(3\gamma-2)}{3(\gamma-1)} \left(\frac{v_{\rm p,max}}{v_w} \right) \right] \left(\frac{v_{\rm p,max}}{\sigma_0} \right)^2 . \tag{3.5}$$

The first factor is the momentum-driven $M_{\rm BH} - \sigma$ relation (divided by 2), the second factor in the square brackets is the inverse of the boosting factor, and the third factor $v_{\rm p,max}^2$ is the square of the speed at maximum boosting. Using the expression obtained for $v_{\rm p,max}$ enables equation (3.5) to be compared with the $M_{\rm BH} - \sigma$ data as shown in Figure 3.1. If protogalaxies were cleared by maximally boosted outflows then the scatter in the $M_{\rm BH} - \sigma$ data can be interpreted as variation in the boosting factor at the time of blowout. Regions of $M_{\rm BH}$ and σ data could be identified as being consistent with energy- or momentum-driven outflows based on the level of boosting. Since the boost factor is determined by the ratio of the wind speed to the outflow speed this hints at regions where winds are expected to be fast or slow relative to the outflow speed. Fast winds are such that the outflow speed is far less than that of the wind and therefore the boost factor is substantially higher, which means energy-driven outflows, and therefore this definition of fast winds can be connected to the definitions introduced in Chapter 2. By distinguishing between momentum- and energy-driven outflows in the

data provides insight into vacancies or overdensities in the data. Finally, by taking data from a small sample of active galaxies it is shown that the observed momentum-boosts can match up well with the predicted boost factor (see Figure 3.1).

It is then shown that the momentum-boost distributions in the SIS halo for which it is defined $2\sigma_0^2 \equiv V_{\rm c,pk}^2$ match those of the Hernquist halo precisely at the peak of the circular speed curve $r_{\rm pk}$. For maximum momentum-boosting the exact same ratio applies between wind and kinetic energies as in the SIS halo. By using the value for the ratio of wind to kinetic energy at $r_{\rm pk}$ the following mass for a maximally boosted shell is obtained:

$$M_{\rm BH} = \frac{f_0 \kappa V_{\rm c,pk}^4}{4\pi\tau G^2} \left[\frac{4(3\gamma-2)}{3(\gamma-1)} \left(\frac{v_{\rm p,max}}{v_w}\right)\right] \left(\frac{v_{\rm p,max}}{V_{\rm c,pk}}\right)^2 . \tag{3.6}$$

If maximum boosting is required when the outflow reaches $r_{\rm pk}$ as this is where the gravitational force is strongest, then equation (3.6) can be viewed as the energy-driven analogue of equation (3.3). The momentum-driven equation (3.3) is recovered (to within a factor of 2) if the upper limit of unity on the momentum boost is used (i.e. the quantity in square brackets is set to unity) and $v_{\rm p,max} \simeq \sqrt{2} V_{\rm c,pk}$, which is the shell velocity of a maximally boosted shell at $r_{\rm pk}$.

3.1 Equation of Motion for the Shell

Consider a shell of shocked swept up ambient medium with mass $M_{\rm sh}$ driven by a time-independent (steady) wind with outwards pressure $P(r)$, and subject to opposing forces from ambient gas pressure $P_g(r)$ and from the gravity of the SMBH mass $M_{\rm BH}$ and dark matter mass $M_{\rm DM}$. The equation of motion for this shell is (see Section 2.3):

$$\frac{d}{dt}\left[M_{\rm sh} v\right] = 4\pi r^2 \left[P(r) - P_g(r)\right] - \frac{G M_{\rm sh}(r)}{r^2}\left[M_{\rm BH} + M_{\rm DM}(r)\right] . \tag{3.7}$$

It is important to note that $v = dr/dt$ is the velocity of the shell (not the wind), and for both the momentum- and energy-driven shells the radius r refers to the contact discontinuity between the shell and the shocked wind region (see Section 2.1). Equation

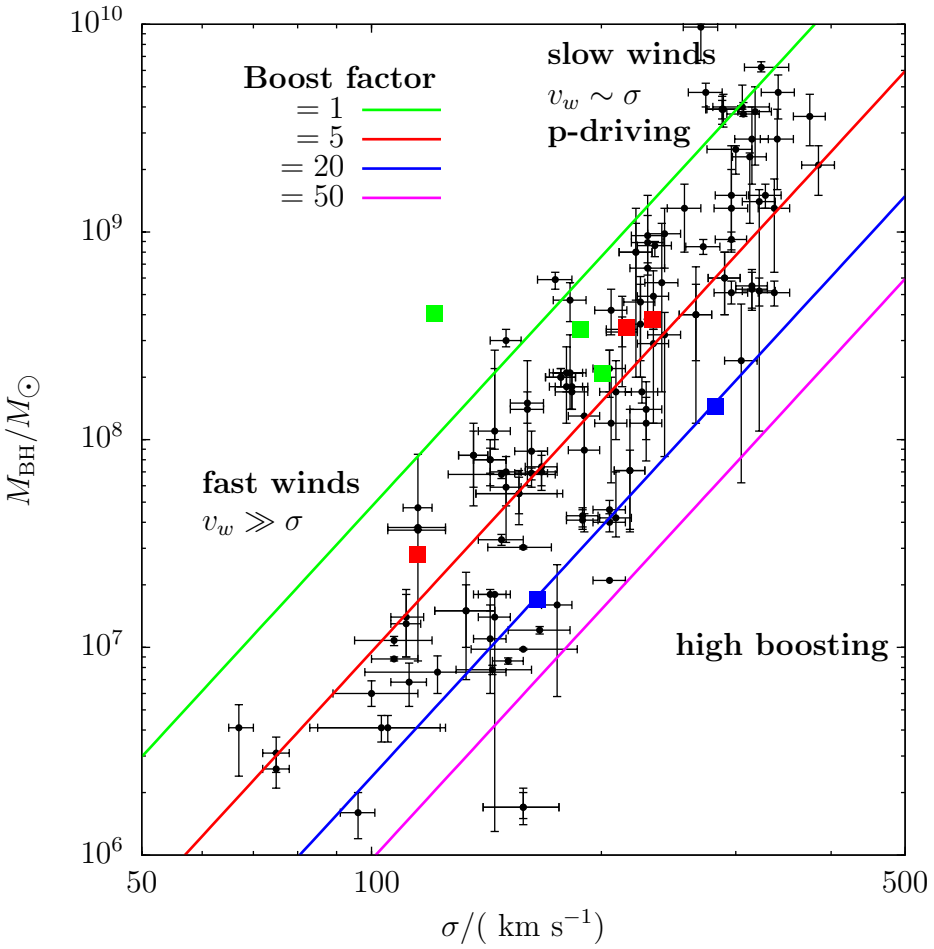

Figure 3.1: Plot of $M_{\rm BH} - \sigma$ data from McConnell & Ma (2013) and Gültekin et al. (2009) against the derived $M_{\rm BH} - \sigma$ relation given by equation (3.5). The data included on the momentum boosts are from Cicone et al. (2014) and Rupke, Gültekin & Veilleux (2017). Their colours correspond to whether the measured momentum boost is numerically close to one of the chosen intervals.

(3.7) was first solved in the case of a momentum-driven shell within an SIS halo with $P_g(r) = 0$ (King 2005), and for the case that the gas traces dark matter directly ($M_{\rm sh}(r) \propto M_{\rm DM}(r)$). By requiring that the shell can reach large radii results in the critical mass given by equation (3.1). The critical mass given by equation (3.1) is

a natural mass scale to use, and masses normalised to this value will be denoted $\widetilde{M} \equiv M/M_\sigma$. This leads to the definition of a characteristic radius:

$$r_\sigma = \frac{GM_\sigma}{\sigma_0^2} = \frac{f_0 \kappa \sigma_0^2}{\tau \pi G} \simeq 49.25 \text{ pc } \left(\frac{\sigma_0}{200 \text{ km s}^{-1}}\right)^2 \left(\frac{f_0}{0.2}\right) \tau^{-1} . \tag{3.8}$$

which will be used as the scale radius for the SIS, and radii normalised to this value will be denoted $\widetilde{r} \equiv r/r_\sigma$. Velocities will be normalised to the characteristic velocity dispersion $\widetilde{v} \equiv v/\sigma_0$.

The method for selecting scales for non-isothermal haloes will be that used by McQuillin & McLaughlin (2012). They utilise the natural scale radius $r_{\rm pk}$ at which the circular speed curve $V_c(r)$ peaks (see Section 1.2). The characteristic velocity dispersion σ_0 can then be given meaning within non-isothermal haloes by relating it to the peak value of circular speed $V_{\rm c,pk} = V_c(r_{\rm pk})$ through the relation:

$$\sigma_0^2 \equiv V_{\rm c,pk}^2/2 . \tag{3.9}$$

This allows the mass and radius scales given by equations (3.1) and (3.8) to be used with non-isothermal haloes, giving:

$$\widetilde{V}_{\rm c,pk}^2 = 2 \tag{3.10}$$

and

$$\widetilde{M}_{\rm DM}(r_{\rm pk}) \equiv \widetilde{M}_{\rm pk} = 2\widetilde{r}_{\rm pk} . \tag{3.11}$$

Normalising all radii to $r_{\rm pk}$ within non-isothermal haloes:

$$x \equiv r/r_{\rm pk} , \tag{3.12}$$

and introducing a dimensionless mass profile $m(x)$ for the halo:

$$\widetilde{M}_{\rm DM}(x) = \widetilde{M}_{\rm pk} m(x) , \tag{3.13}$$

which has the property:

$$\widetilde{M}_{\rm DM}(1) = \widetilde{M}_{\rm pk} \implies m(1) = 1 . \tag{3.14}$$

For any halo with a peaked circular speed curve the normalised mass of the shell will be given by:

$$\widetilde{M}_{\rm sh}(x) \equiv f_0 h(x) \widetilde{M}_{\rm DM}(x) = f_0 h(x) \widetilde{M}_{\rm pk} m(x)\,, \tag{3.15}$$

where $h(x)$ describes how the ambient gas traces the dark matter and f_0 is therefore the gas fraction at $x = 1$. In this chapter it will ultimately be assumed that the gas traces the dark matter directly, i.e. $h(x) \equiv 1$ and therefore $M_{\rm sh}/M_{\rm DM} = f_0 \simeq 0.2$ (King 2003).

Introducing the characteristic timescale $\widetilde{t} = t/t_\sigma$ such that $dx/d\widetilde{t} = \widetilde{v}$:

$$t_\sigma \equiv \frac{r_{\rm pk}}{\sigma_0} \simeq 2.4 \times 10^8 \text{ yr} \left(\frac{r_{\rm pk}}{50 \text{ kpc}}\right) \left(\frac{200 \text{ km s}^{-1}}{\sigma_0}\right)\,, \tag{3.16}$$

Using the mass, radius, and time normalisations $M_\sigma, r_{\rm pk}$ and t_σ allows the equation of motion (3.7) to be written:

$$\frac{d}{d\widetilde{t}}\left[h(x)m(x)\widetilde{v}\right] = 4\pi x^2 \left[\widetilde{P}(x) - \widetilde{P}_g(x)\right] - \frac{2h(x)m(x)}{x^2}\left[\frac{\widetilde{M}_{\rm BH}}{\widetilde{M}_{\rm pk}} + m(x)\right]\,, \tag{3.17}$$

where pressures are normalised in the manner $\widetilde{P} \equiv P/P_\sigma$ with:

$$\begin{aligned} P_\sigma &\equiv \frac{f_0 M_{\rm pk} \sigma_0^2}{r_{\rm pk}^3} \\ &\simeq 6.0 \times 10^{44} \text{ erg pc}^{-3} \left(\frac{f_0}{0.2}\right) \left(\frac{M_{\rm pk}}{4.7 \times 10^{11} M_\odot}\right) \left(\frac{\sigma_0}{200 \text{ km s}^{-1}}\right)^2 \left(\frac{50 \text{ kpc}}{r_{\rm pk}}\right)^3\,. \end{aligned} \tag{3.18}$$

3.1.1 Ambient Gas Pressure

The ambient pressure is given by the equation of hydrostatic support:

$$\frac{dP_g}{dr} = -\rho_g(r) \frac{G\left[M_g(r) + M_{\rm DM}(r)\right]}{r^2}\,, \tag{3.19}$$

which when normalised leads to the following expression for the ambient gas pressure:

$$\widetilde{P}_g(x) = \frac{1}{2\pi} \int_x^\infty \left[1 + f_0\right] \left[\frac{d}{du} h(u) m(u)\right] \frac{m(u)}{u^4}\, du = \widetilde{\rho}_g(x) \widetilde{\sigma}_g^2(x) \tag{3.20}$$

where the density is normalised to:

$$\rho_\sigma \equiv \frac{f_0 M_{\rm pk}}{r_{\rm pk}^3} \simeq 7.5 \times 10^{-4} M_\odot \ {\rm pc}^{-3} \left(\frac{f_0}{0.2}\right) \left(\frac{M_{\rm pk}}{4.7 \times 10^{11} M_\odot}\right) \left(\frac{50 \ {\rm kpc}}{r_{\rm pk}}\right)^3 . \quad (3.21)$$

3.1.2 Infall

When a stall point ($\widetilde{v} = 0$) is reached the shell propagates back into the region swept clear of gas. Within this region the equation of motion changes to:

$$h(x_{\rm stall}) m(x_{\rm stall}) \frac{d\widetilde{v}}{d\widetilde{t}} = 4\pi x^2 P(x) - \frac{2h(x_{\rm stall}) m(x_{\rm stall})}{x^2} \left[\frac{\widetilde{M}_{\rm BH}}{\widetilde{M}_{\rm pk}} + m(x)\right] . \quad (3.22)$$

This assumes that the ambient gas beyond $x_{\rm stall}$ remains static whilst the shell propagates back into the region previously swept clear of gas. This assumption is valid in the limit that the infall timescale $t_{\rm ff}$ of the shell is much shorter than the dynamical collapse timescale $t_{\rm col}$ of the ambient gas. The consistency of this assumption will need to be confirmed when it is required. The opposing limit (not considered in this chapter) would be that the ambient gas falls toward the centre faster than the shell, which means that the ambient gas refills the region previously swept clear of gas, and exerts pressure on the shell as they both infall.

Realistically the scenario would probably be between these two regimes. As the shell stalls and begins to fall inward the ambient pressure would decrease smoothly (rather than shutting off instantly) as the dense shell accelerates back toward the SMBH and eventually outruns the ambient gas completely. If the shell were to stall again and be pushed back out toward the ambient medium it would propagate into a region of newly replenished lower-density ambient gas until it reached its original stall radius. This detailed treatment of infall is not within the scope of this chapter, nor is it in line with its aim, which is to introduce a simple type of infall in order to begin investigating the time evolution of shells.

The precise post-stall behaviour will not affect any conclusions relating to shells that never stall. Requiring that the shell reach large radii without stalling is an example

of a sufficient condition for the escape of a shell. Therefore any critical parameter values which lead to this condition being satisfied are completely independent of how the shell infalls.

3.1.3 Solution Method

Analytical solutions to equations (3.17) and (3.22) cannot always be obtained. This is particularly true for non-isothermal haloes, and for the case that the shell is energy-driven, as the driving pressure term in (3.17) must satisfy an additional equation (see Section 2.3). In general $M_{\rm BH}$ is expected to grow as a function of time, which increases the complexity of the equations of motion, and further motivates the need for a numerical solution method.

In order to solve equation (3.17) a program has been written which utilises a Runge-Kutta adaptive stepsize solution method (Press 2007). This solves equation (3.17) (or equation 3.22 if the shell is infalling) for $x(t)$ and $m(x)\widetilde{v}$, and additionally $dm(x)\widetilde{v}/d\widetilde{t}$ as required in the energy-driven case (see Section 2.3).

For the case that the gas traces the dark matter directly ($h(x) = 1$) it is possible to obtain analytical expressions for the ambient gas pressure $\widetilde{P}_g$ for the dark matter haloes considered in this chapter. These analytical expressions are used within the code to give the gas pressure at any point. If the gas were not to directly trace the dark matter, then the ambient gas pressure would need to be obtained by numerically solving equation (3.20) during the runtime of the program.

3.2 Momentum-Driven Outflows

In the case that the outflow is momentum-driven (see Section 2.2.2) the shell of shocked ambient medium is driven by the ram pressure of the wind, which for an SMBH wind the force is (King & Pounds 2003):

$$4\pi r^2 P(r) = \dot{M}_w v_w = \tau \frac{L_{\rm Edd}}{c}\,, \tag{3.23}$$

which when normalised becomes:

$$4\pi x^2 \widetilde{P}(x) = 2\widetilde{M}_{\rm BH}\,, \tag{3.24}$$

and equation (3.17) becomes:

$$\frac{d}{d\widetilde{t}}\left[h(x)m(x)\widetilde{v}\right] = 2\widetilde{M}_{\rm BH} - 4\pi x^2 \widetilde{P}_g(x) - \frac{2h(x)m(x)}{x^2}\left[\frac{\widetilde{M}_{\rm BH}}{\widetilde{M}_{\rm pk}} + m(x)\right]. \tag{3.25}$$

Equation (3.25) describes the motion of the shell as it propagates into the ambient medium. If the shell stalls and begins to infall then the motion of the shell is no longer described by equation (3.25).

3.2.1 Infall

If a shell reaches a stall point $x_{\rm stall}$ where $\widetilde{v} = 0$ instantaneously, and the acceleration at $x_{\rm stall}$ is negative, then the shell infalls back into the region swept clear of gas. The equation of motion becomes:

$$h(x_{\rm stall})m(x_{\rm stall})\frac{d\widetilde{v}}{d\widetilde{t}} = 2\widetilde{M}_{\rm BH} - \frac{2h(x_{\rm stall})m(x_{\rm stall})}{x^2}\left[\frac{\widetilde{M}_{\rm BH}}{\widetilde{M}_{\rm pk}} + m(x)\right]. \tag{3.26}$$

Equation (3.26) can be solved for the square of the velocity of an infalling shell:

$$\begin{aligned} v_{\rm ff}^2(x) = \frac{4\widetilde{M}_{\rm BH}}{h(x_{\rm stall})m(x_{\rm stall})}(x - x_{\rm stall}) + 4\frac{\widetilde{M}_{\rm BH}}{\widetilde{M}_{\rm pk}}\frac{1}{x}\left(1 - \frac{x}{x_{\rm stall}}\right) \\ -4\int_{x_{\rm stall}}^{x} \frac{m(u)}{u^2}\,du \qquad (x < x_{\rm stall})\,. \end{aligned} \tag{3.27}$$

It is not always analytically possible to obtain the infall timescale $t_{\rm ff}$ from equation (3.27). This means that the assumption $t_{\rm ff} \ll t_{\rm col}$ cannot always be directly confirmed. If this is not possible then the consistency of this assumption can be investigated by comparing the infall velocity with the velocity $v_{\rm col}$ for the dynamical collapse of the ambient gas. If $v_{\rm ff} \gg v_{\rm col}$ throughout the infall peroid, then $t_{\rm ff} \ll t_{\rm col}$ is a reasonable assumption.

3.2.2 The Singular Isothermal Sphere

Equation of Motion

For an SIS halo the mass profile is (see Table 1.1):

$$M_{\rm DM}(r) = \frac{2\sigma_0^2}{G} r \,. \tag{3.28}$$

Normalising the mass to M_σ (equation 3.1) leads to:

$$\widetilde{M}_{\rm DM}(x) = 2x \,. \tag{3.29}$$

where $x \equiv r/r_\sigma$ for this scale-free case. Hence, the general equation of motion (3.25) can be used for the SIS halo with $m(x) = x$, and $\widetilde{M}_{\rm pk} = 2$. Considering the case that gas traces dark matter directly ($h(x) = 1$), then equation (3.20) with $m(u) = u$ gives the normalised pressure of the ambient (hydrostatic) gas in an SIS halo to be:

$$\widetilde{P}_g(x) = \frac{1 + f_0}{4\pi x^2} \,. \tag{3.30}$$

The equation of motion (3.25) becomes:

$$\frac{d}{d\widetilde{t}} \left[x\widetilde{v} \right] = 2 \left(\widetilde{M}_{\rm BH} - 1 \right) - (1 + f_0) - \frac{\widetilde{M}_{\rm BH}}{x} \,. \tag{3.31}$$

Equation (3.31) has no explicit time dependence, which means that it can be reduced to a first order equation in radius:

$$\frac{d}{dx} \left[x^2 \widetilde{v}^2 \right] = 2 \left[2 \left(\widetilde{M}_{\rm BH} - 1 \right) - (1 + f_0) \right] x - 2\widetilde{M}_{\rm BH} \,. \tag{3.32}$$

Aside from the additional factor of $2(1 + f_0)x = 8\pi x^3 \widetilde{P}_g$ equation (3.32) is the same as that solved by McQuillin & McLaughlin (2012). This section will adopt a similar methodology to theirs which begins by solving for the square of the shell velocity, and exploring the asymptotic limits of this expression. This is followed by an analysis of the initial momentum, and how certain values which are unphysical at $x = 0$ can define *launch* solutions which begin at radii $x_{\rm launch} > 0$. The shell stall radii are then

analysed, and a condition on the initial momentum is obtained which results in shells which never stall.

Equation (3.32) has the solution:

$$\widetilde{v}^2 = 2\left(\widetilde{M}_{\rm BH} - 1\right) - (1+f_0) - \frac{2\widetilde{M}_{\rm BH}}{x} + \frac{C}{x^2} \tag{3.33}$$

where $C = m^2(0)\widetilde{v}^2(0)$ is the square of the shell's normalised momentum at $x = 0$. If the ambient pressure is neglected by dropping the factor $1 + f_0$ then the result of McQuillin & McLaughlin (2012) is recovered, and if the SMBH gravity is neglected then the result of King (2005) is recovered.

Large Radii and the Necessary SMBH Mass for the Escape of a Shell

At large radii the velocity tends to a constant:

$$\widetilde{v}^2 = 2\left(\widetilde{M}_{\rm BH} - 1\right) - (1+f_0) \qquad (x \gg 1)\,, \tag{3.34}$$

which in order to be positive requires:

$$\widetilde{M}_{\rm BH} > \widetilde{M}_{\rm BH,crit} = 1 + (1+f_0)/2 \simeq 1.6\,. \tag{3.35}$$

This is the necessary SMBH mass for the shell to reach arbitrarily large radii (c.f. King 2005; McQuillin & McLaughlin 2012). The inclusion of ambient gas pressure increases the critical mass given by equation (3.1) by 60%. This mass alone is not a sufficient condition for escape as it is also required that the shell receives a large enough impulse at $x = 0$ in order to overcome the inward gravitational forces to obtain its coasting speed (McQuillin & McLaughlin 2012).

At large radii, and therefore at late times the shell radius has a linear dependence on time and is independent of the initial shell momentum C:

$$x(\widetilde{t}) = \sqrt{2\left(\widetilde{M}_{\rm BH} - 1\right) - (1+f_0)}\,\widetilde{t} \qquad (\widetilde{t} \gg 1)\,. \tag{3.36}$$

The shell radius at large radii has the same dependence on time as that obtained in Section 2.2.2 for a momentum-driven bubble propagating into an SIS gas distribution

in the absence of gravitational forces (see equation 2.16 with $p = 1$ and $\alpha = 0$). This is because the gravitational force of the dark matter on the shell is constant at all radii in the SIS halo: $M_{\rm DM}(r) \propto M_{\rm sh}(r) \propto r$.

Small Radii

At small radii the C/x^2 term in equation (3.33) becomes dominant:

$$\widetilde{v}^2 = \frac{C}{x^2} - \frac{2\widetilde{M}_{\rm BH}}{x} \qquad (x \ll 1)\,. \tag{3.37}$$

The shell radius as a function of time tends to:

$$x(\widetilde{t}) = \left(2\sqrt{C}\widetilde{t}\right)^{1/2} \qquad (\widetilde{t} \ll 1)\,. \tag{3.38}$$

Launch Solutions

If $C \leq 0 < 2\widetilde{M}_{\rm BH}/x$ then $\widetilde{v}^2$ is negative at small radii, and $x(\widetilde{t})$ is imaginary. However, the derivative $d\widetilde{v}^2/dx$ is greater than zero, which means $\widetilde{v}^2$ will be zero at some larger radius, and it increases beyond this point. These correspond to launch solutions which begin at the radius $x_{\rm launch}$. Combining $\widetilde{v}^2 = 0$ and $d\widetilde{v}^2/dx \geq 0$ with equation (3.33) gives:

$$x_{\rm launch} \times \left[2(\widetilde{M}_{\rm BH} - 1) - (1 + f_0)\right] \geq \widetilde{M}_{\rm BH}\,, \tag{3.39}$$

with ambient gas pressure effects represented by the factor $-(1 + f_0)$. Equation (3.39) shows that launch solutions are only possible if $\widetilde{M}_{\rm BH} > 1 + (1 + f_0)/2$. These launch solutions represent shells that have previously stalled and have been relaunched by the wind (McQuillin & McLaughlin 2012 - see also Figure 1.9 in Section 1.5). Since equation (3.31) (rather than equation 3.32) is to be numerically solved with respect to time (and including infall) these launch solutions can occur as a part of a shell's trajectory if it stalls and is able to resume outward motion.

Stall Points and Required Initial Momentum for Escape

The critical mass given by equation (3.35) means that a shell will have a positive coast-

ing velocity at large radii, but the shell must have a large enough initial impulse to overcome the gravitational and ambient pressure forces in order to reach large radii.

If $C > 0$ then $\widetilde{v}^2$ is large and positive at radii tending to zero, but the derivative $d\widetilde{v}^2/dx$ is negative and so the shell decelerates. If the shell stalls it does so at a radius given by setting equation (3.33) equal to zero, which leads to:

$$x_{\rm stall} = \frac{\widetilde{M}_{\rm BH} - \sqrt{\widetilde{M}_{\rm BH}{}^2 - \left[2\left(\widetilde{M}_{\rm BH} - 1\right) - (1+f_0)\right]C}}{2\left(\widetilde{M}_{\rm BH} - 1\right) - (1+f_0)} \tag{3.40}$$

In the case that $M_{\rm BH} < 1 + (1+f_0)/2$ the discriminant in equation (3.40) is always positive and greater than $\widetilde{M}_{\rm BH}{}^2$. This results in the numerator and denominator in equation (3.40) both being negative, and therefore $x_{\rm stall} > 0$, i.e. the shell will not reach large radii.

If the discriminant is negative, then $x_{\rm stall}$ is complex and $\widetilde{v}^2 = 0$ never occurs. The shell will never stall, and therefore always escape if:

$$\widetilde{M}_{\rm BH}^2 - [2(\widetilde{M}_{\rm BH} - 1) - (1+f_0)]C < 0 \tag{3.41}$$

or in terms of C:

$$C > C_{\rm esc} = \frac{\widetilde{M}_{\rm BH}^2}{2\left(\widetilde{M}_{\rm BH} - 1\right) - (1+f_0)}\,. \tag{3.42}$$

Physically this is a statement that the shell's initial momentum must be large enough for it to overcome the inward forces of gravity and ambient pressure. Therefore a sufficient condition for a shell to reach large radii without stalling is that for a given $M_{\rm BH} > M_\sigma$ the initial momentum must exceed $C_{\rm esc}(\widetilde{M}_{\rm BH})$ (McQuillin & McLaughlin 2012).

Finding the minimum value of $C_{\rm esc}$ by differentiating with respect to $\widetilde{M}_{\rm BH}$ and equating to zero gives $C_{\rm esc} = 2 + (1+f_0)$ when $\widetilde{M}_{\rm BH} = 2 + (1+f_0)$, i.e. when $C_{\rm esc} = \widetilde{M}_{\rm BH}$. Therefore the lower limit of the square of initial momentum for any $\widetilde{M}_{\rm BH}$ is:

$$C > C_{\rm min} = 2 + (1+f_0)\,. \tag{3.43}$$

This is a necessary condition for the escape of shell which all shells must satisfy if they are to reach large radii without stalling. It is not a sufficient condition because for a specific value of $C > C_{\rm min}$ there are two $\widetilde{M}_{\rm BH}$ solutions to equation (3.42) which bound the range of values that $\widetilde{M}_{\rm BH}$ can have in order for a shell to reach large radii without stalling.

Equation (3.41) has a single real solution $M_{\rm BH} = C_{\rm min}$ when $C = C_{\rm min}$. For $C > C_{\rm min}$ equation (3.41) has two real solutions. The smaller of these two solutions corresponds to the SMBH value required (for a given initial C) to overcome the ambient pressure and gravitational forces:

$$\widetilde{M}_{\rm BH,low} = C\left[1 - \sqrt{1 - C_{\rm min}/C}\right] . \tag{3.44}$$

The larger corresponds to the SMBH value that must not be exceeded if the shell is to escape the gravity of the SMBH:

$$\widetilde{M}_{\rm BH,high} = C\left[1 + \sqrt{1 - C_{\rm min}/C}\right] . \tag{3.45}$$

The effects of these two masses can be seen in Figure 3.2 by plotting SMBH mass $\widetilde{M}_{\rm BH}$ against shell radius x for numerical solutions to (3.31) (black curves) alongside the stall solutions $\widetilde{v}^2 = 0$ given by equation (3.33) (blue curves). Three values of C are shown: the lowest value of initial momentum which shells must exceed in order to escape: $C = C_{\rm min}$, and two larger values $C = 5, 10$ are shown for ten $\widetilde{M}_{\rm BH}$ values in logarithmic intervals between 0.001 and 100.

To sum up: for a momentum-driven shell in an SIS halo to never stall and to achieve a positive terminal coasting speed it must be driven by a wind from an SMBH with mass in excess of $M_{\rm BH,crit}$ as given by equation (3.35), and its initial momentum must exceed $C_{\rm esc}$ as given by equation (3.42), or equivalently for a given initial momentum the SMBH mass must lie between $M_{\rm BH,low}$ and $M_{\rm BH,high}$.

Infall

In the case that $C < C_{\rm esc}(\widetilde{M}_{\rm BH})$ then the shell stalls at $x_{\rm stall}$ given by equation (3.40). By using equation (3.40) with (3.31) it can be shown that the acceleration at $x_{\rm stall}$ is

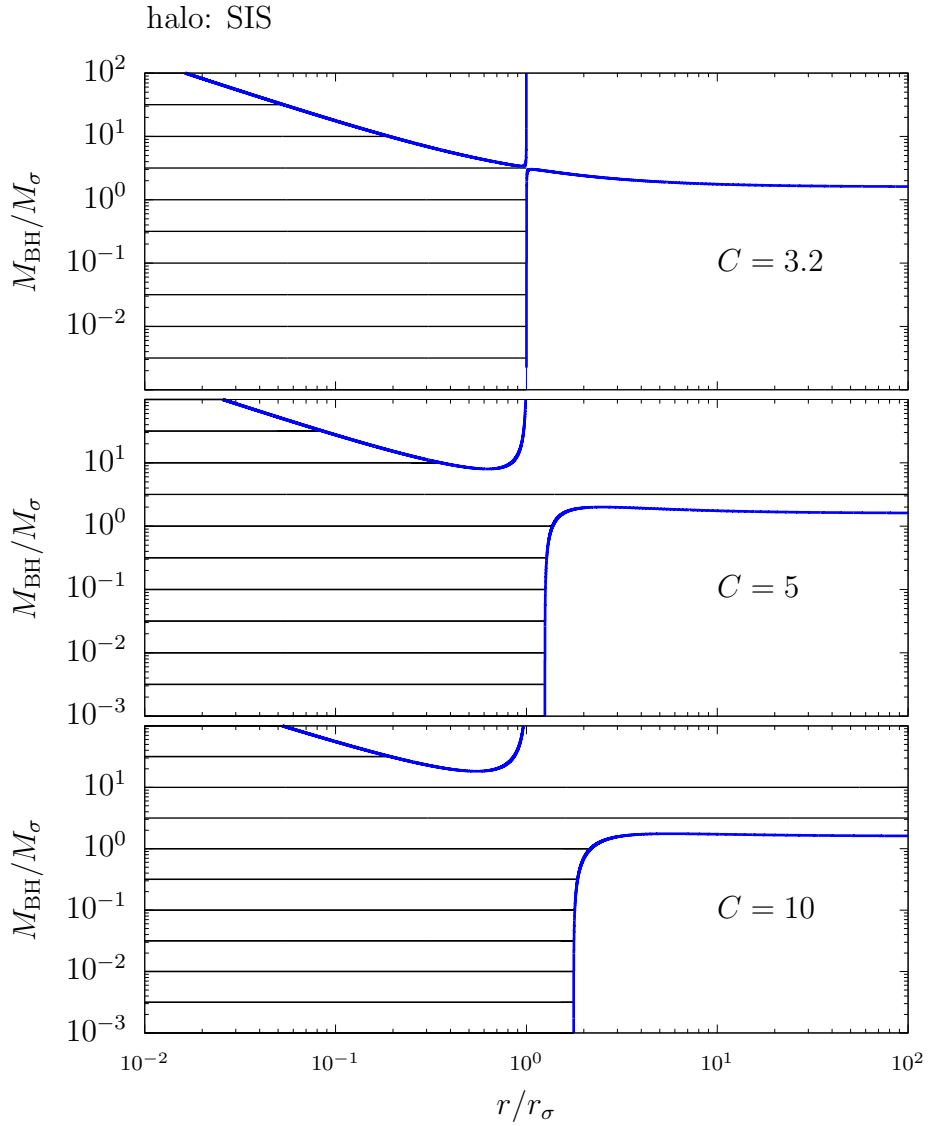

Figure 3.2: SMBH mass against shell radius for momentum-driven shells in an SIS halo for three values of initial momentum. The blue curves show the velocity from equation (3.33) equated to zero and solved for $\widetilde{M}_{\rm BH}$. Equivalently these curves correspond to the stall radii given by equation (3.40). The black lines are individual shell solutions shown simply in terms of their constant SMBH mass. This figure shows how the range of SMBH masses which allows shells to reach large radii without stalling increases with increasing initial momentum.

always negative. This means that the shell will begin to infall, and if it infalls faster than the ambient gas then its equation of motion is:

$$x_{\rm stall}\frac{d\widetilde{v}}{d\widetilde{t}} = 2\widetilde{M}_{\rm BH} - \frac{\widetilde{M}_{\rm BH}x_{\rm stall}}{x^2} - \frac{2x_{\rm stall}}{x} \qquad (x < x_{\rm stall}) \tag{3.46}$$

and the subsequent infall velocity is:

$$\begin{aligned}\widetilde{v}^2(x) =& 4\widetilde{M}_{\rm BH}\left(\frac{x}{x_{\rm stall}} - 1\right) + \frac{2\widetilde{M}_{\rm BH}}{x}\left(1 - \frac{x}{x_{\rm stall}}\right) \\ &+ 4\ln\left(\frac{x_{\rm stall}}{x}\right) \qquad (x < x_{\rm stall})\,.\end{aligned} \tag{3.47}$$

The time $t_{\rm ff}$ taken by the shell with infall velocity given by equation (3.47) to infall from $x_{\rm stall}$ to $x = 0$ is to be compared with the collapse time of the gas $t_{\rm col} \sim \sqrt{1/G\bar{\rho}_g}$. For the SIS halo with gas tracing dark matter directly the collapse time is $t_{\rm col} \sim r/\sigma_0$, and therefore the gas redistributes itself with a velocity $\sim \sigma_0$. Since $t_{\rm ff}$ is not readily solved for in equation (3.47) the infall velocity is instead to be compared with σ_0. If $\widetilde{v} \gg 1$ for much of the infall, then the assumptions regarding the static distribution of the gas as the shell infalls are justified. The infall velocity given by equation (3.47) is shown in Figure 3.3 for a range of SMBH masses and initial momenta. This figure shows that for the range of $\widetilde{M}_{\rm BH}$ and C values chosen that the magnitude of infall velocity exceeds σ_0 over most of its infall trajectory, and that the approximation $t_{\rm ff} \ll t_{\rm col}$ is acceptable.

Just as the shell begins to infall at $x_{\rm stall}$ the force from ambient pressure is removed, and the acceleration may now be less than, equal to, or greater than zero at $x_{\rm stall}$. Equation (3.46) shows that if the acceleration is negative at $x_{\rm stall}$, then it will remain so for $x < x_{\rm stall}$. This means that solutions with negative acceleration at $x_{\rm stall}$ cannot stall again during infall. Instead they simply fall back down to the SMBH. If $\widetilde{M}_{\rm BH} \leq 1$, then by inspection of equation (3.46) it can be seen that the acceleration is negative at $x_{\rm stall}$. If $\widetilde{M}_{\rm BH} > 1$ then requiring that the acceleration in equation (3.46) is negative leads to:

$$x_{\rm stall} < \frac{\widetilde{M}_{\rm BH}}{2(\widetilde{M}_{\rm BH} - 1)} \qquad (\widetilde{M}_{\rm BH} > 1). \tag{3.48}$$

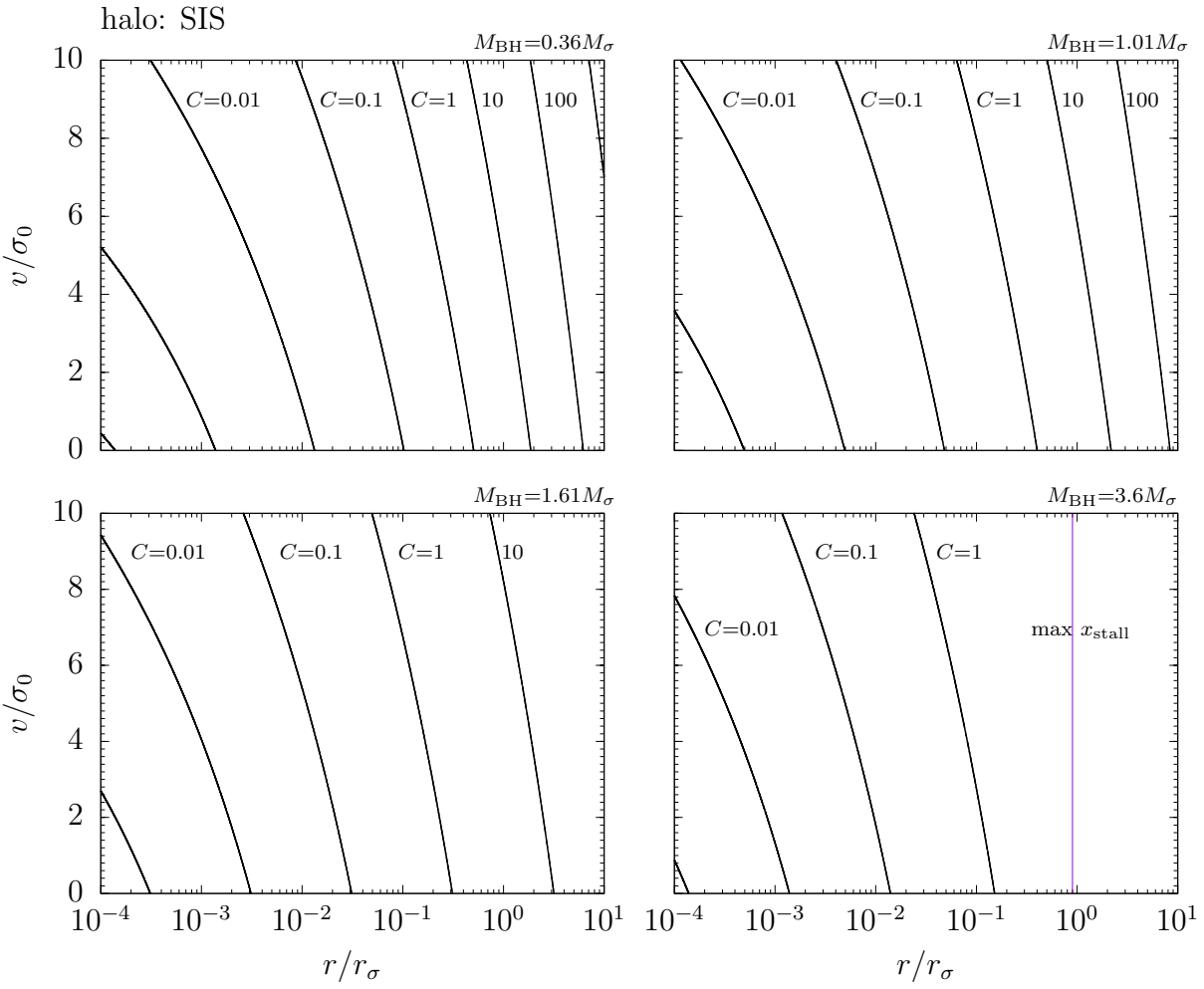

Figure 3.3: Infall velocity fields for momentum-driven shells launched by a steady wind in an SIS halo for a range of SMBH masses. The black curves show the infall velocity fields of shells for a range of initial momenta ($0.0001 < C < 1000$). The dotted red line shows the maximum possible $x_{\rm stall}$ from equation (3.40).

If (3.48) is satisfied then stalled shells driven by winds from SMBHs with masses $\widetilde{M}_{\rm BH} > 1$ will have negative acceleration, and subsequently infall to the SMBH. If equation (3.48) is not satisfied then the shell has positive acceleration at $x_{\rm stall}$, and rather than infalling the shell moves outward. This means that these shells are described by a

launch solution in the absence of ambient pressure (see McQuillin & McLaughlin 2012). This condition can be put in terms of the initial momentum by using equation (3.40) with equation (3.48):

$$C < C_{\rm ff} = \frac{\widetilde{M}_{\rm BH}^2}{4(\widetilde{M}_{\rm BH}-1)^2}\left[2(\widetilde{M}_{\rm BH}-1)+(1+f_0)\right] \qquad (\widetilde{M}_{\rm BH}>1)\,. \tag{3.49}$$

If $\widetilde{M}_{\rm BH} \leq 1$, or $\widetilde{M}_{\rm BH} > 1$ and $C < C_{\rm ff}$ then the shell has negative acceleration at $x_{\rm stall}$ and falls back toward the SMBH without stalling again.

If $C > C_{\rm ff}$ then the shell has positive acceleration at $x_{\rm stall}$. This corresponds to an instantaneous impulse that the shell receives from the wind as the ambient gas pressure drops off suddenly from the shell as it stalls and *just starts* to infall. The result of this is that the overall force on the shell increases by the amount close to that which was being imparted by the ambient pressure which in the SIS halo is $1+f_0$. The shell attempts to move back out until it collides with the stationary ambient medium and is again subject to its ram pressure.

Numerical Solutions

The resultant shell radii x and velocities $\widetilde{v}$ from numerically integrating the equation of motion (3.31) and equation (3.46) (when the shell stalls) are shown in Figure 3.4 as a function of time $\widetilde{t}$. In Figure 3.5 the shell velocity $\widetilde{v}$ and momentum-flux of the shell $\dot{p}_{\rm sh}$ are shown as functions of shell radius x. These figures show solutions with fifteen different values of C in logarithmic intervals within the range $0.001 < C < 1000$. The five SMBH masses: $\widetilde{M}_{\rm BH} = 0.36, 1.01, 1.3, 1.61, 3.6$ display the entire range of shell behaviour and they correspond to a mass significantly below any necessary mass for a shell to escape, a mass slightly above the necessary mass for the escape of a shell in the absence of ambient pressure, an intermediate mass between the two necessary masses without and with ambient pressure, a mass slightly above the necessary mass for the escape of a shell subject to ambient pressure, and a mass significantly above this necessary mass (respectively).

Three possible outcomes exist for the shell: the shell stalls once and falls back

to the SMBH, the shell reaches large radii without ever stalling, or the shell stalls repeatedly as it becomes confined by the ambient pressure.

For $\widetilde{M}_{\rm BH} = 0.36, 1.01, 1.3$ all solutions stall. For $\widetilde{M}_{\rm BH} = 0.36$ all post-stall solutions follow equation (3.47), as do those solutions with $\widetilde{M}_{\rm BH} = 1.01, 1.3$ which have C values which satisfy equation (3.49): $C < C_{\rm ff}$. The momentum-flux plot in Figure 3.5 shows that these are the solutions where the impulse received from the wind (as the ambient pressure drops instantly at a stall) is too weak to result in a positive net force. The solutions for $\widetilde{M}_{\rm BH} = 1.01, 1.3$ with $C > C_{\rm ff}$ do not infall because the instantaneous force of $1 + f_0$ is strong enough to result in a positive net force which pushes the shell outwards again. This impulse results in shells which are similar to the launch solutions obtained when $C < 0$ and the ambient pressure is neglected (see McQuillin & McLaughlin 2012) but with the key difference being that the shell mass is constant. These solutions stall again when the ambient medium and its associated ram pressure are encountered. But because the shell moved briefly without sweeping up mass when it recollides with the ambient gas it does so with a higher force than it had before. It is this which allows the shell to make slow progress despite being pressure confined, and it is shown by the small 'saw-tooth' steps above the blue curves in Figure 3.6. The process repeats indefinitely for these SMBH mass values because the net force with ambient pressure included is never positive since $\widetilde{M}_{\rm BH}$ is less than the critical value of 1.6. This process of repeated stalling does however result in a small average velocity which increases to a constant value as the SMBH gravity becomes negligible. These velocities are shown with blue dashed lines in Figure 3.4 and correspond to $\widetilde{v}_{avg} = 0.008, 0.05$ for $\widetilde{M}_{\rm BH} = 1.01, 1.3$ respectively. This is a new type of shell solution which corresponds to the scenario where the wind is strong enough to prevent the shell from infalling but not so strong that it can overcome the ambient pressure. Therefore the best physical interpretation for these solutions are that they represent confinement by the ambient pressure. This is supported by the approximately constant radii that the shells possess for long intervals of time. However, the repeated stalling and the resultant slow motion are likely to result in the dissolution of the shell's shock structure.

A region where the repetitive stalling behaviour occurs is highlighted in Figure

3.5 in a green box, which is enhanced for a single solution with $C = 100$ in Figure 3.6. The top left panel of Figure 3.6 shows the numerical velocity solution in black alongside the analytical solution from equation (3.33) in green, a launch solution in blue given by equation (3.33) with $C < 0$ and ambient pressure neglected, and an analytical solution in red for when the ambient pressure is reapplied given by equation (3.33) with $C \gg 100$. In the lower left panel the numerical solution for the momentum-flux is shown in black, with the analyical momentum-flux from equation (3.31) in green, the analytical momentum-flux from equation (3.31) without ambient pressure in blue, and the momentum-flux from equation (3.46) in magenta. This shows that when the shell with motion described by equation (3.31) stalls (green curve) the ambient pressure term is dropped and the force suddenly increases by an amount $1 + f_0$ (blue curve). The net force is positive at the stall point and the shell attempts to move outward with constant mass, and because its mass is constant the force becomes larger still (departs from blue force curve). The shell then encounters the ambient medium and its associated ram pressure which causes the force to become instantly negative (green curve). The velocity decreases to zero as the force is negative (red curve in top panel). This repeats indefinitely because the equation of motion (3.31) never permits a positive net force for $\widetilde{M}_{\rm BH} < 1.6$, but the shell makes slow progress because of the small motions with constant mass. The case where $\widetilde{M}_{\rm BH} = 1.61$ is shown in the right hand panels, and this solution does achieve a positive net force after stalling twice.

For the larger SMBH masses: $\widetilde{M}_{\rm BH} = 1.61, 3.6$ the shells only stall if equation (3.42) is not satisfied. A single solution in each case with $C_{\rm ff} < C < C_{\rm esc}$ is shown which stalls multiple times before going on to escape. The solution shown for $\widetilde{M}_{\rm BH} = 1.61$ has a large enough initial momentum that it stalls only a couple of times before going on to escape, whilst the solution for $\widetilde{M}_{\rm BH} = 3.6$ has a low value of initial momentum which results in it stalling many times. The solutions with $C > C_{\rm esc}$ never stall, and the asymptotic late time expressions for x and $\widetilde{v}$ given by equation (3.36) and (3.34) are shown as red dashed curves in Figure 3.4.

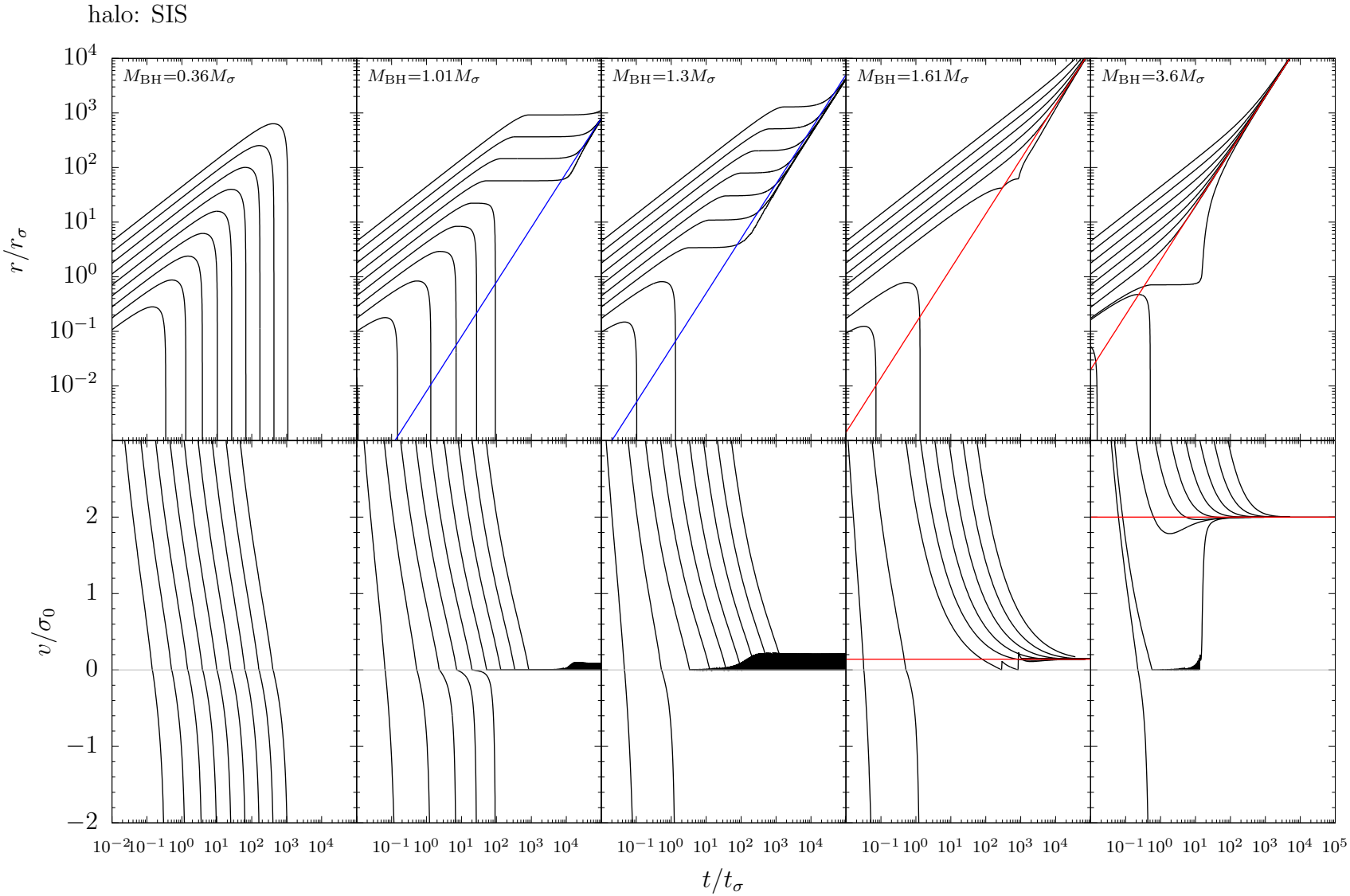

Figure 3.4: Shell radius and velocity versus time for a momentum-driven shell launched by a steady wind in an SIS halo. Blue and red dashed lines show asymptotic stalling and escape solutions respectively. The C values displayed are in logarithmic intervals increasing from bottom to top (upper panels) and left to right (lower panels) between $C = 1$ and $C = 1000$. See main text for discussion.

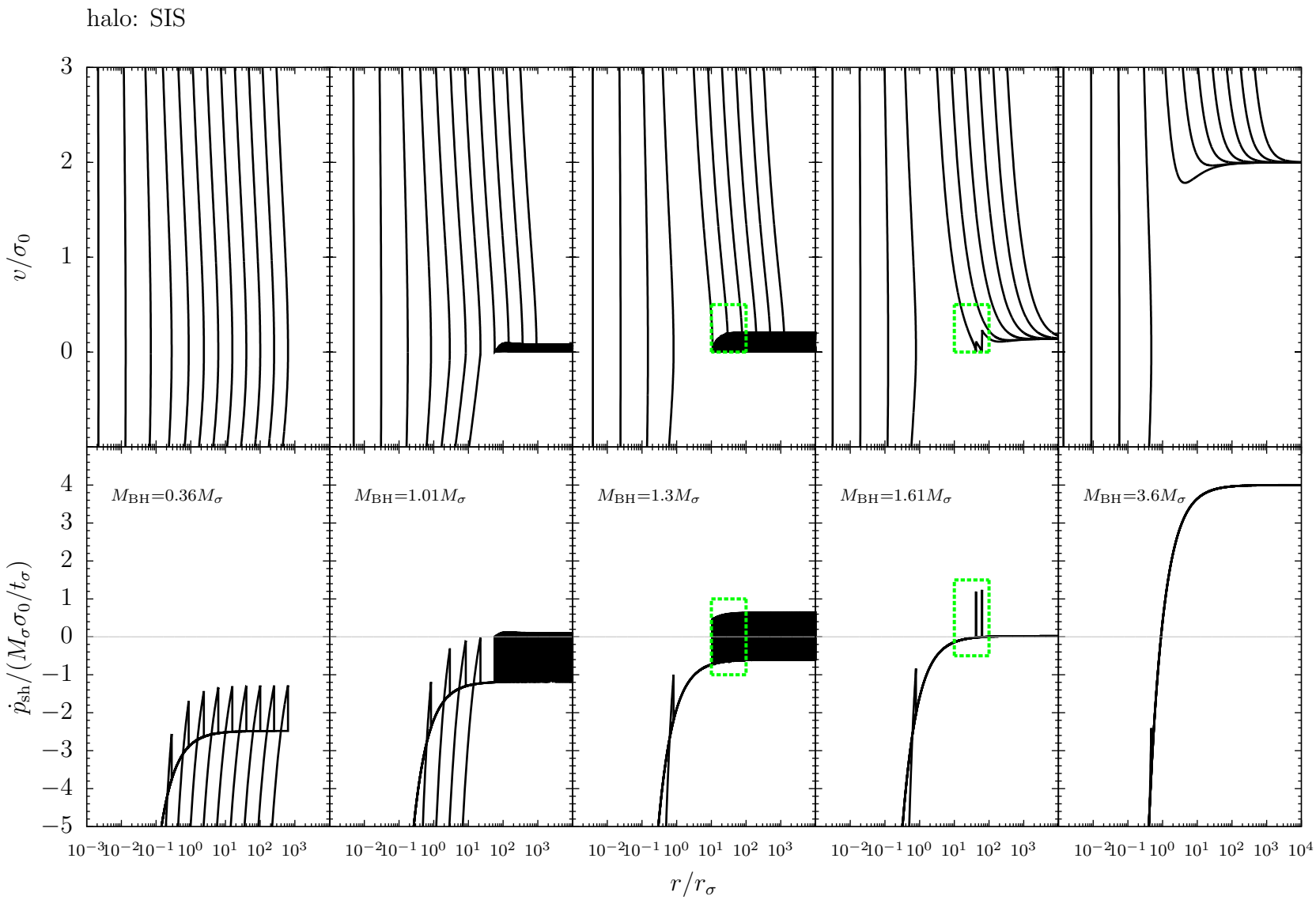

Figure 3.5: Shell velocity and momentum-flux versus radius for a momentum-driven shell launched by a steady wind in an SIS halo. The C values displayed are in logarithmic intervals increasing from left to right between $C = 1$ and $C = 1000$. The regions within green boxes are displayed in Figure 3.6. See main text for discussion.

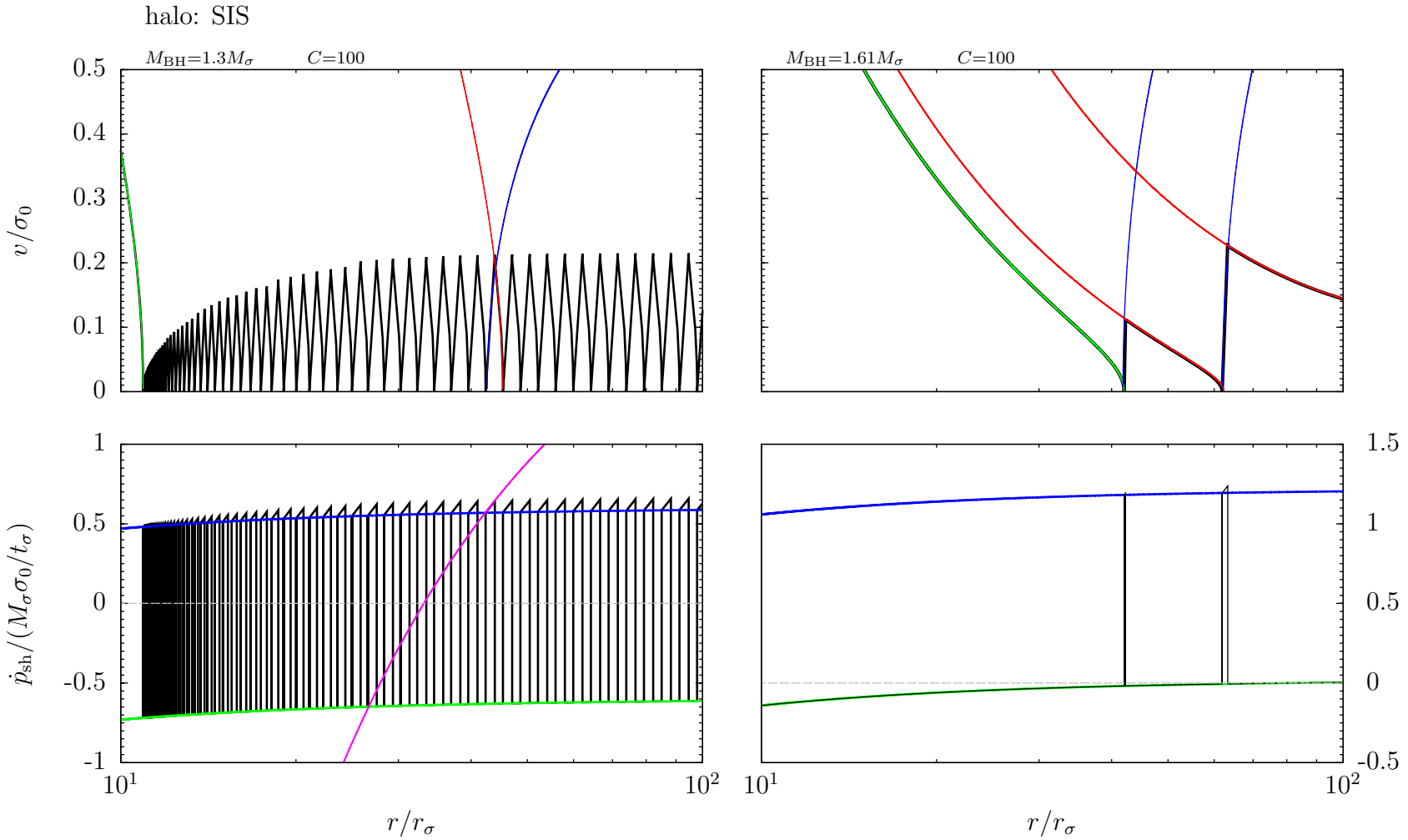

Figure 3.6: Stalling shell velocity and momentum-flux versus radius for a momentum-driven shell launched by a steady wind in an SIS halo. The solutions shown are taken from within the green boxes in Figure 3.5. Numerical velocity solutions are shown in black alongside the analytical solution from equation (3.33) in green, a launch solution in blue given by equation (3.33) with $C < 0$ and ambient pressure neglected, and an analytical solution in red for when the ambient pressure is reapplied given by equation (3.33) with $C \gg 100$. In the lower left panel the numerical solution for the momentum-flux is shown in black, with the analyical momentum-flux from equation (3.31) in green, the analytical momentum-flux from equation (3.31) without ambient pressure in blue, and the momentum-flux from equation (3.46) in magenta.

3.2.3 Hernquist Halo

Equation of Motion

The mass profile for the Hernquist halo is (see Table 1.1):

$$M_{\rm DM}(x) = M_{\rm pk}\frac{4x^2}{(1+x)^2}\,, \tag{3.50}$$

where $x = r/r_{\rm pk}$ and $M_{\rm pk}$ is the mass at $x = 1$. Dividing by $M_{\rm pk}$ gives the function $m(x)$:

$$m(x) = \frac{4x^2}{(1+x)^2}\,. \tag{3.51}$$

In the case that $h(x) \equiv 1$ the normalised pressure of the ambient gas can be found by using equation (3.51) with equation (3.20):

$$\widetilde{P}_g(x) = \frac{16(1+f_0)}{\pi}\left[\ln\left(1+\frac{1}{x}\right) - \frac{2x(3x(2x+7)+26)+25}{12(1+x)^4}\right]\,. \tag{3.52}$$

The equation of motion (3.25) becomes:

$$\begin{aligned}\frac{d}{d\widetilde{t}}\left[\frac{4x^2}{(1+x)^2}\widetilde{v}\right] = 2\widetilde{M}_{\rm BH} &- 64(1+f_0)x^2\left[\ln\left(1+\frac{1}{x}\right) - \frac{2x(3x(2x+7)+26)+25}{12(1+x)^4}\right] \\ &- \frac{8}{(1+x)^2}\left[\frac{\widetilde{M}_{\rm BH}}{\widetilde{M}_{\rm pk}} + \frac{4x^2}{(1+x)^2}\right]\,.\end{aligned} \tag{3.53}$$

The ambient pressure and the ambient pressure force are shown in Figure 3.7.

Asymptotics

The Hernquist halo has a shallower density profile than the SIS halo at small radii which means that the shell sweeps up less mass at smaller radii. A consequence of this is that the SMBH gravity is less significant at small radii in the Hernquist halo. This can be seen by using the fact that $m(x) \to 4x^2$ at small radii and therefore the gravitational force of the SMBH scales with the outward wind force. The shell will have a positive net force at small radii as long as:

$$\widetilde{M}_{\rm BH}\left[1 - \frac{4}{\widetilde{M}_{\rm pk}}\right] > 0 \tag{3.54}$$

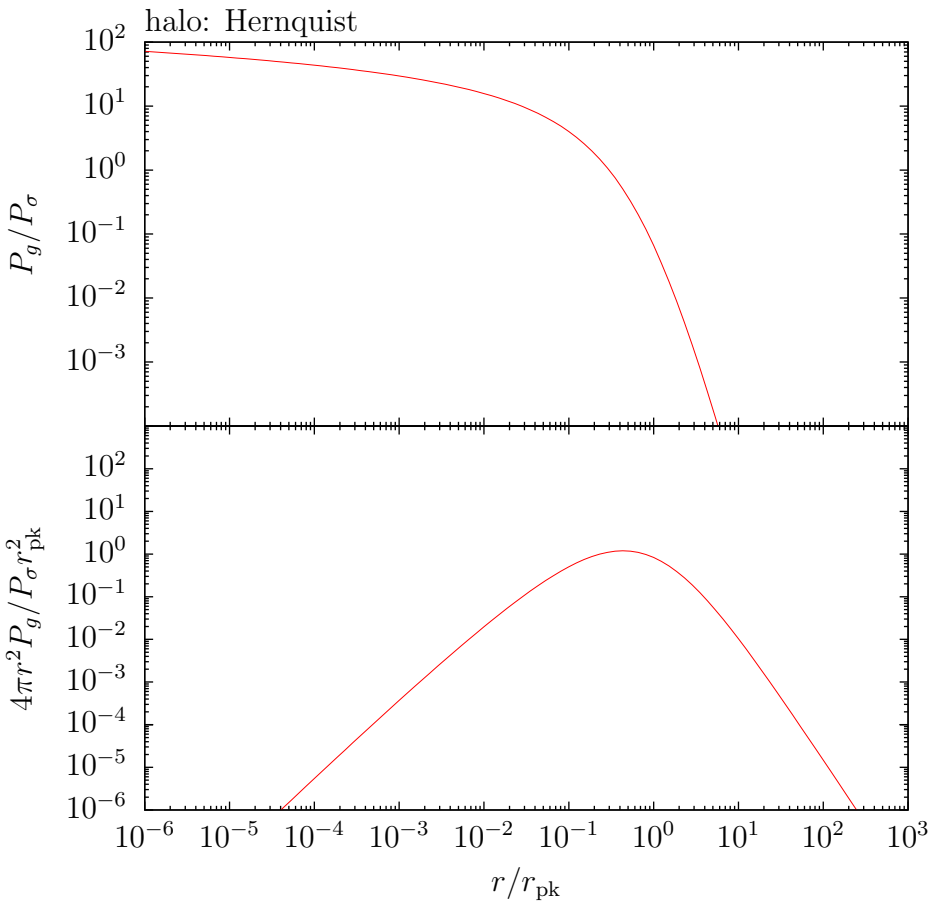

Figure 3.7: Ambient pressure (top) and the ambient pressure force on a shell (bottom) against radius in a Hernquist halo.

and therefore if $\widetilde{M}_{\rm pk} > 4$. This means that unlike the SIS halo the Hernquist halo does not require shells to have a positive initial momentum in order to begin moving outward. If the initial momentum of the shell is zero ($C = 0$), then the shell radius at early times is given by:

$$x(\widetilde{t}) = \left[\frac{3\widetilde{M}_{\rm BH}}{4}\left(1 - \frac{4}{\widetilde{M}_{\rm pk}}\right)\widetilde{t}^2\right]^{1/3} \qquad (\widetilde{t} \ll 1;\, C = 0)\,. \tag{3.55}$$

Because the driving term $2\widetilde{M}_{\rm BH}$ scales with the SMBH gravity term and dominates the ambient pressure and dark matter gravity terms the shell radius solution given by equation (3.55) has the same dependence on time as the radius of a momentum-driven

bubble in the absence of gravity (see equation 2.16 with $p = 2$ and $\alpha = 0$).

If the shell has an initial momentum $C > 0$ then the shell radius at early times is:

$$x(\widetilde{t}) = \left(\frac{3\sqrt{C}\widetilde{t}}{4}\right)^{1/3} \qquad (\widetilde{t} \ll 1;\, C > 0)\,. \tag{3.56}$$

From equations (3.55) and (3.56) the velocity at early times is:

$$\widetilde{v} = \left[\frac{2\widetilde{M}_{\rm BH}}{9}\left(1 - \frac{4}{\widetilde{M}_{\rm pk}}\right)\widetilde{t}^{-1}\right]^{1/3} = \sqrt{\frac{\widetilde{M}_{\rm BH}}{3}\left(1 - \frac{4}{\widetilde{M}_{\rm pk}}\right)x^{-1}} \qquad (\widetilde{t} \ll 1;\, C = 0)\,, \tag{3.57}$$

or if $C > 0$:

$$\widetilde{v} = \frac{1}{3}\left(\frac{3\sqrt{C}\widetilde{t}^{-2}}{4}\right)^{1/3} = \frac{\sqrt{C}}{4x^2} \qquad (\widetilde{t} \ll 1;\, C > 0)\,. \tag{3.58}$$

At late times the mass profile converges ($m(x) \to 4$), and the right hand side of equation (3.53) tends to $2\widetilde{M}_{\rm BH}$. The resultant shell radius is:

$$x(\widetilde{t}) = \frac{\widetilde{M}_{\rm BH}}{4}\widetilde{t}^2 \qquad (\widetilde{t} \gg 1)\,, \tag{3.59}$$

which because the halo mass tends to a constant shows the same dependence on time as the momentum-driven bubble in the absence of gravity (see equation 2.16 with $p = 0$ and $\alpha = 0$). The velocity of the shell is:

$$\widetilde{v} = \frac{\widetilde{M}_{\rm BH}}{2}\widetilde{t} = \sqrt{\widetilde{M}_{\rm BH}x} \qquad (\widetilde{t} \gg 1)\,. \tag{3.60}$$

Infall

In order to determine whether a shell infalls at a stall point its acceleration must be found at that point. If the shell stalls then its acceleration can be determined from

equation (3.53):

$$\begin{aligned}\frac{d\widetilde{v}}{d\widetilde{t}} =& \frac{(1+x_{\rm stall})^2}{4x_{\rm stall}^2}\left\{2\widetilde{M}_{\rm BH}\right. \\ & - 64(1+f_0)x_{\rm stall}^2\left[\ln\left(1+\frac{1}{x_{\rm stall}}\right) - \frac{2x_{\rm stall}(3x_{\rm stall}(2x_{\rm stall}+7)+26)+25}{12(1+x_{\rm stall})^4}\right] \\ & \left. - \frac{8}{(1+x_{\rm stall})^2}\left[\frac{\widetilde{M}_{\rm BH}}{\widetilde{M}_{\rm pk}} + \frac{4x^2}{(1+x_{\rm stall})^2}\right]\right\} \qquad (x = x_{\rm stall})\,.\end{aligned} \tag{3.61}$$

Without an analytical expression for $x_{\rm stall}$ it is not possible to determine the sign of the acceleration at $x_{\rm stall}$ in terms of the parameter values. However, by numerically integrating (3.53) and evaluating (3.61) at $x_{\rm stall}$ for a range of parameters it is apparent that the acceleration is always negative at $x_{\rm stall}$.

At $x_{\rm stall}$ the shell begins to infall. If the infall timescale $t_{\rm ff}$ is much less than the collapse timescale $\widetilde{t}_{\rm col} = (G\rho)^{-1/2} = \sqrt{\pi x(1+x)^2/4}$, then the shell 'outruns' the infalling ambient medium and is no longer subject to its pressure. Numerical solutions show that the stall radii for a physically interesting range of parameters are $x \sim 1$ which means that $\widetilde{t}_{\rm col} \sim 1$. The infall time for a shell however is always $\widetilde{t}_{\rm ff} \ll 1$ for a broad range of parameter values, and therefore $\widetilde{t}_{\rm ff} \ll \widetilde{t}_{\rm col}$ is a justifiable assumption.

The velocity of an infalling shell can be obtained from the equation of motion at radii less than $x_{\rm stall}$ and in the absence of ambient pressure:

$$\frac{4x_{\rm stall}^2}{(1+x_{\rm stall})^2}\frac{d\widetilde{v}}{d\widetilde{t}} = 2\widetilde{M}_{\rm BH} - \frac{8x_{\rm stall}^2}{(1+x_{\rm stall})^2x^2}\left[\frac{\widetilde{M}_{\rm BH}}{\widetilde{M}_{\rm pk}} + \frac{4x^2}{(1+x)^2}\right]. \tag{3.62}$$

If $x_{\rm stall}$ is such that the acceleration in equation (3.62) is negative, i.e. if the force from removing ambient pressure ($4\pi x\widetilde{P}_g$) does not lead to a positive net force, then the shell infalls back to the SMBH with velocity:

$$\widetilde{v}^2(x) = \widetilde{M}_{\rm BH}\frac{(1+x_{\rm stall})^2}{x_{\rm stall}^2}(x - x_{\rm stall}) + 4\frac{\widetilde{M}_{\rm BH}}{\widetilde{M}_{\rm pk}}\frac{1}{x}\left(1 - \frac{x}{x_{\rm stall}}\right) + \frac{16}{1+x}\left(1 - \frac{1+x}{1+x_{\rm stall}}\right). \tag{3.63}$$

However, if $x_{\rm stall}$ is such that the acceleration in equation (3.62) is positive when the ambient pressure is removed, then the shell resumes outward motion, and this makes

it possible for shells to move beyond their initial stall radii.

Numerical Solutions

The equation of motion (3.53) and the infall equation (3.62) have been solved numerically and the shell radius and velocity fields are shown in Figure 3.8 as functions of time $\widetilde{t}$. In Figure 3.9 the shell velocities $\widetilde{v}$ and momentum-fluxes $\dot{p}_{\rm sh}$ are shown as functions of shell radius x. Both figures show solutions with fifteen values of C in logarithmic intervals within the range: $0.001 < C < 1000$ and $C = 0$ (shown in magenta). The five SMBH masses: $\widetilde{M}_{\rm BH} = 0.36, 1.0, 1.01, 1.4, 3.6$ display the range of shell behaviour. In both figures $\widetilde{M}_{\rm pk} = 4000$ which corresponds to a Milky Way sized halo with $\sigma_0 = 120$ km s^{-1} and $r_{\rm pk} = 50$ kpc (McQuillin & McLaughlin 2012).

There are three distinct outcomes for the shell: the shell stalls and infalls back to the SMBH, the shell reaches large radii without stalling, or the shell becomes confined by the ambient pressure. There is a difference for the Hernquist halo which is that the pressure confined shells will either ultimately infall or reach large radii after a long ($t > 100t_\sigma \simeq 10^{10}$ yr) period of stalling. This is because unlike the SIS halo the Hernquist halo is finite, and because of that the ambient pressure force will ultimately tend to zero (see Figure 3.7). However the stalling timescale is certainly large enough that the shell can be effectly considered as permanently pressure confined.

For $\widetilde{M}_{\rm BH} = 0.36$ the three distinct outcomes exist for the shell, while for $\widetilde{M}_{\rm BH} = 1.4, 3.6$ all shells simply escape without stalling. For $\widetilde{M}_{\rm BH} = 1.0$ shells either escape or become confined by the ambient pressure, but at very late times these confined shells eventually infall. In the case that $\widetilde{M}_{\rm BH} = 1.01$ all shells escape or they stall to become pressure confined, and shells that do stall ultimately go on to escape. The difference between these two outcomes is because there is a necessary SMBH mass for escape between these two values. Once again, although these solutions do formally go on to reach large radii they only do so on long ($t > 100t_\sigma$) timescales.

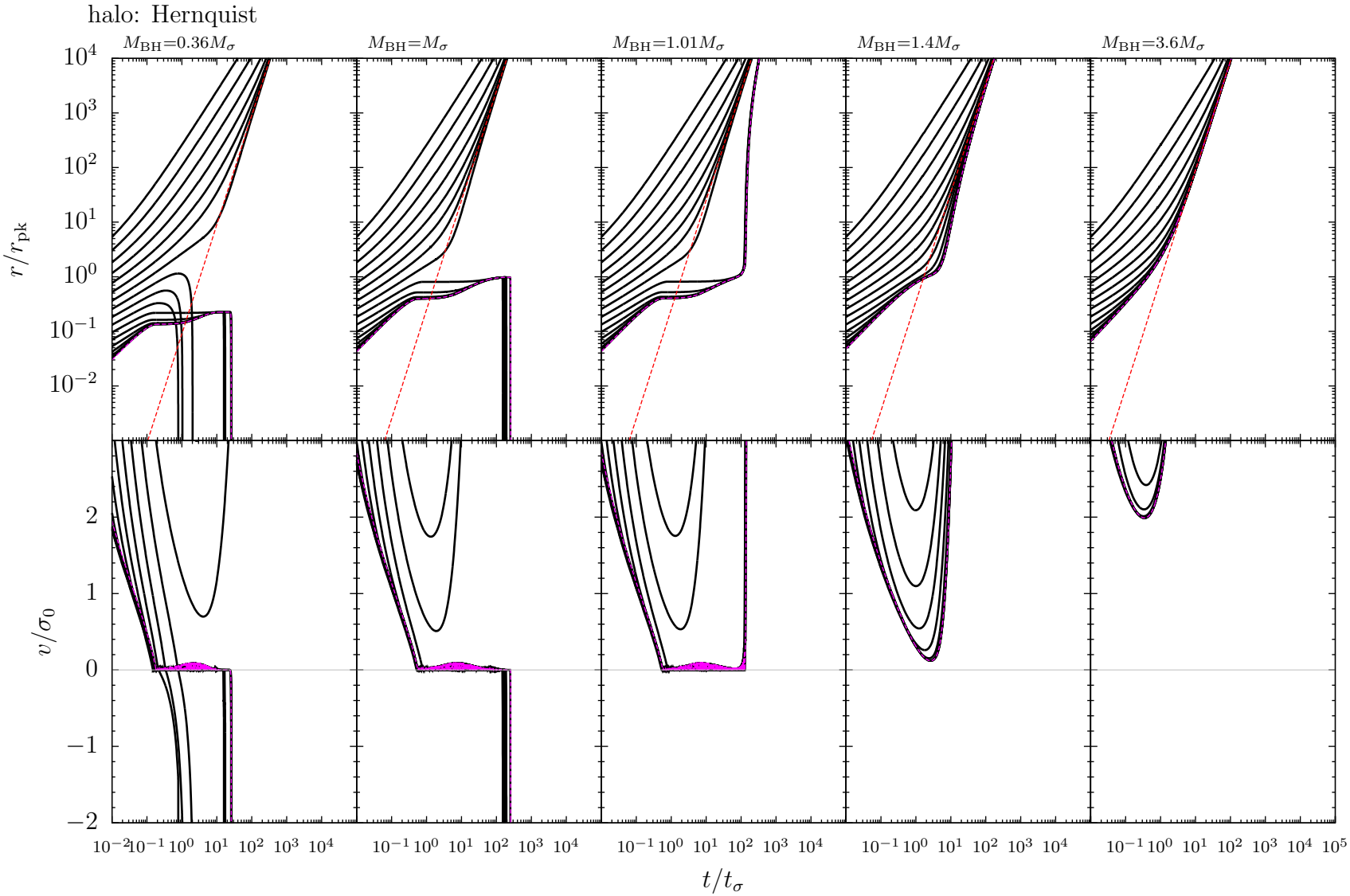

Figure 3.8: Shell radius and velocity versus time for a momentum-driven shell launched by a steady wind in a Hernquist halo. Each black curve corresponds to a numerical solution with initial momentum at logarithmic intervals within the range: $0.001 < C < 1000$, and they increase from bottom to top (upper panels) and left to right (lower panels). The dashed red curves are the asymptotes given by equation (3.59), and the magenta curves are the $C = 0$ numerical solutions.

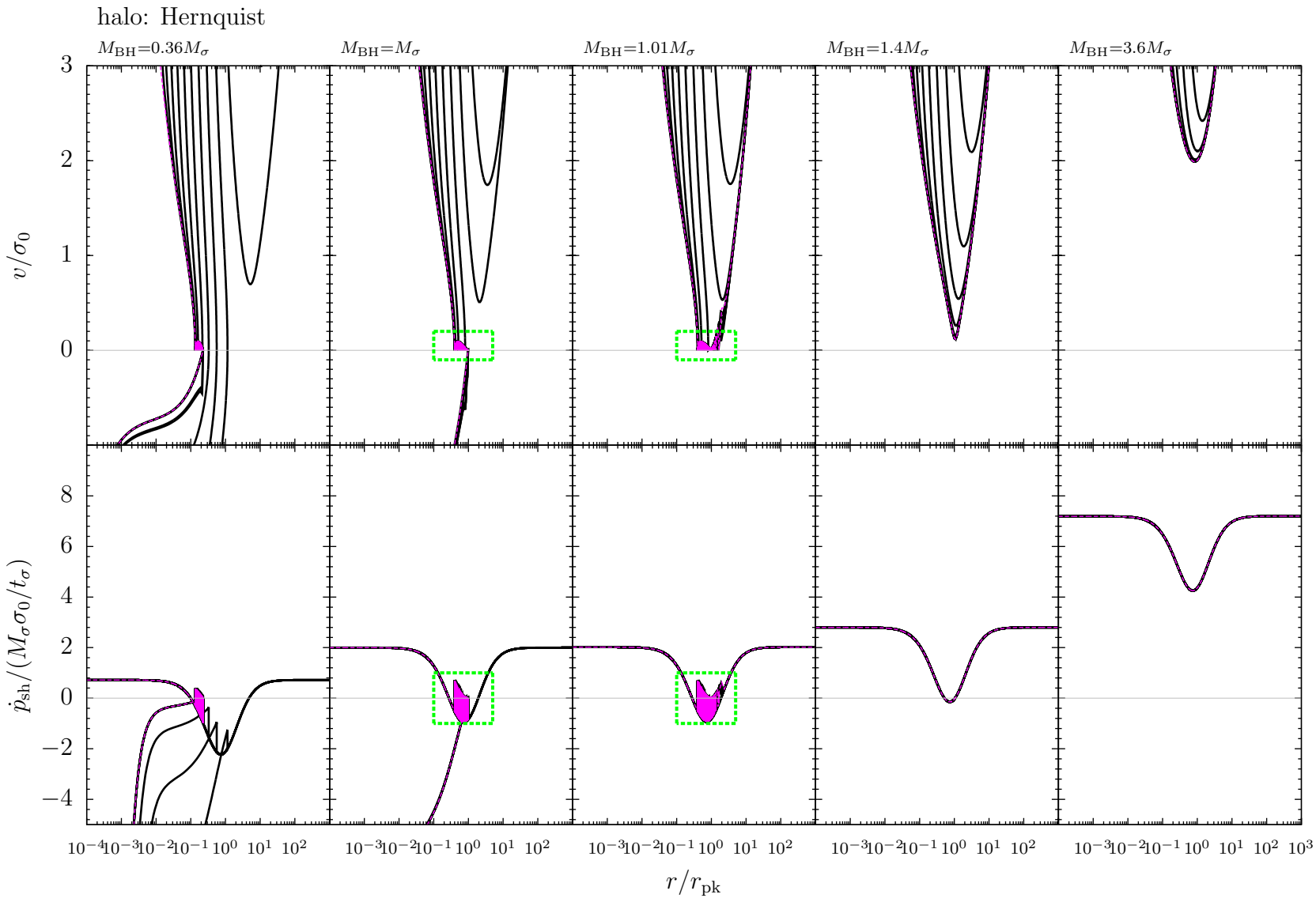

Figure 3.9: Shell velocity and momentum-flux versus radius for a momentum-driven shell launched by a steady wind in a Hernquist halo. Each black curve corresponds to a numerical solution with initial momentum at logarithmic intervals within the range: $0.001 < C < 1000$ (increasing from left to right of the figure), and the magenta curves are the $C = 0$ numerical solutions. The region within green boxes are displayed in greater detail in Figure 3.10.

Necessary and Sufficient SMBH Masses

If a shell never stalls then the critical SMBH mass which defines this case is a sufficient condition for the escape of a shell. McQuillin & McLaughlin (2012) obtained a sufficient mass for the escape of momentum-driven shells within non-isothermal haloes. This was obtained by considering the mass $\widetilde{M}_{\rm crit}$ and radius $x_{\rm crit}$ where the acceleration and the velocity of the shell are both zero (McQuillin & McLaughlin 2012). This critical mass was then maximised (with the corresponding radius $x_{\rm c,max}$) for any initial momentum (see Section 1.5), and was shown to be

$$\widetilde{M}_{\rm crit}^{\rm max} \simeq \frac{m^2(x_{\rm c,max})}{x_{\rm c,max}^2}\left[1-\frac{1}{\widetilde{M}_{\rm pk}}\frac{m(x_{\rm c,max})}{x_{\rm c,max}^2}\right]^{-1} \qquad (\widetilde{M}_{\rm pk}\gg 1)\,, \tag{3.64}$$

where $x_{\rm c,max}$ is given by:

$$\left.\frac{d\ln m}{d\ln x}\right|_{x=x_{\rm c,max}} \simeq 1+\frac{1}{2\widetilde{M}_{\rm pk}}\frac{1}{x_{\rm c,max}}\left.\frac{dm}{dx}\right|_{x=x_{\rm c,max}}. \tag{3.65}$$

Figure 3.10 shows the confinement behaviour for two solutions: one of which is below the necessary mass as given by equation (3.64), and the other is above this mass. The top panels show shell velocity and the bottom panels show the force on the shell. As introduced for the SIS case the shell exhibits repeated stalls which arise from the release of ambient pressure at a stall point causing the total force to become positive and causing the shell to recollide with the ambient medium. Unlike the SIS case the force curve in the absence of ambient pressure (shown in blue) does not tend to a constant, instead it descends into a minimum (at $x = 1$) and then increases beyond this point. Therefore for masses below the sufficient mass in the absence of ambient pressure this minimum drops below zero, and the shell's acceleration is negative even when the ambient pressure shuts off so it must infall (red curve). For SMBH masses above the sufficient mass the force curve in the absence of ambient pressure is always positive so the shell remains pressure confined until it becomes possible to accelerate (beyond the minimum) in the absence of ambient pressure.

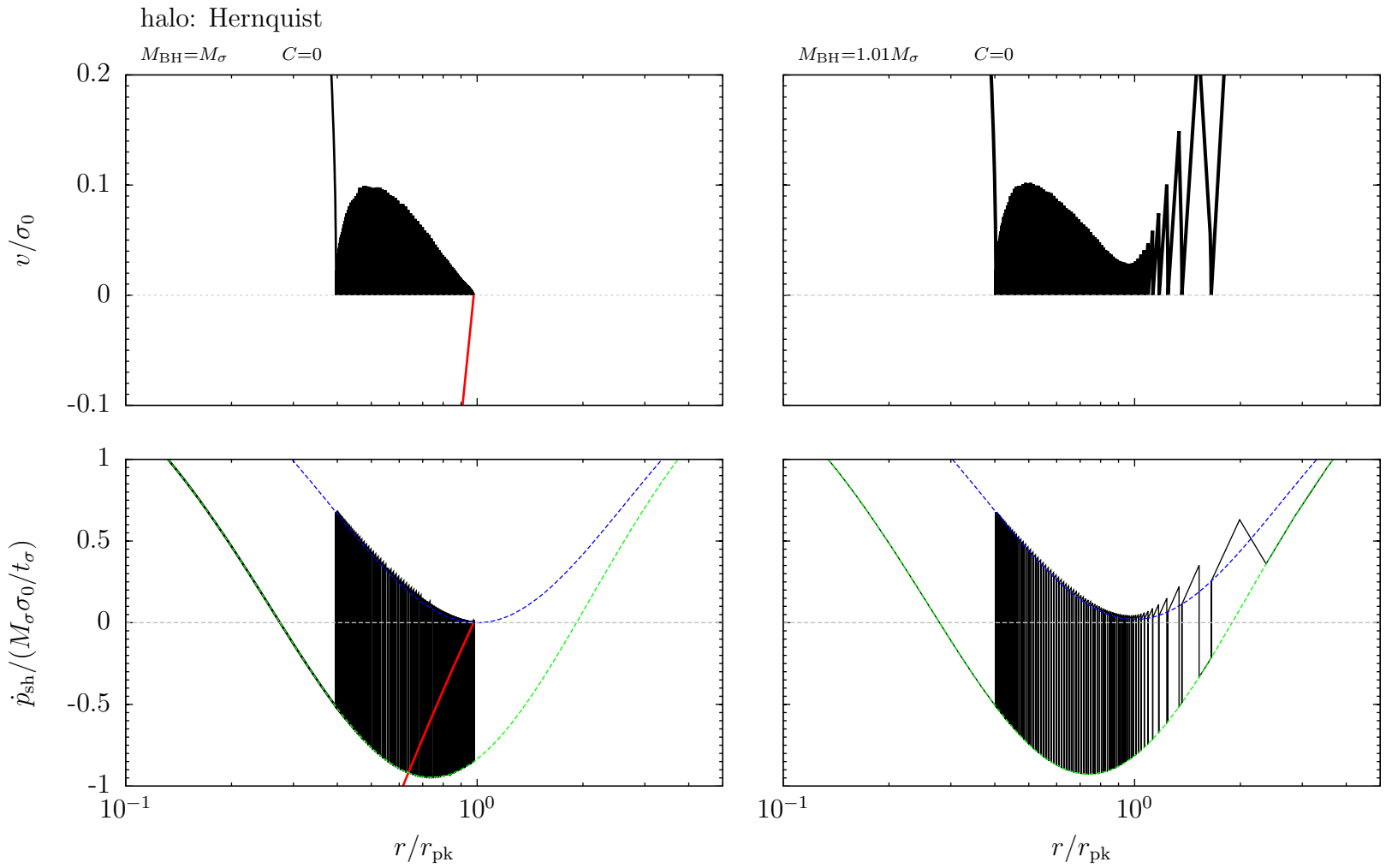

Figure 3.10: Stalling shell velocity and momentum-flux versus radius for a momentum-driven shell launched by a steady wind in a Hernquist halo. The solutions shown are taken from within the green boxes in Figure 3.9. The red curves show infalling solutions, the blue curves shows the force on the shell in the absence of ambient pressure, and the green curves shows the force on the shell subject to ambient pressure.

The necessary and sufficient masses with and without ambient pressure have been found numerically for a range of $\widetilde{M}_{\rm pk}$ for the case that $C = 0$, and are shown in Figure 3.11. If the ambient pressure is included then the SMBH mass which is necessary for escape (i.e. the shell may stall before escaping) is equal to the sufficient SMBH mass for which the shell never stalls in the absence of ambient pressure. The sufficient SMBH mass permitting the shell to reach large radii without ever stalling is approximately 40% larger than the necessary mass, and therefore 40% larger than the sufficient mass in the absence of ambient pressure. It is important to note while shells driven by winds from the necessary mass value formally go on to reach large radii they only do so after an extended period ($100t_\sigma$) of stalling.

Effects of SMBH Gravity

As mentioned earlier, in the Hernquist halo and any other non-isothermal halo with mass scaling like $\widetilde{M}_{\rm DM} \propto x^2$ for $x \ll 1$ the SMBH gravity scales with the wind at small radii. Because of this the shells in the Hernquist halo do not require an initial momentum to overcome the gravity of the SMBH. This is shown by the lack of an upper $\widetilde{v} = 0$ curve in Figure 3.12 which displays the numerical solutions to equation (3.53) in terms of $M_{\rm BH}$ for a range of SMBH masses and initial momenta. The necessary and sufficient masses for $C = 0$ are highlighted within this figure.

3.2.4 Momentum-Fluxes of Momentum-Driven Shells

By their very nature momentum-driven shells which are subject only to gravity and ambient pressure cannot have a force which exceeds that supplied by the driving wind: $\dot{p}_w = \dot{M}_w v_w$. This is evident by simply normalising the equation of motion (3.25) to the driving force of the wind, which in the adopted units is $2\widetilde{M}_{\rm BH}$:

$$\frac{\dot{p}_{\rm sh}}{\dot{M}_w v_w} = 1 - \frac{2\pi x^2 \widetilde{P}_g(x)}{\widetilde{M}_{\rm BH}} - \frac{h(x)m(x)}{x^2}\left[\frac{1}{\widetilde{M}_{\rm pk}} + \frac{m(x)}{\widetilde{M}_{\rm BH}}\right], \tag{3.66}$$

This so-called momentum-boost can never exceed unity for momentum-driven shells. This is not the case for energy-driven shells (see Chapter 2). The dynamics of wind-

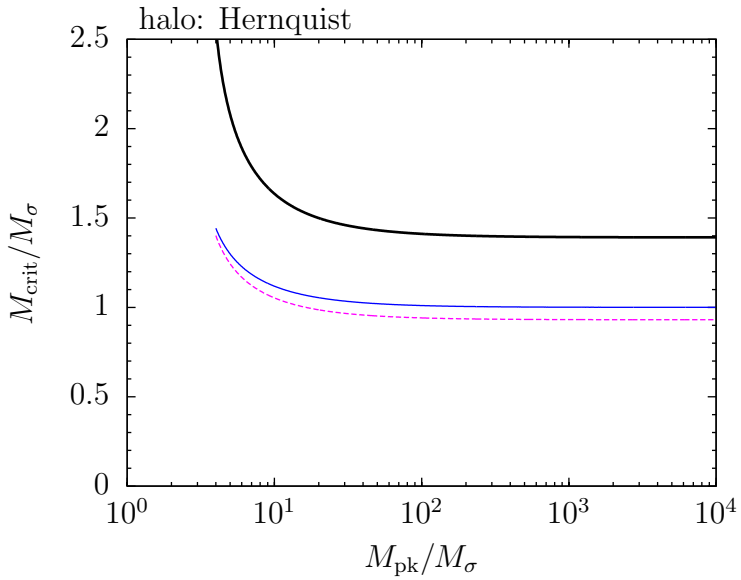

Figure 3.11: Necessary and sufficient masses permitting escape of a momentum-driven shell within a Hernquist halo versus halo mass at the radius where the circular speed curve peaks. The black curve gives the sufficient SMBH mass required for a shell subject to ambient pressure to never stall. The blue curve gives both the necessary SMBH mass required for a shell subject to ambient pressure to reach large radii, and the sufficient SMBH mass required for a shell to never stall in the absence of ambient pressure. The magenta dashed curve gives the necessary SMBH mass required for a shell to reach large radii in the absence of ambient pressure.

driven outflows in active galaxies can therefore be understood by knowing which of the driving regimes applies, and this can be achieved by measuring the momentum-boosts of outflows in active galaxies. For outflows $\dot{M}v$ is used as a proxy for momentum-flux, where $\dot{M} = 4\pi r N v$ and N is the column density of the outflow. Hence, for the shell solutions it is useful to compare values of $\dot{M}_{\rm sh}v$ to the actual momentum-flux $\dot{p}_{\rm sh} = \dot{M}_{\rm sh}v + M_{\rm sh}dv/dt$.

The Singular Isothermal Sphere

Figure 3.13 compares $\dot{p}_{\rm sh}/\dot{M}_w v_w$ and $\dot{M}_{\rm sh}v/\dot{M}_w v_w$ for momentum-driven shells within

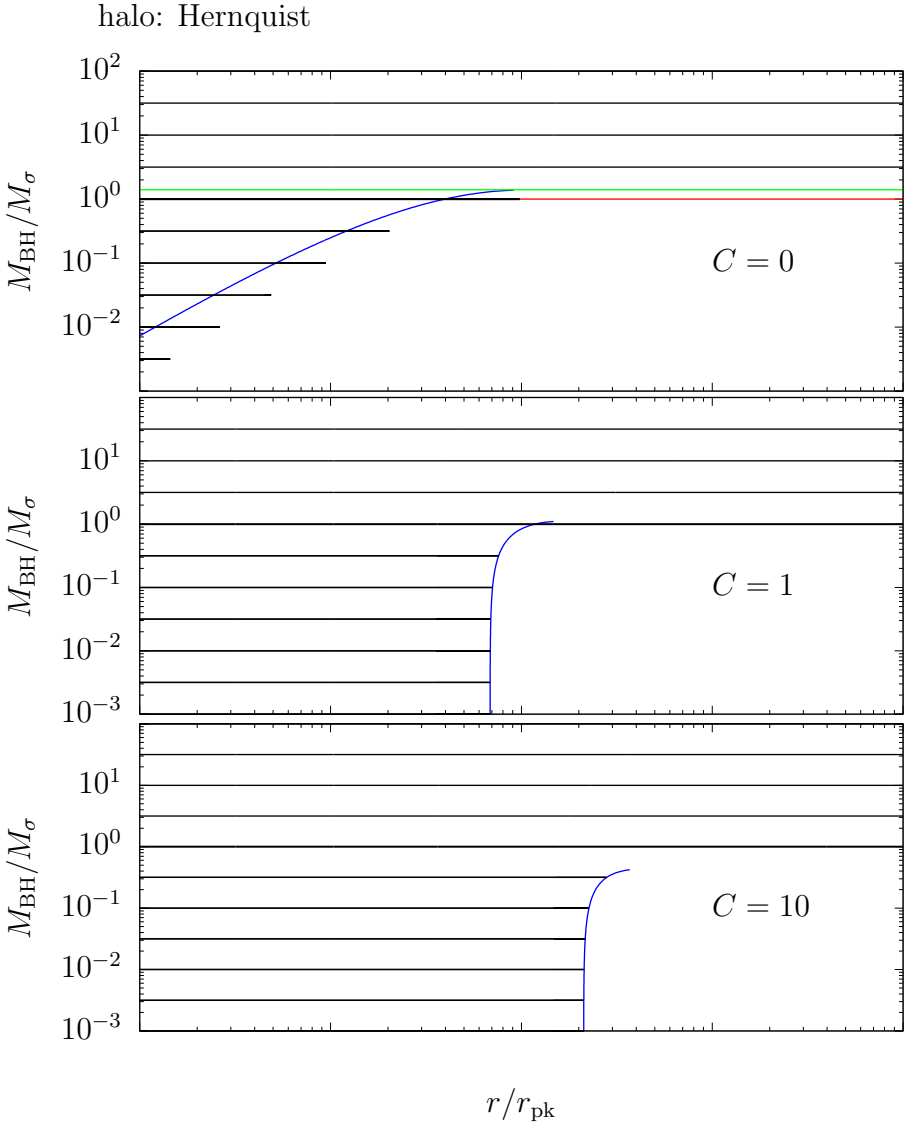

Figure 3.12: SMBH mass versus shell radius of momentum-driven shells in a Hernquist halo. Three initial momenta are considered: $C = 0$ (top), $C = 1$ (middle), and $C = 10$ (bottom). Shown as black curves are the numerical solutions to the equations of motion for a range of $\widetilde{M}_{\rm BH}$ with $\widetilde{M}_{\rm pk} = 4000$. The dashed black curve is the $\widetilde{M}_{\rm BH} = 1$ case. For $C = 0$ the solid red curve is the necessary mass required for escape, and the solid green curve is the sufficient mass required for a shell that never stalls. The blue curves are the numerically determined radii at which the shells first stall.

an SIS halo driven by winds from three different SMBH masses; each with three different values of initial momentum $C = 0.01, 100, 10^6$. Any infall behaviour is excluded

from Figure 3.13. It can be seen that unlike $\dot{p}_{\rm sh}$ the value of $\dot{M}_{\rm sh}v$ is sensitive to the initial momentum, with larger initial momenta increasing the difference between the two quantities at smaller radii. For these solutions $\dot{M}_{\rm sh}v$ is always positive because the shells are always moving outward and always gaining mass. The momentum-flux $\dot{p}_{\rm sh}$ is negative at small radii as a result of the deceleration experienced due to the SMBH gravity. At large radii the shells tend to a constant terminal velocity and therefore $\dot{M}_{\rm sh}v \rightarrow \dot{p}_{\rm sh}$, with larger initial momentum pushing this equality to larger radii.

The quantity $\dot{M}_{\rm sh}v$ serves as a suitable proxy for $\dot{p}_{\rm sh}$ at large radii. This range in radii does coincide with the typical scales $r \sim 10 - 100 r_\sigma \simeq 0.5 - 5$ kpc (for $\sigma_0 = 200$ km s^{-1}) at which large-scale outflows are observed. The quantity $\dot{M}_{\rm sh}v$ for momentum-driven shells is boosted relative to that of the wind at small radii, but this is due to the shell receiving a large initial impulse at early times. At large radii there is no boosting of $\dot{M}_{\rm sh}v$ as it tends to $\dot{p}_{\rm sh}$ which must be less than unity according to equation (3.66). At all radii in the SIS halo the gravitational force of the dark matter and the force of the ambient pressure are constant (see equation 3.31), and therefore at large radii (away from the SMBH) this results in a constant reduction in the terminal momentum-flux of the shell:

$$\frac{\dot{M}_{\rm sh}v}{\dot{M}_w v_w} \rightarrow \frac{\dot{p}_{\rm sh}}{\dot{M}_w v_w} = 1 - \frac{M_{\rm BH,crit}}{M_{\rm BH}} \qquad (x \gg 1; \widetilde{M}_{\rm BH} > \widetilde{M}_{\rm crit}) \,, \tag{3.67}$$

where $M_{\rm BH,crit}$ is given by equation (3.35) which is the SMBH mass required to reach large radii. The constancy of the dark matter and ambient pressure forces is what leads to the momentum-boost for a momentum-driven shell at large radii in an SIS halo to always be less than unity.

Hernquist Halo

Figure 3.14 compares $\dot{p}_{\rm sh}/\dot{M}_w v_w$ and $\dot{M}_{\rm sh}v/\dot{M}_w v_w$ for momentum-driven shells in a Hernquist halo driven by winds from three SMBH masses, each with three different values of initial momentum $C = 0, 100, 10^6$. For the Hernquist halo the density profile is shallower at small radii than the SIS, and since it is assumed that the gas traces the dark matter directly this means that the mass of the shell is much smaller at small

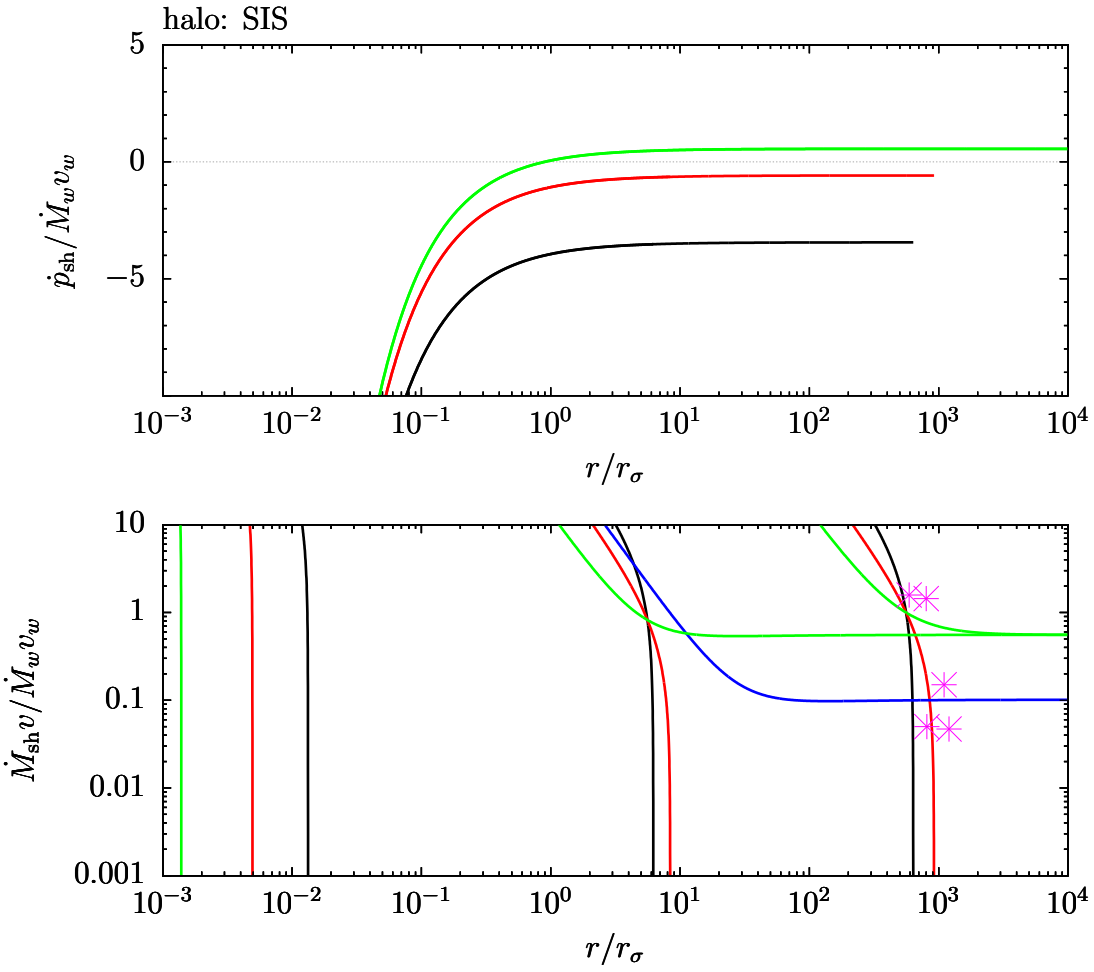

Figure 3.13: The momentum-fluxes of momentum-driven shells within an SIS halo normalised to the momentum-flux of the wind versus shell radius. The top panel shows the normalised momentum-flux $\dot{p}_{\rm sh}/\dot{M}_w v_w$, and the bottom panel shows the quantity $\dot{M}_{\rm sh} v/\dot{M}_w v_w$. The black curves have $\widetilde{M}_{\rm BH} = 0.36$, the red curves have $\widetilde{M}_{\rm BH} = 1.01$, and the green curves have $\widetilde{M}_{\rm BH} = 3.6$. For each value of $M_{\rm BH}$ there are three values of initial momentum: $C = 0.01, 10, 10^6$ (left, middle, and right groupings respectively). Shown in magenta are several observational datapoints taken from Table 3.1 (Rupke, Gültekin & Veilleux 2017) which are approximately consistent with momentum-driving. The blue curve is the solution with the SMBH mass $M_{\rm BH} = 1.11 M_{\rm BH,crit}$ chosen to intercept the plotted points.

radii in a Hernquist halo. Because of this the outward force of the wind dominates the gravitational force of the SMBH, and at small radii the momentum-flux $\dot{p}_{\rm sh}$ tends to that of the wind: $\dot{M}_w v_w$. The shell only begins to accumulate gravitationally significant mass as the shell approaches $r_{\rm pk}$. It is around $r_{\rm pk}$ that the gravitational force of the dark matter contributes strongly and negatively to the momentum-flux of the shell. The total mass of dark matter is finite, and therefore its gravitational force tends to zero as $r \to \infty$ causing the normalised momentum-flux to tend to unity also at large radii. However, the range of radii at which outflows are observed is less than $r_{\rm pk} \sim 50$ kpc (for a Milky Way sized halo), which is the only region where $\dot{M}_{\rm sh} v$ approximates the momentum-flux well, and only in the case that the initial momentum of the shell is small.

The value of $\dot{M}_{\rm sh} v$ at small radii with $C = 0$:

$$\begin{aligned} \frac{\dot{M}_{\rm sh} v}{\dot{M}_w v_w} &= \frac{4}{3}\left(1 - \frac{4}{\widetilde{M}_{\rm pk}}\right) && (x \ll 1; C = 0) \\ &\sim \frac{4}{3} && (x \ll 1; C = 0; \widetilde{M}_{\rm pk} \gg 1)\,. \end{aligned} \tag{3.68}$$

Observational Implications

Overall for momentum-driven shells the momentum-fluxes for small initial momenta are approximated well by $\dot{M}_{\rm sh} v$ at large radii $r \gg r_\sigma$ in the SIS halo, and at small radii $r \ll r_{\rm pk}$ in the Hernquist halo. Observations of outflows are typically made within the range $r_\sigma \ll r \ll r_{\rm pk}$, and therefore the measured values of $\dot{M} v$ are reflective of the actual momentum-flux if the outflow is suitably described by a momentum-driven shell. Outflows have been observed at large radii with momentum-boosts which are consistent with momentum-driven shells (Rupke, Gültekin & Veilleux 2017). Several of these outflows are reproduced in Table 3.1, and are consistent with momentum-driving as shown in Figures 3.13 and 3.14. However, it is important to note that the typical values of momentum-boosts for outflows are much more commonly found to be far in excess of unity (Cicone et al. 2014; Tombesi et al. 2015), and there is a large amount of theoretical support for a transition to energy-driving before reaching large radii (Faucher-Giguère & Quataert 2012).

Name	r (kpc)	$\log(\dot{M}v/L_{\rm AGN}/c)$	$\dot{M}v/(L_{\rm AGN}/c)$	σ (km s^{-1})	$\log M_{\rm BH}/M_\odot$
F07599+6508	8.1	-1.25	0.05	-	8.59
F13218+0552	12	-1.33	0.047	-	8.55
F13342+3932	11	-0.82	0.15	-	9.12
PG1613+658	8	0.16	1.44	-	8.34
F21219−1757	5.9	0.20	1.58	121	8.61

Table 3.1: Momentum-boost data for momentum-driven shells from Rupke, Gültekin & Veilleux (2017).

3.3 Energy-Driven Outflows

In the energy-driven regime the shell of shocked ambient medium is driven by the expansion of the hot shocked wind region (see Section 2.2.3). The equation of motion for the shell is still equation (3.17), but the outward driving pressure on the shell P is given by the energy equation for the hot shocked wind. This equation states that the time rate of change of energy in the hot shocked wind is equal to the rate of mechanical energy input by the wind minus losses due to PdV work and work done against gravity. The rate of mechanical energy input by the wind is given by (McQuillin & McLaughlin 2013):

$$\dot{E}_w = \frac{1}{2}\dot{M}_w v_w^2 = \tau \frac{L_{\rm Edd} v_w}{2c} \tag{3.69}$$

and the amount of this energy transferred to the wind is given by the energy equation:

$$\frac{d}{dt}\left[\frac{4}{3}\pi r^3 \frac{P}{\gamma - 1}\right] = \dot{E}_w - P\frac{d}{dt}\left[\frac{4}{3}\pi r^3\right] - \frac{GM_{\rm sh}(r)v}{r^2}\left[M_{\rm BH}(t) + M_{\rm DM}(r)\right] . \tag{3.70}$$

When normalised to the characteristic quantities given by equations (3.1) and (3.8) equation (3.70) becomes:

$$\frac{d}{d\widetilde{t}}\left[\frac{4}{3}\pi x^3 \frac{\widetilde{P}}{\gamma - 1}\right] = \widetilde{M}_{\rm BH}\widetilde{v}_w - 4\pi x^2 \widetilde{v}\widetilde{P} - \frac{2h(x)m(x)\widetilde{v}}{x^2}\left[\frac{\widetilde{M}_{\rm BH}(\widetilde{t})}{\widetilde{M}_{\rm pk}} + m(x)\right] . \tag{3.71}$$

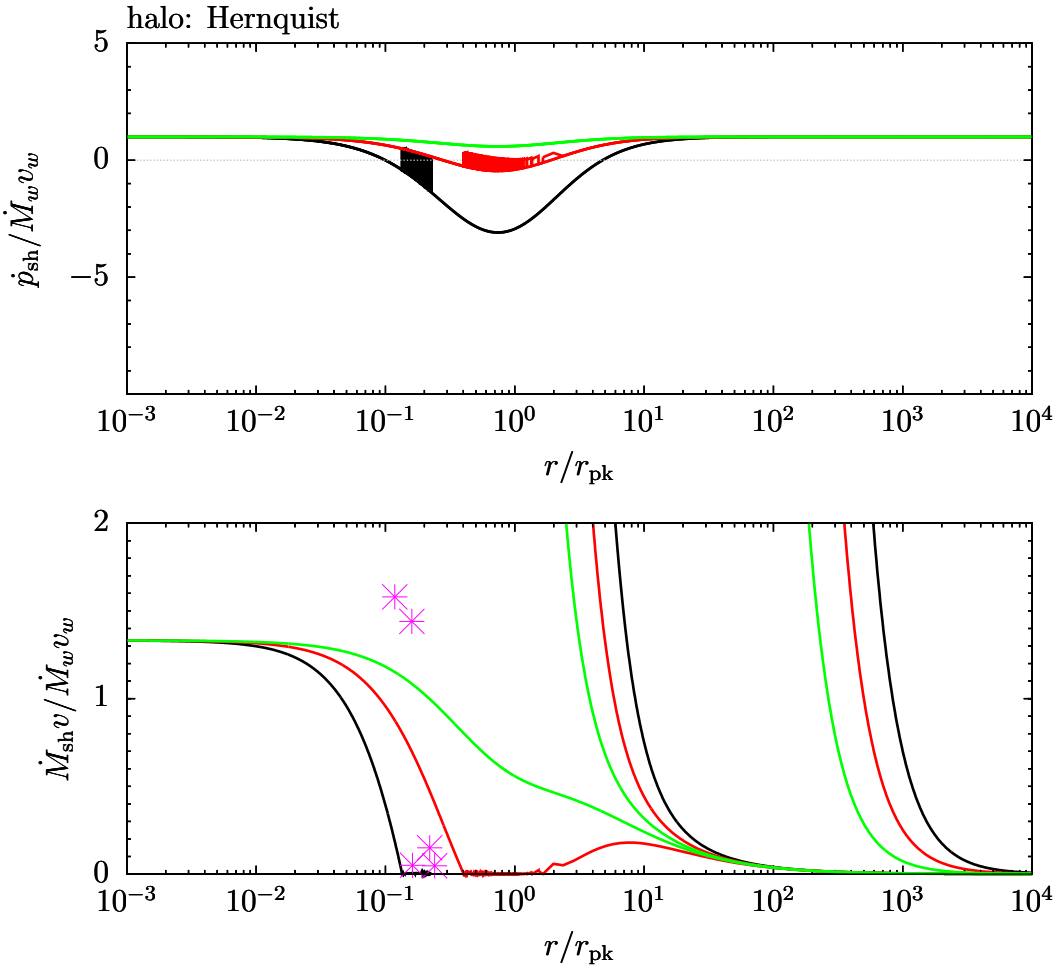

Figure 3.14: The momentum-fluxes of momentum-driven shells within a Hernquist halo normalised to the momentum-flux of the wind versus shell radius. The top figure shows actual normalised momentum-flux $\dot{p}_{\rm sh}/\dot{M}_w v_w$, and the bottom figure shows the quantity $\dot{M}_{\rm sh} v/\dot{M}_w v_w$. The green curves have $\widetilde{M}_{\rm BH} = 3.6$, the red curves have $\widetilde{M}_{\rm BH} = 1.01$, and the black curves have $\widetilde{M}_{\rm BH} = 0.36$. For each value of $\widetilde{M}_{\rm BH}$ there are three values of initial momentum: $C = 0, 100$ and $C = 10^6$.

Combining equation (3.71) with the normalised equation of motion for the shell (3.17) gives:

$$\begin{aligned}\frac{d^2}{d\widetilde{t}^{\,2}}\left[h(x)m(x)\widetilde{v}\right] &= -\frac{2\widetilde{v}}{x^2}\frac{d}{dx}\left\{h(x)m(x)\left[\frac{\widetilde{M}_{\rm BH}}{\widetilde{M}_{\rm pk}}+m(x)\right]\right\} \\ &+\frac{3(\gamma-1)\widetilde{M}_{\rm BH}\widetilde{v}_w}{x}-12\gamma\pi x\widetilde{v}\widetilde{P}_g(x)-4\pi x^2\widetilde{v}\frac{d\widetilde{P}_g}{dx} \\ &-(3\gamma-2)\frac{\widetilde{v}}{x}\frac{d}{d\widetilde{t}}\left[h(x)m(x)\widetilde{v}\right]-2(6\gamma-7)\frac{h(x)m(x)\widetilde{v}}{x^3}\left[\frac{\widetilde{M}_{\rm BH}}{\widetilde{M}_{\rm pk}}+m(x)\right].\end{aligned} \tag{3.72}$$

Equation (3.72) is to be solved numerically for the shell radius $x(\widetilde{t})$, momentum $m(x)\widetilde{v}$, and momentum-flux $d\left[m(x)\widetilde{v}\right]/d\widetilde{t}$. If the shell stalls and begins to infall then equation (3.72) is not used, unless the shell resumes outward motion and returns to its initial stall radius.

3.3.1 Infall

If a stall point $x_{\rm stall}$ is reached where $\widetilde{v}=0$, and if the acceleration $d\widetilde{v}/d\widetilde{t}$ is negative at $x_{\rm stall}$ then the shell begins to infall back into the region swept clear of gas. Assuming that the ambient pressure falls off quickly due to a rapidly infalling shell, then the equation of motion for the infalling shell at $x<x_{\rm stall}$ is:

$$\begin{aligned}h(x_{\rm stall})m(x_{\rm stall})\frac{d^2\widetilde{v}}{d\widetilde{t}^{\,2}} &= -\frac{2h(x_{\rm stall})m(x_{\rm stall})\widetilde{v}}{x^2}\frac{dm}{dx}+\frac{3(\gamma-1)\widetilde{M}_{\rm BH}v_w}{x} \\ &-\frac{(3\gamma-2)h(x_{\rm stall})m(x_{\rm stall})\widetilde{v}}{x}\frac{d\widetilde{v}}{d\widetilde{t}}-2(6\gamma-7)\frac{h(x_{\rm stall})m(x_{\rm stall})\widetilde{v}}{x^3}\left[\frac{\widetilde{M}_{\rm BH}}{\widetilde{M}_{\rm pk}}+m(x)\right].\end{aligned} \tag{3.73}$$

Equation (3.73) is to be solved in conjunction with equation (3.72) in order to obtain the shell radius x, momentum $m(x)\widetilde{v}$, and momentum-flux $d\left[m(x)\widetilde{v}\right]/d\widetilde{t}$ throughout its entire expansion and potential infall.

3.3.2 The Singular Isothermal Sphere

Equation of Motion

The equation of motion for an energy-driven shell propagating into an SIS can be obtained by using the expressions for $M_{\rm DM}(r)$ and $P_g(r)$ from Section 3.2.2 along with $h(x) \equiv 1$ and equation (3.72) to give:

$$\begin{aligned}\frac{d^2}{d\widetilde{t}^{\,2}}\left[x\widetilde{v}\right] = &-\frac{\widetilde{v}}{x^2}\left[\widetilde{M}_{\rm BH}+4x\right] + \frac{3(\gamma-1)\widetilde{M}_{\rm BH}\widetilde{v}_w}{x} - \frac{3\gamma(1+f_0)\widetilde{v}}{x} \\ &+ \frac{2(1+f_0)\widetilde{v}}{x} - (3\gamma-2)\frac{\widetilde{v}}{x}\frac{d}{d\widetilde{t}}\left[x\widetilde{v}\right] - 2(6\gamma-7)\frac{\widetilde{v}}{x^2}\left[\frac{\widetilde{M}_{\rm BH}}{2}+x\right].\end{aligned} \tag{3.74}$$

Asymptotics

In order to explore the early-time behaviour of equation (3.74) a power-law form for $x \propto \widetilde{t}^{\,q}$ can be considered. The only possible case for a shell to move outward at early times is when $q = 1/2$ and it starts with an initial constant momentum (the square of which will be continued to be denoted C for consistency). Therefore the radius of the shell at early times is:

$$x(\widetilde{t}) = \left(2\sqrt{C}\widetilde{t}\right)^{1/2} \qquad (\widetilde{t} \ll 1)\,, \tag{3.75}$$

where C is the (square of) the initial momentum. This is the same small radius solution which applied for the momentum-driven shell (equation 3.38). The velocity at early times is:

$$\widetilde{v}^2 = \frac{\sqrt{C}}{2\widetilde{t}} = \frac{C}{x^2} \qquad (\widetilde{t} \ll 1)\,. \tag{3.76}$$

At large radii the shell velocity tends to a constant $\widetilde{v}_\infty$. This was also the case for the momentum-driven shell in an SIS, and it is also the case for an energy-driven bubble in an SIS gas distribution in the absence of gravity (see equation 2.22 with $\alpha = 1$ and $p = 1$). This arises in each of these cases because the driving force, ambient pressure

force and the gravitational force are constant at all radii. Therefore, when the radially decreasing SMBH gravity is negligible the force on the shell tends to a constant, and hence the shell will always achieve a constant terminal velocity.

The Terminal Coasting Velocity and the Escape Speed

Taking the limit that $x \to \infty$ with equation (3.74) results in a large scale coasting velocity for the energy-driven shell which satisfies the cubic equation:

$$(3\gamma-2)\widetilde{v}_\infty^3+[2(6\gamma-5)+(3\gamma-2)(1+f_0)]\widetilde{v}_\infty = 3(\gamma-1)\widetilde{M}_{\rm BH}\widetilde{v}_w \qquad (\widetilde{t} \gg 1)\,. \quad (3.77)$$

A natural choice for this coasting velocity is the escape velocity for a truncated SIS halo: $v_{\rm esc} = 2\sigma_0$. This can be viewed as an escape condition for a shell which leads to the definition of a critical $M_{\rm BH}v_w$ combination that must be exceeded. Setting the velocity equal to this value ($\widetilde{v}_\infty = 2$) gives:

$$\widetilde{M}_{\rm BH}\widetilde{v}_w = \frac{4(4\gamma-3)}{\gamma-1} + \frac{2(3\gamma-2)(1+f_0)}{3(\gamma-1)} \qquad (\widetilde{v}_\infty = 2)\,. \quad (3.78)$$

The final term in equation (3.78) results from the inclusion of ambient pressure, and if this term is neglected then the result reduces to that obtained by McQuillin & McLaughlin (2013).

For $\gamma = 5/3$ the critical combination is required to be $\widetilde{M}_{\rm BH}\widetilde{v}_w = 22+3(1+f_0) \simeq 25.6$, or with units restored:

$$\left(\frac{M_{\rm BH}}{10^8 M_\odot}\right)\left(\frac{v_w}{c}\right) = 7.78\times10^{-2}\left(\frac{\sigma_0}{200\ {\rm km\ s^{-1}}}\right)^5\left(\frac{f_0}{0.2}\right)\tau^{-1}\,. \quad (3.79)$$

As mentioned in Section 1.5 McQuillin & McLaughlin (2013) used the value of $M_{\rm BH}v_w = 22M_\sigma\sigma_0$ with $M_{\rm BH}$ and σ values from a sample of now quiescent galaxies to infer the wind speeds they would have had during their active phase. This approach interprets the scatter in the $M_{\rm BH}-\sigma$ relation as a distribution of wind speeds. They found for their sample that the median wind speed was $v_w = 0.035c$. This result is changed minimally by the inclusion of ambient pressure.

The Fast and Slow Wind Limits

There are two limits to equation (3.77): the case of a 'fast wind' where the SMBH mass and wind speed combination is very large relative to $M_\sigma\sigma$, and a 'slow wind' where the inverse is true. In the limit of a fast wind the terminal coasting velocity is very large relative to σ_0 and therefore the cubic term in equation (3.77) dominates and the velocity tends to:

$$\widetilde{v}_\infty \to \left[\frac{3(\gamma-1)\widetilde{M}_{\rm BH}\widetilde{v}_w}{3\gamma-2}\right]^{1/3} \qquad (\widetilde{v} \gg \sigma_0,\ \widetilde{t} \gg 1)\,. \tag{3.80}$$

A similar result was obtained by Zubovas & King (2012) for the values $v_w \sim 0.1c$ and $M_{\rm BH} \sim M_\sigma$, i.e. a fast wind. Equation (3.80) can also be obtained if all gravitational and ambient pressure terms are omitted in the shell equation of motion (3.74), and therefore this limit can be interpreted as the case where the wind is strong enough that the effects of gravity and ambient pressure can be completely neglected.

For completeness consider the case of a 'slow wind' where the resultant coasting velocity is small compared to σ. In this case the linear term in equation (3.77) is dominant and therefore:

$$\widetilde{v}_\infty = \frac{3(\gamma-1)\widetilde{M}_{\rm BH}\widetilde{v}_w}{2(6\gamma-5)+(3\gamma-2)(1+f_0)} \qquad (\widetilde{v} \ll \sigma_0,\ \widetilde{t} \gg 1)\,. \tag{3.81}$$

Infall

Any $\widetilde{M}_{\rm BH}\widetilde{v}_w$ combination will result in a terminal coasting velocity. Whether or not the shell stalls before achieving large radii is determined by the value of the initial momentum. If the initial momentum is large enough then it is possible for a shell to attain $\widetilde{v}_\infty$ at large radii without stalling on its way out. However, for smaller values of initial momentum the shell is likely to stall. Numerical solutions to equation (3.74) for a wide range of parameters show that when a shell stalls at a radius $x_{\rm stall}$ that the acceleration is negative, and it will subsequently begin to infall.

Assuming that the shell infalls faster than the typical collapse speed σ_0 of the ambient gas, which was justified in the momentum-driven case, then it leaves the

undisturbed ambient gas situated at $x_{\rm stall}$, and the shell propagates back into the region swept clear of gas. In this case when the ambient gas pressure falls off the equation of motion becomes:

$$\begin{aligned} x_{\rm stall}\frac{d^2\widetilde{v}}{d\widetilde{t}^{\,2}} = &-\frac{2x_{\rm stall}\widetilde{v}}{x^2}+\frac{3(\gamma-1)\widetilde{M}_{\rm BH}v_w}{x}-\frac{(3\gamma-2)x_{\rm stall}\widetilde{v}}{x}\frac{d\widetilde{v}}{d\widetilde{t}} \\ &-2(6\gamma-7)\frac{x_{\rm stall}\widetilde{v}}{x^3}\left[\frac{\widetilde{M}_{\rm BH}}{\widetilde{M}_{\rm pk}}+m(x)\right] \qquad (x<x_{\rm stall})\,. \end{aligned} \tag{3.82}$$

By considering the energy equation for an infalling shell (3.70) it can be seen that because the shell velocity is negative all of the terms in the equation increase. This means that as the volume of the shell decreases the pressure of the shocked wind region increases, and the wind will also continuously deposit energy into the shocked wind. This means that the pressure force on the shell of swept-up ambient medium gets larger in time and with smaller radius as the shell infalls. This ultimately causes the shell to stall again and begin to move back out. When the shell encounters the ambient medium again the force is suddenly decreased. This can cause the shell to stall again and lead to another period of infall. This behaviour will repeat until the time increasing pressure force of the shocked wind region exceeds the radially dependent inward gravitational forces, and the shell can cease stalling and move out to large radii. It appears then that an energy-driven shell cannot fall back to the SMBH, and indeed no numerical solution to equation (3.74) falls back to $x = 0$.

Numerical Solutions

The shell radii x and velocities $\widetilde{v}$ obtained by numerically integrating equation (3.74) are presented against time $\widetilde{t}$ in Figure 3.15. The shell velocities and momentum-fluxes are shown against radius in Figure 3.16. A single value was chosen for the wind speed for the solutions shown: $\widetilde{v}_w = 45$ which is the median wind speed $v_w = 0.03c$ obtained by McQuillin & McLaughlin (2012) normalised to $\sigma_0 = 200$ km s^{-1}. Three SMBH mass values are shown in Figures 3.15 and 3.16: $\widetilde{M}_{\rm BH} = 0.06, 0.14, 0.49$. These values give the SMBH mass - wind speed combinations: $\widetilde{M}_{\rm BH}\widetilde{v}_w = 2.7, 6.3, 22$ which lead to

terminal velocities $\widetilde{v}_\infty \sim 0.5, 1, 2$ respectively as given by equation (3.78) in the absence of ambient pressure. The solutions were obtained for a range of initial momentum values in logarithmic intervals between: $C = 10^{-6} - 10^{6}$, but for clarity only four values of initial momentum are displayed: $C = 0.01, 2.56, 100, 10^{6}$. The velocity fields for the case that ambient pressure is neglected: $\widetilde{P}_g(x) = 0$ are also included in Figures 3.15 and 3.16 for comparison.

These solutions show that there are two outcomes for energy-driven shells: one is that the shell reaches large radii and acquires its coasting velocity without ever stalling, and the other is that it reaches large radii after stalling multiple times. This second outcome can be broadly separated into two outcomes: one where the shell stalls due to the gravity of the dark matter halo or ambient pressure, and the other where the shell stalls due to the gravity of the SMBH. The stalls which occur due to the gravity of the SMBH broadly represent a new type of solution which corresponds to a gravitationally confined, or pressure-supported shell. The source of this confinement is primarily gravitational as shown by turning off the ambient pressure in both figures. Unlike the momentum-driven case where the shell was supported by the ram pressure of the wind, in the energy-driven case the shell is always supported against infall by its thermal pressure.

It can be seen that there are two types of gravitational confinement occurring. The first is the very significant confinement due to the SMBH gravity. This occurs for small initial momenta and is most extreme for larger SMBH masses. Such shells can end up confined by the SMBH gravity for very long periods ($t \gg t_\sigma$), and repeatedly stall at an approximately finite radius (not included in Figures 3.15 and 3.16 for clarity). Away from the SMBH the dark matter gravity can cause the shell to stall, and in this case the initial momentum has little impact on the nature of the stall at large radii except in simply determining where it occurs. The SMBH mass determines the behaviour at the stall point, and in this case the small $M_{\rm BH}$ values lead to increased instances of stalling.

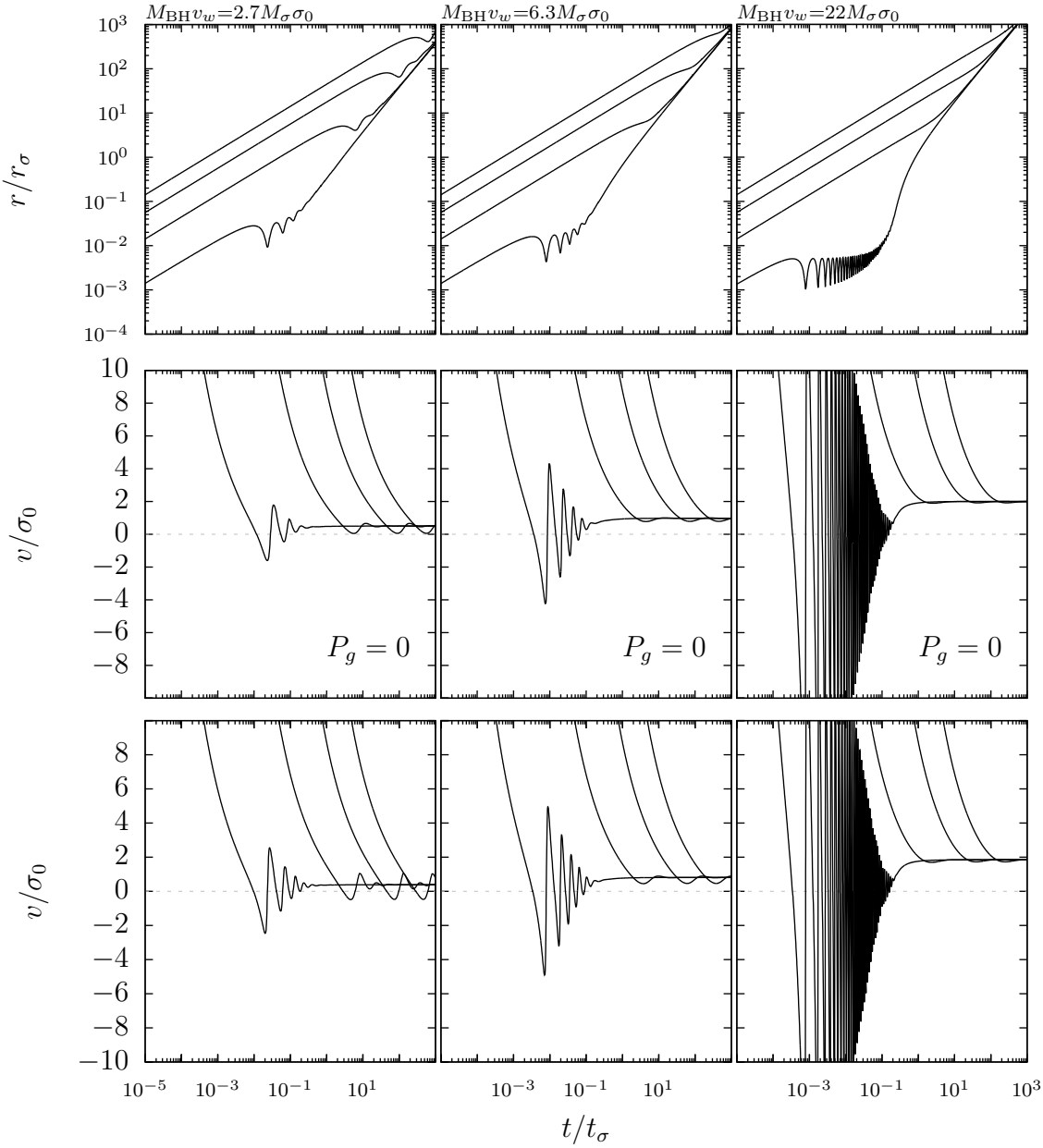

Figure 3.15: Shell radii (top) and velocities (middle and bottom) of energy-driven shells propagating within an SIS halo. For the top and bottom panels which include ambient pressure the gas fraction is set to $f_0 = 0.2$. Three combinations of SMBH mass and wind speed are considered: $\widetilde{M}_{\rm BH}\widetilde{v}_w = 2.7$ (left), 6.3 (middle), and 22 (right). The time scale is $t_\sigma \simeq 2.5 \times 10^5$ yr, and the radius scale is $r_\sigma \simeq 50$ pc for a velocity dispersion of $\sigma_0 = 200$ km s^{-1}. Four values of initial momentum are shown: $C = 0.01, 2.56, 100, 10^6$, which increase from bottom to top (uppermost panel) and from left to right (lower panels).

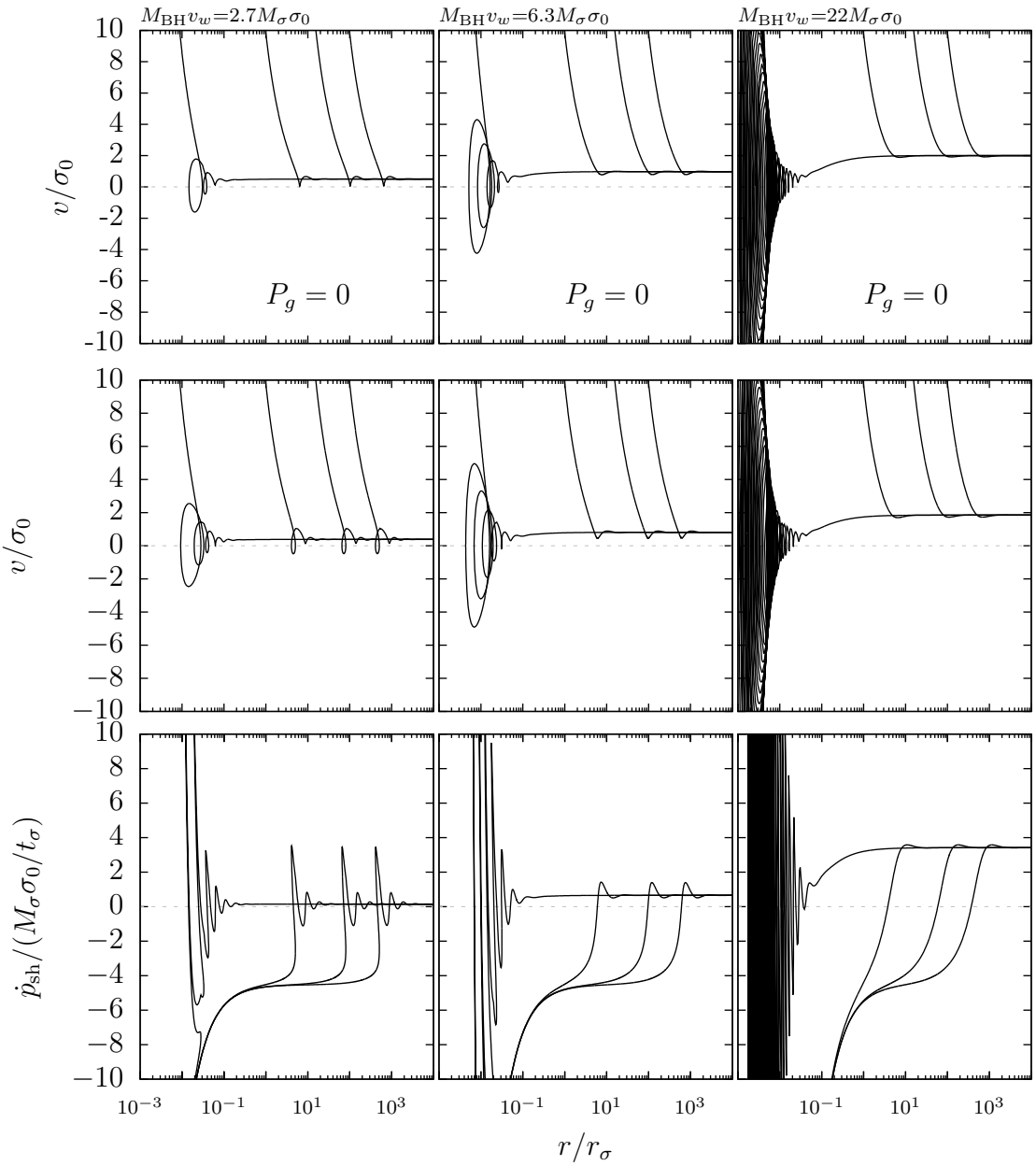

Figure 3.16: Shell velocities (top and middle) and momentum-fluxes (bottom) versus radius of energy-driven shells propagating within an SIS halo. For the panels which include ambient pressure the gas fraction is set to $f_0 = 0.2$. Three combinations of SMBH mass and wind speed are considered: $\widetilde{M}_{\rm BH}\widetilde{v}_w = 2.7$ (left), 6.3 (middle), and 22 (right). The radius scale is $r_\sigma \simeq 50$ pc for a velocity dispersion of $\sigma_0 = 200$ km s^{-1}. Four values of initial momentum are shown: $C = 0.01, 2.56, 100, 10^6$ (from left to right respectively).

3.3.3 Hernquist Halo

Using the expressions for $M_{\rm DM}(r)$ and $P_g(r)$ from Section 3.2.3, and with $h(x) \equiv 1$ equation (3.72) becomes:

$$\begin{aligned}\frac{d^2}{d\widetilde{t}^2}\left[\frac{4x^2}{(1+x)^2}\widetilde{v}\right] &= -\frac{2\widetilde{v}}{x^2}\frac{d}{dx}\left\{\frac{4x^2}{(1+x)^2}\left[\frac{\widetilde{M}_{\rm BH}}{\widetilde{M}_{\rm pk}}+\frac{4x^2}{(1+x)^2}\right]\right\}+\frac{3(\gamma-1)\widetilde{M}_{\rm BH}\widetilde{v}_w}{x}\\ &-192\gamma(1+f_0)x\widetilde{v}\left[\ln\left(1+\frac{1}{x}\right)-\frac{2x(3x(2x+7)+26)+25}{12(1+x)^4}\right]\\ &+\frac{64x\widetilde{v}(1+f_0)}{(1+x)^5}-(3\gamma-2)\frac{\widetilde{v}}{x}\frac{d}{d\widetilde{t}}\left[\frac{4x^2}{(1+x)^2}\widetilde{v}\right]-\frac{8(6\gamma-7)\widetilde{v}}{x(1+x)^2}\left[\frac{\widetilde{M}_{\rm BH}}{\widetilde{M}_{\rm pk}}+\frac{4x^2}{(1+x)^2}\right]\end{aligned} \tag{3.83}$$

In order to move outward the shell must begin with nonzero initial momentum at $\widetilde{t}=0$. This results in the early time shell radius:

$$x(\widetilde{t}) = \left(\frac{3\sqrt{C}\widetilde{t}}{4}\right)^{1/3} \qquad (\widetilde{t} \ll 1;\, C>0)\,, \tag{3.84}$$

and early time shell velocity:

$$\widetilde{v} = \frac{1}{3}\left(\frac{3\sqrt{C}\widetilde{t}^{\,-2}}{4}\right)^{1/3} = \frac{\sqrt{C}}{4x^2} \qquad (\widetilde{t} \ll 1;\, C>0)\,. \tag{3.85}$$

Both of these equations are the same as those obtained for the momentum-driven shell at early times (equations 3.56 and 3.58). The momentum-flux at early times is zero because the initial momentum is the constant value $\sqrt{C}$.

At late times the shell radius tends to:

$$x(\widetilde{t}) = \sqrt{\frac{2(\gamma-1)\widetilde{M}_{\rm BH}\widetilde{v}_w\widetilde{t}^{\,3}}{9\gamma-7}} \qquad (\widetilde{t} \gg 1)\,, \tag{3.86}$$

and the velocity:

$$\widetilde{v} = \sqrt{\frac{(\gamma-1)\widetilde{M}_{\rm BH}\widetilde{v}_w\widetilde{t}}{2\gamma-14/9}} = \left[\frac{3(\gamma-1)\widetilde{M}_{\rm BH}\widetilde{v}_w x}{4\gamma-28/9}\right]^{1/3} \qquad (\widetilde{t} \gg 1)\,. \tag{3.87}$$

The momentum-flux at late times is

$$\frac{d}{d\widetilde{t}}\left[m(x)\widetilde{v}\right] = 2\sqrt{\frac{(\gamma-1)\widetilde{M}_{\rm BH}\widetilde{v}_w}{(2\gamma-14/9)\widetilde{t}}} = \frac{4}{3}\left[\frac{3(\gamma-1)\widetilde{M}_{\rm BH}\widetilde{v}_w}{4\gamma-28/9}\right]^{2/3} x^{-1/3} \qquad (\widetilde{t} \gg 1)\,. \tag{3.88}$$

If the shell stalls at a radius $x_{\rm stall}$, and the acceleration at $x_{\rm stall}$ is negative then the shell will begin to infall. Assuming that the infall timescale is much shorter than the collapse time of the ambient gas, then the ambient gas remains at $x_{\rm stall}$ while the shell infalls. The equation of motion for the infalling shell is:

$$\frac{4x_{\rm stall}^2}{(1+x_{\rm stall})^2}\frac{d^2}{d\widetilde{t}^2}\left[\widetilde{v}\right] = -\frac{64\widetilde{v}x_{\rm stall}^2}{x(1+x_{\rm stall})^2}\left[\frac{1}{(1+x)^3}\right] + \frac{3(\gamma-1)\widetilde{M}_{\rm BH}\widetilde{v}_w}{x}$$
$$-(3\gamma-2)\frac{4\widetilde{v}x_{\rm stall}^2}{x(1+x_{\rm stall})^2}\frac{d\widetilde{v}}{d\widetilde{t}} - \frac{8(6\gamma-7)\widetilde{v}x_{\rm stall}}{x^3(1+x_{\rm stall})^2}\left[\frac{\widetilde{M}_{\rm BH}}{\widetilde{M}_{\rm pk}} + \frac{4x^2}{(1+x)^2}\right]. \tag{3.89}$$

As described in the previous section for the SIS halo the volume of the shell decreases as the shell infalls which causes the pressure in the shocked wind region to increase. This increase in pressure will lead to the shell stalling during infall and resuming its outward motion. Because the outward force has the same scaling as the SMBH gravity in a Hernquist halo this means that energy-driven shells do not become pressure confined at small radii.

The shell radii x and velocities $\widetilde{v}$ of energy-driven shells propagating within a Hernquist halo are presented against time in Figure 3.17. The shell velocities and momentum-fluxes are shown against radius in Figure 3.18. These solutions were obtained by numerically integrating equation (3.83), and also equation (3.89) for when the shell infalls. For the solutions shown the single value of $\widetilde{v}_w = 45$ was again chosen for the wind speed (see Section 3.3.2 for motivation). Using the SMBH values $\widetilde{M}_{\rm BH} = 0.01, 0.06, 0.49$ leads to the SMBH mass - wind speed combinations $\widetilde{M}_{\rm BH}\widetilde{v}_w = 0.45, 4.7, 22$. Three values of initial momentum are selected to reflect the range of shell behaviour: $C = 10^{-8}$ shown in magenta, $C = 1$ shown in red, and $C = 100$ shown in black. Also shown in both figures are the velocity fields in the absence of ambient pressure for comparison.

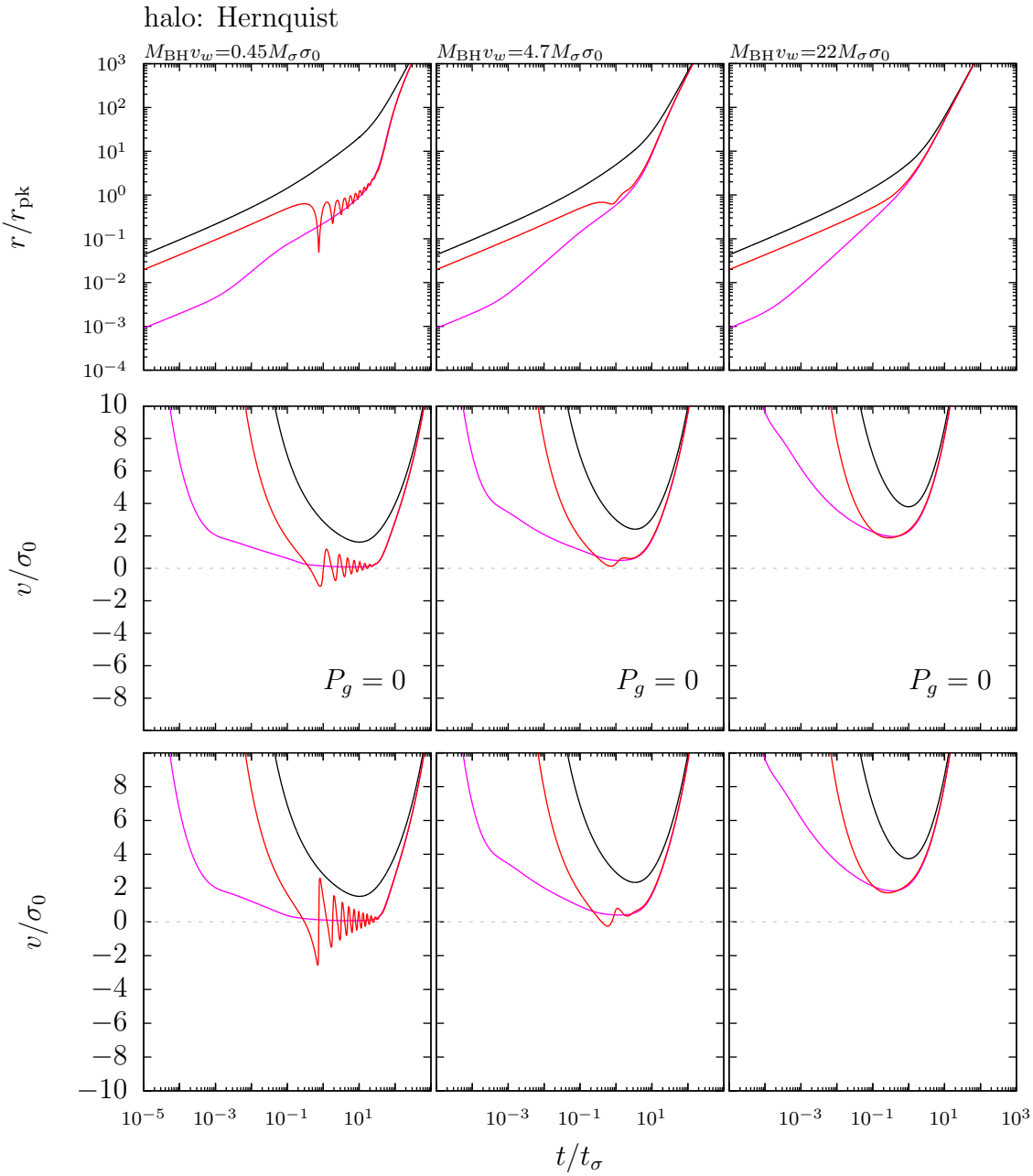

Figure 3.17: Shell radii (top) and velocities (middle and bottom) of energy-driven shells propagating within a Hernquist halo. For the top and bottom panels which include ambient pressure the gas fraction is set to $f_0 = 0.2$. Three combinations of SMBH mass and wind speed are considered: $\widetilde{M}_{\rm BH}\widetilde{v}_w = 0.45$ (left), 2.7 (middle), and 22 (right). The time scale is $t_\sigma = 2.5 \times 10^8$ yr, and the radius scale is $r_{\rm pk} \simeq 50$ kpc for a velocity dispersion of $\sigma_0 = 200$ km s^{-1}. Three values of initial momentum are shown: $C = 10^{-8}$ shown in magenta, $C = 1$ shown in red, and $C = 100$ shown in black.

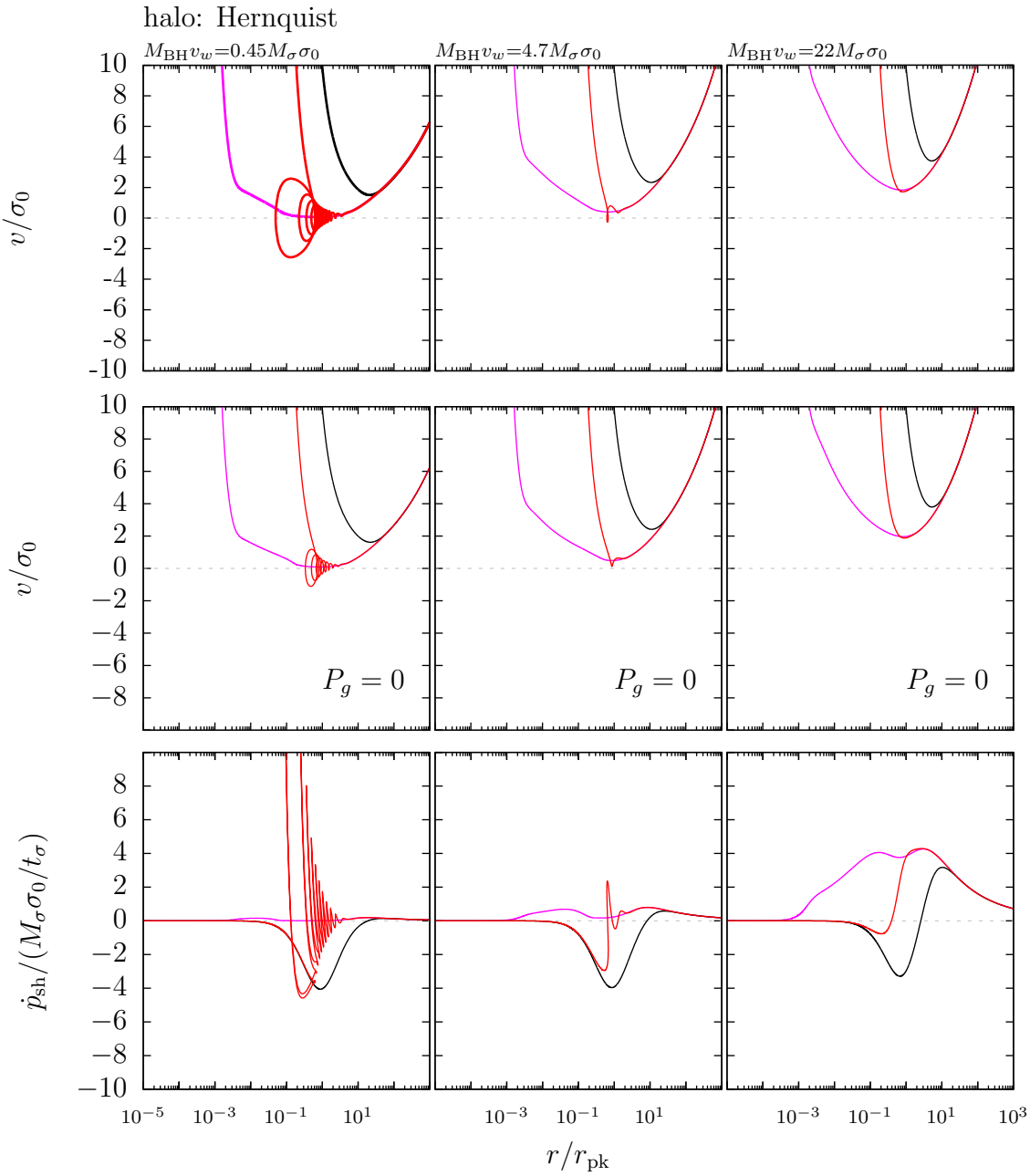

Figure 3.18: Shell velocities (top, middle) and momentum-fluxes (bottom) versus radius of energy-driven shells propagating within a Hernquist halo. For the panels which include ambient pressure the gas fraction is set to $f_0 = 0.2$. Three combinations of SMBH mass and wind speed are considered: $\widetilde{M}_{\rm BH}\widetilde{v}_w = 2.7$ (left), 2.7 (middle), and 22 (right). The radius scale is $r_{\rm pk} \simeq 50$ kpc for a velocity dispersion of $\sigma_0 = 200$ km s^{-1}. Three values of initial momentum are shown: $C = 10^{-8}$ shown in magenta, $C = 1$ shown in red, and $C = 100$ shown in black.

3.3.4 Momentum-Fluxes of Energy-Driven Shells

As introduced at the start of this chapter, observations of outflows within active galaxies have shown that their momentum-fluxes can vary greatly in relation to the radiative momentum-flux of the AGN: $L_{\rm AGN}/c$. One way to understand these 'boosts' in momentum-flux is that the outflow is in an energy-driven regime.

The Singular Isothermal Sphere

For energy-driven shells propagating within an SIS halo the normalised momentum-flux $\dot{p}_{\rm sh}/\dot{M}_w v_w$ and the quantity $\dot{M}_{\rm sh} v/\dot{M}_w v_w$ are compared in Figure 3.19. It shows a single case of initial momentum $C = 0.01$ and three wind speeds: $v_w = 45\sigma_0, 75\sigma_0$ and $100\sigma_0$, which correspond for $\sigma_0 = 200$ km s^{-1} to $v_w = 0.03c, 0.05c$ and $0.07c$. It can be seen that $\dot{M}_{\rm sh} v$ approximates the momentum-flux well over a large range of radii. It is evident that the larger the wind speed the larger the momentum-boost of the energy-driven shell at large radii $r \gg r_\sigma$. Larger values of initial momentum will lead to $\dot{M}_{\rm sh} v$ approximating the momentum-flux only at larger radii. The rapid variation at small radii corresponds to confinement from the SMBH gravity.

In Section 3.3.2 it was shown that the large radius coasting velocity of an energy-driven shell is:

$$(3\gamma-2)\widetilde{v}_\infty^3 + [2(6\gamma-5)+(3\gamma-2)(1+f_0)]\widetilde{v}_\infty = 3(\gamma-1)\widetilde{M}_{\rm BH}\widetilde{v}_w \qquad (\widetilde{t} \gg 1)\,. \quad (3.90)$$

Introducing units back into this equation and making use of the definition of the wind energy: $\dot{E}_w \equiv \tau L_{\rm Edd}/2c = 2\pi G\tau M_{\rm BH} v_w/\kappa$, the shell mass: $\dot{M}_{\rm sh} = 2f_0\sigma_0^2 v_\infty/G$, and the gravitational force on the shell due to dark matter: $F_{\rm grav} = 4f_0\sigma_0^4/G$ it can be shown that:

$$\dot{M}_{\rm sh} v_\infty^2 + \left[\frac{6\gamma-5}{3\gamma-2} + \frac{1+f_0}{2}\right] F_{\rm grav} v_\infty = \frac{3(\gamma-1)}{3\gamma-2}\dot{E}_w\,. \quad (3.91)$$

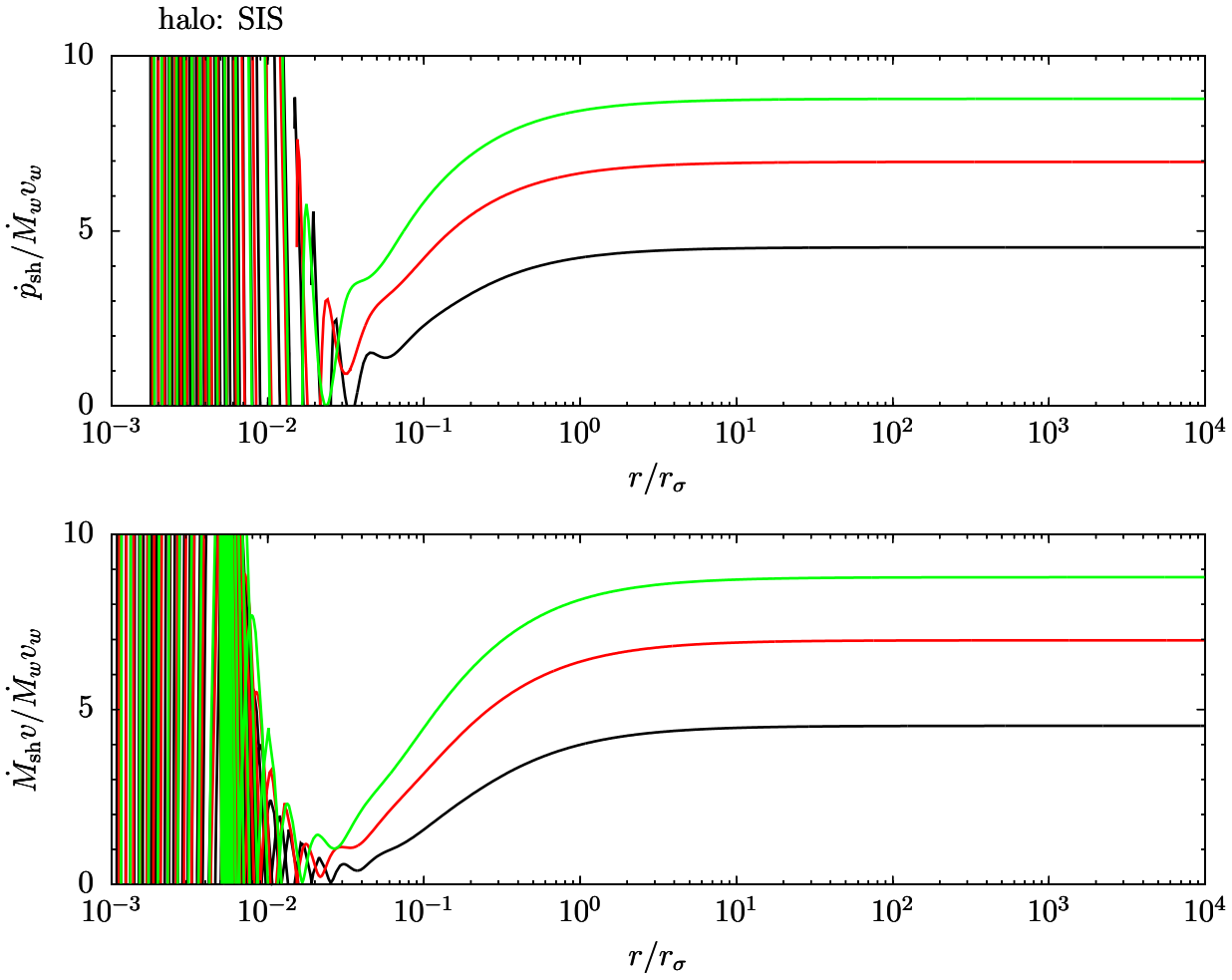

Figure 3.19: The momentum-fluxes of energy-driven shells within an SIS halo normalised to the momentum-flux of the wind versus shell radius. The top figure shows actual normalised momentum-flux $\dot{p}_{\rm sh}/\dot{M}_w v_w$, and the bottom figure shows the quantity $\dot{M}_{\rm sh} v/\dot{M}_w v_w$. All solutions have $\widetilde{M}_{\rm BH} = 0.49$ and $C = 0.01$, but have different values of wind speed $\widetilde{v}_w = 45, 75$ and 100, which for $\sigma_0 = 200$ km s^{-1} are $v_w = 0.03c$ (black), $0.05c$ (red), and $0.067c$ (green) respectively. The value of the scale radius is $r_\sigma \simeq 50$ pc.

The share of energies is therefore:

$$\begin{aligned}
\dot{M}_{\rm sh} v_\infty^2 &= \frac{3(\gamma-1)}{3\gamma-2}\dot{E}_w - \frac{6\gamma-5}{3\gamma-2}F_{\rm grav} v_\infty - \frac{1+f_0}{2}F_{\rm grav} v_\infty \\
&= \dot{E}_w - \frac{\dot{E}_w}{3\gamma-2} + \frac{F_{\rm grav} v_\infty}{3\gamma-2} - 2F_{\rm grav} v_\infty - \frac{1+f_0}{2}F_{\rm grav} v_\infty \\
&= \dot{E}_w - \dot{U} - 2F_{\rm grav} v_\infty - \frac{1+f_0}{2}F_{\rm grav} v_\infty \,,
\end{aligned} \tag{3.92}$$

where the energy equation (3.70) has been used in the last step to introduce the internal energy of the hot shocked wind.

Making use of $\dot{E}_w = \dot{M}_w v_w^2/2$ the top equality of equation (3.92) can be rearranged to give:

$$\begin{aligned}\frac{\dot{M}_{\rm sh} v_\infty^2}{\dot{M}_w v_w^2} &= \frac{3(\gamma-1)}{2(3\gamma-2)} - \left[\frac{6\gamma-5}{3\gamma-2} + \frac{1+f_0}{2}\right] \frac{F_{\rm grav} v_\infty}{\dot{M}_w v_w^2} \\ &= \frac{3(\gamma-1)}{2(3\gamma-2)} - \left[\frac{6\gamma-5}{3\gamma-2} + \frac{1+f_0}{2}\right] \frac{\widetilde{v}_\infty}{\widetilde{M}_{\rm BH}\widetilde{v}_w}\end{aligned} \tag{3.93}$$

Then using (3.90) for $\widetilde{M}_{\rm BH}\widetilde{v}_w$ gives:

$$\frac{\dot{M}_{\rm sh} v_\infty}{\dot{M}_w v_w} = \frac{v_w}{v_\infty}\frac{3(\gamma-1)}{2(3\gamma-2)} \left\{1 + \left[\frac{2(6\gamma-5)}{3\gamma-2} + (1+f_0)\right]\left(\frac{\sigma_0}{v_\infty}\right)^2\right\}^{-1} \tag{3.94}$$

which can be expressed as:

$$\frac{\dot{M}_{\rm sh} v_\infty}{\dot{M}_w v_w} = \frac{v_w}{v_\infty}\frac{3(\gamma-1)}{2(3\gamma-2)} \left\{1 + \left(\frac{v_{\rm p,max}}{v_\infty}\right)^2\right\}^{-1}, \tag{3.95}$$

where $v_{\rm p,max}$ is:

$$\begin{aligned} v_{\rm p,max} &= \sqrt{\frac{2(6\gamma-5)}{3\gamma-2} + (1+f_0)}\ \sigma_0 \\ &\simeq 2.1\sigma_0 \qquad (\gamma = 5/3; f_0 = 0.2)\,. \end{aligned} \tag{3.96}$$

The entire right hand side of (3.95) is essentially the 'boost factor' for energy-driven shells coasting at large radii. If $v_\infty \gg v_{\rm p,max}$ then the momentum-boost tends to:

$$\begin{aligned}\frac{\dot{M}_{\rm sh} v_\infty}{\dot{M}_w v_w} &= \frac{3(\gamma-1)}{2(3\gamma-2)}\frac{v_w}{v_\infty} \\ &= \frac{1}{3}\frac{v_w}{v_\infty} \qquad (\gamma = 5/3)\,.\end{aligned} \tag{3.97}$$

This is consistent with the conclusion drawn by Zubovas & King (2012), and is effectively the equation used with observations of outflows in active galaxies (Tombesi et al. 2015; Feruglio et al. 2015). This relation is shown with data from observed outflows in Figure 1.12.

The limit used to derive equation (3.97) is likely to correspond to fast winds since $v_w > v_\infty \gg v_{\rm p,max} \gtrsim \sigma_0$ according to equation (3.90), or equivalently to low σ systems.

Note that this relation is obtained if all gravitational and pressure terms are dropped in the equations of motion, and therefore this limit is equivalent to an energy-driven shell in the absence of gravity.

In the other limit that $v_\infty \ll v_{\rm p,max}$ then the momentum boost becomes:

$$\begin{aligned} \frac{\dot{M}_{\rm sh} v_\infty}{\dot{M}_w v_w} &= \frac{3(\gamma-1)}{2(3\gamma-2)} \frac{v_w}{v_{\rm p,max}} \frac{v_\infty}{v_{\rm p,max}} \\ &\simeq \frac{1}{3} \frac{v_w}{v_{\rm p,max}} \frac{v_\infty}{v_{\rm p,max}} \qquad (\gamma = 5/3)\,. \end{aligned} \tag{3.98}$$

These shells will have very low momentum boosts resulting from the fact that v_∞ is small compared to $v_{\rm p,max} \sim 2\sigma_0$ (and $v_\infty \gtrsim \sigma_0$ as a lower limit in order the shell to retain its shock structure). In order for these slow shells to occur the SMBH and the wind speed combination according to equation (3.90) must be low relative to $M_\sigma \sigma_0$. Therefore this limit corresponds to slow winds, but considering that $v_\infty \sim \sigma_0$ and that $v_{\rm p,max} \gtrsim 2\sigma_0$ this can only correspond to a narrow range of outflow velocities and wind speeds $v_w > v_{\rm p,max} \gtrsim v_\infty \sim \sigma_0$.

Equation (3.95) is plotted in Figure 3.20 against v_∞ for a constant v_w, and therefore shows the variation in momentum-boosting if the large scale coasting speed were determined solely by variation in $M_{\rm BH}$. This function has a well defined maximum in terms of outflow speed v_∞. The right hand panel shows the variation in momentum-boosting as a function of $M_{\rm BH}$ which has to be the varying quantity if v_w is fixed and v_∞ is varied. Also shown in Figure 3.20 in grey are the limiting solutions given by equation (3.97) where $v_\infty \gg \sigma_0$ which is the case that outflows are assumed to be fast and the winds driving them are also fast.

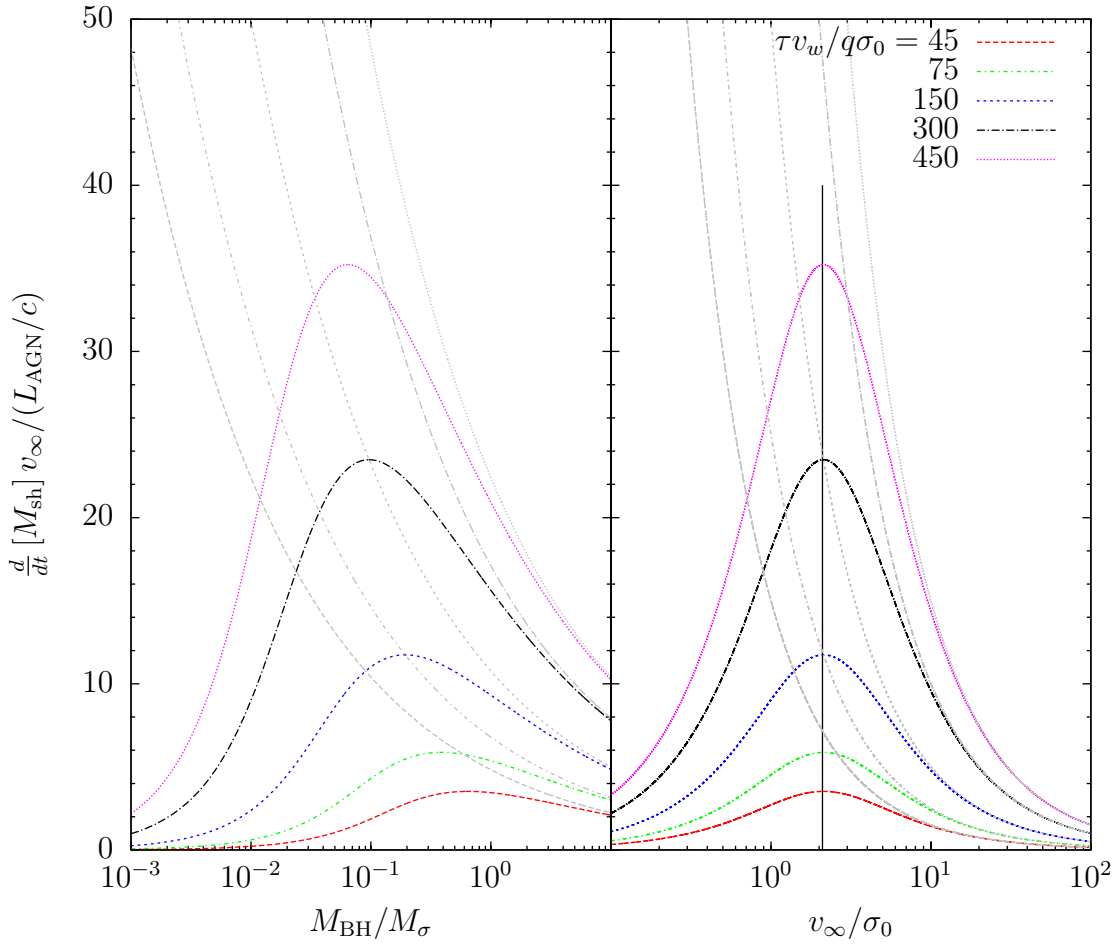

Figure 3.20: Large-scale momentum-flux normalised to that of the wind against velocity and SMBH mass for energy-driven shells propagating within an SIS halo. The left panel shows asymptotic momentum-flux normalised to that of the wind for an energy-driven shell propagating within an SIS halo for a range of wind speeds plotted against SMBH mass (left). The right panel shows the same but plotted against the terminal velocity. In this figure $\gamma = 5/3$. For $\sigma_0 = 200$ km s^{-1} the plotted wind speeds are $0.03c$, $0.05c$, $0.1c$, $0.2c$ and $0.3c$.

Figure 3.20 shows that the terminal momentum-boost of the shell normalised to that of the wind (equation 3.95) has a well defined maximum at a specific outflow speed v_∞. A similar distribution of momentum-boosts has been obtained by Richings & Faucher-Giguère (2018). The velocity at which the maximum occurs is $v_{\rm p,max}$ as given by equation (3.96). This value is close to the circular speed inside the SIS ($\sqrt{2}\sigma_0$), and close to the escape velocity from a truncated SIS ($2\sigma_0$). In fact:

$$\begin{aligned} v_{\rm p,max} &\rightarrow \sqrt{2}\sigma_0 = v_{\rm circ} \qquad (\gamma \rightarrow 1) \\ &\rightarrow 2\sigma_0 = v_{\rm esc} \qquad (\gamma \rightarrow \infty) \end{aligned} \tag{3.99}$$

representing the limits of a very hot shocked wind and very cold shocked wind respectively. The escape velocity for a truncated SIS was used in Section 3.3.2 following McQuillin & McLaughlin (2012) to obtain a critical $M_{\rm BH}v_w$ combination. Because $v_{\rm p,max}$ is close to this escape velocity the conclusions in Section 3.3.2 can be understood in terms of the SMBH mass and wind speed combination which result in maximum momentum-boosting, i.e. using $v_{\rm p,max}$ with equation (3.90) gives $\widetilde{M}_{\rm BH}\widetilde{v}_w \simeq 18.26$ for $\gamma = 5/3$. Hence, by assuming $v_\infty = 2\sigma_0$ the derived $M_{\rm BH} - \sigma$ relation of McQuillin & McLaughlin is close to that for a maximally boosted shell. They use their relation to obtain a median wind speed from a sample of $M_{\rm BH} - \sigma$ data, and find that the resultant value $v_w \simeq 0.03c$ compares well with median wind speeds from samples of local active galaxies.

The large radius outflow velocity at which maximum boosting occurs does not depend on the value of v_w, but the overall level of boosting does. One way to interpret Figure 3.20 is by varying the size of the velocity dispersion σ_0. Maximally boosted outflows with velocities given by (3.96) in high σ_0 systems will have similar $\sim \sigma_0$ high speeds at large radii, and in this case the speed of the wind relative to σ_0 and therefore $v_{\rm p,max}$ will be lower, i.e. slow winds. This means that even though the outflow is at maximum boosting the level of boosting is low in magnitude. In other words these would be systems where if maximal boosting were to be achieved this would require an outflow with speed $v_{\rm p,max} \sim \sigma_0$ which is high and therefore defines a slow $v_w \sim \sigma_0$. From the plot against SMBH mass this would imply a high SMBH mass system. Conversely,

maximally boosted outflows in low σ_0 systems would have very fast winds but slow large-scale outflow speeds relative to the wind, and this would result in large-scale outflows with high magnitudes of boosting. Looking at the plot against SMBH this would correspond to systems with low SMBH masses.

If conditions were such that the momentum-boost were always driven to the upper limit, then the left panel of Figure 3.20 is open to the interpretation that growth in the SMBH mass would lead to a decrease in the wind speed. This would mean that in such systems where the SMBH has grown rapidly there would be much slower winds because the constant momentum-boost would require the wind speed to drop. Conversely for slower growing SMBHs the wind would be able to maintain a high speed for longer periods of time. It is expected that rapid SMBH growth may occur in systems with higher velocity dispersions as these will have contained more gas for feeding the SMBH.

Carrying out the inverse process of fixing the SMBH value simply shows that higher v_w and v_∞ simply increase the momentum-boost which is without a maximum. Therefore, whether or not an outflow has maximum momentum-boosting is not at all related to the speed of the wind, but it is dependent on properties of the galaxy such as $M_{\rm BH}$ or σ. With this knowledge in mind and looking back at equation (3.95) and putting in $v_\infty = v_{\rm p,max}$ for maximum momentum-boosting gives:

$$\begin{aligned} \frac{\dot{M}_{\rm sh} v_{\rm p,max}}{\dot{M}_w v_w} &= \frac{3(\gamma-1)}{4(3\gamma-2)} \frac{v_w}{v_{\rm p,max}} \\ &= \frac{1}{6} \frac{v_w}{v_{\rm p,max}} \qquad (\gamma = 5/3)\,, \end{aligned} \tag{3.100}$$

which means that maximum boosting occurs when the momentum-boost is exactly half of upper limit given by equation (3.97). Multiplying this equation by $v_{\rm p,max}/v_w$ gives the kinetic energy-flux of the outflow with maximum momentum-boosting:

$$\begin{aligned} \frac{\dot{M}_{\rm sh} v_{\rm p,max}^2/2}{\dot{E}_w} &= \frac{3(\gamma-1)}{4(3\gamma-2)} \\ &= \frac{1}{6} \qquad (\gamma = 5/3)\,. \end{aligned} \tag{3.101}$$

This means that the outflow velocity at which maximum momentum boosting occurs is when the kinetic energy flux of the shell is equal to the specific fraction of wind energy

given by equation (3.101). Note that this is completely independent of any changes to the gravitational potential or the inclusion of ambient pressure, i.e. the fraction of wind energy imparted to the kinetic motion of the shell when momentum-boosting is maximal does not depend on the system parameters such as velocity dispersion or SMBH mass.

In order to understand what happens to the rest of the wind energy when maximum boosting occurs equation (3.92) can be used to show that:

$$\begin{aligned}\frac{3(\gamma-1)}{2(3\gamma-2)}\dot{E}_w &= \frac{6\gamma-5}{3\gamma-2}F_{\rm grav}v_{\rm p,max} + (1+f_0)F_{\rm grav}v_{\rm p,max} \\ &= \dot{M}_{\rm sh}v_{\rm p,max}^2\end{aligned} \tag{3.102}$$

i.e. for maximum boosting half of the available wind energy goes into kinetic energy and the other half goes into any resistive losses. Again, the ratio of wind energy in the kinetic energy of the shell is the same regardless of any changes to the gravitational potential, such as including ambient pressure as long as the force is constant at large radii. Changes to the gravitational potential determine the specific velocity $v_{\rm p,max}$ where the peak occurs.

Therefore the maximum in momentum-boosting has the physical interpretation as being the point where twice the kinetic energy of the outflow is equal to all of the work done against gravity. If outflows are driven such that the momentum-boost increases up to (but does not exceed) the upper limit, then the velocity $v_{\rm p,max}$ at which maximum momentum-boosting occurs would be the expected velocity for observed large scale outflows. Figure 3.21 shows how observed large scale momentum-fluxes relative to $L_{\rm AGN}/c$ compare to the theoretical relation given by equation (3.95). The values for the velocities and momentum-fluxes of the outflows were taken from the study of AGN outflows by Cicone et al. (2014). The stated velocity values have a conservative error of $\pm 50\%$, while the error on the momentum rate is taken to be 0.45 dex.

Figure 3.21 shows that the data of Cicone et al. is broadly situated close to the peaks of the momentum-flux curves. The plotted data and inferred wind speeds are presented in Table 3.2.

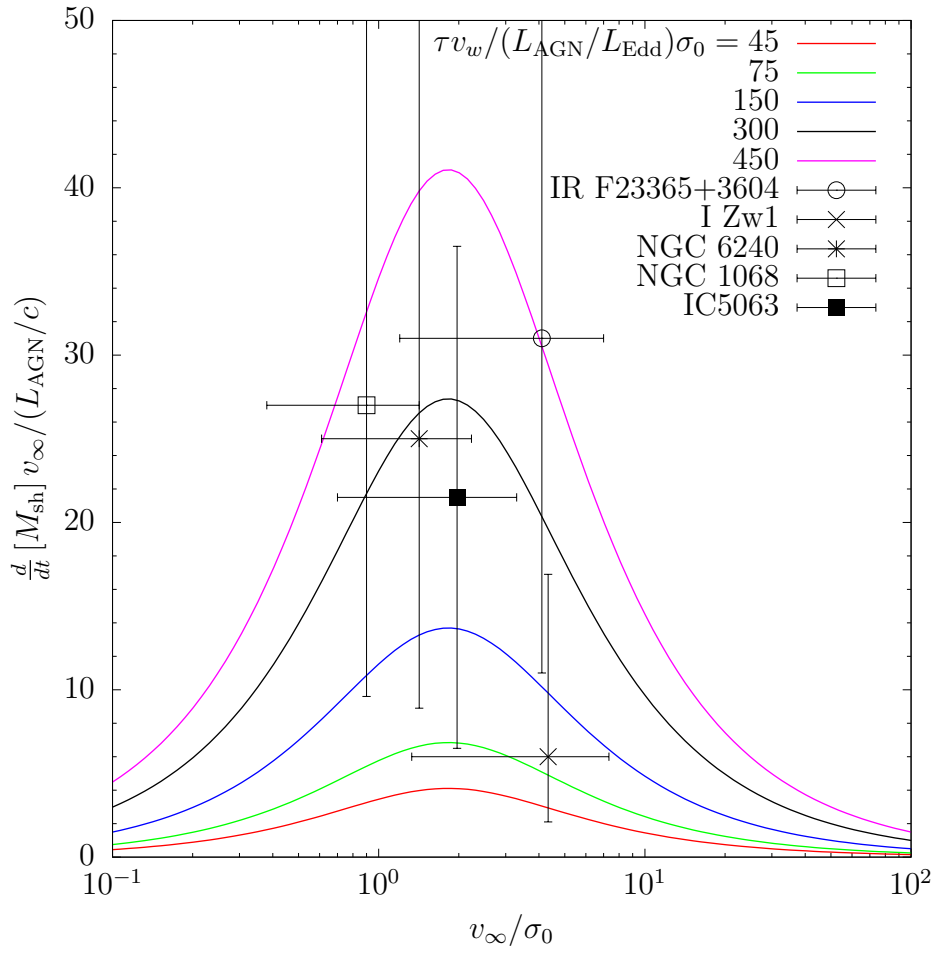

Figure 3.21: Large scale momentum-boosts for an energy-driven shell given by equation (3.95) for a range of $\tau v_w q/l\sigma_0$ values, and $\gamma = 5/3$, plotted alongside the data of Cicone et al. (2014).

Object	v_{out}/ km s^{-1}	σ/ km s^{-1}	v_{out}/σ	$\frac{\dot{M}_{out}v_{out}}{L_{AGN}/c}$	$M_{BH}/(10^8 M_\odot)$	$\frac{\dot{M}_{sh}v_\infty}{\dot{M}_w v_w}$	v_w/c
I Zw I	500 ±250	115 [i]	4.33 ±3.0	6	0.28 ±0.08[1]	-	0.06 : -
NGC 6240	400 ±200	282 ±20[2]	1.42 ±0.81	25	1.44 ±0.6[2]	25 ±12	0.20 : 0.28
NGC 1068	150 ±75	165 ±12[3]	0.9 ±0.52	27	0.17 ±0.13[4]	25 ±15	0.08 : 0.18
IC 5063	300 ±150	152 ±25[3]	1.97 ±1.3	21.5	0.55 [5]	6 ±3	0.17 : 0.15
IR F23365+3604	450 ±210	110 [6]	4.09 ±2.9	31	0.42 [i]	-	0.28 : -

Table 3.2: Table of data for large-scale molecular outflows. (Column 1) Name of the object. (2) Average outflow velocity (Cicone et al. 2014) (3) Velocity dispersion (various sources). (4) Outflow velocity normalised to the velocity dispersion. (5) Outflow momentum-flux normalised to L_{AGN}/c (Cicone et al. 2014). (6) SMBH mass (various sources) (7) Momentum boost calculated from M_{BH} and σ using equation (3.103) (assuming $v_{p,max} = 2\sigma_0$). (8) Wind speed calculated using the values from columns (2) and (5) with equation (3.100), and alternatively using data from columns (3) and (5) with the assumption $v_\infty = 2\sigma_0$. Sources: [1] Vestergaard & Peterson. 2005. [2] Medling et al. 2011. [3] Nelson & Whittle. 1995. [4] Kormendy et al. 1998. [5] Woo & Urry. 2002. [6] Martin & Soto. 2016. [i] Obtained from the $M_{BH} - \sigma$ relation given by equation (3.1). The error on momentum-boost values in column 5 is taken to be 0.45 dex, and this follows over to the derived wind speed values in column 8.

The observed outflows appear to be consistent with having velocities which are close to where maximum-boosting occurs. This supports the idea that maximum boosting may be a common scenario for outflows. Simply requiring that maximum boosting occurs, and therefore rearranging equation (3.101) for the SMBH mass and using $\dot{E}_w = 2\pi G\tau M_{\rm BH} v_w/\kappa$ with $\dot{M}_{\rm sh} v_{\rm p,max} = 2f_0\sigma_0^2 v_{\rm p,max}^2/G$ gives:

$$M_{\rm BH} = \frac{f_0\kappa\sigma_0^4}{2\pi\tau G^2}\left[\frac{4(3\gamma-2)}{3(\gamma-1)}\left(\frac{v_{\rm p,max}}{v_w}\right)\right]\left(\frac{v_{\rm p,max}}{\sigma_0}\right)^2, \tag{3.103}$$

where the quantity inside the square brackets is the inverse of the boost factor which is shown in equation (3.101). Equation (3.103) remains unchanged for variations in the constant inward potential such as including ambient pressure. However, these variations (or variations in γ) will alter the specific value of $v_{\rm p,max}$, but this is expected to always be close to $v_{\rm p,max} \sim 2\sigma_0$. The value of v_w may vary significantly from system to system, and for any variation in γ so will the factor multiplying the wind speed inside the square brackets. These variations are encapsulated as variations in the boost factor.

If $M_{\rm BH}$ and σ are known for an active system, then equation (3.103) can be used to determine the value of the maximum momentum-boost of the outflow at large radii. This has been done in column 7 of Table 3.2, and the values are consistent with the observationally determined values shown in column 5. Furthermore, as shown in column 8, the wind speed can be determined using the observed value of the boost factor and large scale outflow velocity (or alternatively by doubling the velocity dispersion). These results demonstrate how the form of equation (3.103) is an improvement over that of equation (3.2), as it permits the $M_{\rm BH} - \sigma$ relation to be expressed not just in terms of v_w (a parameter determined from observations close to the AGN) like equation (3.2) (if one assumes $v_\infty = 2\sigma_0$), but also in terms of the boost factor (a parameter determined from observations at large galactic radii). For quiescent systems where the $M_{\rm BH}$ and σ values were set by an outflow at high redshift, equation (3.103) can be used to determine the momentum-boost of this outflow and give insight into whether the galaxy was cleared during a minimally boosted (possibly momentum-driven) phase or highly boosted (and therefore energy-driven) phase.

Equation (3.103) has the same scaling $M_{\rm BH} v_w \propto \sigma_0^5$ as found by McQuillin &

McLaughlin (2013), and therefore a highly boosted outflow (i.e. higher wind speed) will result in a smaller SMBH mass. In order to relate this to the momentum-driven shell examined in Section 3.2, consider the force on a momentum-driven shell in the absence of ambient pressure:

$$\begin{aligned} \frac{\dot{p}_{\rm sh}}{\dot{p}_w} &= 1 - \frac{F_{\rm grav}}{\dot{p}_w} \\ &\rightarrow 1 - \frac{1}{\widetilde{M}_{\rm BH}} \qquad (x \gg 1)\,. \end{aligned} \tag{3.104}$$

Equation (3.104) gives the momentum-boost for momentum-driven shells, and if this is inverted and used in equation (3.103) in place of the boosting term, and the equation for the velocity (3.34) is used in place of $v_{\rm p,max}/\sigma_0$, then the equation balances. Considering the case that the initial momentum of the momentum-driven shell is minimised: $C \gtrsim 2$, then this means that $M_{\rm BH} \gtrsim 2M_\sigma$, and the momentum boost from equation (3.104) is $\gtrsim 1/2$, while equation (3.34) gives $v \gtrsim \sqrt{2}\sigma$, then the momentum-driven $M_{\rm BH} - \sigma$ relation (equation 3.1) is recovered (to within a factor of 2). Note that the same result is obtained for the maximally boosted energy-driven shell if the boost factor is unity (and $v_{\rm p,max} = 2\sigma_0$ as expected).

Choosing $v_{\rm p,max}$ to take its value given by equation (3.96) (without ambient pressure) allows it to be plotted against the $M_{\rm BH} - \sigma$ data as shown in Figure 3.1. It also defines the SMBH mass where the boost factor is unity to be about $2M_\sigma$. Note that changing $v_{\rm p,max}$ within the expected range of $1 - 3\sigma$ changes Figure 3.1 minimally. The comparison with observational data shows that the scatter can be interpreted as variations in the boost parameter with higher levels of boosting expected at lower velocity dispersions and higher SMBH masses. There is a clear absence of low momentum-boosting at low σ and low $M_{\rm BH}$. This means that for these galaxies v_w is expected to be high in order to increase the boost factor. Physically this may correspond to the fact that faster winds will inhibit the amount of cooling that an outflow receives, and this will result in only energy-driven outflows. Furthermore, faster winds are likely to clear a protogalaxy of its gas on much smaller timescales which may explain the lower masses at lower σ. At higher σ it can be seen that the data cluster heavily around

the momentum-conserving line (which is coincident with the line where the boost is unity). This means that these systems may have been cleared by momentum-driven shells which have low values for the boost parameter. In order that the parameter can become low it is required that the wind speed is also low. This is consistent with momentum-driving as a slower wind will be subject to cooling for longer timescales. Consequently such slower winds will take longer to clear the galaxy, and this will result in the larger SMBH masses at high σ.

In support of equation (3.103) are the coloured plotted points in Figure 3.1 which correspond to observational data from active galaxies. The colours indicate their proximity to the intervals in boosting. These are data from Cicone et al. (2014) shown in Table 3.2 and from Rupke, Gültekin & Veilleux (2017) (see publication) which include both low and high momentum-boosting. The data for the larger boosted outflows appear to be very consistent with equation (3.103), whereas the smaller boosted outflows deviate more.

This is an interesting result gained from utilising the fact that the share of wind energy in shell kinetic energy is a constant value which is independent of assumptions regarding the constant inward forces. Whether or not this relationship holds in a non-isothermal halo is examined in the following section.

Hernquist Halo

Obtaining a critical mass for outflows with maximal momentum-boosting can be carried out for the Hernquist halo. The most important region in the Hernquist halo is where the force of gravity is strongest. In the absence of ambient pressure this occurs precisely at the peak of the circular speed curve: $r_{\rm pk}$. If the momentum-fluxes of energy-driven shells are: $\dot{p}_{\rm sh}(r_{\rm pk}) \sim \dot{M}_{\rm sh} v(r_{\rm pk})$ then the analysis from the previous section can be used.

Figure 3.22 shows numerical solutions for $\dot{M}_{\rm sh} v$ which are normalised to $\dot{M}_w v_w = \tau L_{\rm Edd}/c$ for a range of $M_{\rm BH}$ masses and wind speeds plotted against the velocity at $r_{\rm pk}$. Note that every point along each curve corresponds to a different velocity and therefore a different value of $M_{\rm BH}$. This figure shows that around $r_{\rm pk}$ the normalised momentum-

flux is a peaked function when plotted against the velocity at $r_{\rm pk}$. The theoretical momentum-flux curves for the SIS halo compare very well with the numerical solutions for the Hernquist halo. Also shown in grey are the 'fast-wind limit' curves given by equation (3.97). Running through centres of both plots are (in the left panel) the kinetic energy fluxes normalised to $\dot{E}_w$ (as given by equation 3.101) and multiplied by a factor of 100 to be visible) and (in the right panel) the work done against gravity normalised to $\dot{E}_w$ (and multiplied by a factor of 10 to be visible). These energy shares at maximum-boosting in the Hernquist halo at $r_{\rm pk}$ are the same as those in the SIS halo for shells at large radii as given by equation (3.102).

This means that an expression can be obtained for the mass of a maximally boosted shell at $r_{\rm pk}$ where the dark matter gravity is strongest. Beginning with equation (3.101) and expressing $\dot{M}_{\rm sh} v_{\rm p,max}$ at $r_{\rm pk}$:

$$\frac{1}{2}\dot{M}_{\rm sh} v_{\rm p,max}^2 = \frac{f_0 M_{\rm pk} v_{\rm p,max}^3}{2 r_{\rm pk}} \left[\frac{dm}{dx}\right]_{x=1} = \frac{3(\gamma-1)}{4(3\gamma-2)}\dot{E}_w$$

which results in:

$$M_{\rm BH} = \frac{f_0 \kappa V_{\rm c,pk}^4}{4\pi G^2} \left[\frac{4(3\gamma-2)}{3(\gamma-1)}\left(\frac{v_{\rm p,max}}{v_w}\right)\right]\left(\frac{v_{\rm p,max}}{V_{\rm c,pk}}\right)^2 \tag{3.105}$$

Including ambient pressure moves the peak in gravitational force to radii inside of $r_{\rm pk}$, but as long as the velocity fields undergo a minimum at this peak the above arguments can be used for systems with ambient pressure included.

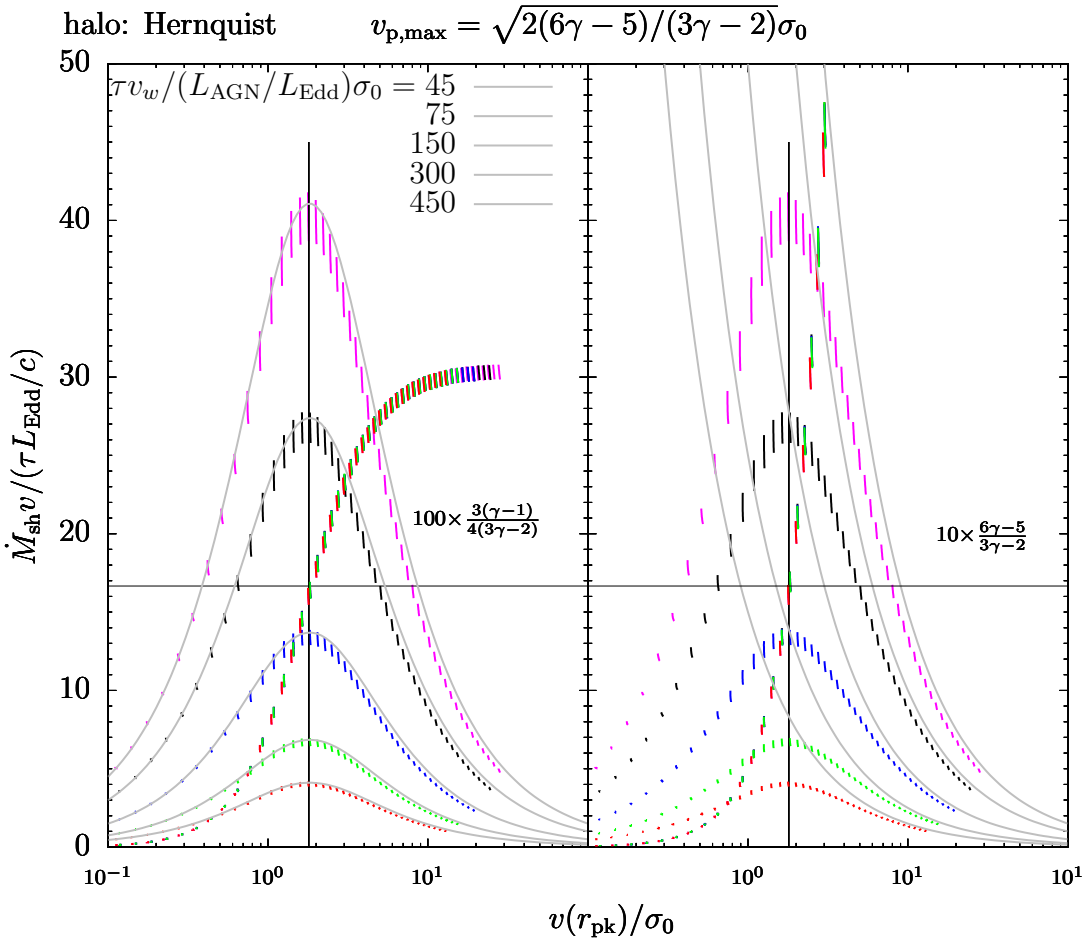

Figure 3.22: The momentum-boosts of energy-driven shells within a Hernquist halo versus shell velocity at $r_{\rm pk}$ for a range of SMBH masses ($0.001M_\sigma \leq M_{\rm BH} < 100M_\sigma$). The peaked coloured curves correspond to shells propagating within a Hernquist halo with radii limited to within $0.9 < r/r_{\rm pk} < 1.1$, whilst the grey curves correspond to the momentum-fluxes given by equation (3.95) (left panel) and its $v \ll \sigma_0$ limit given by equation (3.97) (right panel) for coasting shells within an SIS halo. The multicoloured curves in front of these plots are the ratios of shell kinetic energy with wind energy (left) and gravitational energy (right). The horizontal lines correspond to the values of these ratios expected at maximum boosting. Shells that stall are excluded from the plot. These shells are launched with an initial momentum-flux of $\sqrt{C} = 0.0001$, for the range of wind speeds $\widetilde{v}_w = 45$ (red), 75 (green), 150 (blue), 300 (black) and magenta (450). The Hernquist halo has a peak mass $\widetilde{M}_{\rm pk} = 4000$. The vertical black line is the value of $v_{\rm p,max}$.

3.4 Summary and Discussion

This chapter considered shells driven by steady winds and examined how they evolved in time. This was achieved by tracking the infall behaviour of any shells which stall. Shells experience stalls if the driving wind is not strong enough to overcome the gravity of the SMBH or the dark matter halo. As they have not been studied in their own right the confining effects of ambient pressure were also included.

The dynamics of momentum-driven shells in an SIS halo with ambient pressure included were analysed and it was shown that the previously derived necessary condition for escape given by equation (3.1) (King 2005), and the previously derived condition on the initial momentum of the shell in order to overcome gravitational forces (McQuillin & McLaughlin 2012) are both altered to require higher SMBH masses and higher initial momentum due to the inclusion of ambient pressure. The momentum-fluxes of shells $\dot{p}_{\rm sh}$ are compared with the observable $\dot{M}_{\rm sh}v$ and it is shown that the observable $\dot{M}_{\rm sh}v$ is a good approximation in the large radius limit since momentum-driven shells tend to a constant velocity. It was shown that there are three possible outcomes for momentum-driven shells: (1) they reach large radii without stalling, (2) they stall once and infall back to the SMBH, (3) they become confined by the ambient pressure of the gas. The relationship between the SMBH mass and the initial momentum which lead to shells that never stall was then analysed. It was then shown how for the smallest values of initial momentum there is a narrow range of allowed SMBH masses which lead to escape: those which are too large cause the shell to be confined by the SMBH gravity, and those which are too small mean that the driving force of the shell is too weak to overcome gravity.

The analysis then went on to momentum-driven shells in a Hernquist halo with ambient pressure included, and it was found that the previously required mass (equation 3.3, McQuillin & McLaughlin 2012) in the absence of ambient pressure is no longer a sufficient condition for a shell to escape without stalling. It does however survive as a necessary condition for escape. It was found that the observable $\dot{M}_{\rm sh}v$ is a good approximation for shell momentum-fluxes $\dot{p}_{\rm sh}$ at radii inside of where the circular speed

of the halo peaks: $r \lesssim r_{\rm pk}$. The same three shell outcomes for a momentum-driven shell in the SIS halo occurred in the Hernquist halo, but with a difference for the pressure confined shells. Because the gas pressure and dark matter gravity forces vary radially in the Hernquist halo, any pressure confined shells will make progress when they stall before $r_{\rm pk}$ where the halo gravity is strongest. When they reach $r_{\rm pk}$ whether they infall back to the SMBH or escape to large radii is determined by equation (3.3) which applies for momentum-driven shells in the absence of ambient pressure; if the mass exceeds this value then even pressure confined shells can escape, and hence why equation (3.3) still applies. However the time required for such shells to reach $r_{\rm pk}$ is long enough to consider them as effectively pressure-confined.

Energy-driven outflows propagating within an SIS halo were treated and it was demonstrated that the terminal coasting speed is reduced by the inclusion of ambient pressure, which in turn means that equation (3.2) (McQuillin & McLaughlin 2013) is increased by the inclusion of ambient pressure. There are three possible outcomes for energy-driven shells in an SIS halo: (1) they reach large radii without stalling, (2) they stall several times but go on to reach large radii, (3) they stall so much that they are effectively confined primarily by the gravity of the SMBH. Much like in the momentum-driven case only solutions with high enough initial momentum can avoid being significantly affected by the SMBH.

The momentum-fluxes of energy-driven shells in an SIS halo were examined and it was shown that the equation (3.4) for the momentum-boost of a shell (c.f. Zubovas & King 2012) is the 'fast wind' limit of a momentum-boost relationship which is actually a peaked function of shell terminal velocity v_∞. Expressions for the location of the peak were obtained and it was shown that the maximum momentum-boosting occurs exactly when the shell kinetic-to-wind energy ratio is:

$$\dot{M}_{\rm sh} v_\infty^2 = \frac{3(\gamma-1)}{2(3\gamma-2)} \dot{E}_w \,. \tag{3.106}$$

Note that the relationship between kinetic energy and wind energy at maximum boosting is independent of any changes to the resistive forces such as the inclusion of ambient pressure. Changing these forces changes the velocity at which peak momentum

boosting occurs, but it does not change this relationship. Data from observations of active galaxies indicate that large-scale outflows may be consistent with maximum momentum-boosting, and therefore requiring that a shell is at maximum boosting leads to the SMBH mass given by equation (3.103):

$$M_{\rm BH} = \frac{f_0 \kappa \sigma_0^4}{2\pi\tau G^2} \left[\frac{4(3\gamma-2)}{3(\gamma-1)} \left(\frac{v_{\rm p,max}}{v_w} \right) \right] \left(\frac{v_{\rm p,max}}{\sigma_0} \right)^2 . \tag{3.107}$$

This mass contains a 'boost factor' quantifying the level of momentum boosting, and the scatter in the $M_{\rm BH} - \sigma$ data was interpreted in terms of this factor.

By analysing the momentum-fluxes of energy-driven shells at $r_{\rm pk}$ in a Hernquist dark matter halo it was shown that the $\dot{M}_{\rm sh} v_\infty$ curves for the SIS halo for $\sigma_0 \equiv \sqrt{2} V_{\rm pk}$ match the Hernquist ones very well. It was shown in the absence of ambient pressure that the relations $\dot{M} v^2 = 3(\gamma-1)\dot{E}_w / 2(3\gamma-2)$ and $\dot{M} v^2 = (6\gamma-5) F_{\rm grav} / (3\gamma-2)$ hold true for maximum momentum-boosting at $r_{\rm pk}$. The maximum inward gravitational force due to dark matter occurs at the point where the circular speed curve peaks. Therefore by requiring that the shell has maximum boosting at $r_{\rm pk}$ led to the mass given by equation (3.105). This relation also contains the 'boost factor' but evaluated at $r_{\rm pk}$. Both of the previously derived $M_{\rm BH} - \sigma$ relations can be recovered by specifying values of the velocity at maximum boosting and the boost factor.

Using the derived mass for maximum boosting given by equation (3.103) allowed the scatter in the $M_{\rm BH} - \sigma$ data to be interpreted as variation in momentum-boosts. This could allow for the data to be broadly separated into slow and fast winds using similar definitions as in Chapter 2. This would mean that systems with low velocity dispersions were cleared by outflows driven by fast winds, and are therefore energy-driven. These fast winds could clear the central regions of gas quickly and this could explain why such systems have lower SMBH masses. The vacancy of points in the data at low σ is where low boost factors occur; this interval of σ may represent winds which are too fast to permit momentum-driven shells to occur. Conversely, systems with high velocity dispersions could potentially have been cleared by outflows driven by slow winds which results in a longer timescales for clearing the gas and therefore larger SMBHs. At high velocity dispersions it can be seen that there is less momentum-

boosting and that the data appear to cluster around lower values for the boost factor. This could be interpreted as an interval in σ where outflows were mostly momentum-driven. The fact that slow winds produce momentum-driven shells and fast-winds produce energy-driven shells is consistent with efficient cooling at small radii. This is precisely what is expected for outflows subject to inverse Compton cooling. The conclusion that the scatter can be interpreted as variation in momentum-boosting appears to be supported by the inclusion of some data from observations of active galaxies. From the supplied SMBH values and velocity dispersions this relation predicts momentum-boosts which are in broad agreement with the measured values.

In order to investigate fast and slow winds a time-dependent SMBH mass can be introduced. This will allow for the growth of SMBHs to be incorporated, and will assist in determining whether the conclusions relating to the $M_{\rm BH} - \sigma$ data from this section are justified.

4 Time-Dependent Winds

Chapter 3 concluded with the results relating to maximally boosted energy-driven shells. Supported by observations of local active galaxies which appear to be consistent with maximal boosting it was theorised that if conditions were always such that an outflow were maximally boosted when sweeping its host protogalaxy clear of gas then the resultant supermassive black hole (SMBH) mass would depend on a boost factor and the outflow speed in addition to the velocity dispersion of the galaxy. The scatter in the $M_{\rm BH}-\sigma$ relation was interpreted in terms of these momentum-boosts. This chapter explores the results of introducing a growing SMBH and therefore a growing wind force which drives the shell. The primary aims are to examine the assumptions and conclusions from Chapter 3 within this context. It will be confirmed that momentum-driven shells will have momentum-boosts which are never in excess of unity and do not deviate from unity significantly. It is to be investigated whether the SMBH mass which leads to momentum-driven shells that never stall is not fundamentally altered by including a growing SMBH. It is also to be investigated whether energy-driven shells will continue to have a momentum-boost distribution with a well defined peak corresponding to the even sharing of wind energy as this was required for the analysis in Chapter 3.

This chapter will for the first time include a form for the SMBH mass into the equations of motion (listed at the end of Chapter 2) which is capable of producing results for different SMBH accretion rates. This form is a seed mass M_0 multiplied by a growth factor which depends on the growth timescale t_s, and a parameter α which is related to the rate of accretion onto the SMBH:

$$M_{\rm BH} = M_0 \left(1 + \frac{t}{t_s \alpha}\right)^{\alpha}, \tag{4.1}$$

which recovers the constant SMBH mass for $\alpha \to 0$ and the exponentially growing SMBH mass for $\alpha \to \infty$. The exponentially growing SMBH mass has already been utilised by Gilli et al. (2017) when studying the motion of momentum- and energy-driven shells primarily in uniform gas distributions, but they extend their analysis to

the NFW dark matter halo (Navarro, Frenk & White 1996). This chapter will follow Chapter 3 and include a gas distribution which traces the dark matter directly and includes ambient gas pressure on the shell.

Section 4.1 introduces the functional forms for the SMBH mass, and outlines the ranges to be explored in the SMBH growth parameters such as the Salpeter time for an exponentially growing SMBH. This section also introduces the fiducial value for the Salpeter time for an exponentially growing SMBH. Section 4.2 details the general equations of motion which will be solved throughout this chapter.

Section 4.3 is a treatment of the dynamics of momentum-driven shells driven by growing SMBH winds. It begins by analysing the dynamics of momentum-driven shells within a singular isothermal sphere (SIS) halo for variation in the growth parameter α. The shell dynamics confirm that there is a smooth transition from the constant SMBH mass ($\alpha = 0$) for increasing α to the exponential mass case as $\alpha \to \infty$. It is shown that there is a new shell outcome for momentum-driven shells. This is the ability of an infalling shell to resume outward motion due to the growth of the SMBH wind force. Through variation of the growth timescale t_s it is shown that in order to reach large radii without stalling a shell must exceed the critical mass $M_{\rm BH,low}$ at the radius $x_{\rm stall}$ which were both found in Section 3.2.2 for shells driven by a constant SMBH wind. An approximate timescale is obtained for a growing shell to reach $x_{\rm stall}$ which is dependent on the value of the initial momentum. This timescale is used with the definition of the SMBH mass to provide a relationship between the seed mass M_0 and the growth timescale t_s which will permit shells to escape without stalling. The relationship gives results which are comparable with numerically determined M_0 and t_s values required to reach large radii without stalling, but it overpredicts the required seed mass for smaller values of initial momentum. It is found for rapidly growing SMBHs that there is a necessary SMBH seed mass in order to have real shell solutions at large radii, and that for moderate values of α the necessary value for the seed mass is not significantly different from the required SMBH mass in the steady wind case. A final attempt to estimate the required SMBH mass to reach large radii without stalling is carried out by using the fact that an accelerating shell will go on to reach large radii without

stalling. Finding the time at which the shell acceleration changes sign for shells which just barely accelerate without stalling i.e. those which have low velocity at this point allows the required SMBH mass to be estimated. It is found that these values are very close to the SMBH mass which must be exceeded in the steady wind case for a reasonable range of t_s.

Section 4.3 continues with the analysis of momentum-driven shells driven by time-dependent winds within a Hernquist halo. The smooth transition between solutions is once again confirmed for variation in α. Shells which stall within the Hernquist halo can do so many times before escaping or ultimately infalling. This arises solely from the increasing wind force, and is therefore a new shell behaviour. For the case of zero initial momentum there are substantial differences from the SIS halo regarding the criteria in order to reach large radii without stalling. Due to there being zero initial momentum for the shell there is no fixed stall radius for shells from steady winds which can be compared with. Instead the only method for estimating the SMBH mass required for shells to reach large radii without stalling is to numerically determine the SMBH mass when shells that just barely escape begin to accelerate. The numerical output is not as smooth as was obtained in the SIS halo, and for the fiducial value of t_s it appears that shells with SMBH masses a factor of ten lower than the required steady wind mass can go on to accelerate without stalling. However, for slower growing SMBHs with values above the fiducial t_s the required SMBH mass is close to the steady wind value. This section concludes by showing that the momentum boosts of momentum-driven shells driven by growing SMBH winds in an SIS halo tend to the upper limit of unity at large radii, and that the observable $\dot{M}_{\rm sh}v$ differs from the actual momentum-flux only by a factor of 2 at most at large radii for the fastest growing SMBHs. For the Hernquist halo it is shown that the observable $\dot{M}_{\rm sh}v$ is an acceptable proxy for $\dot{p}_{\rm sh}$ inside the radius $r_{\rm pk}$ where the circular speed curve peaks.

Section 4.4 compares energy-driven shell radii, velocities and momentum-fluxes from non-steady winds with the results from the steady wind case. It is found that the overall shell dynamics at earlier times are not substantially different. This means that shells from non-steady winds experience the same confinement displayed by shells

from steady winds at small radii if the initial velocity is low. The primary difference between the two cases is that energy-driven shells from non-steady winds accelerate at large radii in the SIS halo, and that they accelerate sooner in the Hernquist halo. The momentum-fluxes of energy-driven shells can therefore be significantly higher at large radii than in the steady wind case. The momentum-boosts in the SIS halo no longer tend to a constant at large radii, but $\dot{M}_{\rm sh}v$ continues to serve as a suitable proxy for $\dot{p}_{\rm sh}$ at large radii. Because the momentum-boost is relative to the momentum-flux of the ever-growing wind the momentum-boost tends to zero at large radii. The result is a broad peak in momentum-boosting as a function of radius for any shell solution. This means that a specific radius needs to be chosen in order to analyse the momentum-boosts in terms of shell velocities. Then variation in shell velocities (at a specfic radius) will correspond to variations in M_0 (for a set value of t_s). It is found that the distribution in momentum-boosts as a function of velocity (and therefore seed mass) remains the same for the SIS as long as the selected radius is within a region where the momentum-boost is not expected to be rapidly changing. This is equivalent to requiring the shell to be far enough away from the SMBH such that only the gravity of the dark matter halo is significant, but not so far away such that the shell is rapidly accelerating due to the growth of the SMBH. The conclusion is that as long as the SMBH growth is not too rapid then the analytical momentum-boost distribution for steady winds obtained in Chapter 3 will continue to apply to shells driven by non-steady winds over a dynamically significant range of radii. This means that under these conditions the derived $M_{\rm BH}-\sigma$ relation for maximally boosted shells from steady winds can be extended to apply to shells driven by non-steady winds.

Section 4.4 concludes with an analysis of energy-driven shells in a Hernquist halo. It is shown that the observable $\dot{M}_{\rm sh}v$ remains a suitable proxy for $\dot{p}_{\rm sh}$ at radii within $r_{\rm pk}$, and that while there is a radius within the halo where the analytical momentum-boost curves for the SIS halo are a good approximation this radius is no longer at $r_{\rm pk}$. This means that the derived $M_{\rm BH}-\sigma_0$ relationship obtained in Chapter 3 cannot be readily extended to apply to shells from non-steady winds. However, maximum boosting does occur at a radius inside $r_{\rm pk}$, and this radius will vary subject to selected parameter

values. The significance of the deviation of this radius from $r_{\rm pk}$ and therefore the departure from the steady wind case requires further investigation.

4.1 $M_{\rm BH}$ as a Function of Time

If the SMBH is accreting with accretion efficiency η (see Section 1.1.4), and at a fraction q of the Eddington rate (equation 1.19), then it satisfies the equation:

$$\dot{M}_{\rm BH}(t) = \frac{qL_{\rm Edd}}{\eta c^2} = \frac{4\pi G q M_{\rm BH}}{\eta \kappa c}\,. \tag{4.2}$$

This has the solution:

$$M_{\rm BH}(t) = M_0 \exp\left[\frac{4\pi q G t}{\eta \kappa c}\right]\,, \tag{4.3}$$

where M_0 is the seed mass. The appropriate range for seed mass values is $M_0 \sim 10^2 - 10^5 M_\odot$ (Volonteri 2010, see Section 1.3.1). This range in terms of the characteristic mass M_σ (see Sections 1.5 and 3.1, and equation 3.1) is $M_0 \sim 10^{-7} - 10^{-4} M_\sigma$.

The Salpeter (1964) (or e-folding) time is:

$$t_s = \frac{M_{\rm BH}(t)}{\dot{M}_{\rm BH}(t)} = \frac{\eta\kappa c}{4\pi q G} \simeq (4.7\times10^7)\left(\frac{\eta}{0.1}\right)\left(\frac{1}{q}\right)\ {\rm yr}\quad . \tag{4.4}$$

The mass of the SMBH will more than double during the time t_s which will have a significant effect on the dynamics of the outflow. For an exponentially growing SMBH to reach M_σ from the seed mass $10^{-4}M_\sigma$ it would have to accrete at the Eddington rate for ten Salpeter times.

A very useful functional form for the SMBH mass is:

$$M_{\rm BH} = M_0\left(1 + \frac{t}{t_s\alpha}\right)^\alpha\,, \tag{4.5}$$

as it possesses the following limits:

$$M_{\rm BH} \to M_0 \qquad (\alpha \to 0)\,, \tag{4.6}$$

recovering the constant SMBH mass case, and

$$M_{\rm BH} \to M_0 \exp\left(\frac{t}{t_s}\right) \qquad (\alpha \to \infty)\,, \tag{4.7}$$

recovering the exponential case. The value $\alpha = 1$ is an interesting case as this corresponds to an SMBH which grows at a constant rate:

$$\dot{M}_{\rm BH} = \frac{M_0}{t_s} \,. \tag{4.8}$$

Therefore SMBHs with the time parameter $\alpha < 1$ will have accretion rates which decrease in time, and SMBHs with $\alpha > 1$ will have accretion rates which increase in time.

Assuming that the wind has the momentum-flux $\dot{M}_w v_w = \tau L_{\rm Edd}/c$ (King & Pounds 2003 - see also Section 1.5) then the momentum-flux of the wind is:

$$\dot{M}_w v_w = \frac{4\pi G M_0}{\kappa} \left(1 + \frac{t}{t_s \alpha}\right)^{\alpha} \,. \tag{4.9}$$

At late times (i.e. $t \gg \alpha t_s$) then the mass injection rate grows as a power-law in time:

$$\dot{M}_w = \frac{4\pi G M_0}{\kappa \alpha^a v_w} \left(\frac{t}{t_s}\right)^{\alpha} \,. \tag{4.10}$$

This can be related back to the work in Chapter 2 which assumed a power law mass injection rate. Using this with the wind mass-injection rate given by equation (2.8) in Section 2.2 defines the characteristic quantity as $M_{w,s} \equiv 4\pi G M_0 t_s \tau / v_w \kappa \alpha^{\alpha}$.

4.2 Shell Equations of Motion

The equation of motion for either a momentum-driven or energy-driven shell is similar to equation (3.7) which was solved in Chapter 3 but with time-dependent SMBH masses:

$$\frac{d}{dt}\left[M_{\rm sh} v\right] = 4\pi r^2 \left[P(t) - P_g(r)\right] - \frac{G M_{\rm sh}(r)}{r^2}\left[M_{\rm BH}(t) + M_{\rm DM}(r)\right] \,, \tag{4.11}$$

where it can be seen that the driving pressure term: $P(t)$, and the SMBH gravity now both depend on time. Performing the same normalisation steps as carried out in Section 3.1 leads to the normalised equation of motion:

$$\frac{d}{d\widetilde{t}}\left[h(x)m(x)\widetilde{v}\right] = 4\pi x^2 \left[\widetilde{P}(\widetilde{t}) - \widetilde{P}_g(x)\right] - \frac{2h(x)m(x)}{x^2}\left[\frac{\widetilde{M}_{\rm BH}(\widetilde{t})}{\widetilde{M}_{\rm pk}} + m(x)\right] \,. \tag{4.12}$$

The functional forms of $P_g(x)$ remain the same as those introduced in Section 3.1.1.

If the shell encounters a stall point and the acceleration is negative at this point then the shell will begin to infall. During infall the equation of motion for the shell is:

$$\frac{d\widetilde{v}}{d\widetilde{t}} = \frac{4\pi x^2 \widetilde{P}(\widetilde{t})}{h(x_{\rm stall})m(x_{\rm stall})} - \frac{2}{x^2}\left[\frac{\widetilde{M}_{\rm BH}(\widetilde{t})}{\widetilde{M}_{\rm pk}} + m(x)\right] \qquad (x < x_{\rm stall})\,. \tag{4.13}$$

As in Chapter 3 it is assumed that the infall timescale $t_{\rm ff}$ is much less than the dynamical collapse timescale $t_{\rm col}$ of the ambient gas. The same numerical methods utilised in Chapter 3 will be used to solve equations (4.12) and (4.13) (see Section 3.1.3 for details).

4.3 Momentum-Driven Outflows

In the case that the outflow is momentum-driven the shocked wind region is cooled and it occupies a thin region behind the shell of shocked ambient medium (see Chapter 2 for an overview). Because of this the thin shell of shocked ambient medium is driven directly by the ram pressure of the wind:

$$4\pi r^2 P(t) = \dot{M}_w v_w = \frac{\tau L_{\rm Edd}(t)}{c} = \frac{4\tau\pi G M_{\rm BH}(t)}{\kappa}\,. \tag{4.14}$$

When normalised equation (4.14) becomes:

$$4\pi x^2 \widetilde{P}(\widetilde{t}) = 2\widetilde{M}_{\rm BH}(\widetilde{t})\,. \tag{4.15}$$

The equation of motion (4.12) therefore becomes:

$$\frac{d}{d\widetilde{t}}\left[h(x)m(x)\widetilde{v}\right] = 2\widetilde{M}_{\rm BH}(\widetilde{t}) - 4\pi x^2 \widetilde{P}_g(x) - \frac{2h(x)m(x)}{x^2}\left[\frac{\widetilde{M}_{\rm BH}(\widetilde{t})}{\widetilde{M}_{\rm pk}} + m(x)\right]\,. \tag{4.16}$$

If the shell encounters a stall point $x_{\rm stall}$ where $\widetilde{v} = 0$ instantaneously, and the acceleration $d\widetilde{v}/d\widetilde{t}$ is negative at that point, then the shell will begin to infall. The equation of motion for the infalling shell (4.13) becomes:

$$\frac{d\widetilde{v}}{d\widetilde{t}} = \frac{2\widetilde{M}_{\rm BH}(\widetilde{t})}{h(x_{\rm stall})m(x_{\rm stall})} - \frac{2}{x^2}\left[\frac{\widetilde{M}_{\rm BH}(\widetilde{t})}{\widetilde{M}_{\rm pk}} + m(x)\right] \qquad (x < x_{\rm stall})\,. \tag{4.17}$$

Equations (4.16) and (4.17) are to be solved numerically for the radii, velocities, and momentum-fluxes of momentum-driven shells.

4.3.1 The Singular Isothermal Sphere

For an SIS halo the mass profile is (see Table 1.1):

$$M_{\rm DM}(r) = \frac{2\sigma_0^2}{G} r \,. \tag{4.18}$$

Normalising the mass to M_σ (equation 3.1), and using the definition of r_σ (equation 3.8) leads to:

$$\widetilde{M}_{\rm DM}(x) = 2x \,. \tag{4.19}$$

where $x \equiv r/r_\sigma$ for this scale-free case. Hence, the general equation of motion (4.16) can be used for the SIS halo with $m(x) = x$, and $\widetilde{M}_{\rm pk} = 2$. Considering the case that gas traces dark matter directly ($h(x) = 1$), then the normalised pressure of the ambient (hydrostatic) gas in an SIS halo is (see Section 3.2.2):

$$\widetilde{P}_g(x) = \frac{1 + f_0}{4\pi x^2} \,. \tag{4.20}$$

The equation of motion (4.16) becomes:

$$\frac{d}{d\widetilde{t}} \left[x\widetilde{v} \right] = 2 \left[\widetilde{M}_{\rm BH}(\widetilde{t}) - 1 \right] - (1 + f_0) - \frac{\widetilde{M}_{\rm BH}(\widetilde{t})}{x} \,. \tag{4.21}$$

which is to be compared with the equation of motion obtained when assuming a constant SMBH mass: equation (3.31). If the shell experiences infall in the manner stated for the derivation of equation (4.13) then the equation of motion for an infalling shell from equation (4.17) is:

$$\frac{d\widetilde{v}}{d\widetilde{t}} = \frac{2\widetilde{M}_{\rm BH}(\widetilde{t})}{x_{\rm stall}} - \frac{1}{x^2} \left[\widetilde{M}_{\rm BH}(\widetilde{t}) + 2x \right] \qquad (x < x_{\rm stall}) \,. \tag{4.22}$$

The Salpeter Time

For the SIS halo all times are normalised to t_σ:

$$t_\sigma = \frac{r_\sigma}{\sigma_0} = \frac{f_0 \kappa \sigma_0}{\tau \pi G} \simeq 2.45 \times 10^5 \, \frac{1}{\tau} \left(\frac{\sigma_0}{200 \text{ km s}^{-1}} \right) \text{ yr} \,. \tag{4.23}$$

This means that the Salpeter time given by equation (4.4) in units of t_σ is of order: $\widetilde{t}_s \sim 10^2$ (for $\sigma_0 = 200$ km s^{-1}). Dividing equation (4.4) by (4.23) gives:

$$\frac{t_s}{t_\sigma} = \frac{\eta c \tau}{4 f_0 \sigma_0} \simeq 187.5 \tau \left(\frac{0.2}{f_0} \right) \left(\frac{200 \text{ km s}^{-1}}{\sigma_0} \right) \,. \tag{4.24}$$

By considering the possible ranges of the velocity dispersion, accretion rate, and accretion efficiency, then the appropriate range for the Salpeter time for an exponentially growing SMBH in an SIS will be from $\widetilde{t}_s = 10 - 1000$. If equation (4.5) for the SMBH mass is used then a wider range of the scale time $\widetilde{t}_s$ will be considered: $\widetilde{t}_s = 10^{-5} - 10^5$.

Asymptotics

At very early times the SMBH mass will tend to the seed mass value:

$$\widetilde{M}_{\rm BH}(\widetilde{t}) \to \widetilde{M}_0 \qquad (\widetilde{t} \ll \widetilde{t}_s \alpha) \,, \tag{4.25}$$

for the exponentially growing SMBH this requires that $\widetilde{t} \ll \widetilde{t}_s$. Therefore, as in the constant mass case (see Section 3.2.2) nonzero initial momentum is required for the shell to start moving outwards from $x = 0$. The shell radius at early times is therefore:

$$x^2(\widetilde{t}) = 2\sqrt{C}\widetilde{t} \qquad (\widetilde{t} \ll \widetilde{t}_s \alpha) \,, \tag{4.26}$$

and the velocity at early times is:

$$\widetilde{v}^2 = \frac{C}{x^2} = \frac{\sqrt{C}}{2\widetilde{t}} \qquad (\widetilde{t} \ll \widetilde{t}_s \alpha) \,. \tag{4.27}$$

For times when $\widetilde{t} \ll \widetilde{t}_s \alpha$ the SMBH mass can be approximated by the seed mass, and the shell behaves as described in Section 3.2.2. At times when $\widetilde{t} \gg \alpha \widetilde{t}_s$ the SMBH mass tends to:

$$\widetilde{M}_{\rm BH}(\widetilde{t}) = \widetilde{M}_0 \left(\frac{\widetilde{t}}{\widetilde{t}_s} \right)^\alpha \qquad (\widetilde{t} \gg \widetilde{t}_s \alpha) \,, \tag{4.28}$$

and therefore the shell momentum tends to:

$$x\widetilde{v} \rightarrow \frac{2\widetilde{t}_s\alpha}{\alpha+1}\widetilde{M}_0\left(\frac{\widetilde{t}}{\alpha t_s}\right)^{\alpha+1} - (3+f_0)\widetilde{t} - \int_0^{\widetilde{t}} \frac{\widetilde{M}_0}{x}\left(\frac{\widetilde{t}}{\alpha\widetilde{t}_s}\right)^{\alpha} d\widetilde{t} + \sqrt{C} \qquad (\widetilde{t} \gg \widetilde{t}_s\alpha)\,. \tag{4.29}$$

If the shell radius is to be an increasing function of time then the shell momentum at early times ($\widetilde{t} \ll 1$) will be $\sqrt{C}$, whereas at late times ($\widetilde{t} \gg 1$) the shell momentum will be:

$$x\widetilde{v} \rightarrow \frac{2\widetilde{t}_s\alpha}{\alpha+1}\widetilde{M}_0\left(\frac{\widetilde{t}}{\alpha t_s}\right)^{\alpha+1} - (3+f_0)\widetilde{t} \qquad (\widetilde{t} \gg \widetilde{t}_s\alpha;\ \widetilde{t} \gg 1)\,, \tag{4.30}$$

and therefore the shell radius is:

$$x^2(\widetilde{t}) \rightarrow \frac{4\widetilde{t}_s^2\alpha^2}{(\alpha+1)(\alpha+2)}\widetilde{M}_0\left(\frac{\widetilde{t}}{\alpha t_s}\right)^{\alpha+2} - (3+f_0)\widetilde{t}^2 \qquad (\widetilde{t} \gg \widetilde{t}_s\alpha;\ \widetilde{t} \gg 1)\,, \tag{4.31}$$

where $1+f_0$ represents the influence of ambient pressure on the shell. Equation (4.31) tends to the square of equation (3.36) for the constant SMBH mass case ($\alpha \rightarrow 0$) as required. Note that this has the same dependence on time as the momentum-driven shell in the absence of gravity obtained in Chapter 2. This can be shown by taking the late time limit in equation (2.17) and setting $p = 1$ as appropriate for the SIS gas distribution.

Following the same procedure but using equation (4.7), or taking the limit $\alpha \rightarrow \infty$ in equation (4.31) allows the exponential mass case to be obtained:

$$x^2(\widetilde{t}) = 4\widetilde{M}_0\widetilde{t}_s^2\exp\left(\widetilde{t}/\widetilde{t}_s\right) - (3+f_0)\widetilde{t}^2 \qquad (\widetilde{t} \gg 1)\,. \tag{4.32}$$

For $\alpha > 0$ equation (4.31) gives the late time velocity to be:

$$\widetilde{v}(t) = \sqrt{\frac{\widetilde{M}_0(\alpha+2)}{\alpha+1}}\left(\frac{\widetilde{t}}{\widetilde{t}_s\alpha}\right)^{\alpha/2} = \sqrt{\frac{(\alpha+2)\widetilde{M}_{\rm BH}(\widetilde{t})}{\alpha+1}} \qquad (\widetilde{t} \gg \widetilde{t}_s\alpha;\ \widetilde{t} \gg 1)\,, \tag{4.33}$$

which means that shells with $\alpha > 0$ will have increasing velocity at late times. Since the shell is decelerating at early times but accelerating at late times implies that there

will be at least one minimum in a shell's velocity field where the acceleration changes sign.

Variation in α: Infall and Re-Expansion for Momentum-Driven Shells

Utilising an SMBH mass which grows as a function of time has led to the introduction of three new parameters (M_0, α, t_s) in place of $M_{\rm BH}$ if equation (4.5) is used, or two new parameters (M_0, t_s) if the exponential mass is used. The first step in exploring this parameter space is to confirm in the limit of $\alpha \to 0$ that the shell dynamics are the same as those obtained in Section 3.2.2. It is also expected that there should be a smooth transition of shell dynamics between the constant and exponential SMBH mass as α is varied from 0 to large values.

Equations (4.21) and (4.22) have been solved numerically with the SMBH masses given by equations (4.5) and (4.7). The velocity fields are shown as functions of radius in Figure 4.1. The effects of ambient pressure were shown in Section 3.2.2 to be significant for a momentum-driven shell which stalls. In order to isolate the effects from the growth of the SMBH Figure 4.1 shows the results of varying α with and without ambient pressure included.

In Figure 4.1 the constant ($\alpha = 0$) SMBH mass solutions are shown as magenta curves, the constant growth rate ($\alpha = 1$) solutions are shown as red curves, and the solutions using the exponential SMBH mass are shown as green curves. In addition to these there are a number of nonzero α solutions in the range $0.0001 < \alpha < 500$ which are shown as black curves. The seed mass value is selected to be values between $0.1M_\sigma$ and $2.22M_\sigma$ to show the full range of shell behaviours. For $M_0 = 0.1M_\sigma$ all solutions stall and infall back to the SMBH regardless of growth rate or inclusion of ambient pressure, while for $M_0 = 2.22M_\sigma$ all solutions are able to escape. A single value of the growth timescale is chosen for all solutions: $\widetilde{t}_s = 1$. This is lower than the typical value for normalised Salpeter time given by equation (4.4), however a lower value of $\widetilde{t}_s$ is used to help distinguish between individual α values. For all solutions a single value of initial momentum is chosen to be $C = 4$ which is twice the lower limit on the initial momentum if ambient pressure is excluded (see Section 3.2.2). The radius

scale covers radii from $0.1r_\sigma \simeq 5$ pc to $100r_\sigma \simeq 5$ kpc for a value of velocity dispersion: $\sigma_0 = 200$ km s^{-1} and gas fraction: $f_0 = 0.2$.

In Section 3.2.2 it was shown that there were only two possible outcomes for a momentum-driven shell driven by a steady wind in an SIS halo in the absence of ambient pressure: either the shell stalls and directly infalls back to the SMBH, or the shell never stalls and goes on to reach large radii at constant velocity. The asymptotic speed of the steady wind solutions are shown by the magenta curves at large radii in Figure 4.1. The introduction of a non-steady wind ($\alpha > 0$) means that any solutions that reach large radii now accelerate, and their velocity increases according to equation (4.33). This leads to the minima in velocity fields shown in Figure 4.1.

Another new type of behaviour introduced is the ability of pressure confined shells to now escape (blue curve). This is in contrast to the pressure confined shells of Section 3.2.2, which repeatedly stalled as the terminal force on the shell with ambient pressure never became positive. Now because the outward force is an increasing function of time it is possible for pressure confined shells to overcome the ambient pressure and go on to reach large radii.

A further type of behaviour which has been introduced is the ability of an infalling shell to stall and resume outward motion which ultimately culminates in reaching large radii. This was only seen previously for the energy-driven shells which can resist infall due to their internal pressure. For these momentum-driven shells the SMBH is not large enough to initially push the shell out to large radii and the shell stalls. As it begins to infall the growth of the SMBH is fast enough to allow the shell to stall again and resume its outward motion. This behaviour is shown in Figure 4.1 both with and without ambient pressure for the small seed mass values of $\widetilde{M}_0 = 0.2, 0.21, 0.5$.

Figure 4.1 has shown that there is a smooth transition between the α values of interest (0 and 1 - from magenta to red curves), and between these cases and the exponential case. It is therefore acceptable to focus attention on these key values without excluding any cases that may be dynamically distinct.

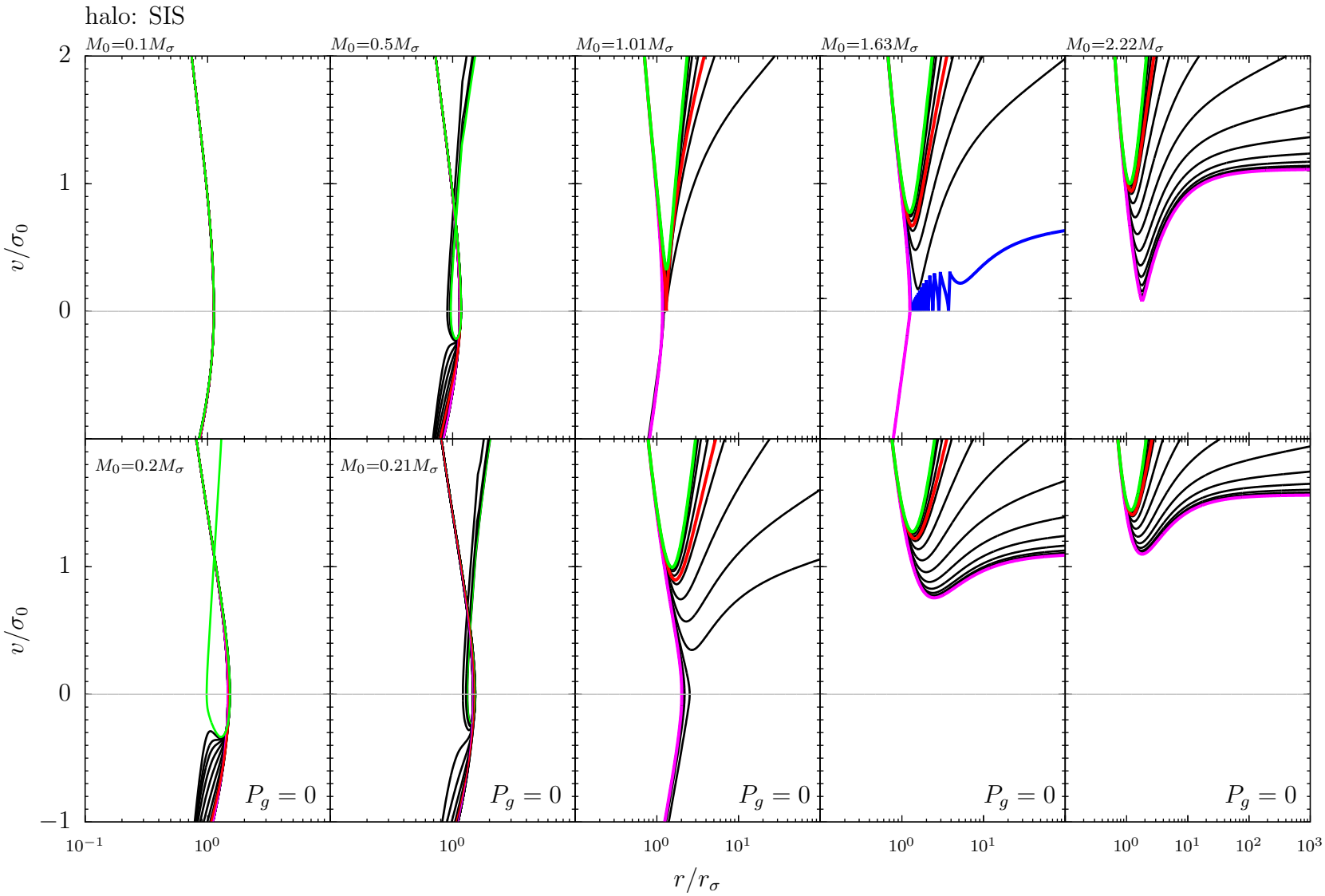

Figure 4.1: Velocity fields against radius for momentum-driven shells driven by steady winds (magenta curves) and non-steady winds with varying time parameter α in an SIS halo. The red curves correspond to $\alpha = 1$, and the green curves correspond to the exponential case. The black curves have α values in logarithmic intervals between 10^{-4} and 500, and increase in magnitude from the magenta to the green curves.

Variation in the Growth Timescale: $\mathbf{t_s}$

The next step is to understand how the solutions change with variation in the growth timescale t_s. For the exponential SMBH this is the Salpeter time and the fiducial value for this is $\widetilde{t}_s \sim 100$ (see equation 4.24). The Salpeter time can be reduced or increased by varying quantities such as the Eddington ratio or the accretion efficiency. For an introduction on how the accretion efficiency can change see Section 1.1.4. Further variation in the normalised value can be introduced by changes to the fiducial timescale given by equation (4.23) through differing velocity dispersions or gas fractions. In light of these restrictions the equation of motion (4.21) is solved for shell solutions which are driven by an exponentially growing SMBH wind with Salpeter times in the range $t_s = 0.1 - 10^4 t_\sigma$. The smaller values correspond to more rapidly growing SMBHs while the larger values correspond to slowly growing SMBHs. The solutions are presented for different seed mass values in Figure 4.2.

Each curve in Figure 4.2 corresponds to a solution with a specific value of t_s. The magenta and green curves are the solutions with the highest and lowest values of t_s respectively, while the red curve is the solution with $\widetilde{t}_s = 100$. The range of seed masses is chosen to extend beyond those presented in Figure 4.1 with the very low seed mass value of $M_0 = 0.0001 M_\sigma$ included to show that shells from the fastest growing SMBH winds are able to escape. For all solutions the value of initial momentum $C = 4$ is selected. This value is simply twice the minimum possible value of initial momentum, and in the constant mass case by equation (3.44) it defines a lower SMBH mass of $M_{\rm BH,low} \simeq 2.1 M_\sigma$ which must be exceeded in order to reach large radii without stalling (see Section 3.2.2).

It is evident from Figure 4.2 that for a given seed mass value there is a particular value of the Salpeter time which determines whether a shell can reach large radii. This implies that a certain value of $M_{\rm BH}(t)$ is required in order for shells to reach large radii. Hence, for a given seed mass there is a value of t_s above which SMBHs do not grow fast enough in order to drive their shells to large radii without stalling. It is clear that for the value of $\widetilde{t}_s = 100$ the seed mass required for escape lies between

$1.61M_\sigma$ and $2.22M_\sigma$, and it has been confirmed numerically that the required value is $M_0 \simeq 2.17M_\sigma$, which itself is not far from the required mass value of $M_{\rm BH,low} = 2.21M_\sigma$ in the case of a steady wind with $C = 4$ (see Section 3.2.2). It is important to note that the rapidly growing SMBHs can grow to values which are far in excess of the upper limit on the SMBH mass defined in the steady wind case by equation (3.45) which is $M_{\rm BH,high} \simeq 5.8M_\sigma$ for $C = 4$. It is found for non-steady winds that the shell solutions do not stall due to high values of the SMBH mass as they do in the steady wind case. For the slower growing SMBHs with Salpeter times of the order of the expected $100t_\sigma$ there appears to be little difference between the seed mass required to reach large radii and the constant SMBH mass $M_{\rm BH,low}$ required to reach large radii. However, for the very small Salpeter times it has been shown that even very small seed masses do not prevent these rapidly growing SMBH winds from driving shells to large radii. Despite such rapidly growing winds representing potentially unphysical solutions the limit of rapid growth is worthy of investigation.

In order to fully explore the variation in the growth timescale parameter t_s the equation of motion (4.21) has also been solved numerically for the shell solutions which are driven by a constantly growing SMBH wind ($\alpha = 1$), and the results are presented in Figure 4.3. In this case the range in growth timescale has been taken to a wider range of values: $t_s = 10^{-4} - 10^4 t_\sigma$.

As before each curve in Figure 4.3 corresponds to a solution with a specific value of t_s. The magenta and green curves are the solutions with the highest ($10^4 t_\sigma$) and lowest ($10^{-4} t_\sigma$) values of t_s respectively. The same range in seed masses as was used for the exponential case is utilised for Figure 4.3, and for all solutions the value of the initial momentum is again chosen to be $C = 4$.

It can be seen from Figure 4.3 that unlike the exponential case no solutions for the selected range of t_s can escape for the seed mass value of $M_0 = 0.0001M_\sigma$. A further difference is that the most rapidly growing solution corresponding to the lowest value of $t_s = 10^{-4}$ (shown in green) can never reach large radii, and that it stalls and infalls on a very short timescale which decreases with increasing seed mass. For increasing seed mass more of the rapidly growing solutions infall at early times, and the solution

which separates these cases from the other solutions is shown in red. Aside from these differences the solutions for $\alpha = 1$ are very similar to those for the exponential mass case. This is particularly true for the lower values of t_s and for the higher seed mass values. Hence, for longer growth timescales t_s the solutions do not vary significantly for changes in the parameter α, which corresponds to differences in the rate of accretion.

Figures 4.2 and 4.3 both imply that in order for a shell to reach large radii without stalling it must have values of t_s and M_0 within a certain range. In other words for a shell to escape the SMBH mass must exceed (or not exceed) a certain value at a specific time or radius. In order to demonstrate this the SMBH mass for the constantly growing case $\alpha = 1$ is plotted against time and radius in Figure 4.4.

Figure 4.4 shows the same solutions from Figure 4.3, and the curve colours represent the same solutions. Importantly, any post-stall shell behaviour is excluded from this plot, and therefore any shells that reach large radii do so without stalling. Also denoted in Figure 4.4 by the dashed blue line is the SMBH mass to be exceeded in order for a shell to reach large radii if the SMBH mass is constant. Because the initial momentum has been selected to be $C = 4$ this is $M_{\rm BH,low} = 2.21 M_\sigma$ by using equation (3.44) from Section 3.2.2. Shown as a black vertical line in the radius plot is the low SMBH mass limit of $x_{\rm stall}$ which was found in Section 3.2.2 to be:

$$\begin{aligned} x_{\rm stall} &= \frac{\widetilde{M}_{\rm BH} - \sqrt{\widetilde{M}_{\rm BH}{}^2 - \left[2\widetilde{M}_{\rm BH} - 3 - f_0\right] C}}{2\widetilde{M}_{\rm BH} - 3 - f_0} \\ &\rightarrow \frac{\sqrt{C}}{\sqrt{3+f_0}} \qquad (\widetilde{M}_{\rm BH} \ll 1). \end{aligned} \tag{4.34}$$

For the chosen value of $C = 4$ this results in a value of $x_{\rm stall} \simeq 1.12$. It is clear from Figure 4.4 that shells driven by SMBHs with masses which exceed $M_{\rm BH,low}$ approximately at $x_{\rm stall}$ are able to reach large radii. If the SMBH mass does not exceed $M_{\rm BH,low}$ by the time the shell reaches $x \sim x_{\rm stall}$ then the shell will stall. This leads to the conclusion that $x_{\rm stall}$ approximately corresponds to a critical radius within which the SMBH must grow to the required value of $M_{\rm BH,low}$. Associated with this radius will be a critical time, and this is also supported by Figure 4.4, as it appears that all shells that stall

do so at a particular time. These same conclusions also apply for other α values and for the exponential mass case.

A possible critical time can be obtained by setting the expression for shell radius at early times ($\widetilde{t} \ll \widetilde{t}_s\alpha$) given by equation (4.26) equal to $x_{\rm stall}$:

$$\widetilde{t}_{\rm stall} = \frac{\sqrt{C}}{6+2f_0} \qquad (\widetilde{t} \ll \widetilde{t}_s\alpha)\,, \tag{4.35}$$

which for $C = 4$ gives $\widetilde{t}_{\rm stall} \simeq 0.31$, and this value is denoted by the black vertical lines in the top panel of Figure 4.4. It is clear that this time is unsatisfactory, and that the actual critical time for $\alpha = 1$ is slightly below t_σ.

Figure 4.4 also shows growth to very large SMBH masses $M_{\rm BH} \gg 100M_\sigma$ as their shells reach large radii. This occurs primarily for the rapid growing cases which have growth timescales t_s far below the expected $t_s \sim 100$ for the Salpeter time.

For a given initial momentum it has been shown that SMBHs must grow to the value $M_{\rm BH,low}$ determined in Section 3.2.2 by the time the shell reaches $x_{\rm stall}$. For the lower and more realistic growth timescales t_s this means that the seed mass must be close to the value of $M_{\rm BH,low}$. Crucially this means that the condition for such shells to reach large radii is not fundamentally different from the one obtained for constant SMBHs. The rapidly growing SMBHs with low values of t_s can achieve the value $M_{\rm BH,low}$ by $x_{\rm stall}$ even if the seed mass is very low, however this results in shells which grow to unphysically large values at typical outflow radii.

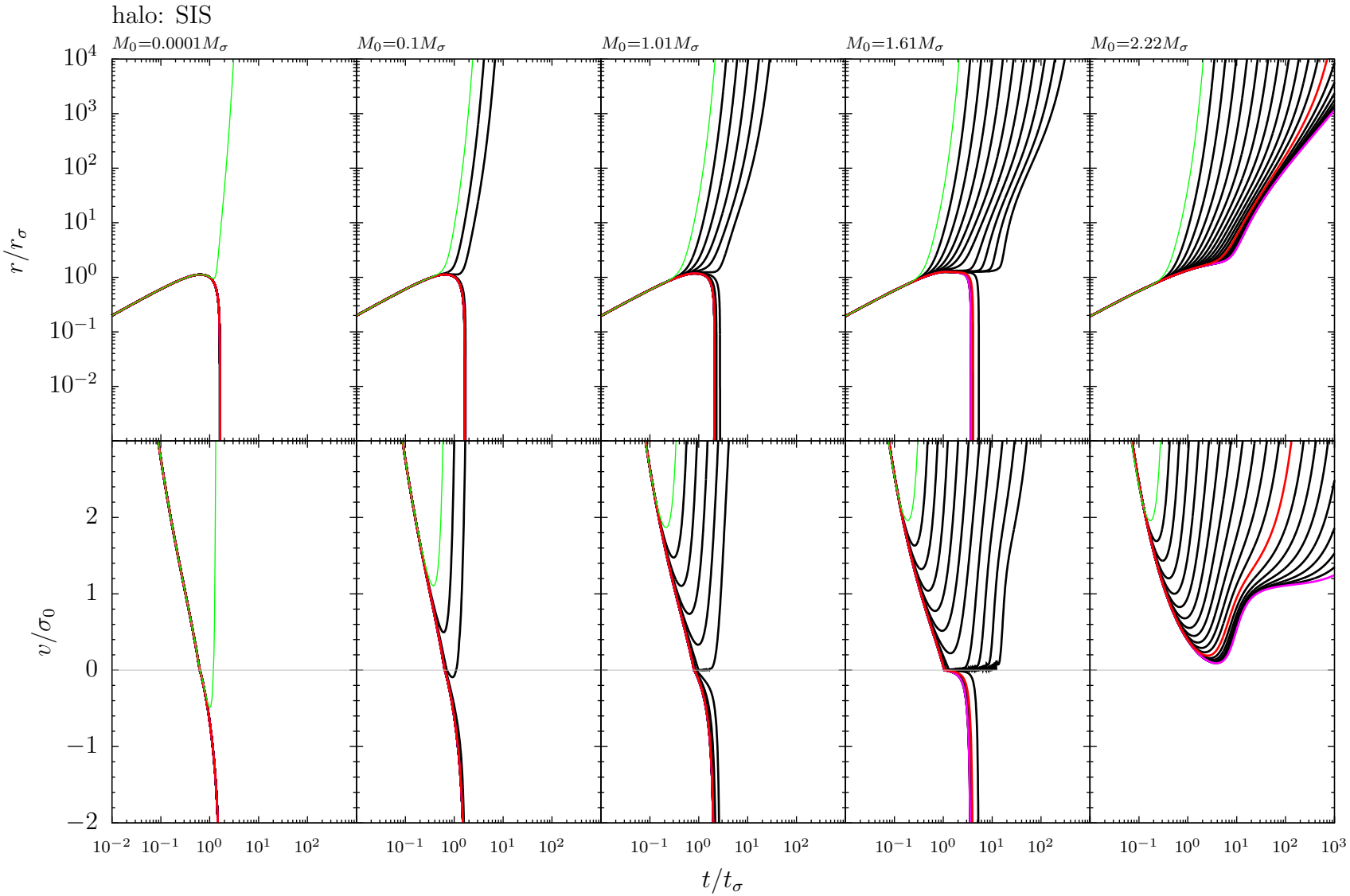

Figure 4.2: Velocity fields against time for momentum-driven shells driven by an exponentially growing SMBH wind with varying time parameter t_s in an SIS halo. The solutions shown correspond to variation in t_s over the range: $t_s = 0.1$ (green curve) to 10^4 (magenta curve), with the red curve corrsponding to the solution with $t_s = 100t_\sigma$. The black curves have t_s values in logarithmic intervals between $0.1 - 10^4 t_\sigma$ which increase from the green to magenta curves, and for all solutions the initial momentum is $C = 4$.

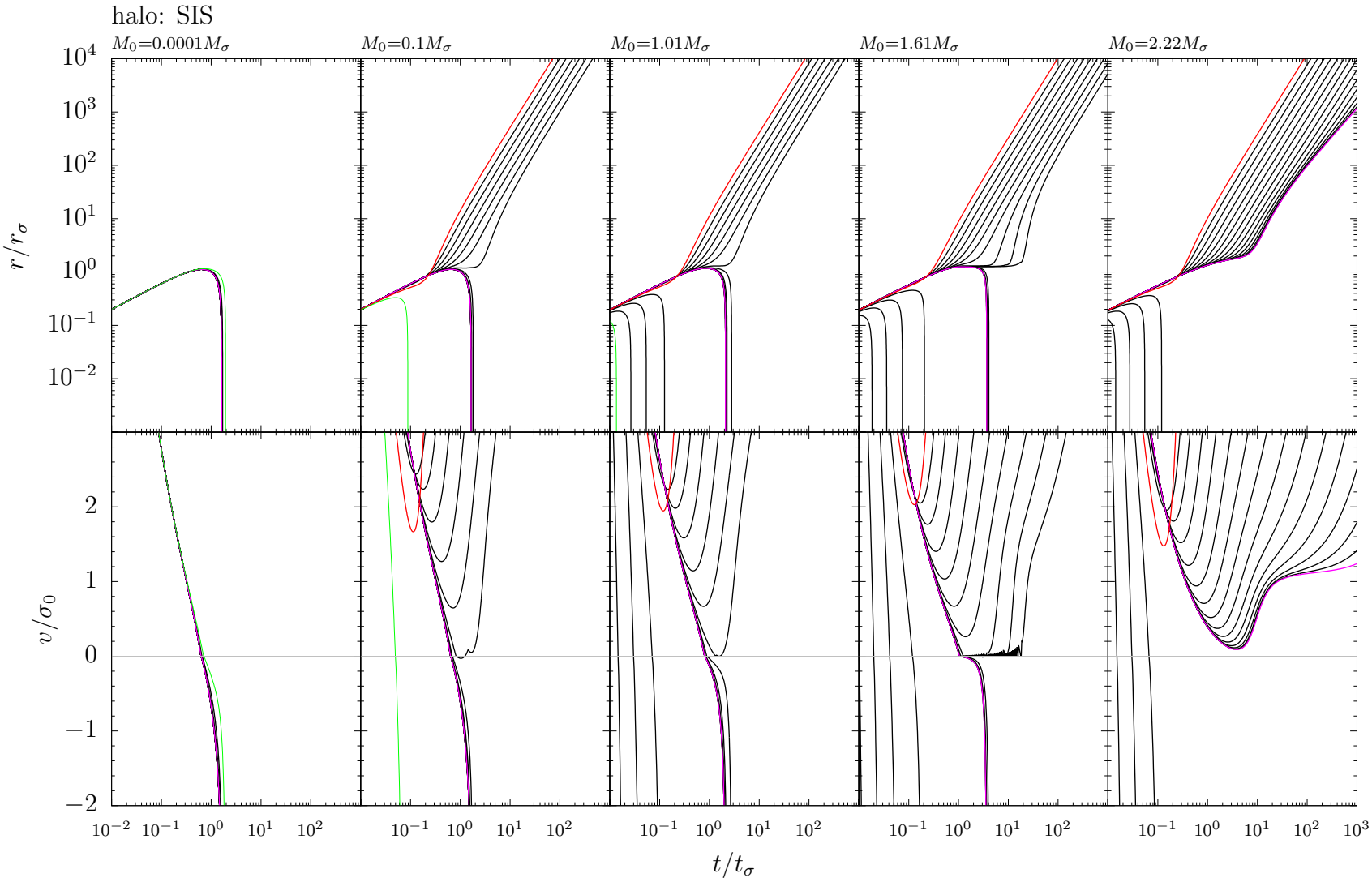

Figure 4.3: Velocity fields against time for momentum-driven shells driven by a constantly growing wind ($\alpha = 1$) with varying time parameter t_s in an SIS halo. The solutions shown correspond to variation in t_s over the range: $t_s = 10^{-4}$ (green curve) to 10^4 (magenta curve), with the red curve corrsponding to the solution with $t_s = 100t_\sigma$. The black curves have t_s values in logarithmic intervals between $10^{-4} - 10^4 t_\sigma$ which increase from the green to magenta curves, and for all solutions the initial momentum is $C = 4$.

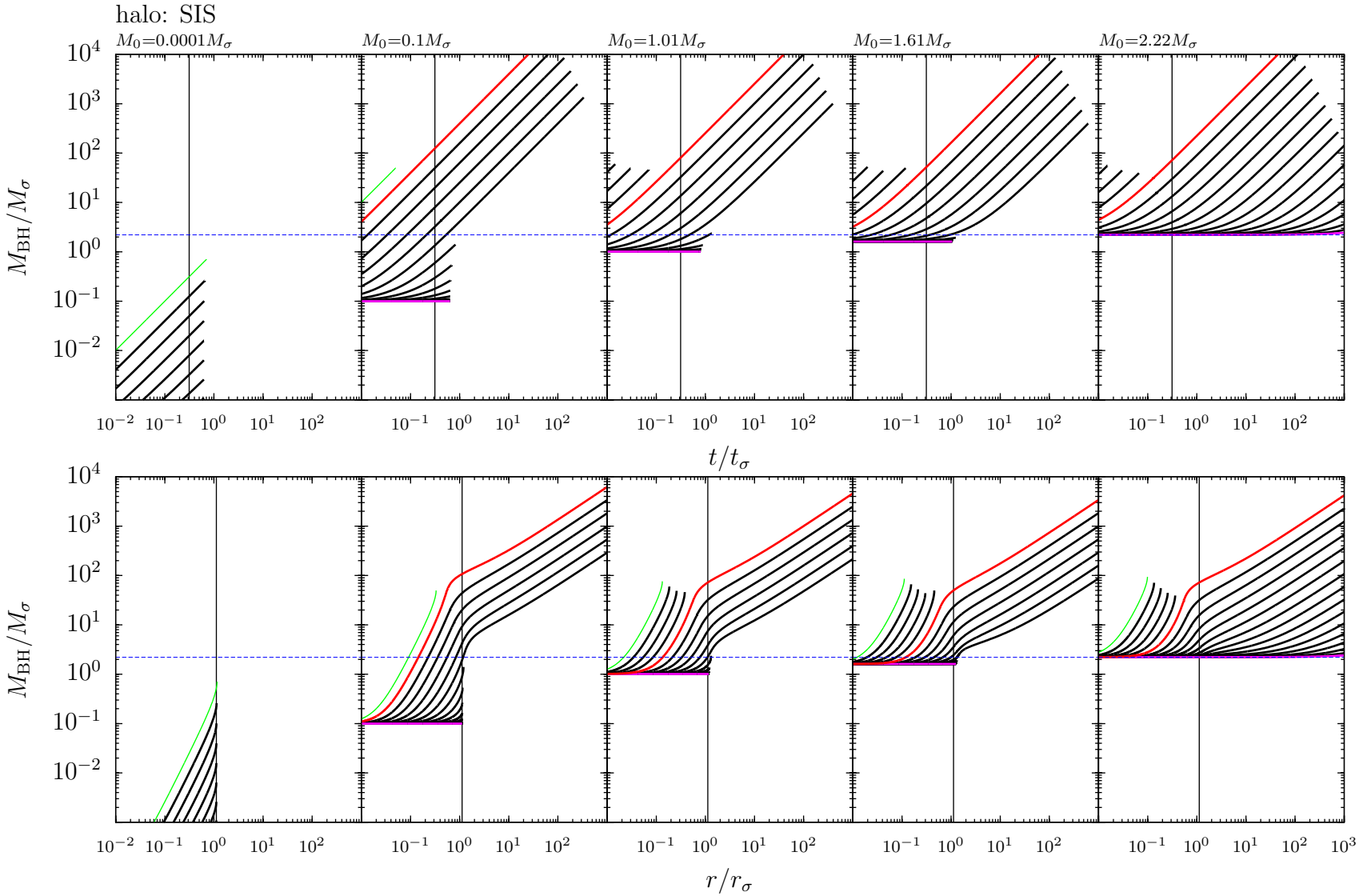

Figure 4.4: SMBH mass against time and shell radius for momentum-driven shells driven by a constantly growing wind ($\alpha = 1$) with varying time parameter t_s in an SIS halo. The same range in values from Figure 4.3 are displayed.

In order to understand how things change by introducing a growing SMBH, Figure 3.2 in Section 3.2.2 is to be re-examined for non-steady winds, and this is shown in Figure 4.5. It shows for an initial momentum of $C = 4$ the steady wind case in the top panel, and the middle and bottom panels show the $\alpha = 1$ and exponential cases respectively. It is shown that the stall ($v = 0$) curves for the constant mass case are still effectively those for the growing mass cases, and that the SMBH mass is required to exceed $M_{\rm BH,low}$ at $x_{\rm stall}$ in order to reach large radii.

SMBH Masses for the Escape of a Shell

As in Section 3.2.2 a necessary mass for escape can be defined by simply requiring that the square of the shell's velocity is positive at large radii. Here instead a necessary mass can be obtained which results in the square of the shell's radius being positive at late times $\widetilde{t} \gg 1$. For times when $t \gg \alpha t_s$ in order to have positive shell radii equation (4.31) requires that:

$$\frac{4\widetilde{M}_0 \widetilde{t}_s^2 \alpha^2}{(\alpha+1)(\alpha+2)} \left(\frac{\widetilde{t}}{\widetilde{t}_s \alpha} \right)^{\alpha+2} > (3+f_0)\, \widetilde{t}^{\,2} \qquad (\widetilde{t} \gg \widetilde{t}_s\alpha; \widetilde{t} \gg 1)\,. \tag{4.36}$$

This leads to:

$$\left(\frac{\widetilde{t}}{\widetilde{t}_s \alpha} \right)^{\alpha} > \frac{(\alpha+1)(\alpha+2)\,(3+f_0)}{4\widetilde{M}_0} \qquad (\widetilde{t} \gg \widetilde{t}_s\alpha; \widetilde{t} \gg 1)\,. \tag{4.37}$$

This can be rearranged to show that:

$$\widetilde{M}_{\rm BH}(\widetilde{t}) = \widetilde{M}_0 \left(\frac{\widetilde{t}}{\alpha \widetilde{t}_s} \right)^{\alpha} > \frac{(\alpha+1)(\alpha+2)}{2} \widetilde{M}_{\rm crit} \qquad (\widetilde{t} \gg \widetilde{t}_s\alpha; \widetilde{t} \gg 1)\,, \tag{4.38}$$

where $\widetilde{M}_{\rm crit} = (3+f_0)/2$ is the SMBH mass required to have a real shell solution at large radii in the constant SMBH mass case (see Section 3.2.2).

Equation (4.38) states that in order to have a real shell solution at large radii it is required that the growing SMBH mass exceeds the constant SMBH mass that was required to have a real shell solution at large radii for a steady wind. The steady

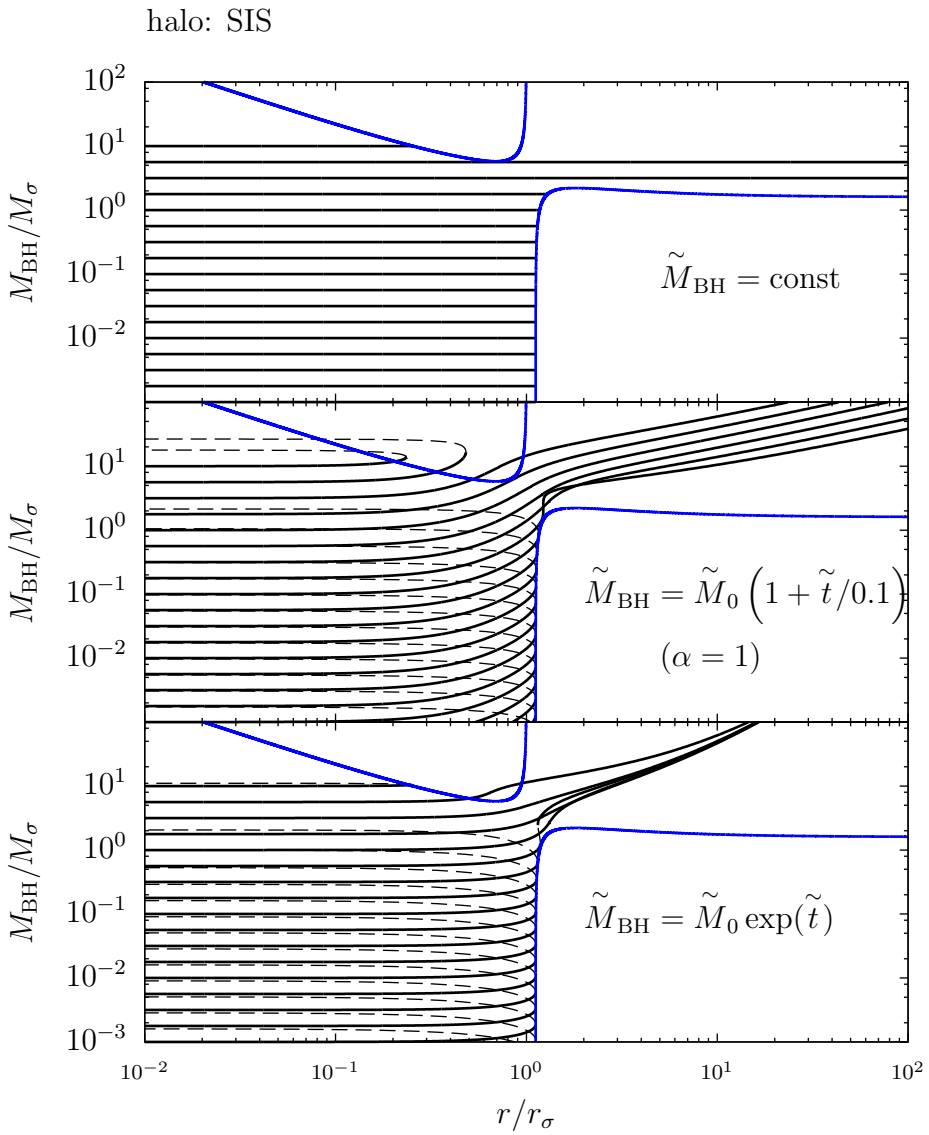

Figure 4.5: SMBH mass with three different functional forms plotted against shell radius for momentum-driven shells in an SIS halo. Each curve has a different value of $\widetilde{M}_{\rm BH}$ (or $\widetilde{M}_0$ in the non-steady cases). The blue curve shows $\widetilde{v}^2 = 0$ for the constant SMBH mass case, with $C = 4 > 3 + f_0$.

wind result is recovered by taking $\alpha \to 0$. For lower values of α it is the case that the necessary mass to have real solutions at large radii is not dissimilar from the constant mass case. However, for larger values of α equation (4.38) requires SMBH masses to be much higher than any observed.

Equation (4.38) can be rearranged for the seed mass:

$$\widetilde{M}_0 = \frac{(\alpha+1)(\alpha+2)\,(3+f_0)}{4}\left(\frac{\widetilde{t}_s\alpha}{\widetilde{t}}\right)^{\alpha} \qquad (\widetilde{t} \gg \widetilde{t}_s\alpha; \widetilde{t} \gg 1)\,, \tag{4.39}$$

which shows that if there is a fixed critical time for all shells like that indicated by Figure 4.4, then the required seed mass values for shells to reach large radii without stalling will have the proportionality: $M_0 \propto t_s^{\alpha}$.

The results from numerically integrating the equation of motion (4.21) to find the necessary and sufficient seed masses $\widetilde{M}_0$ which permit a shell to reach large radii with and without stalling (respectively) are shown in Figure 4.6 for three α values; $\alpha = 0.1$ for a declining SMBH growth rate, $\alpha = 1$ for the constant rate, and the exponential mass case. Three values of initial momentum are selected: $C = 3.21$ which is the minimum allowed initial momentum in the constant mass case (see expression for $C_{\rm esc}$ in Section 3.2.2), and $C = 4, 10$ to show the results for larger initial momentum. It is important to note that if the initial momentum is decreased below $C = 3.21$ then the faster growing SMBHs with lower t_s can still reach large radii without stalling. As the value of C is decreased this limits escape to all but the smallest t_s cases.

In Figure 4.6 the solid coloured lines are the sufficent seed masses which lead to shells which never stall, and the solid black lines in close proximity to these are the necessary masses which correspond to solutions that are able to stall but ultimately reach large radii. As shown in Figure 4.1 the necessary seed masses may lead to shells which stall and become pressure confined but ultimately escape, or shells which stall and are pushed back out by the increasing wind force. The constant SMBH mass required for escape is indicated by the magenta line, and it can be seen that for larger values of the growth timescale t_s that the seed masses required to reach large radii without stalling are not fundamentally different from the constant SMBH mass required for escape. It can also be seen that the $\widetilde{M}_0$ permitting escape does have the $\widetilde{t}_s^{\alpha}$ dependence indicated by equation (4.39).

Figure 4.6 shows for the rapidly growing SMBHs that the sufficient seed mass for escape and the growth timescale t_s are related by a constant factor, and it is evident

that this factor is dependent on the initial momentum. Although it has already been concluded that the critical mass for escape continues to be $M_{\rm BH,low}$ for moderately growing SMBHs, an expression for a sufficient seed mass will be derived which will attempt to reflect the relationship between M_0 and t_s which permit shells to reach large radii without stalling.

This can be achieved by using the expression for the stall time given by equation (4.35) which effectively assumes a steady wind. This was obtained by using equation (4.26) with the value for $x_{\rm stall}$ appropriate for small SMBHs in the case of steady winds. This timescale was shown to be less than the actual time at which shells encountered $x_{\rm stall}$ in Figure 4.4. Therefore if it is required that the SMBH mass exceeds $M_{\rm BH,low}$ at this earlier time, then the SMBH mass will certainly exceed $M_{\rm BH,low}$ by the time it reaches $x_{\rm stall}$. Hence, by setting $M_{\rm BH}(t_{\rm stall}) = M_{\rm BH,low}$ leads to the following expression for the seed mass:

$$\widetilde{M}_0 = \widetilde{M}_{\rm BH,low}\left(1 + \frac{\sqrt{C}}{(6+2f_0)}\widetilde{t}_s\alpha\right)^{-\alpha}. \tag{4.40}$$

Any shell driven by an SMBH with this seed mass for a given α and t_s will be able to reach large radii. This is plotted alongside the necessary and sufficient masses for escape in Figure 4.6 and is shown as coloured dashed curves. Due to the selected time being earlier than the actual time at which shells reach $x_{\rm stall}$ it can be seen that equation (4.40) does overpredict the required seed mass for escape.

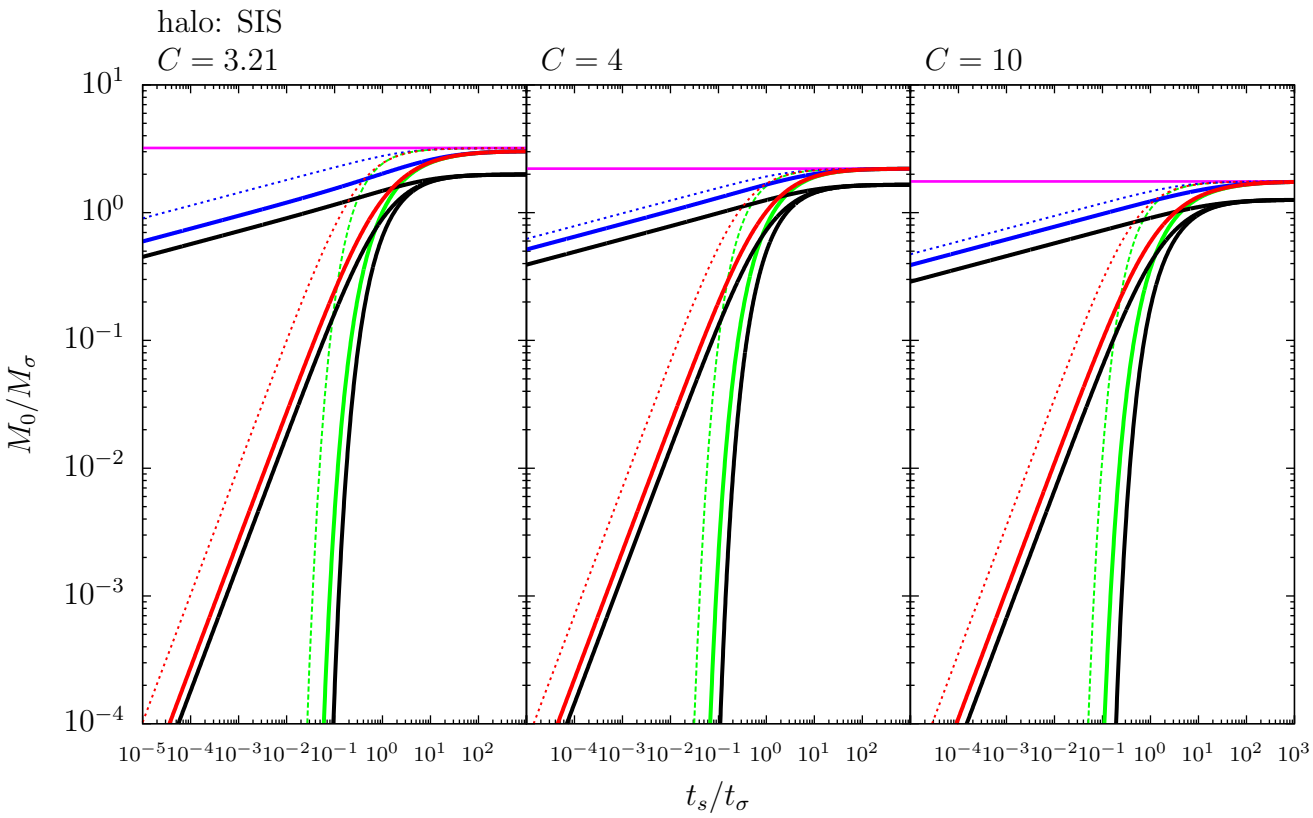

Figure 4.6: Necessary and sufficient seed masses M_0 against growth scale time t_s. The numerically determined sufficient values of M_0 which permit shells to escape without stalling for variation in t_s are shown as solid coloured curves, with $\alpha = 0.1$ shown in blue, $\alpha = 1$ shown in red, and the exponential growth case shown in green. The black curves in close proximity to these are the necessary values of M_0 which lead to shells that can stall and ultimately reach large radii. The magenta curve gives the sufficient SMBH mass required in the steady wind case. The dotted coloured curves are the derived sufficient values of M_0 given by equation (4.40). Each panel corresponds to a different value of initial momentum.

A further way of investigating what may be the required SMBH mass for escape is to find the value of $M_{\rm BH}(t)$ when the solutions shown in Figure 4.6 are at their lowest velocity, i.e. when the acceleration changes sign. This point will be where the shells start to accelerate and ultimately go on to reach large radii. The time $t_{\rm ex}$ at which this minimum in velocity occurs has been found for the solutions shown in Figure 4.6, and the SMBH mass at that time has been calculated over the range of t_s values. The results from this are presented in Figure 4.7. This shows that for the plotted range of t_s that the SMBH mass $M_{\rm BH}(t_{\rm ex})$ at the point of lowest velocity for shells which barely escape without stalling is close to the value required to reach large radii without stalling in the steady wind case: $M_{\rm BH,low} \simeq 2.21 M_\sigma$.

4.3.2 Hernquist Halo

Equation of Motion

For the Hernquist halo the dimensionless mass profile in terms of $x \equiv r/r_{\rm pk}$ is:

$$m(x) = \frac{4x^2}{(1+x)^2}\,, \tag{4.41}$$

as introduced in Section 3.2.3. The ambient gas pressure was also derived in Chapter 3, and it was found to be:

$$\widetilde{P}_g(x) = \frac{16(1+f_0)}{\pi}\left[\ln\left(1+\frac{1}{x}\right) - \frac{12x^3+42x^2+52x+25}{12(1+x)^4}\right]. \tag{4.42}$$

Using these expressions with the equation of motion (4.16) gives:

$$\begin{aligned}\frac{d}{d\widetilde{t}}\left[\frac{4x^2}{(1+x)^2}\widetilde{v}\right] =& 2\widetilde{M}_{\rm BH}(\widetilde{t}) - 64(1+f_0)x^2\left[\ln\left(1+\frac{1}{x}\right) - \frac{12x^3+42x^2+52x+25}{12(1+x)^4}\right] \\ & - \frac{8}{(1+x)^2}\left[\frac{\widetilde{M}_{\rm BH}(\widetilde{t})}{\widetilde{M}_{\rm pk}} + \frac{4x^2}{(1+x)^2}\right].\end{aligned} \tag{4.43}$$

If the shell stalls and the acceleration at the stall point is negative then the shell will begin to infall. If the shell infalls faster than the ambient gas then equation (4.17) with

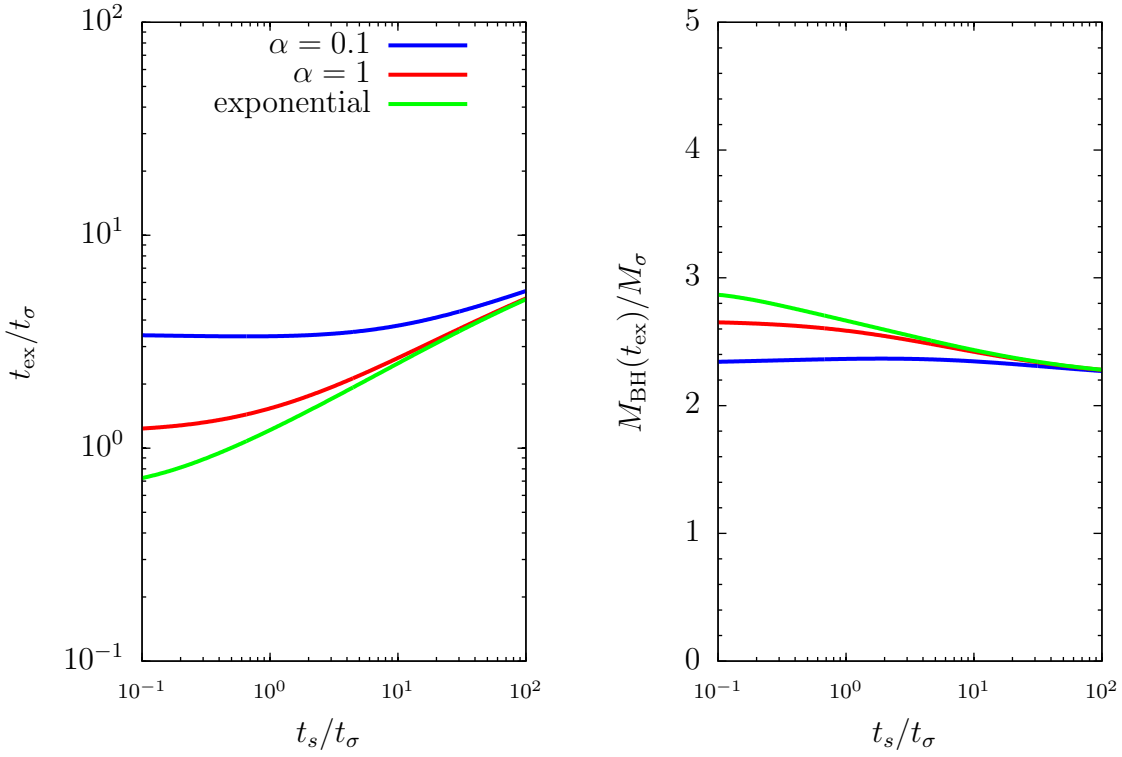

Figure 4.7: Times $t_{\rm ex}$ and SMBH masses at velocity field minima for shells which are just able to accelerate without stalling in an SIS halo plotted against growth scale time t_s. The blue curves show solutions with $\alpha = 0.1$, the red with $\alpha = 1$, and the green with the exponentially growing SMBH mass. The scale time for $\sigma_0 = 200$ km s^{-1} is $t_\sigma \simeq 2.5 \times 10^5$yr.

equations (4.41) and (4.42) gives:

$$\frac{4x_{\rm stall}^2}{(1+x_{\rm stall})^2}\frac{d\widetilde{v}}{d\widetilde{t}} = 2\widetilde{M}_{\rm BH}(\widetilde{t}) - \frac{8}{(1+x)^2}\left[\frac{\widetilde{M}_{\rm BH}(\widetilde{t})}{\widetilde{M}_{\rm pk}} + \frac{4x^2}{(1+x)^2}\right] . \qquad (4.44)$$

Salpeter Time

For the Hernquist halo all times are normalised to $t_\sigma \equiv r_{\rm pk}/\sigma_0$ which is:

$$t_\sigma \equiv \frac{r_{\rm pk}}{\sigma_0} \simeq 2.4 \times 10^8 \text{ yr} \left(\frac{r_{\rm pk}}{50 \text{ kpc}}\right)\left(\frac{200 \text{ km s}^{-1}}{\sigma_0}\right) . \qquad (4.45)$$

This means that the Salpeter time given by equation (4.4) in units of t_σ will be of order $\widetilde{t}_s \sim 0.1$. Combining equations (4.4) with (4.45) gives:

$$\frac{t_s}{t_\sigma} = \frac{\eta\kappa c\sigma_0}{4\pi q G r_{\rm pk}} \simeq 0.18 \left(\frac{\eta}{0.1}\right)\left(\frac{\kappa}{0.04}\right)\left(\frac{1}{q}\right)\left(\frac{\sigma_0}{200\ {\rm km\ s^{-1}}}\right)\left(\frac{50\ {\rm kpc}}{r_{\rm pk}}\right). \qquad (4.46)$$

By considering the typical range in the scale values an appropriate range for $\widetilde{t}_s$ would be $10^{-2} - 10^0$, but this will be extended in order to account for all possible shell behaviours. A similar range to that used for the SIS halo will be adopted for $\widetilde{t}_s$ in the case that equation (4.5) is used.

Asymptotics

At early times such that $\widetilde{t} \ll \widetilde{t}_s\alpha$ the SMBH mass tends to the value of its seed mass. If the shell begins with an initial non-zero momentum (the square of which is denoted C) then the shell radius at early times is:

$$x(\widetilde{t}) = \left[\frac{3\sqrt{C}\widetilde{t}}{4}\right]^{1/3} \qquad (\widetilde{t} \ll \widetilde{t}_s\alpha;\ C > 0), \qquad (4.47)$$

The $C = 0$ solution for the shell radius is:

$$x(\widetilde{t}) = \left[\frac{3\widetilde{M}_0}{4}\left(1 - \frac{4}{\widetilde{M}_{\rm pk}}\right)\widetilde{t}^2\right]^{1/3} \qquad (\widetilde{t} \ll \widetilde{t}_s\alpha;\ C = 0), \qquad (4.48)$$

which was also derived in Section 3.2.3 (see that section for the early-time velocities).

At late times the wind force dominates the equation of motion since $m(x) \to 4$ for the Hernquist halo:

$$\widetilde{v}(\widetilde{t}) = \frac{\widetilde{M}_0\widetilde{t}_s\alpha}{2(\alpha+1)}\left(\frac{\widetilde{t}}{\widetilde{t}_s\alpha}\right)^{\alpha+1} \qquad (\widetilde{t} \ll \widetilde{t}_s\alpha;\ \widetilde{t} \gg 1), \qquad (4.49)$$

which leads to the large scale shell radius:

$$x(\widetilde{t}) = \frac{\widetilde{M}_0(\widetilde{t}_s\alpha)^2}{2(\alpha+1)(\alpha+2)}\left(\frac{\widetilde{t}}{\widetilde{t}_s\alpha}\right)^{\alpha+2} \qquad (\widetilde{t} \ll \widetilde{t}_s\alpha;\ \widetilde{t} \gg 1), \qquad (4.50)$$

This radius has the same dependence on time as the momentum-driven solution for a shell which is not subject to gravity obtained in Section 2.2.2, and this can be shown by setting $p = 0$ at late times in equation (2.17) as required for the Hernquist halo. Equation (4.50) recovers equation (3.59) for $\alpha \to 0$ and the exponential SMBH mass case if $\alpha \to \infty$ (which can be obtained by assuming exponential form throughout):

$$x(\tilde{t}) = \frac{\tilde{M}_0}{2} e^{t/\tilde{t}_s} \qquad (\tilde{t} \gg 1)\,. \tag{4.51}$$

It can be seen from equation (4.47) that at early times the shell is decelerating while at late times equations (4.50) and (4.51) show that the shell is accelerating. This indicates the presence of at least one minimum in the shell's velocity fields where the acceleration changes sign.

Variation in α: Infall and Re-Expansion for Momentum-Driven Shells

Equation (4.43) has been solved numerically for the SMBH mass given by equations (4.5) and (4.7). The velocity fields are shown as functions of time and radius in Figure 4.8. Since the effects of ambient pressure were shown in Section 3.2.3 to be significant for a momentum-driven shell which stalls, in order to isolate the effects occurring from the growth of the SMBH Figure 4.8 shows the results of varying α with ambient pressure included (top row) and with ambient pressure neglected (bottom row). To better observe the detailed behaviour of the solutions, specific values of α are selected: $\alpha = 0$ (magenta curve) for a constant SMBH mass, $\alpha = 1$ (red curve) for a constantly growing SMBH, an exponential SMBH mass (green curve), and some intermediate values of α selected to display the full range of shell behaviours. For the Hernquist halo a wider range of seed mass values can be explored which lead to shells that escape than was available for the SIS halo, and therefore the range is selected to be from $M_0 = 0.0001 - 1.4 M_\sigma$. A single value of the growth timescale $t_s = 0.1 t_\sigma$ is selected as this is close to the value of the Salpeter time in units of t_σ. A single value of initial momentum $C = 0$ is selected for all shell solutions, and a single value is taken for the mass of dark matter at $r_{\rm pk}$: $M_{\rm pk} = 4000 M_\sigma$. The plotted range is $r = 10^{-4} - 100 r_{\rm pk}$ which for a typical value of $r_{\rm pk} \simeq 50$ kpc gives a plotted range from 5pc to 5000kpc.

Figure 4.8 shows that there are four distinct possible outcomes for a momentum-driven shell driven by a growing wind force in a Hernquist halo: (1) the shell stalls and directly infalls back to the SMBH, (2) the shell stalls repeatedly and eventually infalls back to the SMBH (low seed mass solutions in black), (3) the shell stalls multiple times and goes on to reach large radii (low seed mass solutions in blue), (4) the shell never stalls and reaches large radii.

In the case that ambient pressure is neglected the introduction of a growing SMBH has therefore brought about two new outcomes for the shell which were not experienced by shells driven by steady winds. The ability of the shell in the absence of ambient pressure to stall during infall and resume outward motion is not possible for a shell driven by a steady wind. For a growing wind it can be seen that this can lead to temporary support at a specific radius by the wind before the shell ultimately infalls or escapes. Aside from the rapidity of the stalling around a point of confinement it can be seen (particularly for the lowest seed mass) that the overall behaviour with and without ambient pressure is very similar. The primary difference being that the strength of the impulse on the shell (shown as increasing velocity) as it makes slow progress increases if ambient pressure is present but decreases if it is not. If the shell is subject to ambient pressure this increasing impulse occurs because the shell has a very small infall time before it is pushed back into the ambient gas, and therefore each time this happens the wind force has grown by a small amount. If the shell is not subject to ambient pressure then the strength of the force on the shell when it reencounters the ambient medium has increased, but the size of the increase is determined by the length of infall time before the shell resumes outward motion. For an increasing wind force the infall time decreases, and therefore the change in force between stalling an re-encountering the ambient medium decreases in time.

It can be seen that shells driven by growing winds do go on to accelerate at large radii, however this was also the case for shells driven by a steady wind (see Section 3.2.3). As was found for the SIS halo there is a smooth transition between the $\alpha = 0$ through $\alpha = 1$ to the exponential solutions. Focus can therefore be maintained on particular values of α without excluding any dynamically distinct cases.

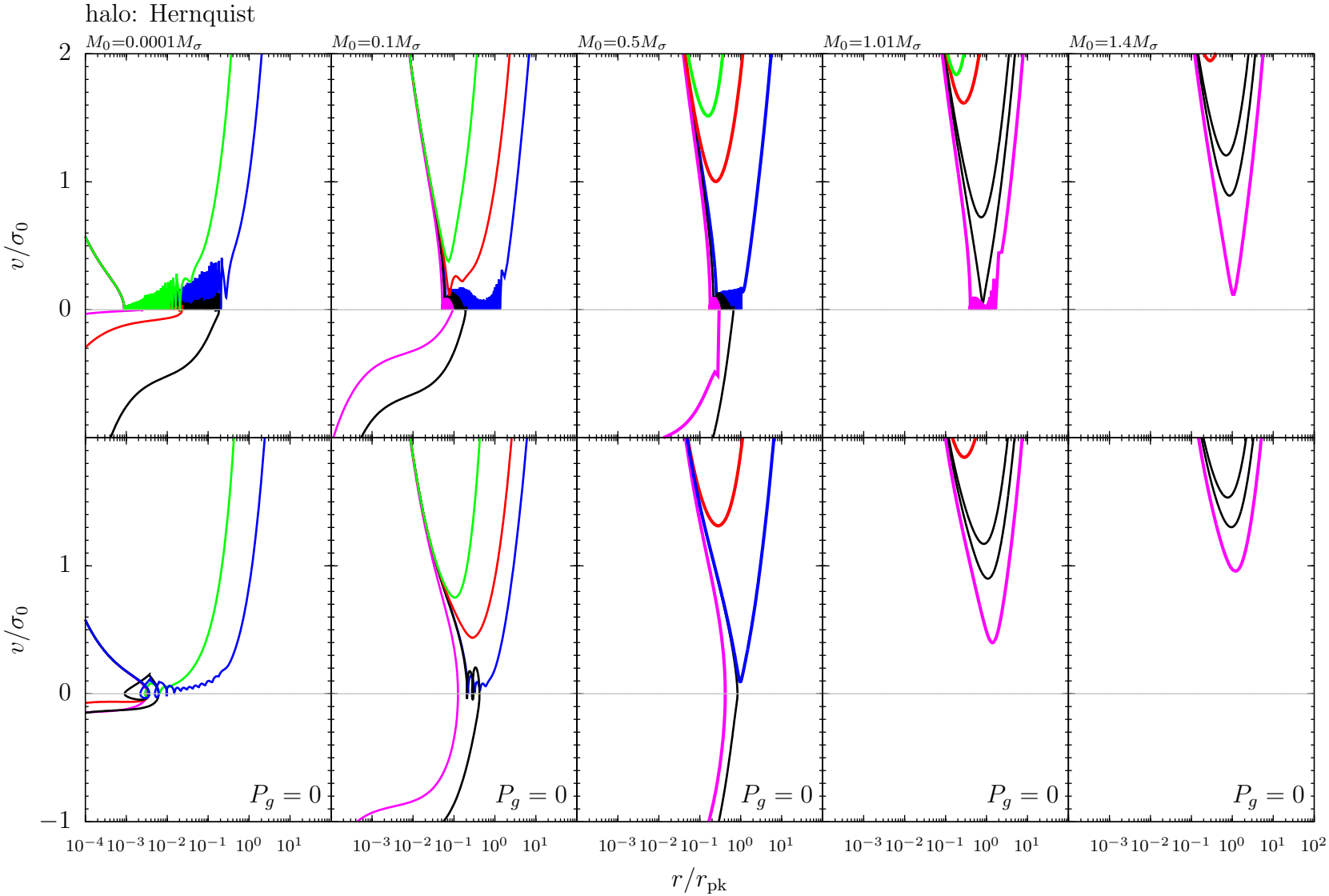

Figure 4.8: Velocity fields against radius for momentum-driven shells from steady and non-steady winds with a varying time parameter α in a Hernquist halo. The $\alpha = 0$ case is shown in magenta, the $\alpha = 1$ case in red, and the exponential SMBH mass case is shown in green. The blue curves correspond to the case where the shell stalls but ultimately escapes. The black curves correspond to α values between zero and one.

Variation in the Growth Timescale: $\mathbf{t_s}$

As was carried out for the SIS halo the next step is to analyse how the solutions change with variation in the growth timescale t_s. For the exponential SMBH mass the variation in t_s corresponds to variation in the Salpeter time. Physically this corresponds to changes in the accretion efficiency of the SMBH or changes to its accretion rate relative to the Eddington rate (see Section 1.1.4). The equation of motion (4.43) has been solved numerically for shell solutions driven by an exponentially increasing SMBH wind for a range in Salpeter times, and the results are shown in Figure 4.9. The range in the Salpeter times has been taken to be $0.0001t_\sigma < t_s < 1000t_\sigma$. The solutions with $t_s = 0.0001t_\sigma$ are shown as green curves, and those with $t_s = 1000t_\sigma$ are shown as magenta curves. The physically interesting case of $t_s = 0.2t_\sigma$ is represented by the red curves.

The range in seed masses is chosen to show the cases where the solution with $t_s = 0.2$ stalls but ultimately escapes ($M_0 = 0.0001M_\sigma$), where it narrowly avoids stalling ($M_0 = 0.1$), and where its minimum in velocity has a value of $v \sim \sigma_0$ ($M_0 = 0.5M_\sigma$). The seed masses $M_0 = 1.01M_\sigma$ and $M_0 = 1.4M_\sigma$ show the cases where the smallest value of t_s (for an approximately constant SMBH) stalls but ultimately reaches large radii, and where it reaches large radii without stalling respectively. For all solutions $M_{\rm pk} = 4000M_\sigma$ and the value of $C = 0$ has been chosen, but for higher values of C the same shell behaviour is exhibited but typically with higher velocities (see Section 3.2.3 for a review of varying this parameter).

It can be seen from Figure 4.9 that there is a combination of M_0 and t_s which allows a shell to reach large radii without stalling. The constant SMBH mass required in order to reach large radii without stalling was found in Section 3.2.3 to be $M_{\rm BH} \simeq 1.4M_\sigma$ (see Figure 3.11). For the solution with a Salpeter time of $t_s = 0.2t_\sigma$ a seed mass which is less than a tenth of this value is large enough to guarantee the shell reaches large radii without stalling. It has been confirmed numerically that the required seed mass value for $t_s = 0.2t_\sigma$ to have a shell reach large radii without stalling is $M_0 \simeq 0.09M_\sigma$.

In order to explore the relationship between sufficient values of t_s and M_0 further,

the equation of motion (4.43) has been solved for the case that the SMBH grows at a constant rate ($\alpha = 1$) and the results are shown in Figure 4.10. The same range of t_s is considered as was used in the exponential case, and the same seed mass values have also been used. The initial momentum is again set to $C = 0$.

The overall shell dynamics for $\alpha = 1$ are very similar to the exponential case with the strongest apparent difference being a higher number of stalling shells for the smallest seed mass case. Unlike the SIS case there are no solutions which stall due to growing too rapidly. This is because the gravitational force of the SMBH on the shell in the Hernquist halo is much weaker than in the SIS due to the lower shell mass at small radii. Figures 4.9 and 4.10 both show that there must be a specific combination of M_0 and t_s which allow shells to reach large radii without stalling. This implies that there is a specific SMBH mass $M_{\rm BH}(t)$ which must be exceeded at a given time in order for the shell not to stall, and that the required t_s enables the SMBH to acquire this value before stalling. In order to investigate this further the SMBH mass for each of the shell solutions is to be plotted against time and radius.

Figure 4.11 shows the same exponential SMBH mass solutions as Figure 4.9, and as before the red curve corresponds to the $t_s = 0.2t_\sigma$ case. The same range in seed masses is used as before, and $C = 4$ for all solutions. Any post-stall shell behaviour is excluded from the diagram. The horizontal dashed blue lines show the sufficient mass required for escape in the constant mass case: $M_{\rm BH} \simeq 1.4M_\sigma$ as found in Section 3.2.3. The solid blue lines are the analytical $v = 0$ curves for the steady wind case in the absence of ambient pressure. These are obtained from the full solution for the velocity of a momentum-driven shell (see McQuillin & McLaughlin 2012):

$$\begin{aligned}\widetilde{v}^2 = \widetilde{M}_{\rm BH}\left(\frac{1+x}{x}\right)^4\left[1+x-\frac{1}{1+x}-2\ln(1+x)\right] \\ +\left(\frac{C}{16}-\frac{4}{3}\frac{\widetilde{M}_{\rm BH}}{\widetilde{M}_{\rm pk}}\right)\frac{1+x}{x}-\frac{16}{5}\frac{x}{1+x}\,.\end{aligned} \tag{4.52}$$

Equation (4.52) can be set to zero and rearranged for the SMBH mass:

$$\widetilde{M}_{\rm BH}(x_{\rm stall}) = \left(\frac{C}{16}\frac{1+x}{x} - \frac{16}{5}\frac{x_{\rm stall}}{1+x_{\rm stall}}\right) \times \left\{\frac{4}{3}\frac{1+x_{\rm stall}}{\widetilde{M}_{\rm pk}x_{\rm stall}} - \left(\frac{1+x_{\rm stall}}{x_{\rm stall}}\right)^4\left[1+x_{\rm stall} - \frac{1}{1+x_{\rm stall}} - 2\ln(1+x_{\rm stall})\right]\right\}^{-1}, \quad (4.53)$$

giving the SMBH mass leading to a stall in terms of stall radius $x_{\rm stall}$. Note that all of this assumes that ambient pressure is negligible which explains why the curves in Figure 4.11 do not touch the numerically determined solutions which included ambient pressure. The solutions which exclude ambient pressure are shown in greater detail in Figure 4.12 where it can be seen that the escaping solutions are in close proximity to the $v = 0$ curve.

Figure 4.11 shows that if there is a critical time or radius at which the shell must exceed a particular SMBH value then it clearly is not an approximately constant value as was found in the SIS halo for a nonzero value of initial momentum. It is to be noted also that the sufficient SMBH mass obtained in the constant mass case made use of the fact the minima in the velocity fields of all shells occurred at $r_{\rm pk}$ (McQuillin & McLaughlin 2012). If growing SMBHs are included in the equation of motion then this is no longer the case as shown in Figures 4.8, 4.9, and 4.10.

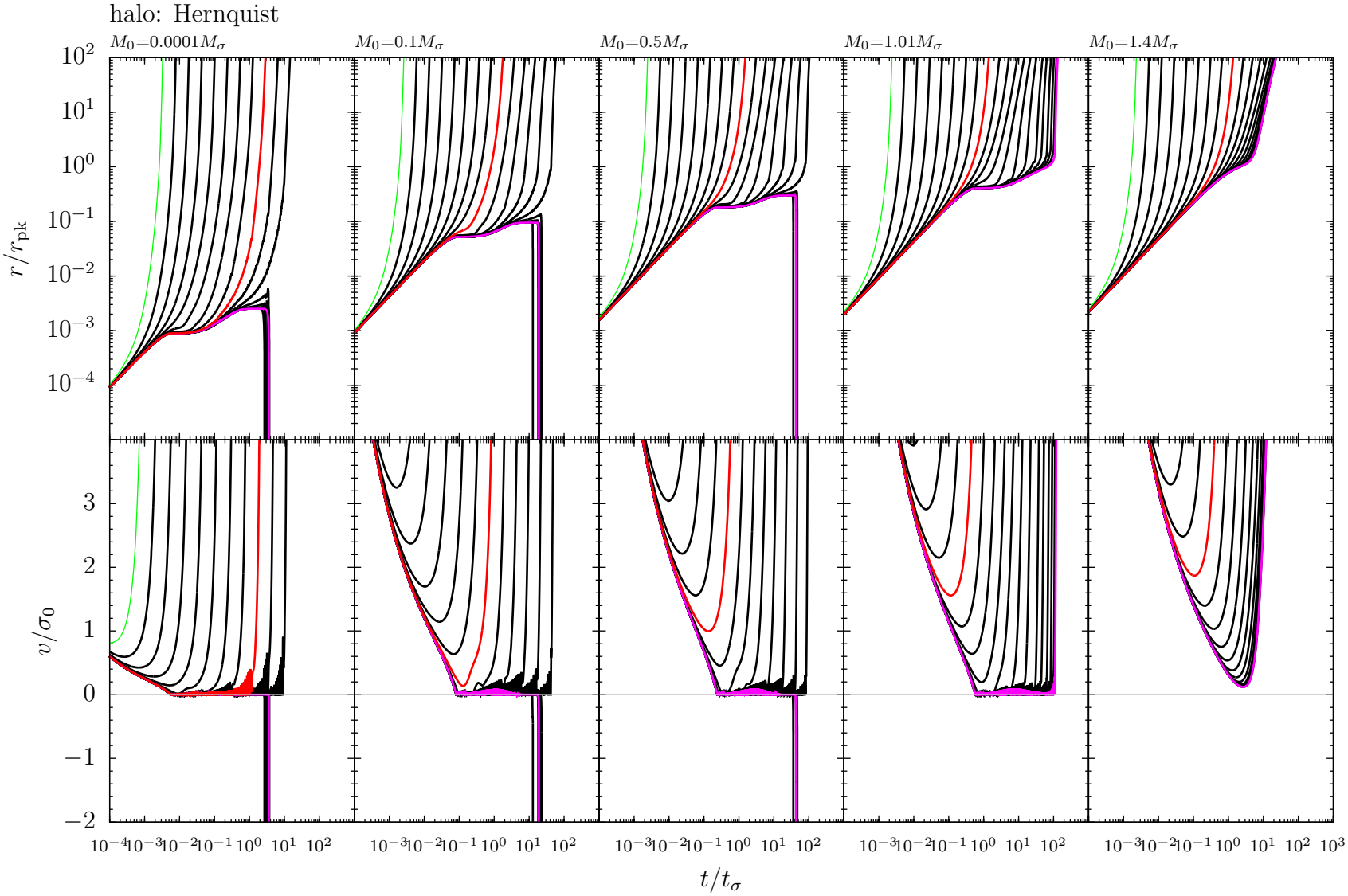

Figure 4.9: Velocity fields against time for momentum-driven shells driven by an exponentially growing SMBH wind with varying time parameter in a Hernquist halo. The solutions with $t_s = 0.0001t_\sigma$ are shown as green curves, those with $t_s = 1000t_\sigma$ are the magenta curves, and those with $t_s = 0.2t_\sigma$ are the red curves. The black curves have t_s values in logarithmic intervals between $10^{-4} - 10^3 t_\sigma$ which increase from the green to red to magenta curves.

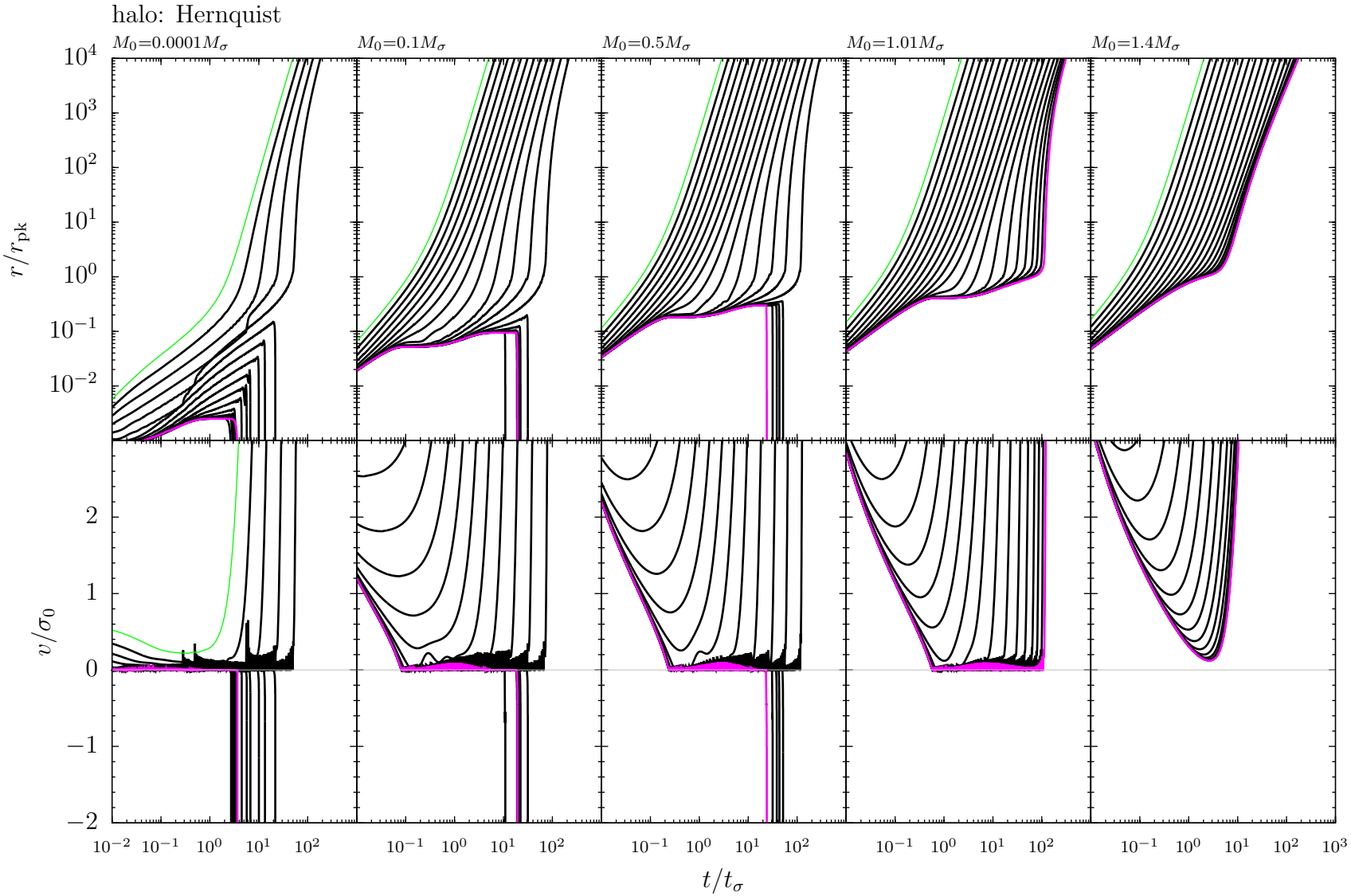

Figure 4.10: Velocity fields against time for momentum-driven shells driven by a constantly growing wind ($\alpha = 1$) with varying time parameter t_s in a Hernquist halo. The solutions with $t_s = 0.0001t_\sigma$ are shown as green curves, and those with $t_s = 1000t_\sigma$ are the magenta curves. The black curves have t_s values in logarithmic intervals between $10^{-4} - 10^3 t_\sigma$ which increase from the green to magenta curves.

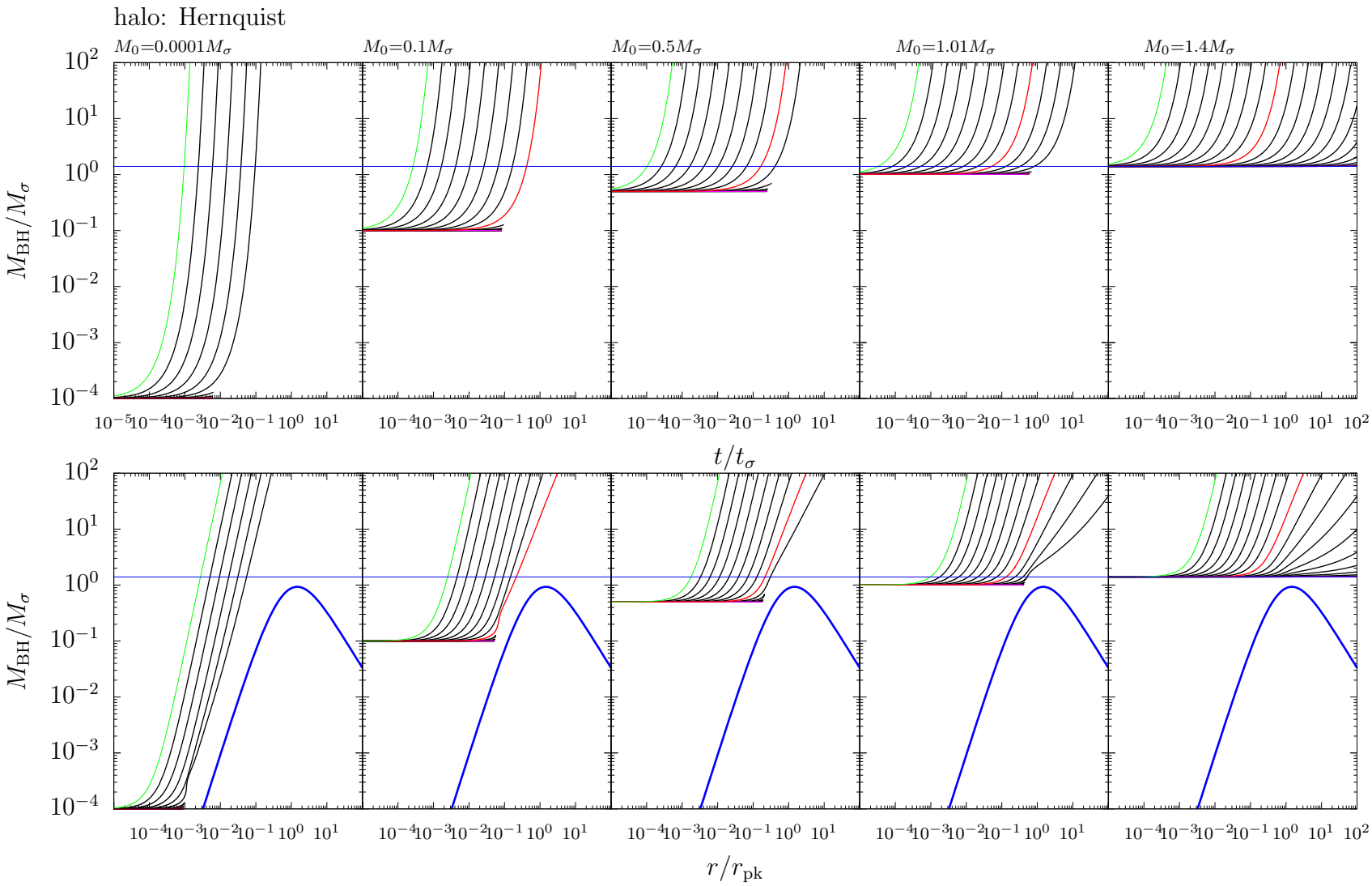

Figure 4.11: SMBH mass against time and shell radius for momentum-driven shells driven by an exponentially growing wind with varying time parameter in a Hernquist halo. The solutions with $t_s = 0.0001t_\sigma$ are shown as green curves, those with $t_s = 1000t_\sigma$ are the magenta curves, and those with $t_s = 0.2t_\sigma$ are the red curves. The blue curves correspond to $v = 0$ in the constant SMBH mass case. The black curves have t_s values in logarithmic intervals between $10^{-4} - 10^3 t_\sigma$ which increase from the green to red to magenta curves.

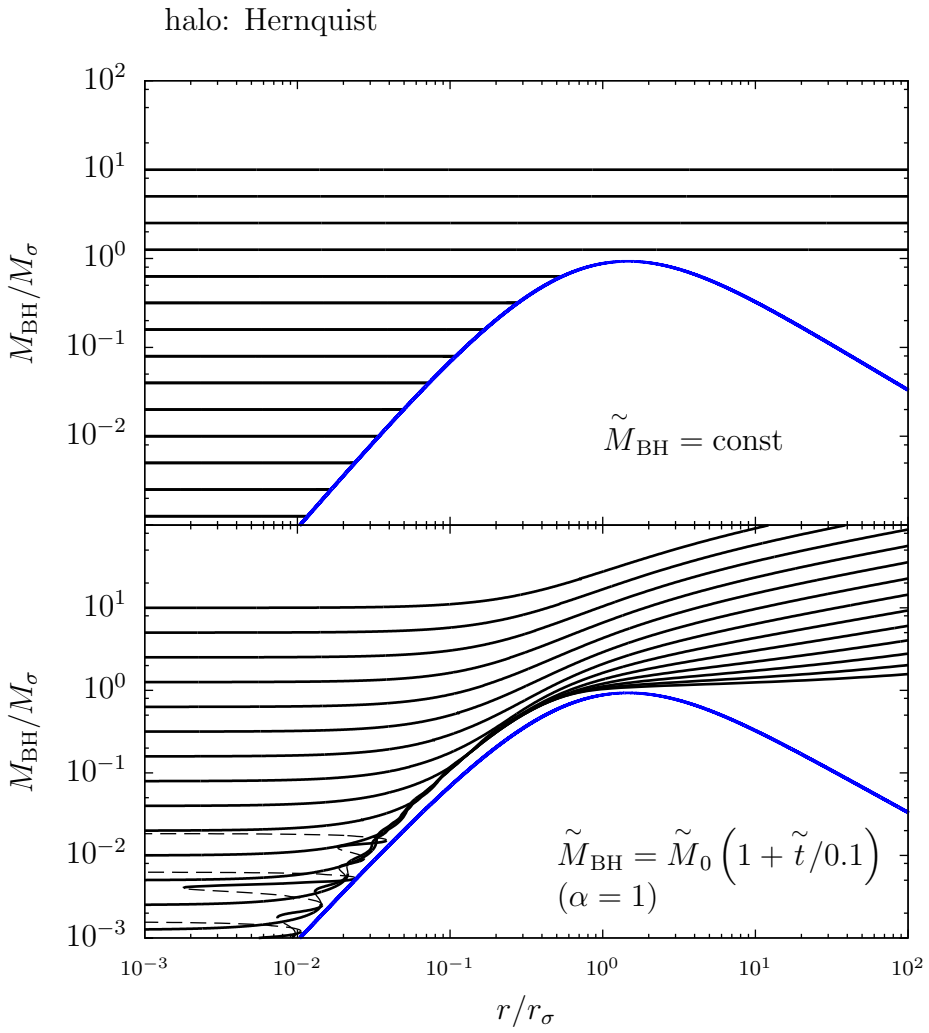

Figure 4.12: SMBH mass plotted against shell radius for a momentum-driven shell propagating within an Hernquist halo. The curves show a range of seed mass values $M_0 = 0.00001 - 10M_\sigma$, for the constant mass ($\alpha = 0$) and $\alpha = 1$ cases for the SMBH mass profile given by equation (4.5). Shown in blue is the $v = 0$ curve for the $\alpha = 0$ case, and dashed portions indicate that the shell is infalling. The initial momentum is chosen to be zero, and the Salpeter time is set to $t_s = 0.1t_\sigma$. Note that ambient pressure is excluded from the solutions presented.

Critical SMBH Masses

Equation (4.43) has been integrated numerically to find the necessary SMBH seed masses which lead to shells that may stall but ultimately reach large radii, and the sufficient SMBH seed masses which lead to shells that reach large radii without stalling. These solutions are shown in Figure 4.13 for the case that $C = 0$. For nonzero initial momentum the stall radius for constant mass shells tends to a finite value in the limit of small SMBH mass. Because of this the same approach as utilised for the SIS halo can be used to obtain a sufficient SMBH mass for shells launched with finite initial momentum in a Hernquist halo. It is important to emphasise that the sufficient SMBH seed masses are independent of any assumptions relating to the infall behaviour of shells. The coloured curves show the sufficient seed masses with $\alpha = 0.1$ as the blue curve, $\alpha = 1$ as the red curve, and the exponential case as the green curve. The black curves are the necessary seed masses which correspond to (from top-to-bottom) the values $\alpha = 0.1, 1$ and the exponential case.

The most prominent aspect of Figure 4.13 is that the necessary and sufficient masses are so wildly different. This occurs because of the effects shown in Figure 4.8 where shells can stall multiple times but still go on to reach large radii. The solutions also show the same $M_0 \propto t_s^{\alpha}$ scaling as was found for shells with nonzero initial momenta in the SIS halo, but this behaviour occurs at much lower seed mass values.

A further way of investigating what may be the required mass for escape is to find the value of $M_{\rm BH}(t_{\rm ex})$ when the solutions shown in Figure 4.13 are at their lowest velocity at the time $t_{\rm ex}$. This point will be where the shells will be close to stalling before they start to accelerate and ultimately go on to reach large radii. The time $t_{\rm ex}$ at which this minimum in velocity occurs and the SMBH mass at this time have been calculated for the solutions shown in Figure 4.6 over a range of t_s values. The results from this are presented in Figure 4.14. The results are quite different from those obtained in the SIS case. It is clearly shown that for lower values of t_s the SMBH mass can be far from the sufficient mass required in the steady wind case: $M_{\rm BH} \gtrsim 1.4 M_{\sigma}$ (see Section 3.2.3). However for lower values of α and for higher values of t_s the SMBH mass at $t_{\rm ex}$ is close to the sufficient mass in the steady wind case.

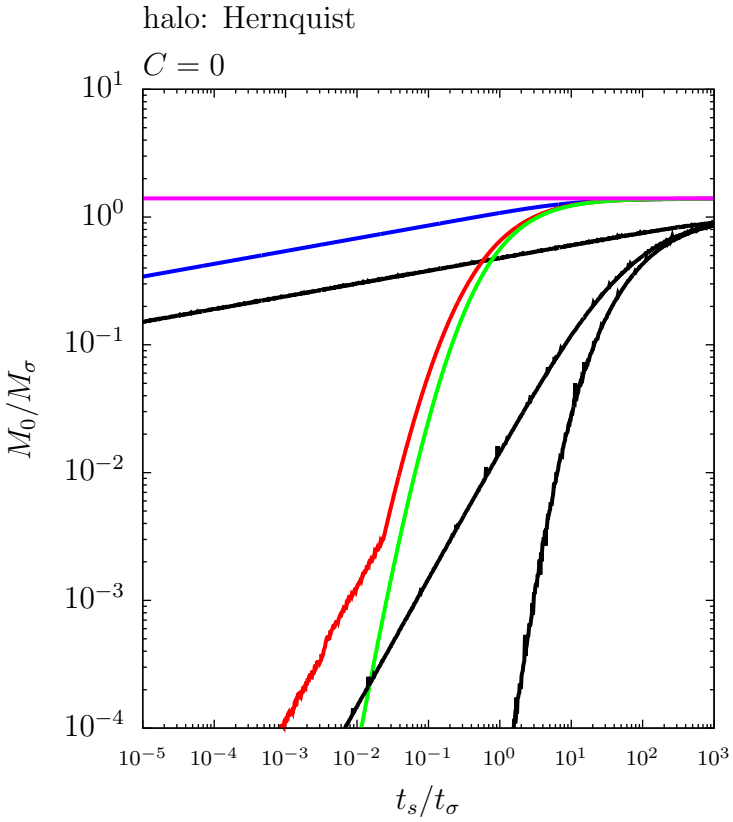

Figure 4.13: Necessary and sufficient seed masses M_0 which lead to momentum-driven shells that reach large radii in a Hernquist halo plotted against accretion scale time t_s. The coloured curves show the sufficient seed masses which lead to shells that never stall for the $\alpha = 0.1$ case (shown in blue) and the $\alpha = 1$ case (shown in red), and the exponential case (shown in green). The black curves from top-to-bottom ($\alpha = 0.1, 1$ and exponential) are the necessary seed masses which lead to shells that reach large radii but may stall many times before doing so. The magenta curve is the sufficient mass in the steady wind case.

4.3.3 Momentum-Boosts of Momentum-Driven Shells

The Singular Isothermal Sphere

An important aspect of shell dynamics to be addressed is whether the momentum-boost of the outflow is changed by the inclusion of a growing SMBH. This is especially important if the conclusions from Chapter 3 are to be generalised to the case of growing

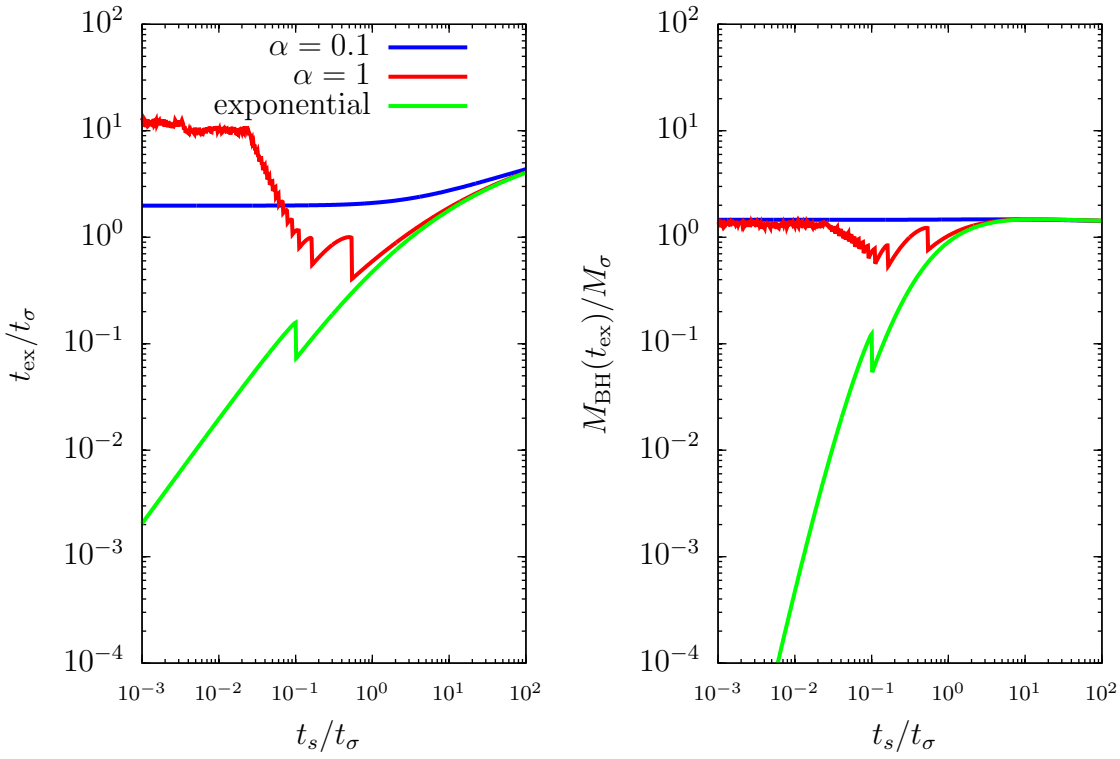

Figure 4.14: Times $t_{\rm ex}$ and SMBH masses $M_{\rm BH}(t_{\rm ex})$ at velocity field minima for shells which are just able to reach large radii without stalling in a Hernquist halo plotted against accretion scale time.

SMBHs. Figure 4.15 shows the momentum-fluxes and the observable $\dot{M}_{\rm sh}v$ (normalised to the wind force $\dot{p}_w$) for shells driven by an SMBH which grows at a constant rate ($\alpha = 1$) for a range of growth timescales t_s in an SIS halo. Each panel corresponds to a different seed mass M_0 value, and each curve corresponds to a different growth timescale t_s value. The green curves highlight the fastest growing case, the magenta curves the slowest growing case and the red curves are the solutions which separate shells which stall due to growing too quickly from those which do not stall.

It can be seen from Figure 4.15 that both quantities representing momentum boosting tend to a constant at large radii. The actual momentum-boosts $\dot{p}_{\rm sh}/\dot{p}_w$ all

tend to unity at large enough radii, whereas the quantity $\dot{M}_{\rm sh}v/\dot{p}_w$ tends to the value of 3/4. Therefore unlike the steady wind case where $\dot{p}_{\rm sh}$ and $\dot{M}_{\rm sh}v$ are equal at large radii (due to constant terminal speed) for a growing SMBH the two quantities differ by a factor of 3/4. This can be understood by looking at the value of $\dot{p}_{\rm sh}/\dot{p}_w$ from equation (4.21):

$$\frac{\dot{p}_{\rm sh}}{\dot{p}_w} = 1 - \frac{1-f_0}{2\widetilde{M}_{\rm BH}(\widetilde{t})} \qquad (\widetilde{t} \gg 1) \tag{4.54}$$

which tends to unity at late times with increasing SMBH mass.

The observable $\dot{M}_{\rm sh}v$ for the SIS scales like the square of the velocity. In normalised units $\dot{M}_{\rm sh}v$ is simply $\widetilde{v}^2$ for the SIS. Using the velocity given by equation (4.33) and dividing by the normalised wind force $2\widetilde{M}_{\rm BH}$ gives the momentum-boost at late times:

$$\frac{\dot{M}_{\rm sh}v}{\dot{p}_w} = \frac{\widetilde{v}^2}{2\widetilde{M}_{\rm BH}} = \frac{1}{2}\left(1 + \frac{1}{\alpha+1}\right) \qquad (\alpha > 0;\ \widetilde{t}_s \gg 1)\,. \tag{4.55}$$

In the limit that $\alpha \to 0$ this tends to unity, however in order to obtain this late time expression it was assumed that $\alpha > 0$, and therefore terms are missing. For $\alpha = 1$ the momentum-boost has a value of 3/4 as shown in Figure 4.15, and for $\alpha \to \infty$ this tends to a lower limit of 1/2. So for growing SMBHs the maximum momentum-boost as given by $\dot{M}_{\rm sh}v$ for momentum-driven shells will be between 1/2 and unity. This means that by using $\dot{M}_{\rm sh}v/\dot{p}_w$ as a proxy for the actual momentum-boost could lead to results which are out by up to a factor of 2. However, this deviation is less for the slower growing SMBHs as shown in Figure 4.15 by the magenta curve and those close to it. As was found for the constant mass case in Section 3.2.4 it can be seen that $\dot{M}_{\rm sh}v$ approximates $\dot{p}_{\rm sh}$ at large scales in the SIS halo.

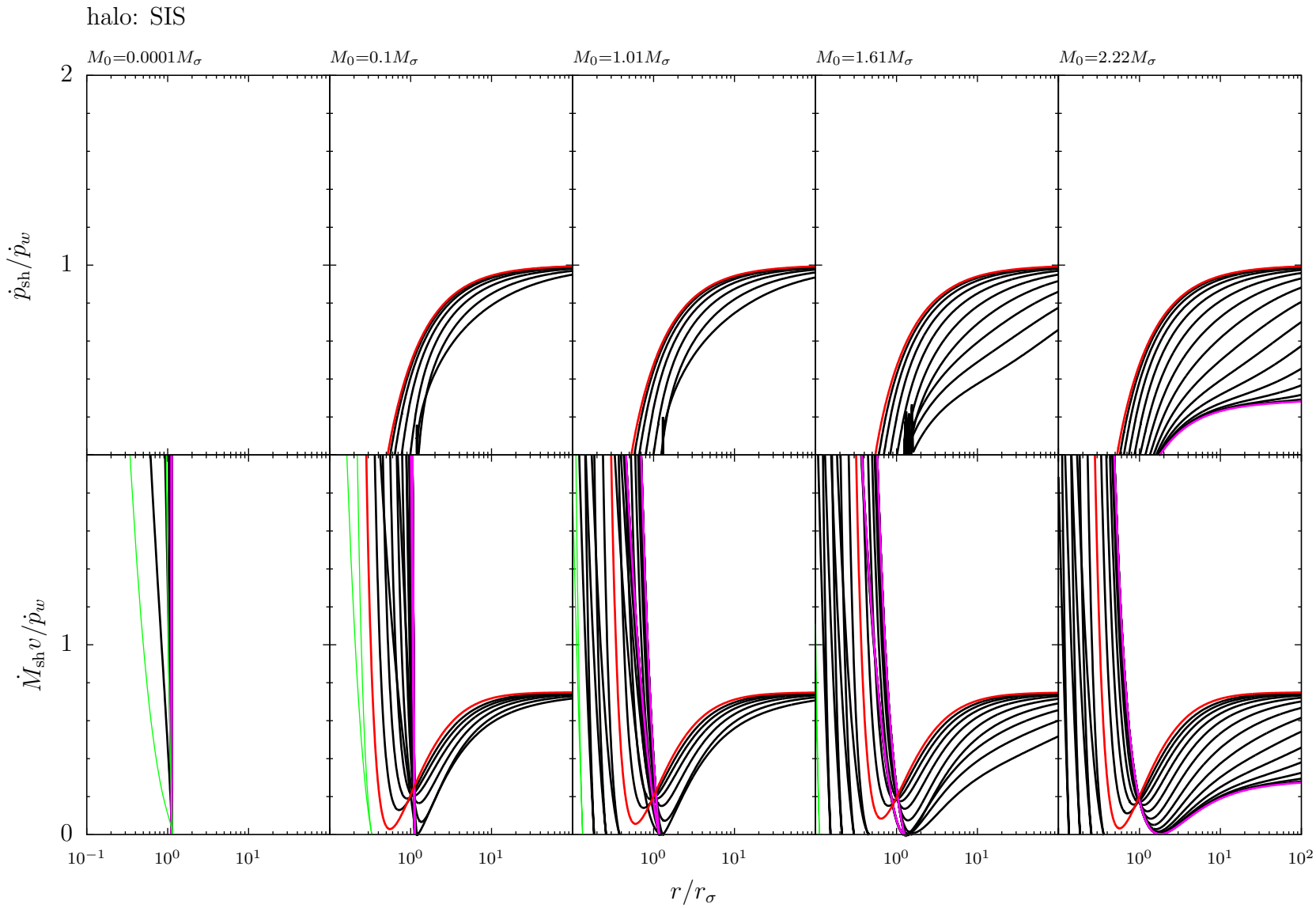

Figure 4.15: Momentum-boosts of shells driven by a wind from a constantly growing SMBH in an SIS halo plotted against radius. The solutions shown correspond to variation in t_s over the range: $t_s = 10^{-4}$ (green curve) to 10^4 (magenta curve), with the red curve corrsponding to the solution with $t_s = 100t_\sigma$. For all solutions the initial momentum is: $C = 4$.

Hernquist Halo

Figure 4.16 shows the momentum-fluxes and the observable $\dot{M}_{\rm sh}v$ (normalised to the wind force $\dot{p}_w$) for shells driven by an SMBH which grows at a constant rate ($\alpha = 1$) for a range of growth timescales t_s in a Hernquist halo. Each panel corresponds to a different seed mass M_0, and each curve corresponds to a different growth timescale t_s. The green curves highlight the fastest growing case, and the magenta curves the slowest growing case. For clarity, any infall behaviour is excluded from the plot, and the initial momentum and mass of dark matter at $r_{\rm pk}$ take the usual values of $C = 0$ and $M_{\rm pk} = 4000 M_\sigma$ respectively.

The momentum-boosts $\dot{p}_{\rm sh}/\dot{p}_w$ are similar to those obtained in the constant mass case in Section 3.2.4 shown in Figure 3.14. The expression for the momentum-boost from equation (4.43) is:

$$\frac{\dot{p}_{\rm sh}}{\dot{p}_w} = 1 - \frac{4\pi x^2 \widetilde{P}_g(x)}{2\widetilde{M}_{\rm BH}(\widetilde{t})} - \frac{8}{(1+x)^2}\left[\frac{1}{2\widetilde{M}_{\rm pk}} + \frac{2x^2}{(1+x)^2\widetilde{M}_{\rm BH}(\widetilde{t})}\right], \tag{4.56}$$

which shows that the momentum-boost tends to unity at small and late times, and therefore at small and large radii. The observable quantity $\dot{M}_{\rm sh}v$ is given by:

$$\dot{M}_{\rm sh}v = \frac{dM_{\rm sh}}{dx}v^2 = M_{\rm pk}\frac{dm}{dx}v^2 = \frac{8M_{\rm pk}xv^2}{(1+x)^3}\,. \tag{4.57}$$

At early times equation (4.48) gives the shell radius, and the velocity is therefore:

$$\widetilde{v}(\widetilde{t}) \to \frac{2}{3}\left[\frac{3\widetilde{M}_0}{4}\left(1 - \frac{4}{\widetilde{M}_{\rm pk}}\right)\right]^{1/3} \widetilde{t}^{\,-1/3} \qquad . \tag{4.58}$$

Using equation (4.57) at small radii with equations (4.48) and (4.58) shows that $\dot{M}_{\rm sh}v/\dot{p}_w$ at early times tends to:

$$\frac{\dot{M}_{\rm sh}v}{\dot{p}_w} = \frac{4}{3}\left(1 - \frac{4}{\widetilde{M}_{\rm pk}}\right). \tag{4.59}$$

For the value of $\widetilde{M}_{\rm pk} = 4000$ assumed throughout equation (4.59) gives a value of $\dot{M}_{\rm sh}v/\dot{p}_w \simeq 4/3$ at early times as shown in Figure 4.16. At late times and therefore

large radii the leading factor corresponding to dm/dx tends to zero, and therefore so does $\dot{M}_{\rm sh}v/\dot{p}_w$.

It is not directly clear from Figure 4.16 how well the observable $\dot{M}_{\rm sh}v$ represents the actual momentum-boost $\dot{p}_{\rm sh}/\dot{p}_w$. In order to investigate this the ratio of the two quantities shown in Figure 4.16 is taken and is shown in Figure 4.17. While the ratio does spike where $\dot{M}_{\rm sh}v$ becomes small it can be seen that for all but the smallest seed mass $\dot{M}_{\rm sh}v$ is a reasonable approximation to $\dot{p}_w$ for shell radii inside of $r_{\rm pk}$ as was also found for the constant SMBH mass case. This means that the momentum-fluxes of shells are well approximated by $\dot{M}_{\rm sh}v$ over a significant range of observable radii.

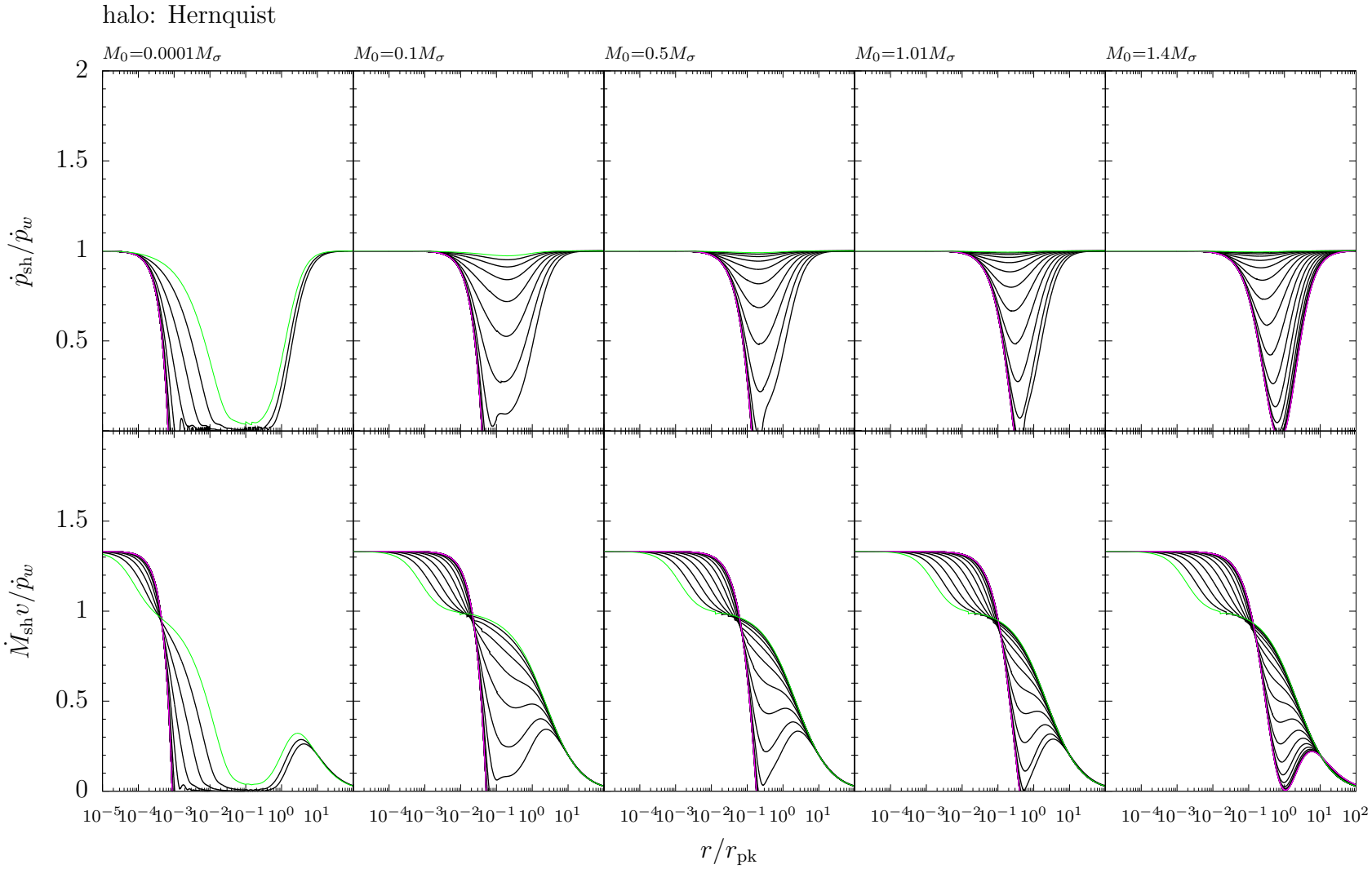

Figure 4.16: Momentum-boosts of shells driven by a constantly growing SMBH wind ($\alpha = 1$) plotted against radius for variations in the time parameter t_s. The solutions with $t_s = 0.0001t_\sigma$ are shown as green curves, and those with $t_s = 1000t_\sigma$ are the magenta curves. The black curves have t_s values in logarithmic intervals between $10^{-4} - 10^3 t_\sigma$ which increase from the green to magenta curves.

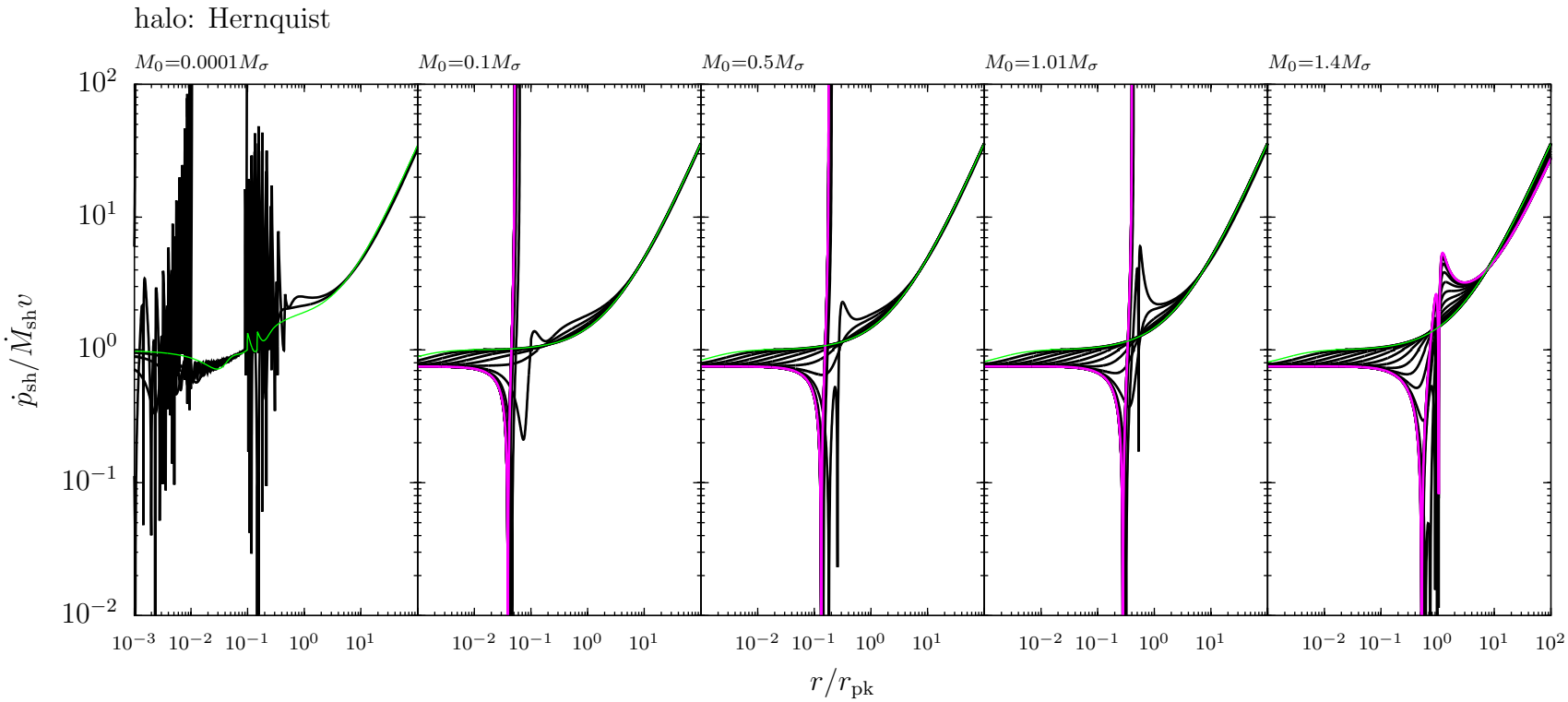

Figure 4.17: Momentum-boosts of shells driven by a constantly growing SMBH wind ($\alpha = 1$) plotted against radius for variations in the time parameter t_s. The solutions with $t_s = 0.0001t_\sigma$ are shown as green curves, and those with $t_s = 1000t_\sigma$ are the magenta curves. The black curves have t_s values in logarithmic intervals between $10^{-4} - 10^3 t_\sigma$ which increase from the green to magenta curves.

4.4 Energy-Driven Outflows

This section analyses the effects of introducing a growing SMBH into the equations of motion for an energy-driven shell. The equation of motion for the energy-driven shell is that given by equation (4.12). This is to be combined with the normalised energy equation for the hot shocked wind region:

$$\frac{d}{d\widetilde{t}}\left[\frac{4}{3}\pi x^3\frac{\widetilde{P}}{\gamma-1}\right]=\widetilde{M}_{\rm BH}(\widetilde{t})\widetilde{v}_w-4\pi x^2\widetilde{v}\widetilde{P}-\frac{2h(x)m(x)\widetilde{v}}{x^2}\left[\frac{\widetilde{M}_{\rm BH}(\widetilde{t})}{\widetilde{M}_{\rm pk}}+m(x)\right], \quad (4.60)$$

which results in the following dimensionless equation of motion for the shell:

$$\begin{aligned}&\frac{d^2}{d\widetilde{t}^2}\left[h(x)m(x)\widetilde{v}\right]=-\frac{2}{x^2}\frac{d}{d\widetilde{t}}\left\{h(x)m(x)\left[\frac{\widetilde{M}_{\rm BH}(\widetilde{t})}{\widetilde{M}_{\rm pk}}+m(x)\right]\right\}\\&+\frac{3(\gamma-1)\widetilde{M}_{\rm BH}(\widetilde{t})\widetilde{v}_w}{x}-12\gamma\pi x\widetilde{v}\widetilde{P}_g(x)-4\pi x^2\widetilde{v}\frac{d\widetilde{P}_g}{dx}\\&-(3\gamma-2)\frac{\widetilde{v}}{x}\frac{d}{d\widetilde{t}}\left[h(x)m(x)\widetilde{v}\right]-2(6\gamma-7)\frac{h(x)m(x)\widetilde{v}}{x^3}\left[\frac{\widetilde{M}_{\rm BH}(\widetilde{t})}{\widetilde{M}_{\rm pk}}+m(x)\right].\end{aligned} \quad (4.61)$$

For a shell experiencing infall equation (4.61) reduces to:

$$\begin{aligned}&h(x_{\rm stall})m(x_{\rm stall})\frac{d^2\widetilde{v}}{d\widetilde{t}^2}=-\frac{2h(x_{\rm stall})m(x_{\rm stall})}{x^2}\frac{d}{d\widetilde{t}}\left[\frac{\widetilde{M}_{\rm BH}(\widetilde{t})}{\widetilde{M}_{\rm pk}}+m(x)\right]\\&+\frac{3(\gamma-1)\widetilde{M}_{\rm BH}(\widetilde{t})\widetilde{v}_w}{x}-(3\gamma-2)\frac{h(x_{\rm stall})m(x_{\rm stall})\widetilde{v}}{x}\frac{d\widetilde{v}}{d\widetilde{t}}\\&-2(6\gamma-7)\frac{h(x_{\rm stall})m(x_{\rm stall})\widetilde{v}}{x^3}\left[\frac{\widetilde{M}_{\rm BH}(\widetilde{t})}{\widetilde{M}_{\rm pk}}+m(x)\right],\end{aligned} \quad (4.62)$$

corresponding to a constant mass shell falling back into the region cleared of gas and free from ambient pressure.

4.4.1 The Singular Isothermal Sphere

Equation of Motion

For the SIS halo the mass function is $m(x)=x$, and for this halo $\widetilde{M}_{\rm pk}=2$. Therefore

equation (4.61) becomes:

$$\begin{aligned}\frac{d^2}{d\widetilde{t}^2}\left[x\widetilde{v}\right] &= -\frac{2}{x^2}\frac{d}{d\widetilde{t}}\left\{x\left[\frac{\widetilde{M}_{\rm BH}(\widetilde{t})}{2}+x\right]\right\} \\ &+\frac{3(\gamma-1)\widetilde{M}_{\rm BH}(\widetilde{t})\widetilde{v}_w}{x}-(3\gamma-2)(1+f_0)\frac{\widetilde{v}}{x} \\ &-(3\gamma-2)\frac{\widetilde{v}}{x}\frac{d}{d\widetilde{t}}\left[x\widetilde{v}\right]-2(6\gamma-7)\frac{\widetilde{v}}{x^2}\left[\frac{\widetilde{M}_{\rm BH}(\widetilde{t})}{2}+x\right],\end{aligned} \tag{4.63}$$

with the corresponding infall equation:

$$\begin{aligned}\frac{d^2\widetilde{v}}{d\widetilde{t}^2} &= -\frac{2}{x^2}\frac{d}{d\widetilde{t}}\left[\frac{\widetilde{M}_{\rm BH}(\widetilde{t})}{2}+x\right]+\frac{3(\gamma-1)\widetilde{M}_{\rm BH}(\widetilde{t})\widetilde{v}_w}{xx_{\rm stall}} \\ &-(3\gamma-2)\frac{\widetilde{v}}{x}\frac{d\widetilde{v}}{d\widetilde{t}}-2(6\gamma-7)\frac{\widetilde{v}}{x^3}\left[\frac{\widetilde{M}_{\rm BH}(\widetilde{t})}{2}+x\right].\end{aligned} \tag{4.64}$$

Asymptotics

At early enough times the SMBH always tends to the seed mass value $\widetilde{M}_0$. Then for the reasons outlined in Chapter 3 the energy-driven shell must begin with an initial impulse in order to start motion. In this case the early time radius and velocity are given by equations (4.26) and (4.27).

At late times by assuming that $x(\widetilde{t})$ is an increasing power of $\widetilde{t}$ then the following applies:

$$\frac{d^2}{d\widetilde{t}^2}\left[x\widetilde{v}\right]\rightarrow\frac{3(\gamma-1)\widetilde{M}_0\widetilde{v}_w}{x}\left(\frac{\widetilde{t}}{\widetilde{t}_s\alpha}\right)^{\alpha}\qquad(\widetilde{t}\ll\widetilde{t}_s\alpha;\widetilde{t}\gg1)\,. \tag{4.65}$$

This leads to:

$$x(\widetilde{t})=3\left[\frac{3(\gamma-1)\widetilde{M}_0\widetilde{v}_w\widetilde{t}^3}{2\alpha(2\alpha+3)(\alpha+3)}\left(\frac{\widetilde{t}}{\widetilde{t}_s\alpha}\right)^{\alpha}\right]^{1/3}\qquad(\widetilde{t}\gg\widetilde{t}_s\alpha;\widetilde{t}\gg1)\,, \tag{4.66}$$

which has the same scaling in time as obtained for the energy-driven bubble in the absence of gravity in Section 2.2.3 given by equation (2.22) with $p=1$ as required for

the SIS halo. The velocity at late times is therefore:

$$\widetilde{v}(\widetilde{t}) = \left[\frac{3(\gamma-1)(\alpha+3)^2\widetilde{M}_0\widetilde{v}_w}{2\alpha(2\alpha+3)}\left(\frac{\widetilde{t}}{\widetilde{t}_s\alpha}\right)^{\alpha}\right]^{1/3} \qquad (\widetilde{t} \gg \widetilde{t}_s\alpha; \widetilde{t} \gg 1)\,, \qquad (4.67)$$

which means that shells will be accelerating at late times.

Variation in α

The numerical solutions to equation (4.63) for different SMBH mass growth rates are shown in Figures 4.18 and 4.19. Figure 4.18 shows shell radii and velocities against time, and also shows the shell velocities in the absence of ambient pressure. Figure 4.19 shows the velocities and momentum-fluxes against radius, and also shows the shell velocities in the absence of ambient pressure. In order to compare with the constant SMBH mass case analysed in Chapter 3 the same SMBH mass values will be used for the seed mass: $M_0 = 0.06, 0.14, 0.49M_\sigma$. The wind speed in both figures has been set to $v_w = 45\sigma_0$ which for $\sigma_0 = 200$ km s^{-1} is $v_w \simeq 0.03c$. This is the median wind speed found by McQuillin & McLaughlin (2013) for a sample of active galaxies. These values give the SMBH seed mass and wind speed combinations: $\widetilde{M}_0\widetilde{v}_w = 2.7, 6.3, 22$. The solutions were obtained for a range of initial momentum values in logarithmic intervals between: $C = 10^{-6} - 10^6$, but for clarity only four values of initial momentum are displayed: $C = 0.01, 2.56, 100, 10^6$. The growth timescale has been set to the value $t_s = t_\sigma$ which is much smaller than the Salpeter time $t_s \simeq 100t_\sigma$. This has been done in order to show the departures from the constant mass case for a rapidly growing SMBH as the differences between the constant mass case and the case where $t_s \simeq 100t_\sigma$ are minimal. The black curves correspond to the steady wind solutions from Section 3.3.2, the red curves correspond to solutions with $\alpha = 1$, and the green curves correspond to the exponential mass case.

As can be seen from Figures 4.18 and 4.19 the shells driven by winds from growing SMBHs go on to accelerate as expected rather than coasting with a terminal velocity. At early times the solutions differ minimally from the constant mass case as this is when the SMBH mass can be approximated by the seed mass. For lower seed mass

values it can be seen that much like the constant SMBH mass case the shells become confined by the gravity of the SMBH and stall multiple times, but when a large enough radius is reached the shell is able to cease stalling and goes on to accelerate.

Fundamentally, aside from the large radius accelerations of the shells there is minimal difference in terms of the overall shell dynamics from introducing a growing SMBH for energy-driven shells in an SIS halo. Importantly, it is left to confirm that the momentum-boosts are not significantly changed by the inclusion of a growing SMBH, and that there still exists a well defined peak in momentum-boosting.

4.4.2 Hernquist Halo

Equation of Motion

Using the dimensionless mass function $m(x) = 4x^2/(1+x)^2$ with equation (4.61) gives:

$$\begin{aligned}\frac{d^2}{d\widetilde{t}^2}\left[\frac{4x^2}{(1+x)^2}\widetilde{v}\right] &= -\frac{2}{x^2}\frac{d}{d\widetilde{t}}\left\{\frac{4x^2}{(1+x)^2}\left[\frac{\widetilde{M}_{\rm BH}(\widetilde{t})}{\widetilde{M}_{\rm pk}}+\frac{4x^2}{(1+x)^2}\right]\right\}\\ &+\frac{3(\gamma-1)\widetilde{M}_{\rm BH}(\widetilde{t})\widetilde{v}_w}{x}-12\gamma\pi x\widetilde{v}\widetilde{P}_g(x)-4\pi x^2\widetilde{v}\frac{d\widetilde{P}_g}{dx}\\ &-(3\gamma-2)\frac{\widetilde{v}}{x}\frac{d}{d\widetilde{t}}\left[\frac{4x^2}{(1+x)^2}\widetilde{v}\right]-2(6\gamma-7)\frac{4\widetilde{v}}{x(1+x)^2}\left[\frac{\widetilde{M}_{\rm BH}(\widetilde{t})}{\widetilde{M}_{\rm pk}}+\frac{4x^2}{(1+x)^2}\right],\end{aligned} \tag{4.68}$$

where the ambient pressure terms are:

$$\widetilde{P}_g(x) = \frac{16(1+f_0)}{\pi}\left[\ln\left(1+\frac{1}{x}\right)-\frac{12x^3+42x^2+52x+25}{12(1+x)^4}\right], \tag{4.69}$$

and:

$$\frac{d\widetilde{P}_g}{dx} = \frac{16(1+f_0)}{\pi x(1+x)^5}. \tag{4.70}$$

For a shell experiencing infall equation (4.68) reduces to

$$\begin{aligned}\frac{d^2\widetilde{v}}{d\widetilde{t}^2} &= -\frac{2}{x^2}\frac{d}{d\widetilde{t}}\left[\frac{\widetilde{M}_{\rm BH}(\widetilde{t})}{\widetilde{M}_{\rm pk}}+\frac{4x^2}{(1+x)^2}\right]+\frac{3(\gamma-1)(1+x_{\rm stall})^2\widetilde{M}_{\rm BH}(\widetilde{t})\widetilde{v}_w}{4xx_{\rm stall}^2}\\ &-(3\gamma-2)\frac{\widetilde{v}}{x}\frac{d\widetilde{v}}{d\widetilde{t}}-2(6\gamma-7)\frac{\widetilde{v}}{x^3}\left[\frac{\widetilde{M}_{\rm BH}(\widetilde{t})}{\widetilde{M}_{\rm pk}}+\frac{4x^2}{(1+x)^2}\right].\end{aligned} \tag{4.71}$$

Asymptotics

Much like energy-driven shells in the SIS halo those in the Hernquist halo must also begin with a nonzero value of initial momentum, and therefore equation (4.47) applies at early times. At late times by assuming that $x(\widetilde{t})$ is a positive power of $\widetilde{t}$ means that $m(x) \to 4$ at late times. This leads to the following result:

$$\frac{d^2\widetilde{v}}{d\widetilde{t}^2} + (3\gamma - 2)\frac{\widetilde{v}}{x}\frac{d\widetilde{v}}{d\widetilde{t}} = \frac{3(\gamma-1)\widetilde{M}_0\widetilde{v}_w}{4x}\left(\frac{\widetilde{t}}{\widetilde{t}_s\alpha}\right)^{\alpha} \qquad (\widetilde{t} \gg \widetilde{t}_s\alpha; \widetilde{t} \gg 1)\,. \tag{4.72}$$

Solving this for $x(\widetilde{t})$ as a positive power of $\widetilde{t}$:

$$x(\widetilde{t}) = 2\left\{\frac{3(\gamma-1)\widetilde{v}_w\widetilde{M}_0\widetilde{t}^3}{2(\alpha+3)(\alpha+1)[\alpha-1+(\alpha+3)(3\gamma-2)]}\left(\frac{\widetilde{t}}{\widetilde{t}_s\alpha}\right)^{\alpha}\right\}^{1/2}, \tag{4.73}$$

which has the same scaling as the energy-driven bubble in the absence of gravity from Section 2.2.3 given by equation (2.22) with $p = 0$ as required for the Hernquist halo. The velocity at late times is therefore:

$$\widetilde{v}(\widetilde{t}) = \left\{\frac{3(\gamma-1)(\alpha+3)\widetilde{v}_w\widetilde{M}_0\widetilde{t}}{2(\alpha+1)[\alpha-1+(\alpha+3)(3\gamma-2)]}\left(\frac{\widetilde{t}}{\widetilde{t}_s\alpha}\right)^{\alpha}\right\}^{1/2}, \tag{4.74}$$

which implies accelerating solutions at large radii.

Variation in α

Equation (4.68) has been solved numerically for different SMBH mass growth rates and the solutions are displayed in Figures 4.20 and 4.21. The top panel of Figure 4.20 shows shell radii against time and the bottom panel shows shell velocities against time. Both panels include the effects of ambient pressure. The middle panel shows shell velocities against time with ambient pressure neglected. The top panel of Figure 4.21 shows shell velocities versus shell radius and the bottom panel shows the momentum-fluxes against shell radius. Both panels include the effects of ambient pressure. The middle panel shows shell velocities against radius with ambient pressure neglected. The seed mass values have been chosen to be the same as the constant SMBH mass values used

in Section 3.3.3: $M_0 = 0.01, 0.06, 0.49 M_\sigma$. The wind speed is set to $v_w = 45\sigma_0$, and the resultant SMBH mass and wind speed combinations are indicated at the top of each Figure. The mass at $r_{\rm pk}$ is selected to be $M_{\rm pk} = 4000 M_\sigma$ for all solutions. Each plot shows three groups of three shell solutions which are grouped based on the value of initial momentum. The values of initial momentum are: $C = 0.0001, 1, 10$ in order to demonstrate the range of shell behaviours, and to be in agreement with those used in Section 3.3.3. For each of these initial momenta there are three solutions which differ by the form of the SMBH mass. The black curves show the constant SMBH mass results from Section 3.3.3, the red curves show the results for a constantly growing SMBH ($\alpha = 1$), and the green curves show the results for an exponentially growing SMBH. For all of the solutions which have a growing SMBH the value of the growth timescale is set to be the Salpeter time given by equation (4.4): $t_s = 0.2 t_\sigma$.

As expected from equation (4.74) Figures 4.20 and 4.21 show that all shells ultimately go on to accelerate. These figures show that there are no significant differences in the shell dynamics from the inclusion of a growing SMBH mass. The solutions with a growing SMBH mass accelerate much earlier than the constant SMBH mass case, and the shells driven exponential SMBH mass wind accelerate earlier than the $\alpha = 1$ solutions. This is expected as the outward force in the exponential mass case will always exceed the $\alpha = 1$ case if t_s is the same value for both. The most striking difference from the constant SMBH mass case is in the shell momentum-fluxes. Rather than tending to zero over the plotted range the values are significantly higher beyond $r_{\rm pk}$. It can be seen that larger seed masses lead to these values of momentum-flux to be much larger. This prompts the question of whether or not the large-scale momentum-boosts around $r_{\rm pk}$ will differ substantially from the constant SMBH mass case.

4.4.3 Momentum-Boosts of Energy-Driven Shells

The Singular Isothermal Sphere

Figure 4.22 shows the momentum-boosts for energy-driven shells driven by an exponentially growing SMBH wind in an SIS halo. There are two groups of solutions in

each panel, with one group having the wind speed $v_w = 45\sigma_0$, and the other having $v_w = 150\sigma_0$. For each of these wind speeds the growth timescale is varied over three values $t_s/t_\sigma = 1, 100, 1000$ which are coloured magenta, red and green respectively. A single value of initial momentum is selected to be $C = 0.1$ as this value is not so small that it leads to an extended period of confinement, nor is it so large that the shell only begins to accelerate at very large radii. A single value for the seed mass is also selected: $M_0 = 0.14M_\sigma$ which is the value which, when combined with a wind speed of $v_w = 45\sigma_0$, leads to a terminal outflow speed of $v \sim \sigma_0$ in the steady wind case.

It can be seen from Figure 4.22 that a larger wind speed leads to a larger momentum-boost. The figure also shows that $\dot{M}_{\rm sh}v$ serves as a suitable proxy for $\dot{p}_{\rm sh}$ at large radii. The confining effects of the SMBH and dark matter gravity can be seen at small radii. The momentum-boosts for the non-steady winds no longer tend to a constant value, but instead now are a peaked distribution in shell radius. The peak of this curve is coincident with the steady wind case, and the breadth of the coincidence is determined by the growth timescale t_s. The shorter this timescale is the smaller the interval in radii the peak occupies. For the fiducial value of $t_s = 100t_\sigma$ the peak occupies a range which spans $1 - 50r_\sigma$. Before this range in radii the gravitational force of the SMBH causes the boost to be lower, and after this range the growing SMBH causes the boost to diminish because the wind momentum-flux is growing as well.

Figure 4.23 shows for two different radii (r_σ and $10r_\sigma$) the momentum-boost distribution for energy-driven shells driven by an exponentially growing SMBH wind in an SIS halo in the absence of ambient pressure. In order to obtain these solutions the growth timescale was set to the fiducial value: $t_s = 100t_\sigma$, and the initial momentum was set to $C = 0.1$. The seed mass was then varied through a large range of values in $M_0 = 0.0001 - 100M_\sigma$ in order to obtain a significant range about $v_{\rm p,max}$ in velocity space.

The momentum-boosts in Figure 4.23 show that even for non-steady winds the analytical expressions obtained in Section 3.3.4 continue to accurately describe the momentum-flux distribution. Furthermore, it is also shown in Figure 4.23 that maximum momentum-boosting occurs at the same velocity given by equation (3.96) and

with the same ratio of kinetic to wind energy. This means that the derived $M_{\rm BH} - \sigma$ relation given by equation (3.103) can be extended to shells driven by non-steady winds.

Hernquist Halo

The momentum-boosts for energy-driven shells in a Hernquist halo are shown in Figure 4.24, and it can be seen that the momentum-boosts vary significantly with radius. The $M_{\rm BH} - V_{\rm c,pk}$ relation given by equation (3.105) was obtained by finding that the momentum-boost distribution in terms of shell velocities at $r_{\rm pk}$ was precisely matched by the analytical curves for the SIS halo. Figure 4.25 shows that this is no longer the case at $r_{\rm pk}$ but that at the smaller radius of $0.3r_{\rm pk}$ the analytical curves provide a better match. This means that the $M_{\rm BH} - V_{\rm c,pk}$ relation given by equation (3.105) is unlikely to apply for outflows from non-steady winds. However, in the case that the wind grows slowly it may suffice as a reasonable approximation for the SMBH mass of maximally boosted outflows in a Hernquist halo.

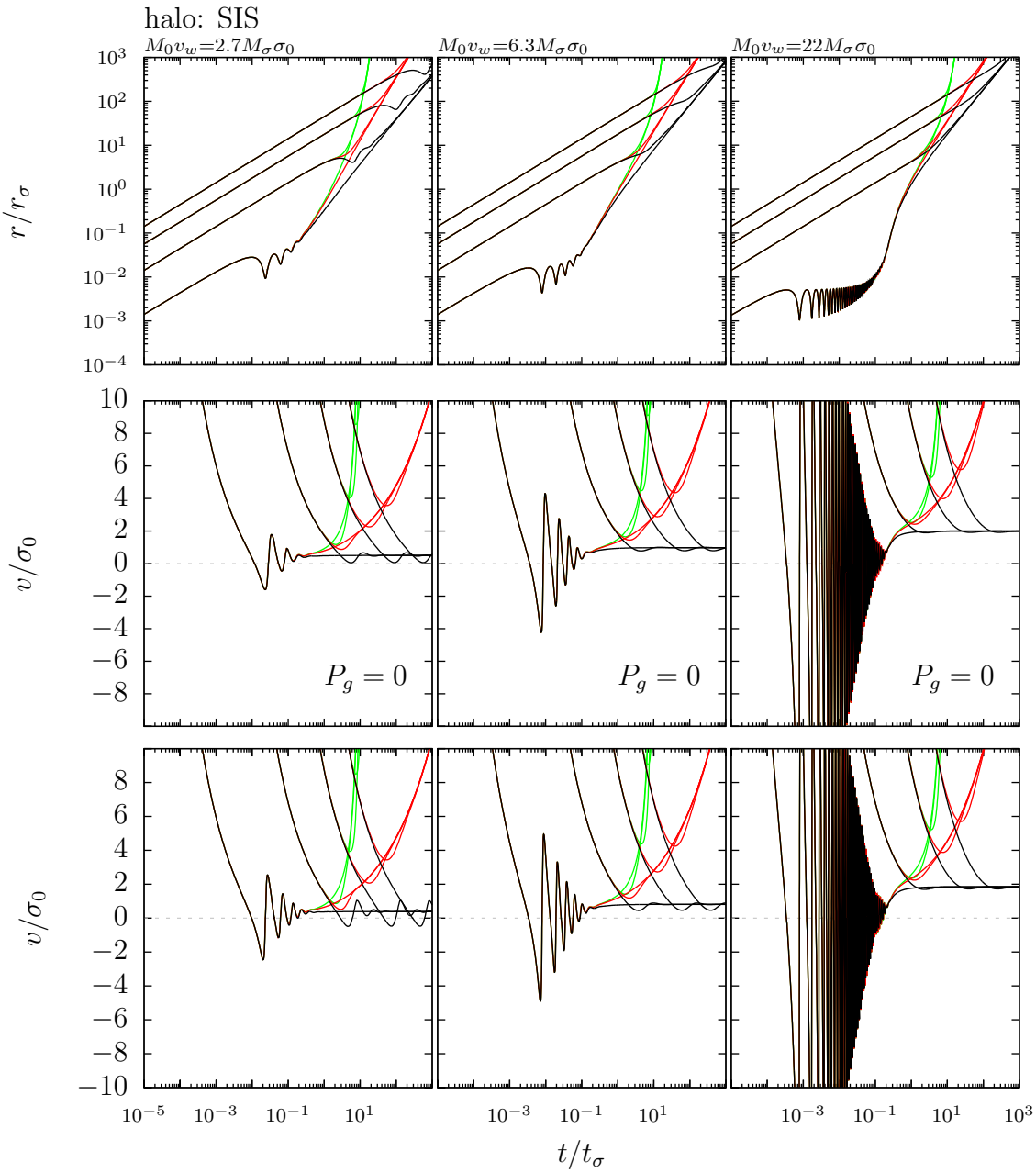

Figure 4.18: Shell radii (top) and velocities (middle and bottom) of energy-driven shells propagating within an SIS halo. For the top and bottom panels which include ambient pressure the gas fraction is set to $f_0 = 0.2$. Three combinations of SMBH mass and wind speed are considered: $\widetilde{M}_0\widetilde{v}_w = 2.7$ (left), 6.3 (middle), and 22 (right). The time scale is $t_\sigma = 2.5 \times 10^5$ yr for a velocity dispersion of $\sigma_0 = 200$ km s^{-1}. Black curves correspond to shell solutions driven by a constant SMBH wind, red curves correspond to solutions driven by an SMBH wind which grows at a constant rate ($\alpha = 1$), and the green curves correspond to solutions driven by an exponentially increasing SMBH wind. Four values of initial momentum are shown: $C = 0.01, 2.56, 100, 10^6$. For the growing cases the growth timescale has been set to $t_s = t_\sigma \simeq 10^5$ yr.

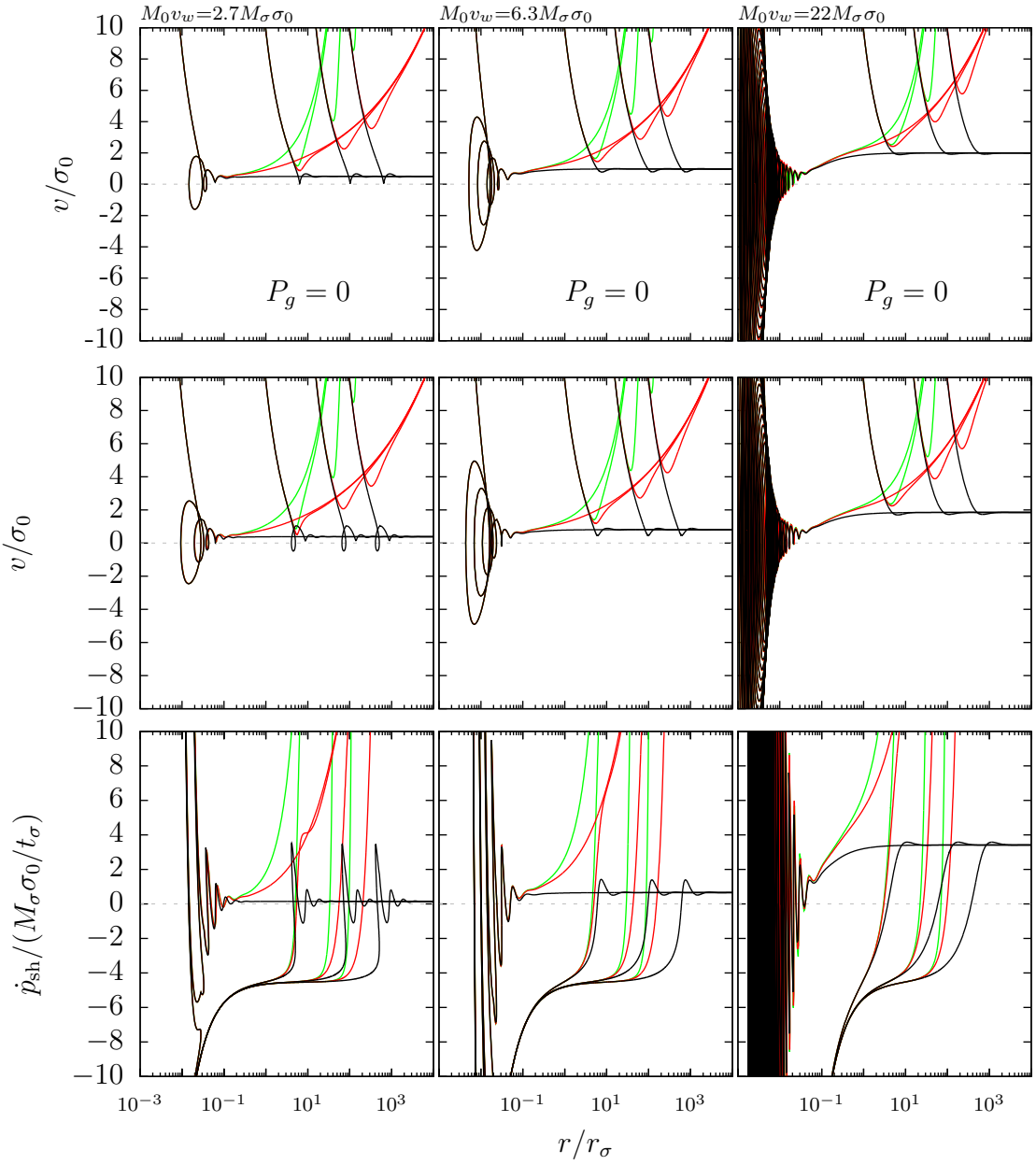

Figure 4.19: Shell velocities (top and middle) and momentum-fluxes (bottom) versus radius of energy-driven shells propagating within an SIS halo. For the panels which include ambient pressure the gas fraction is set to $f_0 = 0.2$. Three combinations of SMBH mass and wind speed are considered: $\widetilde{M}_{\rm BH}\widetilde{v}_w = 2.7$ (left), 6.3 (middle), and 22 (right). Four values of initial momentum are shown: $C = 0.01, 2.56, 100, 10^6$. The radius scale is $r_\sigma = 49.25$ pc for a velocity dispersion of $\sigma_0 = 200$ km s^{-1}.

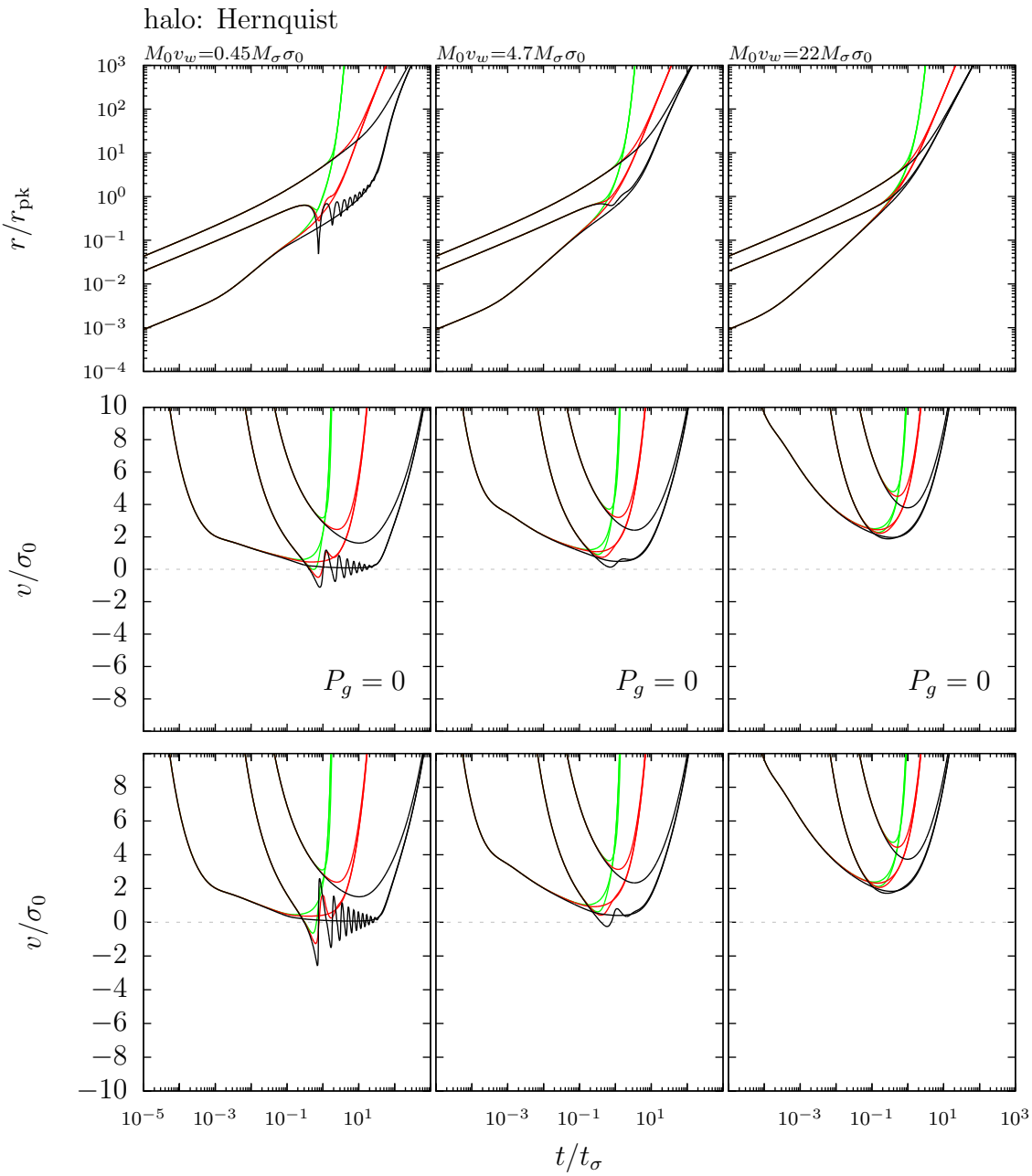

Figure 4.20: Shell radii (top) and velocities (middle and bottom) of energy-driven shells propagating within a Hernquist halo. For the top and bottom panels which include ambient pressure the gas fraction is set to $f_0 = 0.2$. Three combinations of SMBH mass and wind speed are considered: $\widetilde{M}_0\widetilde{v}_w = 0.45$ (left), 4.7 (middle), and 22 (right). The time scale is $t_\sigma = 1.5\times10^8$ yr for a velocity dispersion of $\sigma_0 = 120$ km s^{-1}. Black curves correspond to shell solutions driven by a constant SMBH wind, red curves correspond to solutions driven by an SMBH wind which grows at a constant rate ($\alpha = 1$), and the green curves correspond to solutions driven by an exponentially increasing SMBH wind. For the growing cases the growth timescale has been set to $t_s = 0.02t_\sigma \simeq 3 \times 10^7$ yr. Three values of initial momentum are shown: $C = 10^{-8}, 1, 100$.

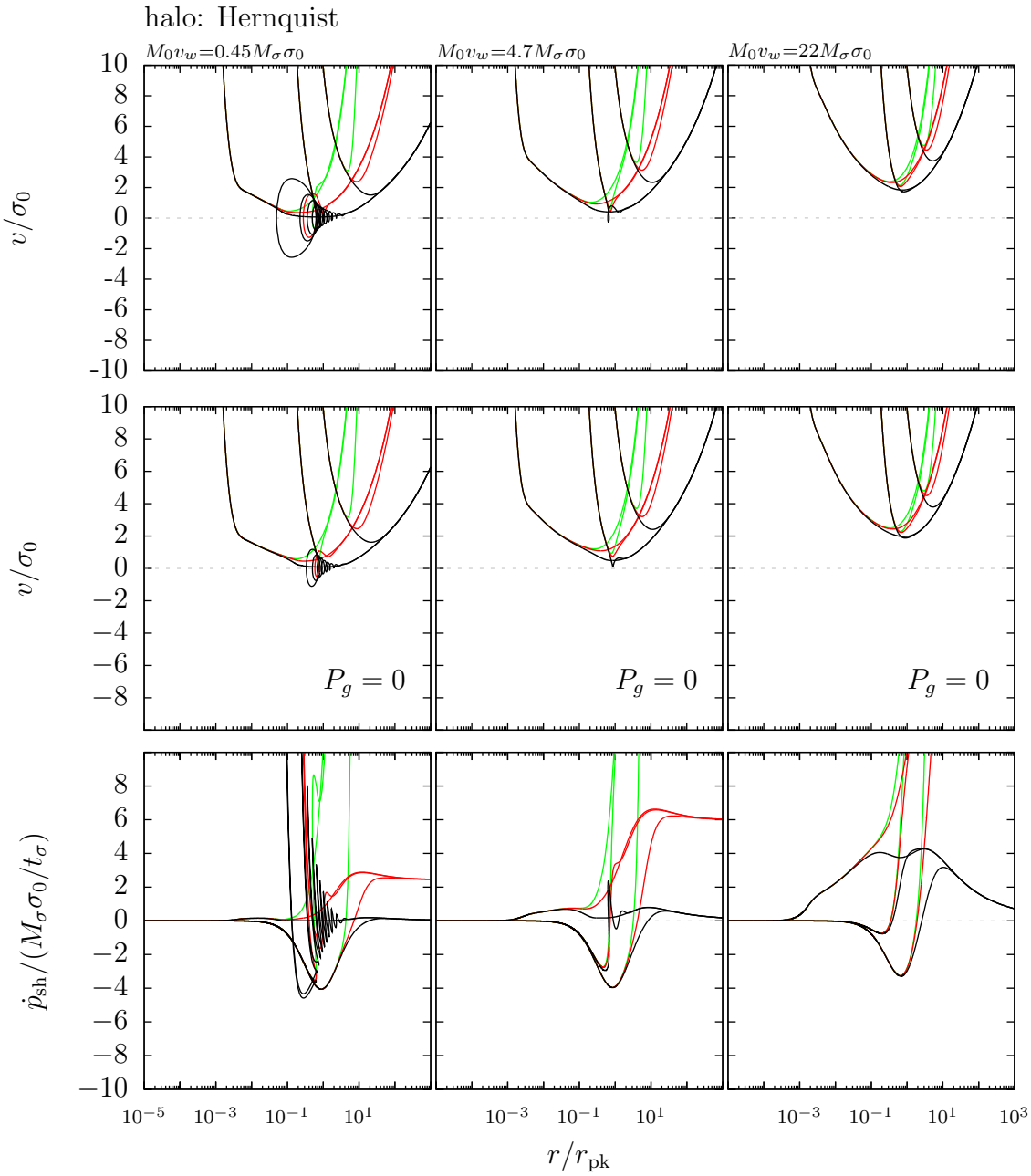

Figure 4.21: Shell velocities (top and middle) and momentum-fluxes (bottom) of energy-driven shells propagating within a Hernquist halo. For the top and bottom panels which include ambient pressure the gas fraction is set to $f_0 = 0.2$. Three combinations of SMBH mass and wind speed are considered: $\widetilde{M}_0\widetilde{v}_w = 0.45$ (left), 4.7 (middle), and 22 (right). The time scale is $t_\sigma = 1.5 \times 10^8$ yr for a velocity dispersion of $\sigma_0 = 120$ km s^{-1}. Black curves correspond to shell solutions driven by a constant SMBH wind, red curves correspond to solutions driven by an SMBH wind which grows at a constant rate ($\alpha = 1$), and the green curves correspond to solutions driven by an exponentially increasing SMBH wind. For the growing cases the growth timescale has been set to $t_s = 0.02 t_\sigma \simeq 3 \times 10^7$ yr. Three values of initial momentum are shown: $C = 10^{-8}, 1, 100$.

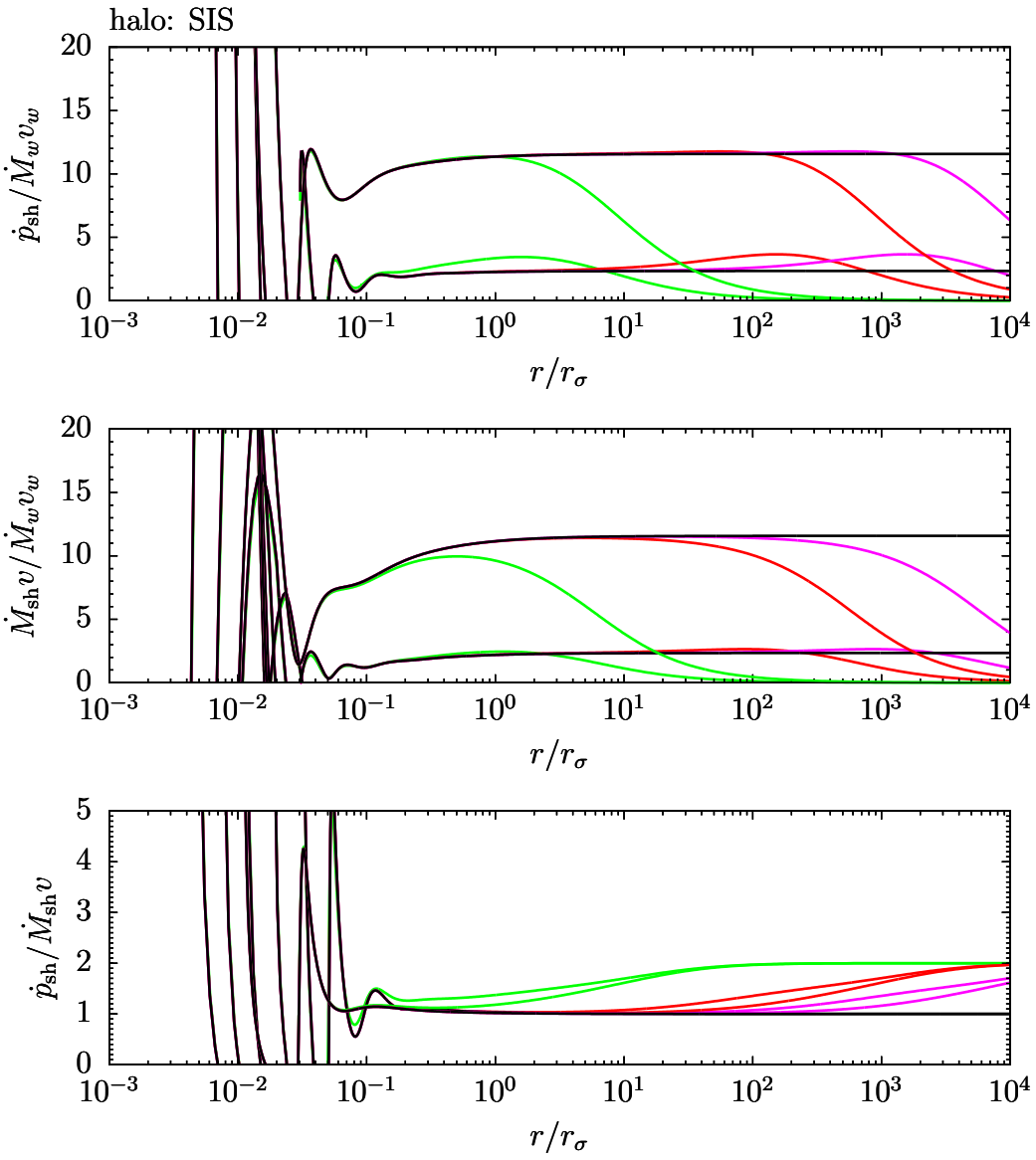

Figure 4.22: Momentum-boosts of shells in an SIS halo driven by a wind from an exponentially growing SMBH plotted against radius. The top panel shows the momentum-boost of the shell defined in terms of $\dot{p}_{\rm sh}$ against shell radius, the middle panel shows the observable momentum-boost defined in terms of $\dot{M}_{\rm sh} v$ against shell radius, and the bottom panel shows the ratio of $\dot{p}_{\rm sh}$ and $\dot{M}_{\rm sh} v$ against shell radius. Each panel shows two groups of solutions which are separated by the value of the wind speed. The more boosted solutions have a wind speed of $v_w = 150\sigma_0$ and the less boosted solutions have a wind speed of $v_w = 45\sigma_0$. All solutions have the same seed mass value of $M_0 = 0.14 M_\sigma$. For each wind speed there are three values of the growth timescale: $t_s = 1, 100, 1000 t_\sigma$ which are shown in green, red and magenta respectively.

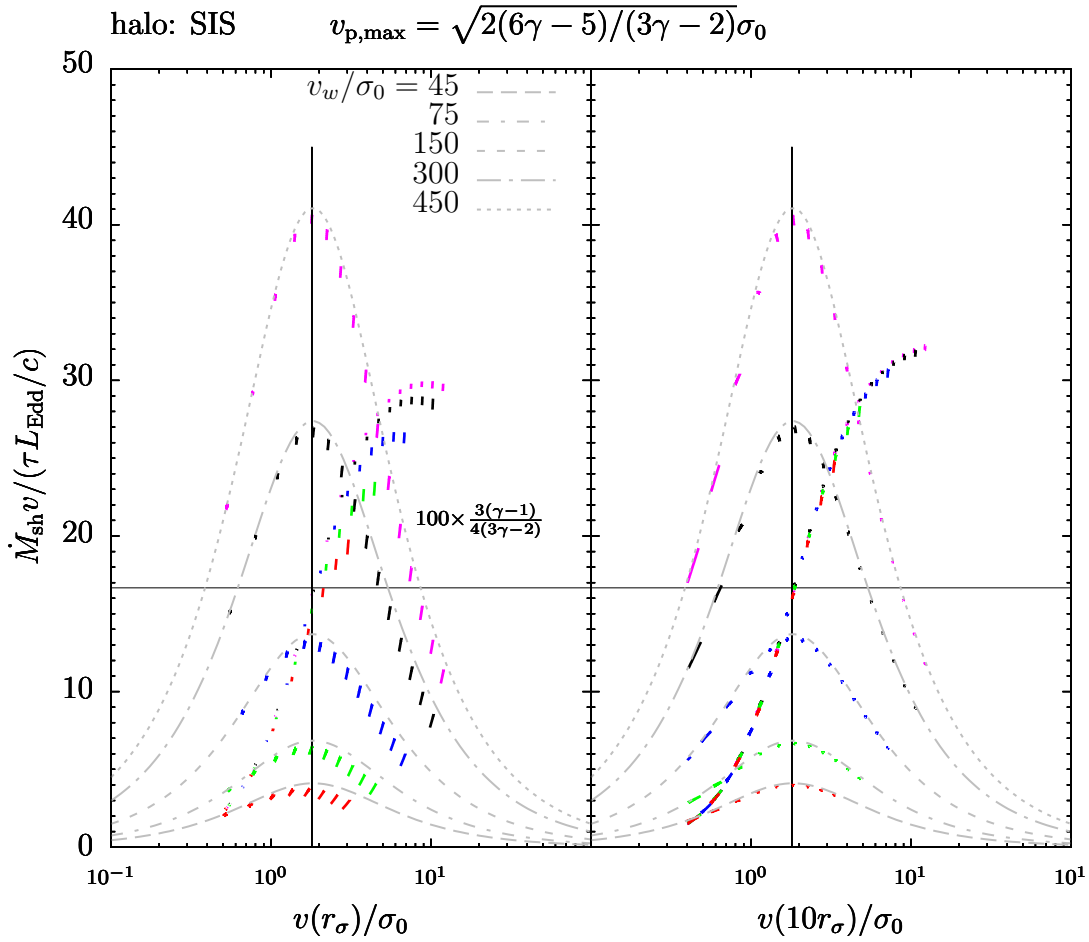

Figure 4.23: Momentum-boosts of shells in an SIS halo driven by a wind from an exponentially growing SMBH plotted against velocity. Each point on the peaked coloured curves corresponds to a velocity which occurs at the specified radius and is determined by a seed mass value M_0 as $t_s = 100t_\sigma$. The coloured curves that rise through the centres of the plots are the ratios of the kinetic energy with the wind energy. Shown as a black vertical line is the value of $v_{\rm p,max}$ which is the velocity for maximum boosting for steady winds, and the horizontal black lines are the exact values for kinetic energy to wind energy ratio. It can be seen that this exact ratio occurs at $10r_\sigma \simeq 500$ pc. The colours correspond to different wind speeds with $v_w = 45, 75, 150, 300, 450\sigma_0$ shown in red, green, blue, black, and magenta.

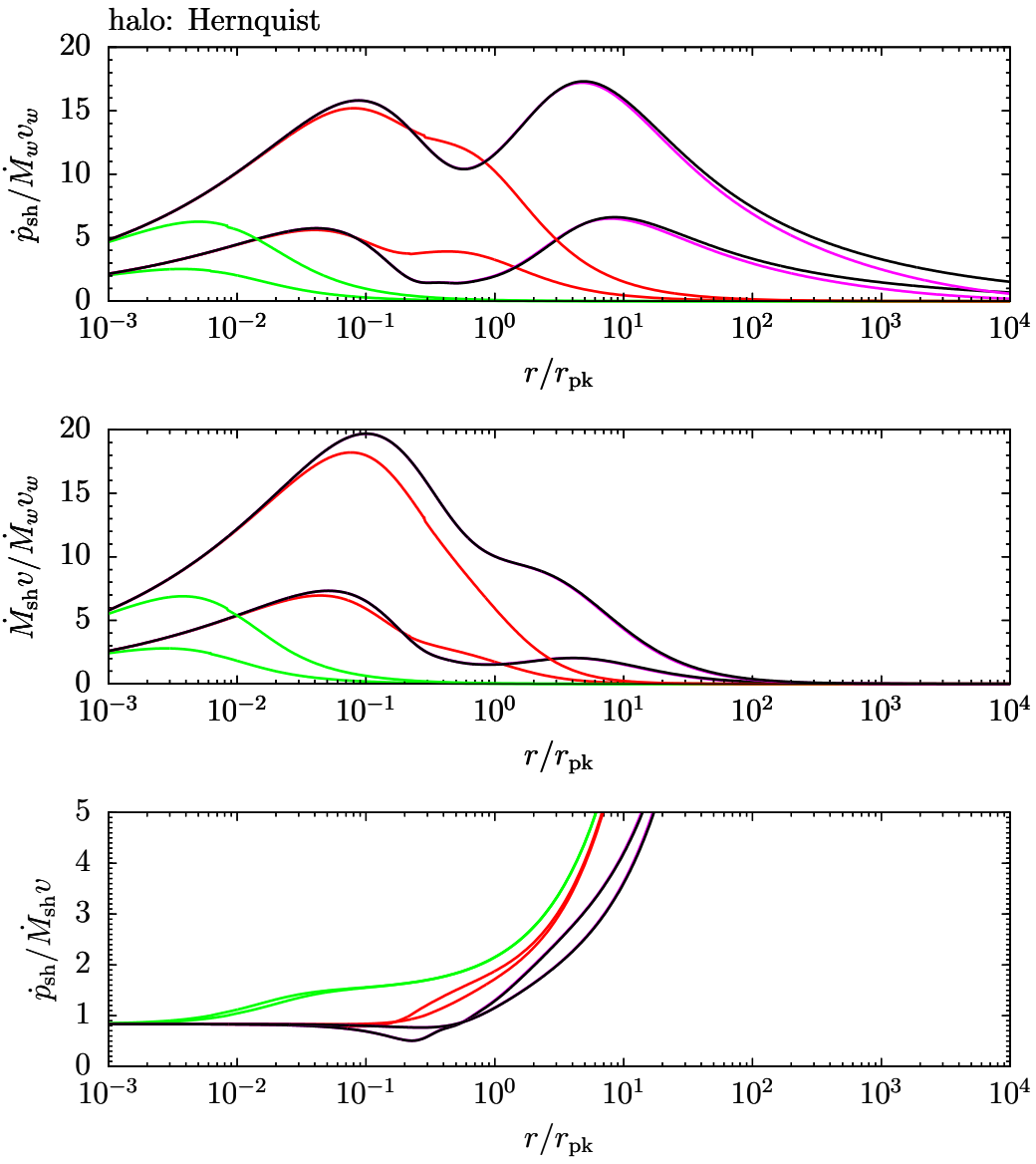

Figure 4.24: Momentum-boosts of shells in a Hernquist halo driven by a wind from an exponentially growing SMBH plotted against radius. The top panel shows the momentum-boost of the shell defined in terms of $\dot{p}_{\rm sh}$ against shell radius, the middle panel shows the observable momentum-boost defined in terms of $\dot{M}_{\rm sh} v$ against shell radius, and the bottom panel shows the ratio of $\dot{p}_{\rm sh}$ and $\dot{M}_{\rm sh} v$ against shell radius. Each panel shows two groups of solutions which are separated by the value of the wind speed. The more boosted solutions have a wind speed of $v_w = 150\sigma_0$ and the less boosted solutions have a wind speed of $v_w = 45\sigma_0$. All solutions have the same seed mass value of $M_0 = 0.06 M_\sigma$. For each wind speed there are three values of the growth timescale: $t_s = 0.001, 0.2, 100 t_\sigma$ which are shown in green, red and magenta respectively.

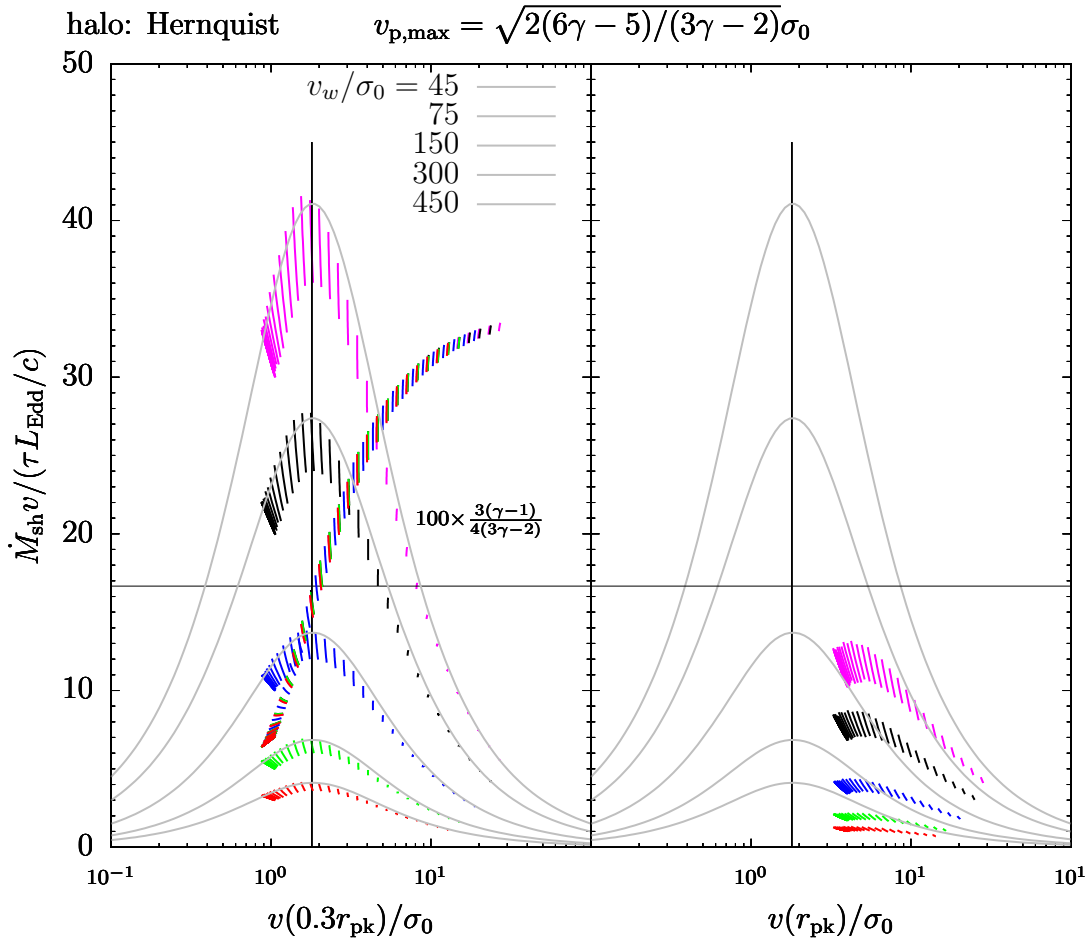

Figure 4.25: Momentum-boosts of shells in a Hernquist halo driven by a wind from an exponentially growing SMBH plotted against velocity. The coloured curves correspond to the momentum boosts over a range in velocity values which occur at the radii $0.3r_{\rm pk}$ and $r_{\rm pk}$. Since $t_s = 0.2t_\sigma$ where $t_\sigma \simeq 1.5\times10^8$ yr each point along the curves corresponds to a seed mass value M_0. The colours correspond to different wind speeds with $v_w = 45, 75, 150, 300, 450\sigma_0$ shown in red, green, blue, black, and magenta. The coloured curves that rise through the centres of the plots are the ratios of the kinetic energy with the wind energy. Shown as a black vertical line is the value of $v_{\rm p,max}$ which is the velocity for maximum boosting for steady winds, and the horizontal black lines are the exact values for kinetic energy to wind ratio.

4.5 Summary and Discussion

This chapter investigated the dynamics of shells driven by non-steady winds into isothermal and non-isothermal haloes. It was found for momentum-driven shells propagating into SIS and Hernquist haloes that there is a new type of shell behaviour where shells can stall repeatedly but are ultimately pushed out to large radii by the growing wind force. The SMBH mass required for solutions to reach large radii without stalling was sought. For the SIS halo it was found that if the SMBH exceeded the sufficient SMBH mass from the steady wind case by the time the shell reached $x_{\rm stall}$ (from the steady wind case) then the shell was able to reach large radii without stalling. This was confirmed by finding the sufficient seed mass M_0 and growth time t_s combinations which resulted in shells that never stalled, and it was found that when these shells were at their lowest velocities (i.e. just avoiding a stall point) the SMBH masses were comparable to the sufficient SMBH mass from the steady wind case. By treating the winds as being steady at early times it was possible to obtain a sufficient SMBH mass expression which permits shells to reach large radii without stalling. For momentum-driven shells in the Hernquist halo it was found that obtaining an estimate of the sufficient SMBH mass was not as simple. The numerically determined sufficient M_0 and t_s combinations showed that the SMBH mass at the minimum in velocity for these shells was close to the sufficient SMBH mass in the steady wind case, but that it departed significantly from this value for smaller t_s. The momentum-boosts of momentum-driven shells from non-steady winds were confirmed to always be less than unity, and that $\dot{M}_{\rm sh}v$ continued to be a suitable proxy for $\dot{p}_{\rm sh}$.

The energy-driven shells from non-steady winds in the SIS halo were shown to accelerate at large radii rather than tend to a constant velocity as was the case for steady winds. These shells display confinement behaviour at small radii where the force of SMBH gravity is dominant. Shells driven by non-steady winds in the Hernquist halo were found to simply accelerate at earlier times than their steady wind counterparts, but otherwise the dynamics were not substantially altered by the inclusion of a growing wind force. The momentum-boosts of energy-driven shells were investigated and it

was shown that in the SIS halo the large scale momentum-boosts as a function of shell velocity were still accurately described by the analytical expression obtained in the steady wind case. This means that shells from non-steady winds continue to have a maximum momentum-boost at the velocity determined in the steady wind case, and that the ratio between shell kinetic and wind energy is the same as that found in the steady wind case. This allows the derived $M_{\rm BH} - \sigma$ relation for energy-driven shells driven by steady winds to be extended to non-steady winds. The conditions used in order to derive the $M_{\rm BH} - V_{\rm c,pk}$ relation in the steady wind case were found no longer to apply for shells blown by non-steady winds for typical parameter values, however maximum boosting was found to occur at a smaller radius. How this radius for non-isothermal haloes depends on parameter values, and how it departs from the steady wind case is worthy of further investigation.

5 Summary and Discussion

5.1 Summary

Quasar-mode feedback is a critical aspect of galaxy formation as outlined in Chapter 1, and a possible mechanism for this feedback is a wind from an accreting black hole. This wind is capable of driving large outflows of gas into the galaxy as observed in local active galaxies. Such a process may be responsible for establishing the observed correlations between the central supermassive black hole (SMBH) and global properties of now inactive galaxies. The aim of this thesis has been to model the dynamics of wind-driven gas outflows in order to better understand the observed correlations in inactive galaxies and the properties of outflows in active galaxies.

In Chapter 2 the theory of outflows was introduced, and the solutions were revisited for momentum- and energy-driven shells which propagate in the absence of gravity. Much of the theory relating to these outflow regimes has previously been developed within the context of stellar wind bubbles. This chapter extended previous work on bubble evolution (Koo & McKee 1992a) by including a power law form for the cooling function to allow for the different cooling processes expected to be dominant for outflows from SMBH winds.

In Chapter 3 the dynamics of momentum- and energy-driven shells were analysed for the scenario that they propagate into a gaseous ambient medium which traces dark matter directly and exerts an inward pressure on the shell. Analytical and numerical solutions for shell radii and velocities were obtained as functions of time for two different dark matter haloes; the singular isothermal sphere (SIS) and Hernquist halo, and therefore two forms of ambient pressure and gravitational force were utilised. By following the infall behaviour of shells it was shown that momentum-driven shells can become pressure confined. This outcome has not been analysed in its own right within the context of SMBH winds. It was also demonstrated that the previously derived $M_{\rm BH} - \sigma$ correlations change to have higher SMBH masses due to the inclusion of

ambient pressure. The momentum-fluxes of shells were also examined and it was shown that energy-driven shells have a peaked distribution of momentum-flux relative to that of the wind as a function of large scale outflow velocity (which is set by $M_{\rm BH}$). When compared with data on large-scale outflows in active galaxies (Cicone et al. 2014) it was shown that these so-called momentum-boosts are consistent with maximum momentum-boosting, and therefore maximum possible boosting may be a typical state for wind-driven outflows. By requiring that energy-driven shells are maximally boosted leads to the derivation of a new $M_{\rm BH} - \sigma$ relation which allows the scatter in the $M_{\rm BH} - \sigma$ data to be interpretted as a range in momentum-boosts, and which can recover previously derived momentum- and energy-driven relations.

In Chapter 4 the previous work was extended to include a growing SMBH, and therefore a growing wind force. A new form for the SMBH mass was introduced which allows for a range of growth rates from constant to exponential growth to be analysed. By numerically solving the equation of motion for momentum- and energy-driven shells it was shown that it is possible for an infalling shell to resume outward motion due to the growth of the wind force. It was also demonstrated that the requirement for shells from growing SMBH winds to reach large radii without stalling is that they effectively exceed the required SMBH mass derived in the steady wind case. It was also shown that the exact peaked distribution in momentum-boosting which was obtained for energy-driven shells from steady winds is still maintained for shells from growing winds but that it now occurs for a smaller range in radii. Hence, this chapter concludes that the introduction of a growing SMBH wind does not fundamentally alter the results obtained for steady winds in Chapter 3, i.e. outflows from non-steady winds with momentum-boosts of about unity will still be around the $M_{\rm BH} \sim M_{\sigma}$ line, and the derived $M_{\rm BH} - \sigma$ relation from Chapter 3 still applies for outflows from non-steady winds at large radii.

The following sections examine the results of each chapter in more detail and discuss any improvements and potential future research.

5.2 Dynamics of Wind-Driven Bubbles

Chapter 2 extended the work of Koo & McKee (1992a) to include a power-law cooling function. Koo & McKee developed a rigorous treatment of wind-blown bubbles by building on earlier work which typically focused on stellar wind bubbles (Avedisova 1972; Weaver et al. 1977). By using a power-law energy injection rate (scaling like t^{α}) and a power-law gas mass distribution (scaling like r^{p}) they were able to introduce and derive timescales which separate the outflow regimes of the shell. The most featured of these timescales is the fiducial timescale t_f defined to mark the end of the free-expansion stage. This timescale is independent of the cooling function and therefore remains unrevised in Chapter 2. Potential future work involving this timescale would be to use the SMBH mass defined in Chapter 4 by equation (4.5) in order to find the fiducial time for an SMBH which grows from a seed mass. This will recover the timescale used by Koo & McKee in the limit that the ratio t/t_s is very large and the SMBH mass is reduced to a power law in time. Further investigation into free-expansion could be carried out by using a double-power law gas mass profile such as the Hernquist profile utilised throughout this thesis.

Koo & McKee restricted their attention to decelerating bubbles, as accelerating bubbles are expected to be subject to the Rayleigh-Taylor instability. This limits their attention to a specific set of values for α and p, for example if the gas mass profile is an SIS then $p = 1$, which limits the value of the injection rate parameter to: $\alpha < 1$. Based on the work in Chapter 4 it is shown that if gravity is included then shells are decelerating in an SIS halo for all α, and therefore the parameter space for stable shells is extended by including gravity.

In Chapter 2 the cooling timescales for the shocked wind and shocked ambient medium have been extended for the case of a power law cooling function. This allows for different cooling processes to be used when deriving the timescales which separate the possible driving regimes. In order to have a momentum-driven shell during free-expansion a restriction is placed on the parameter values α, p and the new cooling parameter β. A three-dimensional plot in Figure 2.5 was produced along with Table 2.1

which showed the value of β which must not be exceeded in order to have a momentum-driven shell at early times. This plot and the associated table show that the value of β in order to meet this restriction is lower for higher values of p. Within the context of SMBH winds the dominant cooling process is inverse Compton scattering (King 2003; McQuillin & McLaughlin 2012), and how this relates to the values in Table 2.1 is worthy of further investigation. Costa, Sijacki & Haehnelt (2014) state that for the higher temperatures expected for the shocked wind region that the cooling function for inverse Compton scattering may have $\beta = 1 - 2$ which would lead to an energy-driven shell at early times for mass profiles such as Hernquist at small radii.

The characteristic cooling timescale t_1 which was introduced is useful for being approximately greater than the cooling time of the shocked wind $t_{\rm cool,sw}$, and therefore allows for the critical wind velocity separating slow and fast winds to be conveniently defined. It was shown for variation in β that t_1 becomes equal to and exceeds the value of $t_{\rm cool,sw}$ for a substantial range of parameter space for higher β. This shows once again the reversal of momentum- and energy-driven shells for higher β values. It was also shown that the cooling time of the shocked ambient medium $t_{\rm cool,sa}$ is also more likely to exceed t_1 for higher β.

The critical wind velocity $v_{\rm cr}$ is defined by requiring $t_f = t_1$ for a momentum-driven shell, and therefore if a wind is *slow*: $v_w \ll v_{\rm cr}$ then it will be subject to cooling when it leaves the free-expansion stage and will therefore still be momentum-driven. If the inverse is true then the wind is *fast* and the shell is no longer subject to cooling when it leaves free-expansion. For particular combinations of α and p this definition is reversed and slow winds lead to energy-driven shells and fast to momentum-driven. The combinations which result in the reversal are shown to occupy a greater region of parameter space for a larger value of β, i.e for $\beta = 2$, constant ($\alpha = 0$) slow winds will lead to energy-driven shells emerging from free-expansion rather than momentum-driven.

Later on, in Chapter 3 the scatter in the $M_{\rm BH} - \sigma$ data was interpreted as a distribution in momentum-boosts, and therefore as a distribution in wind speeds (as previously concluded by McQuillin & McLaughlin 2013). This permits regions of the

$M_{\rm BH} - \sigma$ data to be classified as corresponding to outflows which were blown by fast or slow winds. Future work would therefore be to obtain values for $v_{\rm cr}$ for appropriate values of α, p, and β which allow such an interpretation to be made. This can also be extended to observations of active galaxies where observations of the small scale wind velocity and the large scale outflow can be made (Tombesi et al. 2015; Feruglio et al. 2015). Using the results from such observations will allow conclusions to be drawn regarding $v_{\rm cr}$ and the efficiency of cooling by using the momentum-boost to determine whether the outflow is momentum- or energy-driven.

Chapter 2 concluded with an overview of the equations of motion for momentum- and energy-driven shells subject to gravitational and ambient pressure forces. Future work for a more complete treatment of outflow dynamics can be achieved by finding solutions to the equations of motion which account for the mass of the shocked wind region and the crossing time of the wind. A potential next step is to introduce a functional form for the cooling function which depends on shell radius and time. This will allow for the transitions between momentum- and energy-driven shells to be studied and for the analysis of the intermediate partially radiative bubble stage (Koo & McKee 1992a). A preliminary attempt to introduce cooling into these equations has been carried out by Faucher-Giguère & Quataert (2012), and they concluded that SMBH wind driven outflows are expected to be energy-driven over much of their lifetimes.

5.3 Aspects of Steady Winds

Chapter 3 began by extending the work of McQuillin & McLaughlin (2012) to include the effects of ambient pressure and infall. Ambient pressure has been included in previous analyses (Faucher-Giguère & Quataert 2012), but its effects have yet to be studied in their own right. The analysis in Chapter 3 started with momentum-driven outflows in SIS and Hernquist dark matter haloes. It was found that the inclusion of ambient pressure leads to a new type of solution for the momentum-driven shell which corresponds to pressure confinement (see Koo & McKee 1992a for discussion). Strictly

speaking these shell solutions are able to make slow progress before reaching large radii, but due to the outflow time taken ($t > 10^{10}$ yr), and that the numerical solution method required discrete steps, it is likely that these shells remain static. Future work may be to improve this issue by allowing for the gradual release of ambient pressure as the shell begins to infall (rather than its discontinuous instant release). However, the shock structure of a shell that has stalled is unlikely to persist, and therefore future work should also include an examination of the conditions for which momentum-driven shells remain stable. Ultimately, the derived $M_{\rm BH} - \sigma$ relations for momentum-driven shells are only slightly affected by the inclusion of ambient pressure, with the normalisation of the newly required SMBH masses (for the shell to reach large radii without stalling) being increased by approximately a half.

The second half of Chapter 3 analysed the dynamics of energy-driven shells. This work included ambient pressure and it showed that there are solutions which correspond to confined energy-driven shells. These shells are confined by gravitational forces and the ambient pressure, but are supported against infall by their own thermal pressure (see Koo & McKee 1992a). The momentum-boosts of energy-driven shells were then analysed in detail, and it was found that the distribution of momentum-boosts in terms of shell terminal velocity (v_∞) is a peaked function. This means that there is a specific outflow velocity $v_{\rm p,max}$ at which maximum momentum-boosting occurs. The momentum-boost result from Zubovas & King (2012) which was obtained in the limit that $v_\infty \gg \sigma_0$ for high outflow speeds at large scales can be understood as being the limit that $v_\infty \gg v_{\rm p,max}$ (since $v_{\rm p,max} \sim 2\sigma_0$ for typical values of γ), and being equivalent to neglecting the effects of gravity. By neglecting gravity all of the available wind kinetic energy is imparted on the bulk motion of the shell, which means for lower wind speeds the momentum-boost tends to infinity. This limit has been used with observational data to infer wind speeds, or to confirm energy-driving (Tombesi et al. 2015; Feruglio et al. 2015). The actual (peaked) distribution would be better used with observational data (i.e. equation 3.95 rather than 3.97) as observed outflows do not always have $v_{\rm p,max} \gg \sigma$ (see Cicone et al. 2014 and Table 3.2). Instead, such outflows seem to occur at velocities which put the momentum-boosts around this peaked distribution,

as shown in Figure 3.21.

If Zubovas & King (2012) were to have chosen an outlow velocity then this would result in an $M_{\rm BH}v_w - \sigma_0$ relation which applies when the maximum available wind energy is imparted on the shell, i.e. the low gravity limit. In their work McQuillin & McLaughlin (2013) set the terminal shell velocity equal to $2\sigma_0$ to obtain an $M_{\rm BH}v_w - \sigma_0$ relation. In my work I required maximum momentum-boosting which gave a different $M_{\rm BH}v_w - \sigma_0$ relation as this requires the velocity to be the value $v_{\rm p,max}$. For $\gamma = 5/3$ this leads to a velocity: $v_{\rm p,max} \sim 2\sigma_0$, and therefore an $M_{\rm BH}v_w$ value which is not dissimilar from that of McQuillin & McLaughlin. This means that their result and subsequent analysis can be understood in terms of maximally boosted energy-driven shells. However, rather than specify a value for $v_{\rm p,max}$, as it formally depends on γ and any inward forces on the shell (such as ambient pressure), it is retained as a parameter in equation (3.103) in Chapter 3. By doing so, this allows an $M_{\rm BH}-\sigma$ relation to be defined which incorporates the momentum-boost as a distinct parameter, and therefore now allows $M_{\rm BH}$ to be expressed solely in terms of large scale observational parameters (large-scale outflow velocity and momentum-boost). This means that if two of the parameters out of $M_{\rm BH}$, $v_{\rm p,max}$ (which is approximately 2σ), or the momentum-boost can be determined observationally for an active galaxy, then the other can be determined using equation (3.103). This was done for the momentum-boosts of three systems in Table 3.2 using known $M_{\rm BH}$ and σ values, and the resultant boosts were found to be in agreement with the observed values. Furthermore, if an observer can determine the large scale momentum-boost of an outflow, then the small scale wind speed can be estimated using the expression for the boost factor. Note that using this equation does presume that the observed outflows are maximally boosted at large scales (in addition to the other assumptions utilised in this model). A direction for further research is to investigate whether or not outflows are likely to be maximally boosted at large radii, and this can be achieved by obtaining more observational data to test this hypothesis. A possibility for further theoretical research would be to examine what the physical processes responsible for maximum boosting may be.

McQuillin & McLaughlin (2013) interpret the scatter in the $M_{\rm BH} - \sigma$ data as

variation in the wind speeds which drove outflows in protogalaxies to clear their hosts of gas. They derive a median wind speed from the $M_{\rm BH} - \sigma$ data by using their $M_{\rm BH} v_w - \sigma$ relation, and show that this compares well with the median wind speeds from samples of small scale observations of local AGN. Equation (3.103) permits the variation in wind speed to also be interpreted as a variation in momentum-boosts, and therefore a similar analysis to McQuillin & McLaughlin could be carried out but with a median momentum-boost, and samples of large scale observations of galactic outflows, rather than small scale AGN winds. The scatter in the $M_{\rm BH} - \sigma$ data can therefore be interpretted as a distribution in the momentum-boosts which were present when the protogalaxies were cleared of gas by the outflow. It was shown in Chapter 3 that the maximally boosted momentum-driven $M_{\rm BH} - \sigma$ relation (i.e. $M_{\rm BH} = 2M_\sigma$) is coincident with the energy-driven relation for the case that the boost is unity. This occurs if the wind speed is not significantly in excess of $v_{\rm p,max}$ (which is approximately 2σ), and therefore this leads to the notion that the high $M_{\rm BH}$ and high σ data which are intersected by the momentum-driven line (where the boost is unity) may correspond to protogalactic systems which were cleared by a momentum-driven outflow, which itself was driven by a slow wind (relative to σ). This is consistent with the conclusions from Chapter 2, where slow winds (relative to a critical velocity) produce momentum-driven outflows (for a specific range of parameter values), and fast winds produce energy-driven outflows. This is also consistent with conclusions drawn regarding the prevelance of energy-driving (Faucher-Giguère & Quataert 2012; Costa, Sijacki & Haehnelt 2014), as most of the data in Figure 3.1 is coincident with curves corresponding boosted energy-driven shells. However, it is important to note that slow and fast winds are defined relative to different quantities in Chapters 2 and 3. Consequently, there is scope for future work to reconcile the outcomes in these chapters to gain a better understanding of slow and fast winds, and the driving regimes that they produce.

An encouraging result from the analysis in Chapter 3 is that when data from large-scale observations of active galaxies are included alongside the $M_{\rm BH} - \sigma$ data, the predicted values for the momentum-boosts are in broad agreement with the measured values (Cicone et al. 2014; Rupke, Gültekin & Veilleux 2017). As new measurements of

$M_{\rm BH}$, σ, $v_{\rm p,max}$, v_w, and momentum-boosts are gathered for active systems the more the predictions (and the model on which it is built) of equation (3.103) can be tested. For example, recent (Mizumoto, Izumi & Kohno 2019) observations of small scale winds in the systems listed in Table 3.2 give wind speeds of $0.24c$, $0.12c$, $0.28c$, and $0.31c$, which are comparable to the corresponding theoretical values $0.06c$, $0.20c$, $0.18c$, and $0.17c$ listed in Table 3.2. However, these theoretical values have a significant degree of uncertainty which comes from the 0.45 dex error in the momentum-boost. As future projects are carried out and higher resolution measurements of systems can be made at both small and large radii, the suitability of equation (3.103) and its underlying theory of maximally boosted shells can be more effectively assessed. Such projects will include the X-ray Imaging and Spectroscopy Mission (XRISM - with a launch date of 2022), which may be followed by further X-ray missions in the form of the Advanced Telescope for High Energy Astrophysics (ATHENA) and Lynx (with proposed launch dates 2031 and 2035 respectively). These X-ray projects will provide small scale observations of high energy winds (giving values for v_w and $\dot{M}_w v_w$), while the proposed Origins Space Telescope (OST) with a launch date of 2035 will provide infrared observations of the galactic scale outflows (giving values for $v_{\rm p,max}$ and the boost factor).

Finally, by comparing the momentum-boost curves obtained for outflows in a Hernquist halo with the analytical curves from the SIS halo a clear match is found at $r_{\rm pk}$. Requiring that energy-driven shells have a maximum momentum-boost at $r_{\rm pk}$ (where the halo gravity is strongest) results in an $M_{\rm BH} - V_{\rm c,pk}$ relation for energy-driven outflows. The form of this relation can be compared with that obtained by McQuillin & McLaughlin (2012) for momentum-driven shells which reach large radii without stalling. An important issue to be highlighted is that the theory in Chapter 3 assumes that the protogalactic σ_0 at the time of gas blowout can be related directly to the observed σ today. It has been shown that the $M_{\rm BH} - V_{\rm c,pk}$ relation (McQuillin & McLaughlin 2012) for a momentum-driven outflow can lead to a curve which fits right through the $M_{\rm BH} - \sigma$ data by taking into account the redshift evolution of σ (Larkin & McLaughlin 2016). A similar analysis could be carried out but using instead the energy-driven $M_{\rm BH} - V_{\rm c,pk}$ relation given by equation (3.105) to determine if the

conclusions in Chapter 3 remain valid when the relationship between $V_{\rm c,pk}$ and σ is properly accounted for.

5.4 Time-Dependent Winds

Chapter 4 introduced a functional form for the SMBH mass which can recover the constant and exponential SMBH masses for specific values of its growth parameter α. An intermediate case between these two masses can also be used for $\alpha = 1$ which corresponds to a constantly accreting SMBH.

It was found for infalling momentum-driven shells blown by growing winds that they were capable of resuming outward motion and ultimately reaching large radii. The dynamics of outflows were investigated for variation in the growth timescale t_s, and an expression for a sufficient SMBH mass which permits shells to reach large radii without stalling was sought. A satisfactory expression could not be obtained, but instead estimates for the sufficient mass were found. This was achieved for the SIS halo by showing that shells could reach large radii without stalling if they exceeded the sufficient mass from the steady wind case. Specifically it was shown that they must exceed this value by the time they reach the stall radius of a shell blown by a steady wind, which is determined by the value of the initial momentum. This was confirmed by obtaining sufficient seed mass values M_0 for a range of t_s, and it was shown for these shells, which just barely reach large radii without stalling, that the mass of the SMBH when the velocity is at its lowest is close to the steady wind sufficient mass. For the Hernquist halo only solutions with $C = 0$ were examined in detail as the methods used for the SIS halo can be extended to the Hernquist halo if the shell has nonzero initial momentum. The $C = 0$ case is therefore distinct, and it was shown that obtaining a sufficient SMBH mass for this case is more difficult. In the end the numerically determined values for the sufficient M_0 for a range in t_s were examined, and they show that the SMBH mass can depart significantly from the sufficient mass for the steady wind case over a physically interesting range of t_s. However for slower growing winds,

which produce shells that just barely go on to accelerate, the SMBH mass at their velocity minima is approximately the steady wind sufficient SMBH mass. Despite the complexities associated with the momentum-driven shells in the Hernquist halo this chapter achieved its aims of showing (at least for the SIS halo) that the conclusions from Chapter 3 regarding momentum-driven shells are not significantly altered by the inclusion of a growing SMBH wind.

The second part of this chapter focussed on energy-driven shells blown by non-steady winds. It was shown that energy-driven shells in the SIS halo now accelerate at large radii, but at smaller radii the dynamics are not fundamentally different. It was demonstrated that energy-driven shells at large radii in the SIS halo have the same peaked distribution of momentum-boosts in terms of shell velocity, that this peak occurs at $v_{\rm p,max}$ as defined in Chapter 3, and that this occurs when the shell kinetic and wind energies are in the required ratio. Through the analysis of the large-scale momentum-boosts in the SIS halo for the fiducial growth timescale considered it was shown that analytical relationships derived in Chapter 3 for shells driven by steady winds continued to apply, but for a narrower range of radii. Hence the SMBH mass for these shells driven by non-steady winds will continue to be given by the $M_{\rm BH}-\sigma_0$ relation (equation 3.103) derived in Chapter 3. Future work would examine the true limits of this relation for non-steady winds as it is likely to not be applicable to rapidly growing SMBH. This chapter can be extended further by analysing the boosts in terms of the seed mass (or SMBH mass), and assessing whether the momentum-boost distributions correspond to physically realistic values of $M_{\rm BH}$, rather than simply being shown in terms of outflow velocity. For the Hernquist halo it was found that the shells driven by non-steady winds simply accelerate earlier than their steady-wind driven counterparts, but that this impacts the conclusions drawn in Chapter 3, as the characteristic distribution of momentum-flux with outflow velocity occurs at smaller radii than $r_{\rm pk}$. The main focus of this chapter was to simply examine the conclusions of Chapter 3 within the context of non-steady winds, which means that there are significant extensions which can be made by developing these results within a more physical and observational context. For example, by introducing typical or expected accretion, cooling, and flow timescales

into the analysis of shell dynamics, which in turn will enable earlier concepts such as critical wind velocity and cooling to be revisited. Finally, since all energy-driven shells from non-steady winds are accelerating at large radii this work could be extended by analysing the stability of such shells, either in terms of Rayleigh-Taylor instabilities, or gravitational instabilities (Vishniac 1983).

A Glossary of Acronyms

ATHENA	Advanced Telescope for High Energy Astrophysics
AGN	Active Galactic Nucleus
BH	Black Hole
BLR	Broad emission Line Region
BLRG	Broad Line Radio Galaxy
CDM	Cold Dark Matter
IC	Index Catalogue (of nebulae and clusters of stars)
IRAS	Infrared Astronomical Satellite
LINER	Low Ionisation Nuclear Emission Line Region
NFW	Navarro, Frenk & White
NGC	New General Catalogue
NLRG	Narrow Line Radio Galaxy
PRB	Partially Radiative Bubble
SIS	Singular Isothermal Sphere
SF	Star Formation
SMBH	Supermassive Black Hole
ULIRG	Ultra Luminous Infrared Galaxy
XRISM	X-ray Imaging and Spectroscopy Mission

B Glossary of Symbols

α	Black hole mass/wind growth parameter
α'	Dark matter density profile parameter
a	Apparent major axis of an elliptical galaxy
a'	Scaling parameter in the Faber-Jackson relation
A'	Fundamental plane parameter
$\mathcal{A}$	Cooling time constant
β	Cooling function parameter
β'	Dark matter density profile parameter
$\beta_{\rm crit}$	Critical cooling function parameter
b	Apparent minor axis of an elliptical galaxy
b_N	Sérsic parameter
$B(r)$	Anisotropy parameter
B'	Fundamental plane parameter
c	Speed of light in vacuo
c_s	Sound speed
$c_{s,1}$	Pre-shock sound speed
C	The square of a shell's initial momentum
$\mathcal{C}$	Cooling time constant
C'	Fundamental plane parameter
$C_{\rm esc}$	The square of a shell's initial momentum required to reach large radii
$C_{\rm ff}$	Initial momentum required for a shell to escape after stalling
$C_{\rm min}$	The lowest value of the shell's initial momentum which is required to reach large radii
C_P	Specific heat at constant pressure
C_V	Specific heat at constant volume
η	Accretion efficiency
η'	Power on velocity disperion in the empirical relation between dark matter density, velocity dispersion, and radius.
E_*	Pseudo-energy of a particle
E_∞	Energy of a particle at infinity
$E_{\rm acc}$	Energy released during accretion
E_b	Binding energy of a particle
$E_{\rm bulge}$	Binding energy of a bulge
$\dot{E}_w$	Energy released by the wind
$f(\mathbf{x}, \mathbf{v}, t)$	Distribution function for a stellar system
f_0	Gas to dark matter ratio
f_P	Ratio of ram pressures
F	Factor taking into account geometry of BLR
$F_{\rm grav}$	Gravitational force
$F_{\rm rad}$	Force from radiation pressure

γ	Ratio specific heats
γ'	Dark matter density profile parameter
$\gamma_{\rm sw}$	Ratio of specific heats in the shocked wind region
g	Subfunction of the continuum cooling function
G	Gravitational constant
h	Disk scale length
$h(x)$	Function describing how the ambient gas traces dark matter
H	Scaled Hubble constant
$I(R)$	Surface brightness function
I_0	Central surface brightness
I_e	Intensity at the effective radius
$\langle I_e \rangle$	Average effective surface brightness
κ	Thomson scattering opacity
k_B	Boltzmann constant
K	Global kinetic energy of a stellar system
λ_d	Mean free path
Λ	Cooling function
$\Lambda_{\rm coll}$	Cooling function fore collisional ionisation
$\Lambda_{\rm Compton}$	Cooling function for Compton scattering
$\Lambda_{\rm cont}$	Cooling function for continuum emission
$\Lambda_{\rm lines}$	Cooling function for collisional line radiation
$\Lambda_{\rm photo}$	Cooling function for photoionisation
$\Lambda_{\rm rec}$	Cooling function for recombination processes
Λ_s	Value of the cooling function at the scale temperature
l	Angular momentum of a particle
$L_\odot$	Solar luminosity
$L_{K_\odot}$	Solar luminosity in the K band
$L_{\rm AGN}$	AGN luminosity
$L_{\rm bulge}$	Bulge luminosity
$L_{\rm K,bulge}$	Bulge luminosity in the K band
$L_{\rm Edd}$	Eddington luminosity
$L_{\rm gal}$	Galaxy luminosity
$L_{\rm gal,B}$	Galaxy luminosity in the B band
$L_{\rm gal,H}$	Galaxy luminosity in the H band
$L_{\rm MW}$	Milky Way luminosity
L_X	X-ray luminosity
μ_H	Mean mass per hydrogen nucleus
m	Mass of an individual particle
$m(x)$	The ratio of shell mass to dark matter interior to x
m_0	Rest mass of a particle
$\dot{m}$	Eddingtion ratio
$\mathscr{M}$	Mach number

M	Mass of a stellar system
$\widetilde{M}$	Mass normalised to M_σ
$M_\odot$	Solar mass
M_*	Stellar mass
M_σ	Critical SMBH mass required for a shell to escape in an SIS halo
M_0	Seed mass
$M_{\rm BH}$	Black hole mass
$M_{\rm BH,crit}$	Necessary SMBH mass required for a shell to reach large radii
$M_{\rm BH,low}$	The lowest necessary SMBH mass which is required for a shell to reach large radii
$M_{\rm BH,high}$	The highest necessary SMBH mass which is required for a shell to reach large radii
$M_{\rm bulge}$	Bulge mass
$M_{\rm crit}$	The SMBH mass which results in a shell with both acceleration and velocity equal to zero
$M_{\rm DM}$	Dark matter mass
M_g	Mass of swept-up ambient gas
$M_{\rm crit}^{\rm max}$	The highest critical SMBH mass for a range of initial momentum values
$M_{\rm pk}$	Mass of a dark matter interior to $r_{\rm pk}$
$M_{\rm sh}$	Shell mass
$M_{\rm sp}$	Spiral galaxy mass
M_w	Wind mass
$M_{\rm w,s}$	Wind mass at scale time
$\dot{M}_{\rm BH}$	Black hole growth rate
$\dot{M}_{\rm Edd}$	Eddington mass rate
$\dot{M}_{\rm out}$	Outflow mass rate
$\dot{M}_{\rm pk}$	Dark matter mass at $r_{\rm pk}$
$\dot{M}_w$	Wind mass rate
n	Sérsic index
n_e	Number density of electrons
n_H	Number density of hydrogen
n'	Number density of hydrogen
N	Elliptical galaxy parameter
N'	Column density of an outflow
Φ	Gravitational potential
p	Parameter for power law mass profile
$p_{\rm crit}$	Critical value of the parameter for power law mass profile
$\dot{p}_{\rm sh}$	Momentum-flux of a shell
P	Shocked wind pressure
P_1	Pre-shock gas pressure
P_2	Post-shock gas pressure
P_g	Gas pressure
q	Ratio of accretion rate to Eddington rate

ρ	Density of stellar system
$\bar{\rho}$	Mean density
ρ_1	Pre-shock gas density
ρ_2	Post-shock gas density
$\rho_{\rm DM}$	Dark matter density
ρ_g	Gas density
$\bar{\rho}_g$	Mean gas density.
$\rho_{\rm gr}$	Density at gravitational radius
$\rho_{\rm pk}$	Density at $r_{\rm pk}$
ρ_σ	Characteristic density
ρ_s	Density at characteristic radius r_0
$\rho_{\rm sc}$	Density at scale radius $r_{\rm sc}$
r	Radius from galactic centre
$\tilde{r}$	Radius normalised to r_σ
r_{-2}	Radius at which the logarithmic slope of the dark matter density profile is -2
r_σ	Characteristic radius
r_c	Radius of contact discontinuity
r_f	Fiducial radius
r_g	Gravitational radius
$r_{\rm inf}$	Influence radius of an SMBH
r_m	Radius of extrema in effective potential
$r_{\rm min}$	Radius of smallest stable orbit
$r_{\rm pk}$	Radius at which the peak of the dark matter circular speed curve peaks
r_s	Radius of the forward shock
$r_{\rm sc}$	Scale radius
$r_{\rm sw}$	Radius of the wind shock
r_S	Schwarzschild radius
R	Projected distance from galactic centre
$R_{\rm BLR}$	Radius of the BLR
R_e	Effective radius
σ	Stellar velocity dispersion
σ_0	Characteristic velocity dispersion
$\sigma_{\rm ap}$	Stellar velocity dispersion measured within an aperture
σ_g	Velocity dispersion of the ambient gas
$\sigma_{\rm l.o.s}$	Line of sight stellar velocity dispersion
σ_ϕ	Stellar velocity dispersion in the ϕ direction
σ_r	Stellar velocity dispersion in the radial direction
σ_θ	Stellar velocity dispersion in the θ direction
σ_T	Thomson cross section
s	Proper time
S	Flux density
τ	Scattering parameter

t	Time
t_1	Characteristic cooling time
$t_{\rm age}$	Galaxy age
$t_{\rm col}$	Collapse timescale of the ambient gas
$t_{\rm cool}$	Cooling time
$t_{\rm cool,sa}$	Cooling time of shocked ambient medium
$t_{\rm cool,sw}$	Cooling time of shocked wind
$t_{\rm cr}$	Crossing time
$t_{\rm en}$	Transition time to an energy-driven bubble
$t_{\rm ex}$	Time when a when reaches a minimum in velocity
t_f	Fiducial time
$t_{\rm ff}$	Infall timescale of the shell
$t_{\rm out}$	Time taken for the collapse of the shocked ambient medium
$t_{\rm stall}$	Stall time of a shell
t_r	Transition time to a partially radiative bubble
t_σ	Characteristic time scale
t_s	Scale time
t_S	Salpteter time
T	Temperature
T_s	Scale temperature
U	Internal energy of shocked wind
$\mathbf{v}$	Three-dimensional velocity of a star
v	Forward shock velocity
v_1	Pre-shock gas velocity
v_2	Post-shock gas velocity
v_∞	Coasting velocity at large radii
$v_{\rm crit}$	Critical wind speed
v_c	Velocity of contact discontinuity
$v_{\rm circ}$	Circular velocity
$v_{\rm col}$	Collapse velocity of the ambient gas
$v_{\rm esc}$	Escape velocity
$v_{\rm ff}$	Infall velocity of the shell
$v_{\rm out}$	Observed outflow velocity
$v_{\rm p,max}$	Velocity of shell at peak momentum-boosting
v_w	Wind speed
$v_{\rm sw}$	Velocity of the wind shock
$v_{\rm sw,w}$	Velocity of wind shock relative to the wind
$\langle v \rangle$	Average stellar speed
$\langle v^2 \rangle$	Mean square stellar speed
V	Gas volume

V_c	Circular speed
$V_{\rm c,pk}$	Peak circular speed
$V_{\rm eff}$	Effective potential
$V_{\rm rot}$	Rotational velocity
W	Gravitational potential energy of a stellar system
ξ	Parameter for the scaling of the ratio dark matter density with velocity dispersion
ξ'	Numerical constant of order unity
x	Galactic radius divided by $r_{\rm pk}$
$\mathbf{x}$	Three-dimensional position of a star
$x_{\rm c,max}$	The $x_{\rm c,crit}$ associated with $M_{\rm crit}^{\rm max}$
$x_{\rm crit}$	The radius where the acceleration and the velocity of the shell are both zero
$x_{\rm launch}$	Launch radius for a shell
$x_{\rm stall}$	Stall radius of a shell
x_t	Number of particles per hydrogen nucleus
z	Redshift
Z	Metallicity
$Z_\odot$	Solar metallicity

Bibliography

Aaronson M., Mould J., 1983, ApJ, 265, 1

Aird J., Coil A. L., Georgakakis A., Nandra K., Barro G., Pérez-González P. G., 2015, MNRAS, 451, 1892

An J., Zhao H., 2013, MNRAS, 428, 2805

Antonucci R., 1993, A&A, 31, 473

Avedisova V. S., 1972, Soviet Ast., 15, 708

Baes M., Buyle P., Hau G. K. T., Dejonghe H., 2003, MNRAS, 341, L44

Balick B., Brown R. L., 1974, ApJ, 194, 265

Barth A. J., Martini P., Nelson C. H., Ho L. C., 2003, ApJ, 594, L95

Barth A. J., Darling J., Baker A. J., Boizelle B. D., Buote D. A., Ho L. C., Walsh J. L., 2016, ApJ, 823, 51

Becklin E. E., Neugebauer G., 1968, ApJ, 151, 145

Beifiori A., Sarzi M., Corsini E. M., Dalla Bontà E., Pizzella A., Coccato L., Bertola F., 2009, ApJ, 692, 856

Beifiori A., Courteau S., Corsini E. M., Zhu Y., 2012, MNRAS, 419, 2497

Benson A. J., 2010, PhR, 495, 33

Benson A. J., Bower R. G., Frenk C. S., Lacey C. G., Baugh C. M., Cole S., 2003, ApJ, 599, 38

Binney J., Merrifield M., 1998, Galactic Astronomy, Princeton University Press, 1 edition

Binney J., Tremaine S., 2008, Galactic Dynamics, Princeton University Press, 2 edition

Blandford R. D., McKee C. F., 1982, ApJ, 255, 419

Blumenthal G., Faber S., Primack J., Rees M., 1984, Nature, 311, 517

Bouwens R. J., Illingworth G. D., Oesch P. A., Labbé I., Trenti M., van Dokkum P., Franx M., Stiavelli M., Carollo C. M., Magee D., Gonzalez V., 2011, ApJ, 737, 90

Bouwens R. J., Illingworth G. D., Oesch P. A., Trenti M., Labbé I., Bradley L., Carollo M., van Dokkum P. G., Gonzalez V., Holwerda B., Franx M., Spitler L., Smit R., Magee D., 2015, ApJ, 803, 34

Bower R. G., Benson A. J., Malbon R., Helly J. C., Frenk C. S., Baugh C. M., Cole S., Lacey C. G., 2006, MNRAS, 370, 645

Burkert A., 1995, ApJ, 447, L25

Cappi M., Panessa F., Bassani L., Dadina M., Di Cocco G., Comastri A., della Ceca R., Filippenko A. V., Gianotti F., Ho L. C., Malaguti G., Mulchaey J. S., Palumbo G. G. C., Piconcelli E., Sargent W. L. W., Stephen J., Trifoglio M., Weaver K. A., 2006, A&A, 446, 459

Castor J., McCray R., Weaver R., 1975, ApJ, 200, L107

Chartas G., Brandt W. N., Gallagher S. C., Garmire G. P., 2002, ApJ, 579, 169

Choudhuri A., 1998, The Physics of Fluids and Plasmas: An Introduction for Astrophysicists, Cambridge University Press, 1st edition

Cicone C., Feruglio C., Maiolino R., Fiore F., Piconcelli E., Menci N., Aussel H., Sturm E., 2012, A&A, 543, A99

Cicone C., Maiolino R., Sturm E., Graciá-Carpio J., Feruglio C., Neri R., Aalto S., Davies R., Fiore F., Fischer J., García-Burillo S., González-Alfonso E., Hailey-Dunsheath S., Piconcelli E., Veilleux S., 2014, A&A, 562, A21

Ciotti L., Ostriker J. P., 1997, ApJ, 487, L105

Costa T., Sijacki D., Haehnelt M., 2014, MNRAS, 444, 2355

Côté P., McLaughlin D., Cohen J., Blakeslee J., 2003, A&A, 591, 850

Croton D. J., Springel V., White S. D. M., De Lucia G., Frenk C. S., Gao L., Jenkins A., Kauffmann G., Navarro J. F., Yoshida N., 2006, MNRAS, 365, 11

Davis T. A., Bureau M., Cappellari M., Sarzi M., Blitz L., 2013, Nature, 494, 328

Davis T. A., Bureau M., Onishi K., Cappellari M., Iguchi S., Sarzi M., 2017, MNRAS, 468, 4675

Davis T. A., Bureau M., Onishi K., van de Voort F., Cappellari M., Iguchi S., Liu L., North E. V., Sarzi M., Smith M. D., 2018, MNRAS, 473, 3818

de Vaucouleurs G., 1948, Annales d'Astrophysique, 11, 247

Debuhr J., Quataert E., Ma C.-P., 2011, MNRAS, 412, 1341

Debuhr J., Quataert E., Ma C.-P., 2012, MNRAS, 420, 2221

Dehnen W., McLaughlin D. E., 2005, MNRAS, 363, 1057

Devecchi B., Volonteri M., 2009, ApJ, 694, 302

Di Matteo T., Springel V., Hernquist L., 2005, Nature, 433, 604

D'Onofrio M., Valentinuzzi T., Secco L., Caimmi R., Bindoni D., 2006, NewAR, 50, 447

Draine B. T., 2011, Physics of the Interstellar and Intergalactic Medium, Princeton University Press

Dressler A., Richstone D. O., 1988, ApJ, 324, 701

Dressler A., 1989, in Osterbrock D. E., Miller J. S., eds, Active Galactic Nuclei, IAU Symposium Vol. 134, p. 217

Dubinski J., Carlberg R. G., 1991, A&A, 378, 496

Einasto J., 1965, Trudy Astrofizicheskogo Instituta Alma-Ata, 5, 87

Faber S. M., Jackson R. E., 1976, ApJ, 204, 668

Fabian A., 1999, MNRAS, 308, L39

Faucher-Giguère C., Quataert E., 2012, MNRAS, 425, 605

Ferrarese L., Ford H., 2005, Sp. Sci. Rev., 116, 523

Ferrarese L., Merritt D., 2000, ApJ, 539, L9

Ferrarese L., 2002, ApJ, 578, 90

Ferrarese L., Ford H. C., Jaffe W., 1996, ApJ, 470, 444

Feruglio C., Maiolino R., Piconcelli E., Menci N., Aussel H., Lamastra A., Fiore F., 2010, A&A, 518, L155

Feruglio C., Fiore F., Carniani S., Piconcelli E., Zappacosta L., Bongiorno A., Cicone C., Maiolino R., Marconi A., Menci N., Puccetti S., Veilleux S., 2015, A&A, 583, A99

Feruglio C., Ferrara A., Bischetti M., Downes D., Neri R., Ceccarelli C., Cicone C., Fiore F., Gallerani S., Maiolino R., Menci N., Piconcelli E., Vietri G., Vignali C., Zappacosta L., 2017, A&A, 608, A30

Fiore F., Feruglio C., Shankar F., Bischetti M., Bongiorno A., Brusa M., Carniani S., Cicone C., Duras F., Lamastra A., Mainieri V., Marconi A., Menci N., Maiolino R., Piconelli E., Vietri G., Zappacosta L., 2017, A&A, 601, 21

Frank J., King A., Raine D., 2002, Accretion Power in Astrophysics, Cambridge University Press, 3rd edition

Frenk, C S., White S., 2012, Annalen der Physik, 524, 507

Gaibler V., Khochfar S., Krause M., Silk J., 2012, MNRAS, 425, 438

Ganguly R., Brotherton M. S., Cales S., Scoggins B., Shang Z., Vestergaard M., 2007, ApJ, 665, 990

Gebhardt K., Bender R., Bower G., Dressler A., Faber S., Filippenko A., Green R., Grillmair C., Ho L., Kormendy J., Lauer T., Magorrian J., Pinkney J., Richstone D., Tremaine S., 2000, ApJ, 539, L13

Gebhardt K., Richstone D., Tremaine S., Lauer T. R., Bender R., Bower G., Dressler A., Faber S. M., Filippenko A. V., Green R., Grillmair C., Ho L. C., Kormendy J., Magorrian J., Pinkney J., 2003, ApJ, 583, 92

Genzel R., Eisenhauer F., Gillessen S., 2010, Reviews of Modern Physics, 82, 3121

Gerhard O., Kronawitter A., Saglia R. P., Bender R., 2001, AJ, 121, 1936

Gillessen S., Eisenhauer F., Trippe S., Alexander T., Genzel R., Martins F., Ott T., 2009, ApJ, 692, 1075

Gilli R., Calura F., D'Ercole A., Norman C., 2017, A&A, 603, A69

Gofford J., Reeves J., Tombesi F., Braito V., Turner T., Miller L., Cappi M., 2013, MNRAS, 430, 60

González-Alfonso E., Fischer J., Graciá-Carpio J., Falstad N., Sturm E., Meléndez M., Spoon H. W. W., Verma A., Davies R. I., Lutz D., Aalto S., Polisensky E., Poglitsch A., Veilleux S., Contursi A., 2014, A&A, 561, A27

González-Alfonso E., Fischer J., Spoon H. W. W., Stewart K. P., Ashby M. L. N., Veilleux S., Smith H. A., Sturm E., Farrah D., Falstad N., Meléndez M., Graciá-Carpio J., Janssen A. W., Lebouteiller V., 2017, ApJ, 836, 11

Graham A., Guzmán R., 2003, A&A, 125, 2936

Graham A., 2001, A&A, 121, 820

Greene J. E., Zakamska N. L., Smith P. S., 2012, ApJ, 746, 86

Grier C. J., Peterson B. M., Pogge R. W., Denney K. D., Bentz M. C., Martini P., Sergeev S. G., Kaspi S., Minezaki T., Zu Y., Kochanek C. S., Siverd R., Shappee B., Stanek K. Z., Araya Salvo C., Beatty T. G., Bird J. C., Bord D. J., Borman G. A., Che X., Chen C., Cohen S. A., Dietrich M., Doroshenko V. T., Drake T., Efimov Y. S., Free N., Ginsburg I., Henderson C. B., King A. L., Koshida S., Mogren K., Molina M., Mosquera A. M., Nazarov S. V., Okhmat D. N., Pejcha O., Rafter S., Shields J. C., Skowron J., Szczygiel D. M., Valluri M., van Saders J. L., 2012, ApJ, 755, 60

Gruppioni C., Calura F., Pozzi F., Delvecchio I., Berta S., De Lucia G., Fontanot F., Franceschini A., Marchetti L., Menci N., Monaco P., Vaccari M., 2015, MNRAS, 451, 3419

Gültekin K., Richstone D., Gebhardt K., Lauer T., Tremaine S., Aller M., Bender R., Dressler A., Faber S., Filippenko A., Green R., Ho L., Kormendy J., Magorrian J., Pinkney J., Siopsis C., 2009, ApJ, 698, 198

Haehnelt M. G., Rees M. J., 1993, MNRAS, 263, 168

Haehnelt M., Natarajan P., Rees M., 1998, MNRAS, 300, 817

Halpern J. P., 1984, ApJ, 281, 90

Hansen S., 2004, MNRAS, 352, L41

Häring N., Rix H.-W., 2004, ApJ, 604, L89

Harms R. J., Ford H. C., Tsvetanov Z. I., Hartig G. F., Dressel L. L., Kriss G. A., Bohlin R., Davidsen A. F., Margon B., Kochhar A. K., 1994, ApJ, 435, L35

Harrison C. M., 2014, in Mickaelian A. M., Sanders D. B., eds, Multiwavelength AGN Surveys and Studies, IAU Symposium Vol. 304, p. 284

Harrison C. M., Alexander D. M., Swinbank A. M., Smail I., Alaghband-Zadeh S., Bauer F. E., Chapman S. C., Del Moro A., Hickox R. C., Ivison R. J., Menéndez-Delmestre K., Mullaney J. R., Nesvadba N. P. H., 2012, MNRAS, 426, 1073

Hartwig T., Volonteri M., Dashyan G., 2018, MNRAS, 476, 2288

Hernquist L., 1990, ApJ, 356, 359

Ho L. C., 2007, ApJ, 668, 94

Hopkins P. F., Cox T. J., Kereš D., Hernquist L., 2008, ApJS, 175, 390

Hubble E., 1926, ApJ, 64, 321

Hubble E., 1936, Realm of the Nebulae, Yale University Press, 1 edition

Ishibashi W., Fabian A., 2012, MNRAS, 427, 2998

Ishibashi W., Fabian A. C., Canning R. E. A., 2013, MNRAS, 431, 2350

Ishibashi W., Fabian A. C., Maiolino R., 2018, MNRAS, 476, 512

Kaspi S., Smith P. S., Netzer H., Maoz D., Jannuzi B. T., Giveon U., 2000, ApJ, 533, 631

King A., Pounds K., 2003, MNRAS, 345, 657

King A., Pounds K., 2015, Annu. Rev. Astron. Astrophys., 53, 115

King A., 2003, ApJ, 596, L27

King A., 2005, ApJ, 635, L121

King A., 2009, ApJ, 695, L107

Koo B.-C., McKee C. F., 1992a, ApJ, 388, 103

Koo B.-C., McKee C. F., 1992b, ApJ, 388, 93

Kormendy J., Bender R., 2011, Nature, 469, 377

Kormendy J., Bender R., 2012, The Astrophyscial Journal Supplement, 198, 40

Kormendy J., Ho L., 2013, Annu. Rev. Astron. Astrophys., 51, 511

Kormendy J., McClure R. D., 1993, AJ, 105, 1793

Kormendy J., Richstone D., 1992, ApJ, 393, 559

Kormendy J., Richstone D., 1995, ARA&A, 33, 581

Krolik J., 1999, Active galactic nuclei - from the central black hole to the galactic environment, Princeton University Press, 1 edition

Larkin A., McLaughlin D., 2016, MNRAS, 462, 1864

Lintott C., Schawinski K., Slosar A., Land K., Bamford S., Thomas D., Raddick M. J., Nichol R., Szalay A., Andreescu D., Murray P., Vandenberg J., 2008, MNRAS, 389, 1179

Lynden-Bell D., 1969, Nature, 223, 690

Madau P., Dickinson M., 2014, ARA&A, 52, 415

Madau P., Rees M. J., 2001, ApJ, 551, L27

Magorrian J., Tremaine S., Richstone D., Bender R., Bower G., Dressler A., Faber S., Gebhardt K., Green R., Grillmair C., Kormendy J., Lauer T., 1998, AJ, 115, 2285

Maiolino R., Gallerani S., Neri R., Cicone C., Ferrara A., Genzel R., Lutz D., Sturm E., Tacconi L. J., Walter F., Feruglio C., Fiore F., Piconcelli E., 2012, MNRAS, 425, L66

Marconi A., Hunt L. K., 2003, ApJ, 589, L21

McConnell N. J., Ma C.-P., 2013, ApJ, 764, 184

McKee C. F., Hollenbach D. J., 1987, ApJ, 322, 275

McQuillin R., McLaughlin D., 2012, MNRAS, 423, 2162

McQuillin R., McLaughlin D., 2013, MNRAS, 434, 1332

Merritt D., 2013, Dynamics and evolution of galactic nuclei, Princeton University Press, 1 edition

Merritt D., Graham A., Moore B., Diemand J., Terzić B., 2006, ApJ, 132, 2685

Miller J., 1994, in Bicknell G. V., Dopita M. A., Quinn P. J., eds, The Physics of Active Galaxies, Astronomical Society of the Pacific Conference Series Vol. 54, p. 149

Mizumoto M., Izumi T., Kohno K., 2019, ApJ, 871, 156

Moore B., Governato F., Quinn T., Stadel J., Lake G., 1998, ApJ, 499, L5

Moore B., Ghigna S., Governato F., Lake G., Quinn T., Stadel J., Tozzi P., 1999, ApJ, 524, L19

Murray N., Quataert E., Thompson T. A., 2005, ApJ, 618, 569

Navarro J., Frenk C., White S., 1996, ApJ, 462, 563

Navarro J., Frenk C., White S., 1997, ApJ, 490, 493

Netzer H., Peterson B. M., 1997, in Maoz D., Sternberg A., Leibowitz E. M., eds, Astronomical Time Series, Astrophysics and Space Science Library Vol. 218, p. 85

Onishi K., Iguchi S., Sheth K., Kohno K., 2015, ApJ, 806, 39

Ostriker J. P., McKee C. F., 1988, Reviews of Modern Physics, 60, 1

Ostriker J., Peebles P., Yahil A., 1974, ApJ, 193, L1

Peterson B. M., Bentz M. C., 2006, NewAR, 50, 796

Planck collaboration ., 2016, A&A, 594, 63

Pounds K. A., Reeves J. N., 2007, MNRAS, 374, 823

Pounds K. A., Reeves J. N., 2009, MNRAS, 397, 249

Pounds K., King A., Page K., O'Brien P., 2003a, MNRAS, 346, 1025

Pounds K., Reeves J., King A., Page K., O'Brien P., Turner M., 2003b, MNRAS, 345, 705

Press, H. Teukolsky S. V. W. F. B., 2007, Numerical recipes: the art of scientific computing, Cambridge University Press

Rees M. J., Ostriker J. P., 1977, MNRAS, 179, 541

Rees M., 1977, Nature, 266, 333

Rees M. J., 1978, The Observatory, 98, 210

Reeves J. N., O'Brien P. T., Braito V., Behar E., Miller L., Turner T. J., Fabian A. C., Kaspi S., Mushotzky R., Ward M., 2009, ApJ, 701, 493

Reeves J. N., O'Brien P. T., Ward M. J., 2003, ApJ, 593, L65

Reynolds C. S., Fabian A. C., 1995, MNRAS, 273, 1167

Richings A. J., Faucher-Giguère C.-A., 2018, MNRAS, 478, 3100

Rubin V., Ford W., 1970, ApJ, 159, 379

Rupke D. S. N., Veilleux S., 2011, ApJ, 729, L27

Rupke D. S. N., Gültekin K., Veilleux S., 2017, ApJ, 850, 40

Sako M., Kahn S., Behar E., Kaastra J., Brinkman A., Boller T., Puchnarewicz E., Starling R., Liedahl D., Clavel J., Santos-Lleo M., 2001, A&A, 365, L168

Salpeter E., 1964, ApJ, 140, 796

Sandage A., 1961, The Hubble Atlas of Galaxies, Carnegie Inst., 1 edition

Sandage A., 1965, ApJ, 141, 1560

Santini P., Fontana A., Grazian A., Salimbeni S., Fiore F., Fontanot F., Boutsia K., Castellano M., Cristiani S., de Santis C., Gallozzi S., Giallongo E., Menci N., Nonino M., Paris D., Pentericci L., Vanzella E., 2009, A&A, 504, 751

Sargent W. L. W., Young P. J., Boksenberg A., Shortridge K., Lynds C. R., Hartwick F. D. A., 1978, ApJ, 221, 731

Sarzi M., Rix H.-W., Shields J. C., McIntosh D. H., Ho L. C., Rudnick G., Filippenko A. V., Sargent W. L. W., Barth A. J., 2002, ApJ, 567, 237

Sazonov S. Y., Ostriker J. P., Ciotti L., Sunyaev R. A., 2005, MNRAS, 358, 168

Schawinksi K., Urry C., Simmons B., Fortson L., Kaviraj S., Keel W., Lintott C., Masters K., Nichol R., Sarzi M., Skibba R., Treister E., Willet K., Wong O., Yi S., 2014, MNRAS, 440, 889

Schmidt M., 1963, Nature, 197, 1040

Schwarzschild M., 1979, ApJ, 232, 236

Schwarzschild M., 1993, ApJ, 409, 563

Sérsic J., 1968, Atlas de galaxias australes, Cordoba, 1 edition

Silk J., Rees M., 1998, A&A, 331, L1

Smith M. D., Bureau M., Davis T. A., Cappellari M., Liu L., North E. V., Onishi K., Iguchi S., Sarzi M., 2019, MNRAS, 485, 4359

Soltan A., 1982, MNRAS, 200, 115

Springel V., Di Matteo T., Hernquist L., 2005, MNRAS, 361, 776

Steigman G., Strittmatter P. A., Williams R. E., 1975, ApJ, 198, 575

Sturm E., González-Alfonso E., Veilleux S., Fischer J., Graciá-Carpio J., Hailey-Dunsheath S., Contursi A., Poglitsch A., Sternberg A., Davies R., Genzel R., Lutz D., Tacconi L., Verma A., Maiolino R., De Jong J., 2011, ApJ, 733, L16

Sutherland R. S., Dopita M. A., 1993, ApJS, 88, 253

Taylor J., Navarro J., 2001, ApJ, 563, 483

Tombesi F., Cappi M., Reeves J., Palumbo G., Yaqoob T., Braito V., Dadina M., 2010, A&A, 521, A57

Tombesi F., Cappi M., Reeves J. N., Palumbo G. G. C., Braito V., Dadina M., 2011, ApJ, 742, 44

Tombesi F., Meléndez M., Veilleux S., Reeves J., Gonzélez-Alfonso E., Reynolds C., 2015, Nature, 519, 436

Tombesi F., Veilleux S., Meléndez M., Lohfink A., Reeves J. N., Piconcelli E., Fiore F., Feruglio C., 2017, ApJ, 850, 151

Tully R. B., Fisher J. R., 1977, A&A, 54, 661

Urry C. M., Padovani P., 1995, PASP, 107, 803

Veilleux S., Cecil G., Bland-Hawthorn J., 2005, ARA&A, 43, 769

Vishniac E., 1983, ApJ, 274, 152

Volonteri M., 2010, A&A Rv, 18, 279

Volonteri M., Natarajan P., Gültekin K., 2011, ApJ, 737, 50

Weaver R., McCray R., Castor J., Shapiro P., Moore R., 1977, ApJ, 218, 377

Weymann R. J., Morris S. L., Foltz C. B., Hewett P. C., 1991, ApJ, 373, 23

White S. D. M., Frenk C. S., 1991, ApJ, 379, 52

White S. D. M., Rees M. J., 1978, MNRAS, 183, 341

Zubovas K., King A., 2012, ApJ, 745, L34

Zubovas K., Nayakshin S., 2014, MNRAS, 440, 2625

Zubovas K., Nayakshin S., King A., Wilkinson M., 2013, MNRAS, 433, 3079

Zwicky F., 1933, Helvetica Physica Acta, 6, 110